MASS TRANSFER ENHANCEMENT IN CARBON DIOXIDE GAS HYDRATE FORMATION FOR EFFECTIVE CARBON SEPARATION AND STORAGE

Fengyuan Zhang

A thesis submitted for the degree of
Doctor of Philosophy
The Australian National University

June 2022

© Copyright by Fengyuan Zhang 2022
All Rights Reserved

Declaration

This thesis contains no material which has been accepted for the award of any other degree or diploma in any university. To the best of the author's knowledge, it contains no material previously published or written by another person, except where due reference is made in the text.

Fengyuan Zhang

Fengyuan Zhang
June 2022

Acknowledgments

There are many people whom I must thank. This thesis would not have been possible without the help and support of many people.

I am enormously grateful to my supervisor, Dr Xiaolin (Shannon) Wang and Prof. Wojciech Lipiński, for their continuous support and guidance. They provided professional suggestions and invested abundant time in the project. Every stage of this work has their vital involvement. Without their tremendous efforts, this work could not have been possible.

Many thanks go to Prof. Xia Lou at Curtin University. As my co-supervisor, she provided significant support in the analysis of the experimental results and the writing of the thesis. What touched me the most was that Prof. Lou helped me to revise papers until the early morning several times. I still remember visiting her in Perth with Shannon. Three years have passed in a flash. Special thanks to Prof. Song Wang for vital guidance on numerical calculation.

I want to thank the technical support team at The Australian National University, Dr Beatriz Velasco, Dr Jason Chen, Mr Neil Kaines, Mr Colin Carvolth, Mr Kevin Carvolth, and Mr Erasmo Scipione, for their kind help with the preparation of the experimental setup.

Thanks also go to my friends in the Solar Thermal Group at ANU, Dr Ye Wang, Dr Bo Wang, Dr Lifeng Li, Dr Song Yang, Dr Meige Zheng, Mr Shuang Wang, Miss Jingjing Chen, and Mr Yifan Guo, for their encouragement and assistance.

I would also like to thank Chen Fu Wong, my housemate and best friend in Australia. When I first moved to Australia, he taught me many life skills and cheered me up when I was tired.

Lastly, I want to thank my parents whose constant support and care kept me motivated and confident. I will be eternally grateful for their unwavering love and support throughout my PhD studies and every day.

Abstract

Carbon dioxide (CO_2) is widely acknowledged as a significant contributor to global warming. Hydrate-based carbon capture (HBCC) technology holds high potential in delivering cost-effective and environmentally friendly carbon capture solutions. However, the relatively severe formation conditions and low formation rate of gas hydrates limit its practical applications. This thesis focuses on the mass transfer enhancement methods for effective CO_2 hydrate formation through experimental and numerical studies.

The thermodynamic and kinetic promotion experiments on CO_2 hydrate formation using chemical promoters are implemented in tetra-*n*-butyl ammonium bromide (TBAB) solution with surfactants. TBAB, as a thermodynamic promoter, can moderate hydrate phase equilibrium by forming CO_2–TBAB semiclathrate hydrates. However, it decreases CO_2 gas uptake yields. Three kinds of surfactants, namely anionic surfactant sodium dodecyl sulfate (SDS), cationic surfactant dodecyl-trimethylammonium chloride (DTAC), and non-ionic surfactant Tween 80 (T-80), are added in the system to increase the formation rate and offset the low gas uptake yields. Induction time, normalized gas uptake, split fraction and separation factor are the performance metrics.

The results in TBAB systems show that the hydrate formation is most accelerated with the addition of SDS, but DTAC shows better CO_2 separation performance. Similar results of rapid formation rate with the addition of non-ionic surfactant T-80 are also found. Analysis of variance is used to analyze the difference among experimental results, and a decision box is proposed to evaluate the performance of the systems studied. Compared with SDS and DTAC, 2000-ppm T-80 shows the best CO_2 separation performance in semiclathrate hydrates.

The mass transfer can also be enhanced by adding microparticles due to their considerable surface areas. The kinetic promotion experiments of CO_2 hydrate formation are thus further studied in "dry water" and silica gel (SG) microparticles of different sizes. The experimental results reveal that "dry water" particles with 8-wt% silica has the highest normalized gas uptakes. However, "dry water" are broken after a repeat cycle. SDS and DTAC are added to the SG system to further enhance gas–water mass transfer. With the addition of surfactants in 100-nm SGs, SDS systems save up to 23.7%–49.3% time to achieve the same amount of gas uptake, while DTAC systems save 16% of the time. SGs show better stability and promotion effect than "dry water".

A modified shrinking core model (SCM) is established to study the CO_2 hydrate formation kinetics in both "dry water" particles and SG pores. It is the first model that integrates the effects of CO_2 solubility, capillary effect, volume expansion, and heat transfer model. The hydrate formation in both pure CO_2 and CO_2/N_2 gas mixtures are simulated to reveal the different roles of CO_2 and N_2 molecule diffusion and reaction in hydrate formation. In "dry water" particles, the water consumed through capillaries accounts for less than 10% of the total water consumed. The decoupled heat transfer model reveals that the instantaneous temperature gradient in the hydrate shell is of a small magnitude of 10^{-2} K m^{-1}. In SG pores, the initial proportion of water consumed by capillary effect is only 1%–26.6%, but it can be up to 74.9% in small pores with surfactants.

This work provides comprehensive insights into gas hydrate formation in both water systems and microparticles. It contributes a theoretical basis for the improvement of gas hydrate kinetics through mass transfer enhancement. The modeling strategies in this work can be applied to hydrate formation mechanisms in other porous materials.

Table of Contents

Declaration i

Acknowledgments iii

Abstract v

Table of Contents vii

List of Publications xiii

Nomenclature xv

List of Tables xix

List of Figures xxi

Chapter 1 Introduction 1

- 1.1 Gas hydrates 1
  - 1.1.1 Gas hydrate crystal structures 1
  - 1.1.2 Properties of gas hydrate 4
- 1.2 Hydrate formation kinetics 5
- 1.3 Methods for promoting hydrate formation 8
  - 1.3.1 Thermodynamic promotion 8
  - 1.3.2 Kinetic promotion 10
  - 1.3.3 Combined effects of thermodynamic and kinetic promotion 11
  - 1.3.4 Hydrate formation in porous media 12
- 1.4 Kinetics models of hydrate growth 13
- 1.5 Hydrate-based carbon capture 15
- 1.6 Research objectives 17

Chapter 2 Thermodynamic and kinetic promotions of CO_2 hydrate formation using chemical promoters..21

2.1 Introduction..21

2.2 CO_2–TBAB semiclathrate hydrate formation...22

2.3 Experimental study on combined effects of TBAB and ionic surfactants.....24

2.3.1 Experimental methods 25

2.3.2 Performance metrics 28

2.4 Results and discussion of combined effects of TBAB and ionic surfactants 31

2.4.1 Induction time 31

2.4.2 Gas uptake during hydrate formation 32

2.4.3 CO_2 recovery during hydrate formation 37

2.4.4 Effect of subcooling on CO_2 hydrate formation 40

2.4.5 CO_2 uptake rate and intensive uptake period of hydrate formation.....42

2.5 Experimental study on combined effects of TBAB and non-ionic surfactant... 46

2.5.1 Experimental procedure...46

2.5.2 Experimental conditions 47

2.6 Results and discussion of combined effects of TBAB and non-ionic surfactant 49

2.6.1 Induction time 49

2.6.2 CO_2 gas uptake..49

2.6.3 Percent water conversion 55

2.6.4 CO_2 hydrate growth rate 56

2.6.5 CO_2 recovery and separation 57

2.7 Decision box for optimal systems...63

2.8 Summary..64

Chapter 3 Kinetic promotion of CO_2 hydrate formation in microparticles...67

3.1 Introduction..67

3.2 Experimental study of hydrate formation in dry water.................................68

3.2.1 Preparation of dry water....................68

3.2.2 Apparatus and procedures....................69

3.3 CO_2 hydrate formation kinetics in dry water....................71

3.3.1 Pressure and temperature profile of hydrate formation in dry water...71

3.3.2 Normalized gas uptake of hydrate formation in dry water....................72

3.3.3 Cyclic performance of dry water in hydrate formation....................74

3.4 Experimental study of hydrate formation in silica gels....................76

3.4.1 Preparation of saturated silica gels....................76

3.4.2 Experimental procedures....................77

3.5 CO_2 hydrate formation kinetics in silica gels....................78

3.5.1 Normalized gas uptake of hydrate formation in silica gels....................78

3.5.2 Percent water conversion....................79

3.6 Summary....................80

Chapter 4 CO_2 hydrate formation in silica gel pores in the presence of surfactants 81

4.1 Introduction....................81

4.2 Experimental study....................82

4.2.1 Experimental materials....................82

4.2.2 Apparatus and procedures....................82

4.3 Results and discussion....................84

4.3.1 Effect of surfactants concentration....................84

4.3.2 Effect of silica gel pore size....................86

4.3.3 CO_2 recovery and separation performance....................88

4.3.4 Induction time....................88

4.3.5 Percent water conversion....................89

4.4 Summary....................90

Chapter 5 Modeling study of CO_2 hydrate formation kinetics in microparticles 93

5.1 Introduction....93
5.2 System description and assumptions....94
5.2.1 Hydrate formation in dry water particles....94
5.2.2 Hydrate formation in silica gel pores....95
5.3 Hydrate growth at the hydrate–water interface....96
5.3.1 Diffusion-controlled functions....96
5.3.2 Reaction-controlled functions....97
5.3.3 Mass balance of gas....99
5.4 Capillary effect of the hydrate shell....99
5.5 Mass balance of water....101
5.6 Effective diffusion coefficient and capillary structure parameter....103
5.7 Model validation and extraction of kinetic constants....104
5.7.1 CO_2 hydrate formation in dry water....105
5.7.2 CO_2 hydrate formation in silica gels....106
5.7.3 CO_2/N_2 hydrate formation in silica gels....109
5.8 Simulation results of CO_2 hydrate formation in dry water....111
5.8.1 Volume change as hydrate forms....111
5.8.2 Effective diffusion coefficient....112
5.8.3 Water consumption and capillary effect....115
5.8.4 Heat transfer of hydrate formation in dry water....116
5.9 Simulation results of CO_2 hydrate formation in silica gels....119
5.9.1 Combined reaction rate constant....119
5.9.2 Effective diffusion coefficient....120
5.9.3 Variation of hydrate shell radius....121
5.9.4 Water consumption by capillary effect....122
5.10 Simulation results of CO_2/N_2 hydrate formation in silica gels....125
5.10.1 Combined reaction rate constant....125
5.10.2 Effective diffusion coefficient....126

5.10.3 Variation of hydrate shell radius....................128

5.11 Summary....................129

Chapter 6 Conclusions and outlook....................133

6.1 Summary and conclusions....................133

6.2 Outlook....................136

Appendix A Two-film theory and population balance....................139

A.1 Introduction....................139

A.2 Homogeneous reaction rate and two-film theory....................139

A.3 Population balance....................144

Appendix B Calculation of fugacity by Peng–Robinson equation of state...149

B.1 Introduction....................149

B.2 PR cubic expression....................149

B.3 Fugacity coefficient....................151

B.4 Calculation of other parameters....................151

B.4.1 Density and molar volume of gas mixtures....................151

B.4.2 Departure internal energy, departure enthalpy and departure entropy..........................152

Appendix C Student's *t*-distribution and Analysis of Variance....................153

C.1 Introduction....................153

C.2 Analysis of Variance....................154

C.3 The *p*-value analysis....................154

Bibliography....................157

List of Publications

The following peer-reviewed journal papers accompany this research:

[1] **Zhang F**, Wang X*, Wang B, Lou X, Lipiński W*. The effect of silica gel nanopores and surfactants on CO_2 hydrate formation kinetics: An experimental and modeling study based on shrinking core model. Chemical Engineering Science. 2022;262:118002.

[2] **Zhang F**, Bhatia SK, Wang B, Chalermsinsuwand B, Wang X*. Experimental and numerical study on the kinetics of CO_2–N_2 clathrate hydrates formation in silica gel column with dodecyltrimethylammonium chloride for effective carbon capture. Journal of Molecular Liquids. 2022;363:119764.

[3] **Zhang F**, Wang X*, Lou X, Lipiński W*. Effects of Tween 80 on clathrate and semiclathrate CO_2 hydrates formation kinetics for carbon capture from rich-CO_2 gas mixtures. Carbon Capture Science & Technology. 2022;4:100053.

[4] **Zhang F**, Wang X*, Wang B, Lou X*, Lipiński W*. Experimental and numerical analysis of CO_2 and CH_4 hydrate formation kinetics in microparticles: A comparative study based on shrinking core model. Chemical Engineering Journal. 2022;446:137247.

[5] **Zhang F**, Wang X, Lou X, Lipiński W*. The effect of sodium dodecyl sulfate and dodecyltrimethylammonium chloride on the kinetics of CO_2 hydrate formation in the presence of tetra-n-butyl ammonium bromide for carbon capture applications. Energy. 2021;227:120424

[6] Wang X*, **Zhang F**, Lipiński W. Carbon dioxide hydrates for cold thermal energy storage: A review. Solar Energy. 2020;211:11–30.

[7] Wang X*, **Zhang F**, Lipiński W. Research progress and challenges in hydrate-based carbon dioxide capture applications. Applied Energy. 2020;269:114928.

The following peer-reviewed conference papers accompany this research:

[1] **Zhang F**, Wang X*, Lipiński W*. Feasibility study on hydrate-based carbon capture driven by solar thermal sorption chiller. Solar World Congress, ISES Conference Proceedings, 2021, doi:10.18086/swc.2021.26.07.

[2] **Zhang F**, Wang X[*], Lipiński W[*]. Solar thermal driven hydrate-based carbon capture enabled by tetra-*n*-butylammonium bromide and sodium dodecyl sulphate. AlChE Solar Energy Systems Conference, 2021.

[3] Wang X[*], **Zhang F**, Lipiński W. Recent research progress in CO_2 hydrate based cold thermal energy storage. Solar World Congress, ISES Conference Proceedings, 2019.

[4] Wang X[*], Dennis M, **Zhang F**. CO_2 gas hydrate technology in cold thermal energy storage applications and its challenges. Refrigeration Conference of AIRAH, Melbourne, 2019.

Nomenclature

Variables

c_{HG}	gas concentration at the hydrate–gas interface, mol m^{-3}
c_{HL}	gas concentration at the hydrate–liquid interface, mol m^{-3}
D_{s}	effective diffusion coefficient, m^2s^{-1}
$D_{\mathrm{s},0}$	initial effective diffusion coefficient, m^2s^{-1}
f	fugacity of gas, MPa
K^*	combined reaction rate constant, mol $m^{-2}MPa^{-1}s^{-1}$
K_{d}	mass-transfer rate constant, mol $m^{-2}MPa^{-1}s^{-1}$
K_{r}	“reaction” rate constant, mol $m^{-2}MPa^{-1}s^{-1}$
k_{H}	Henry’s constant, mol $m^{-3}MPa^{-1}$
M_{w}	molar mass of water, g mol^{-1}
n	amount of gas consumed, mol
n_{c}	number of capillary tubes
$n_{\mathrm{CO_2},0}$	initial amount of CO_2 in the reactor, mol
$n_{\mathrm{g},0}$	initial amount of gas pressurized into the reactor, mol
$n_{\mathrm{g},t}$	amount of gas in the reactor at any given time t, mol
$n_{\mathrm{H_2O}}$	total amount of water initially in the reactor, mol
$n_{\mathrm{CO_2}}^{\mathrm{H}}$	amount of CO_2 in the hydrate phase at the end of the experiment, mol
$n_{\mathrm{CO_2}}^{\mathrm{gas}}$	amount of CO_2 in the gas phase at the end of the experiment, mol
$n_{\mathrm{N_2}}^{\mathrm{H}}$	amount of N_2 in the hydrate phase at the end of the experiment, mol

$n_{\mathrm{N_2}}^{\mathrm{gas}}$	amount of N_2 in the gas phase at the end of the experiment, mol
NG_t	normalized gas uptake at any given time t, $\mathrm{mol}_{(\mathrm{gas})}/\mathrm{mol}_{(\mathrm{water})}$
$\mathrm{NR}_{30,\mathrm{CO_2}}$	normalized rate of CO_2 hydrate growth for the first 30 min after the CO_2 hydrate formation, mol $\mathrm{min}^{-1}\mathrm{m}^{-3}$
P_0	initial pressure in the reactor, Pa
P_{eq}	phase equilibrium pressure, MPa
P_{exp}	experimental pressure, MPa
P_t	pressure in the reactor at time t, Pa
R	ideal gas constant
r	radius, m
r_{c}	radius of capillary tubes, m
r_{i}	inner radius of hydrate shell, m
r_{o}	outer radius of hydrate shell, m
s	solubility, mol m^{-3}
T_{exp}	experimental temperature, K
$v_{\mathrm{w,cap}}$	water consumption rate in capillaries, $\mathrm{m}^3\mathrm{s}^{-1}$
$V_{\mathrm{w,cap}}$	water consumption in capillaries, m^3
$V_{\mathrm{w,ini}}$	initial volume of water in a single SG, m^3
$v_{\mathrm{w,total}}$	total water consumption rate, $\mathrm{m}^3\mathrm{s}^{-1}$
$V_{\mathrm{w,total}}$	total water consumption, m^3
Z_0	gas compressibility factor at $t = 0$
Z_t	gas compressibility factor at time t

Greek symbols

α	porosity of silica gels
β	hydration number
μ_{w}	dynamic viscosity, Pa s
$\varepsilon_{\mathrm{cap}}$	capillary structure parameter, $\mathrm{m}^2\mathrm{N}\ \mathrm{Pa}^{-1}\mathrm{s}^{-1}$

$\varepsilon_{\mathrm{cap},0}$	initial capillary structure parameter, $\mathrm{m^2 N\ Pa^{-1} s^{-1}}$
θ	contact angle
ξ	reduction factor of effective diffusion coefficient
ς	reduction factor of the capillary structure parameter
σ	surface tension, $\mathrm{N\ m^{-1}}$
τ	tortuosity of the capillary
$\Phi_{\mathrm{g,\,d}}$	gas diffusion rate at the hydrate–liquid interface, $\mathrm{mol\ s^{-1}}$
$\Phi_{\mathrm{g,\,r}}$	gas consumption rate at the hydrate–liquid interface, $\mathrm{mol\ s^{-1}}$
$\Phi_{\mathrm{g,\,s}}$	pre-dissolved gas consumption rate, $\mathrm{mol\ s^{-1}}$
ρ_{w}	water density, $\mathrm{g\ m^{-3}}$

Subscripts

eq	phase equilibrium state
HG	hydrate–gas interface
HL	hydrate–liquid interface
w	water

Abbreviations

HBCC	hydrate-based carbon capture
MAPE	mean absolute percentage error
PWC	present water conversion
SCM	shrinking core model
SG	silica gel

List of Tables

Table 1.1. Geometry of cages. 3

Table 1.2. Densities of common gas hydrates at 273.15 K...4

Table 1.3. Thermal properties of gas hydrates...5

Table 1.4. The chemical structure of various chemical additives [9]. 9

Table 1.5. Hydrate growth models..15

Table 2.1. Apparatus and materials properties..26

Table 2.2. Experimental conditions for the studied CO_2 hydrate formation systems. 27

Table 2.3. The intensive uptake periods of TBAB+SDS (SDS at 500 ppm) and TBAB+DTAC (DTAC at 0.1 wt%) systems at three subcooling degrees. 44

Table 2.4. Summary of experimental conditions and measured data. 47

Table 2.5. Summary of experimental findings..62

Table 3.1. The preparation process and the average measured sizes of “dry water”. 69

Table 3.2. Experimental conditions and measured induction time of hydrate formation in “dry water”...71

Table 3.3. Gas uptake yield in 1000 min and percent reduction of yield for repeat runs. 74

Table 3.4. Structural properties of silica gels..77

Table 3.5. Summary of experimental conditions. 78

Table 3.6. Percent water conversion at the end of CO_2 hydrate formation (600 min). 80

Table 4.1. Summary of experimental conditions. 83

Table 4.2. Separation performance for CO_2/N_2 hydrates formation with DTAC. 88

Table 5.1. Summary of optimal parameters of CO_2 hydrate formation in “dry water”. 107

Table 5.2. Summary of optimal parameters of CO_2 hydrate formation in silica gels. 109

Table 5.3. Summary of optimal parameters of CO_2/N_2 hydrate formation in silica gels. 110

Table C.1. Critical values for student’s *t*-distribution. 153

Table C.2. Calculation of *F*-statistic. 154

List of Figures

Figure 1.1. Hydrate crystal unit structures: (a) sI, (b) sII, and (c) sH [1]. 2

Figure 1.2. Three cavities in gas clathrate hydrates: (a) pentagonal dodecahedron (5^{12}), (b) tetrakaidecahedron ($5^{12}6^{2}$), (c) hexakaidecahedron ($5^{12}6^{4}$), (d) irregular dodecahedron ($4^{3}5^{6}6^{3}$), and (e) icosahedron ($5^{12}6^{8}$) [1]............3

Figure 1.3. Hypothesis picture of hydrate growth at a crystal [1]. 6

Figure 1.4. Typical gas uptake curve during hydrate formation in a stirred tank reactor [7]..7

Figure 1.5. Low-temperature (at 163 K) SEM image for methane hydrates formed in porous silica gels [2]. 13

Figure 1.6. Mechanism of hydrate-based CO_2 capture [21]. 16

Figure 2.1. Phase equilibrium of CO_2–TBAB hydrate at various mass fraction [13]. 22

Figure 2.2. CO_2 gas uptake at various feed pressures and TBAB mass fractions [13]. 23

Figure 2.3. Schematic diagram of the experimental apparatus.................................26

Figure 2.4. Phase diagram for CO_2 hydrate in the water system and CO_2–TBAB semiclathrate hydrate at different TBAB concentrations [25]................27

Figure 2.5. Induction time for the experimental runs investigated in this study. For the water system, the experimental temperature is 276.45 K; for the TBAB system, the experimental temperature is 283.15 K...............................32

Figure 2.6. Normalized CO_2 gas uptake with SDS at 276.45 K. Vertical error bars correspond to 95% confidence intervals...33

Figure 2.7. Normalized CO_2 gas uptake with DTAC at 276.45 K. Vertical error bars correspond to 95% confidence intervals. 34

Figure 2.8. Normalized CO_2 gas uptake in TBAB+SDS solution at 283.15 K. Vertical error bars correspond to 95% confidence intervals. 35

Figure 2.9. Normalized CO_2 gas uptake in TBAB+DTAC solution at 283.15 K. Vertical error bars correspond to 95% confidence intervals. 36

Figure 2.10. Normalized rate of CO_2 hydrate growth, NR_{30,CO_2}. For DTAC and SDS in water system, $T_{exp} = 276.45$ K. For TBAB+DTAC and TBAB+SDS, $T_{exp} = 283.15$ K. Horizontal error bars correspond to 95% confidence intervals. 37

Figure 2.11. Split fraction after hydrate formed for 6 hours. For DTAC and SDS in water systems, $T_{exp} = 276.45$ K; for DTAC and SDS in TBAB systems $T_{exp} = 283.15$ K. Horizontal error bars correspond to 95% confidence intervals. 39

Figure 2.12. Separation factor after hydrate formed for 6 hours. For DTAC and SDS in water systems, $T_{exp} = 276.45$ K; for DTAC and SDS in TBAB systems, $T_{exp} = 283.15$ K. Horizontal error bars correspond to 95% confidence intervals. 39

Figure 2.13. Effect of subcooling for TBAB+SDS system with SDS of 500 ppm. .. 40

Figure 2.14. Effect of subcooling for TBAB+DTAC with DTAC of 1000 ppm. 41

Figure 2.15. Effect of subcooling on split fraction. 42

Figure 2.16. Effect of subcooling on separation factor. 42

Figure 2.17. Normalized CO_2 gas uptake rate for TBAB+SDS (SDS at 500 ppm) and TBAB+DTAC (DTAC at 1000 ppm) systems at subcooling of 2.69 K. The scatter lines represent the normalized CO_2 gas uptake, and the dash lines are the 1st derivatives of the normalized CO_2 uptake. 43

Figure 2.18. CO_2 hydrates formation with 2000-ppm DTAC with/without TBAB in the hydrate reactor: (a1) and (b1) before hydrate formation; (a2) and (b2) hydrate film thickness less than CHFT; (a3) and (b3) hydrate film thickness reaches CHFT; (a4) and (b4) end of hydrate formation. 45

Figure 2.19. A typical temperature and pressure curve (For exp. no. 4). 50

Figure 2.20. Induction time in the experimental runs of different systems at $P_{\text{exp}} = 3.8$ MPa. For clathrate hydrates, $T_{\text{exp}} = 276.45$ K; for semiclathrate hydrates, $T_{\text{exp}} = 283.15$ K...50

Figure 2.21. Normalized CO_2 uptake in clathrate hydrates with T-80 at 276.45 K, 3.8 MPa..52

Figure 2.22. The *p*-value of the normalized CO_2 uptakes in clathrate hydrates. 52

Figure 2.23. Normalized CO_2 uptake in semiclathrate hydrates at 283.15 K, 3.8 MPa. 53

Figure 2.24. The *p*-value of the normalized CO_2 uptakes in semiclathrate hydrates.54

Figure 2.25. Photographs of hydrate formation at $t = 360$ min. For clathrate hydrates, $T_{\text{exp}} = 276.45$ K, $P_{\text{exp}} = 3.8$ MPa; for semiclathrate hydrates, $T_{\text{exp}} = 283.15$ K, $P_{\text{exp}} = 3.8$ MPa. (a1) T-80 at 1000 ppm, (a2) T-80 at 2000 ppm, (a3) T-80 at 3000 ppm; (b1) TBAB with 1000-ppm T-80, (b2) TBAB with 2000-ppm T-80, (b3) TBAB with 3000-ppm T-80. 54

Figure 2.26. Effect of initial pressure on CO_2 gas uptake in clathrate and semiclathrate hydrates with 1000-ppm T-80...55

Figure 2.27. Percent water conversion for all the studied runs at 126 min and 360 min, $P_{\text{exp}} = 3.8$ MPa. 56

Figure 2.28. CO_2 hydrate growth rate of all experimental runs at $P_{\text{exp}} = 3.8$ MPa. In clathrate hydrates, $T_{\text{exp}} = 276.45$ K. In semiclathrate hydrates, $T_{\text{exp}} = 283.15$ K. 57

Figure 2.29. CO_2 split fraction of all experiment runs ($P_{\text{exp}} = 3.8$ MPa). 58

Figure 2.30. CO_2 separation factor of all experiment runs ($P_{\text{exp}} = 3.8$ MPa)............58

Figure 2.31. Effect of initial pressure on CO_2 split fraction. 60

Figure 2.32. Effect of initial pressure on CO_2 separation factor...............................61

Figure 2.33. Comparison of the kinetic promotion performance of the optimal concentration of three surfactants—T-80, SDS and DTAC in 10-wt% TBAB solutions. 61

Figure 2.34. Eisenhower Decision Box for optimal systems. The vertical axis shows the percent water conversion of samples at the end of intensive uptake period (t = 126 min). 63

Figure 3.1. Appearance of “dry water” synthesized from hydrophobic silica “H18” and deionized water. 68

Figure 3.2. Micrographs of “dry water” particles: (a) with 3-wt% silica; (b) with 5-wt% silica; and (c) with 8-wt% silica. 69

Figure 3.3. Schematic diagram of the experimental setup. 70

Figure 3.4. P-t and T-t profiles at the start of CO_2 hydrate formation in “dry water” with 5-wt% silica at T_{exp} = 277.15 K. 72

Figure 3.5. Normalized CO_2 gas uptake in the fresh cycle of different sizes of “dry water” particles. 73

Figure 3.6. CO_2 uptake in fresh and repeat hydrate formations in “dry water” at a constant temperature of 277.15 K: (a) with 8-wt% silica, (b) with 5-wt% silica, and (c) with 3-wt% silica. 75

Figure 3.7. “Dry water” with 3-wt% silica in the reactor after two cycles of CO_2 hydrate formation 76

Figure 3.8. Percent water conversion after 1000 min of CO_2 hydrate formation. 76

Figure 3.9. Structure of the spherical hydrophilic silica gel used in this work. (Copyright Nouryon–image used with permission) 77

Figure 3.10. Normalized CO_2 gas uptake in SGs of different pore sizes 79

Figure 4.1. Schematic diagram of the experimental system. 83

Figure 4.2. Normalized CO_2 gas uptake in 100-nm SGs with different SDS concentrations in pure CO_2 systems (Exp. no. 1, 4 and 5). 84

Figure 4.3. Normalized CO_2 gas uptake in 100-nm SGs with varied DTAC concentrations in pure CO_2 systems (Exp. no. 1, 8 and 9). 85

Figure 4.4. Effect of DTAC concentration on the normalized CO_2 gas uptake in 100-nm SGs (CO_2/N_2 systems, Exp. no. 10, 13, 14 and 15). 86

Figure 4.5. Effects of 500-ppm SDS on CO_2 hydrate formation in 30-nm SGs and 50-nm SGs in pure CO_2 systems (Exp. no. 2, 3, 6 and 7). 87

Figure 4.6. Effect of silica gel pore size on the normalized CO_2 gas uptake for CO_2/N_2 gas mixture systems (Exp. no. 10, 11 and 12). 87

Figure 4.7. Induction time of CO_2/N_2 hydrates formation with DTAC. 89

Figure 4.8. Percent water conversion at the end of each experiment (600 min)........90

Figure 5.1. Schematic diagram of the physical model for hydrate growth in "dry water". 95

Figure 5.2. Physical model for CO_2 hydrate formation within a SG particle. 96

Figure 5.3. Simulated gas consumptions during hydrate formation in "dry water" using the SCM: (a) CO_2 with 3-wt% silica; (b) CO_2 with 5-wt% silica; (c) CO_2 with 8-wt% silica; and (d) CH_4 with 5-wt% silica...............................106

Figure 5.4. Experimental and simulation results of gas consumption in CO_2 hydrate formation in SGs. 108

Figure 5.5. Experimental and simulation results of CO_2/N_2 hydrate formation in silica gels. 110

Figure 5.6. Schematic diagrams of hydrate formation in a "dry water" particle. 111

Figure 5.7. The variation of radius of hydrate shell and inner water droplets during hydrate formation in "dry water": (a) CO_2 with 3-wt% silica; (b) CO_2 with 5-wt% silica; (c) CO_2 with 8-wt% silica; and (d) CH_4 with 5-wt% silica. 113

Figure 5.8. Effective diffusion coefficient of CO_2 through formed hydrate in "dry water" particles of different sizes. 114

Figure 5.9. Water consumption at hydrate–water interface and by capillary effect in hydrate formation in “dry water”: (a) CO_2 with 3-wt% silica; (b) CO_2 with 5-wt% silica; (c) CO_2 with 8-wt% silica; and (d) CH_4 with 5-wt% silica. 116

Figure 5.10. The schematic diagram for heat transfer at the hydrate–water interface. 117

Figure 5.11. Temperature profile of CO_2 hydrate shell in “dry water” particle with 8-wt% silica at (a) $t = 100$ min; (b) $t = 300$ min; and (c) $t = 500$ min. 119

Figure 5.12. Effective diffusion coefficient of CO_2 through hydrate shell in SG pores. 121

Figure 5.13. Hydrate shell thickness during CO_2 hydrate formation. 122

Figure 5.14. Water consumption during CO_2 hydrate formation in SG pores. (a1)–(a7) water consumed by capillary effect; (b1)–(b7) total water consumption. 123

Figure 5.15. Initial proportion of water consumed by capillaries. 124

Figure 5.16. Indicative illustration of initial changes of capillaries with the addition of surfactants. 125

Figure 5.17. Effective diffusion coefficient of CO_2 through the hydrate shell with percent water conversion. 128

Figure 5.18. Radius change of hydrate shell during the gas hydrate formation. (a) in pure water systems; (b) in 100-nm SGs. 129

Figure A.1. Schematic diagram of gas dissolved through the film. 140

Figure A.2. Schematic diagram of two-film theory. 141

Chapter 1 Introduction

1.1 Gas hydrates

Carbon dioxide (CO_2) is widely acknowledged as a significant contributor to global warming. Carbon capture and storage (CCS) technology is considered as one of the effective strategies to mitigate climate change in the short term. Conventional carbon capture technologies bring issues including high energy consumption and solvent pollution. Clathrate hydrate technology holds high potential in delivering cost-effective and environmentally friendly carbon capture solutions.

Gas hydrates are crystalline solids composed of water and gas. The gas molecules (guests) are trapped in water cavities (host) that are composed of hydrogen-bonded water molecules. Typical gas molecules include methane (CH_4), ethane (C_2H_6), hydrogen (H_2), and CO_2. The formation conditions of hydrates vary widely depending on the species of gas molecules. However, the crystal structures of the formed hydrates are limited. All common gas hydrates are classified into three crystal structures: cubic structure I (sI), cubic structure II (sII), and hexagonal structure H (sH).

1.1.1 Gas hydrate crystal structures

The host water molecules are connected by hydrogen bonds to form a series of polyhedral cavities of different sizes. These cavities are connected by vertices or surfaces and develop to form cage-like hydrate lattices. Without guest molecules, the empty hydrate lattice can be considered as a kind of unstable ice. When the cavities of this unstable ice are partially filled with guest molecules, it becomes a stable gas hydrate. The higher the percentage filled, the more stable it is.

The three crystal structures of hydrates, i.e., cubic structure I (sI), cubic structure II (sII), or hexagonal structure H (sH), are shown in Figure 1.1. One cavity can generally hold only one guest molecule, unless under high pressure when it can also hold two small molecules. The guest molecule and the host molecule are connected by van der Waals force, which is the key to the formation and stable existence of the hydrate.

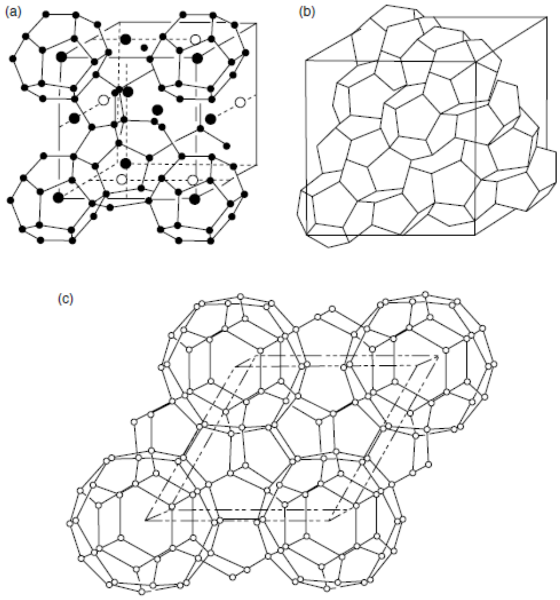

Figure 1.1. Hydrate crystal unit structures: (a) sI, (b) sII, and (c) sH [1].

Structure I is formed with guest molecules having diameters between 4.2 Å and 6.0 Å, such as CH_4, C_2H_6, CO_2, and hydrogen sulfide. Nitrogen (N_2) and small molecules, including hydrogen (H_2, $d < 4.2$ Å), form structure II as single guests. Larger (6Å < d < 7Å) single guest molecules such as propane or iso-butane will form structure II. Much larger molecules (typically 7Å < d < 9Å) such as iso-pentane or neohexane (2, 2-dimethylbutane) can form structure H when accompanied by smaller molecules such as CH_4, hydrogen sulfide (H_2S), or N_2.

All of the hydrate structures in Figure 1.1 are composed of five polyhedra formed by hydrogen-bonded water molecules shown in Figure 1.2, with properties tabulated in Table 1.1. The nomenclature description $n_i^{m_i}$ is often used for these polyhedra, where n_i is the number of edges in face type “i”, and m_i is the number of faces with n_i edges.

The pentagonal dodecahedron (12-sided cavity) of Figure 1.2 is labelled 5^{12} because it has 12 pentagonal faces ($n_i = 5$, $m_i = 12$) with equal edge lengths and equal angles. The 14-sided cavity (tetrakaidecahedron) is called $5^{12}6^2$ because it has 12 pentagonal and 2 hexagonal faces. The 16-hedron (hexakaidecahedral cavity) is denoted $5^{12}6^4$ because in addition to 12 pentagonal faces, it contains 4 hexagonal faces. The irregular dodecahedron cavity ($4^35^66^3$) has three square faces and six pentagonal faces, in addition to three hexagonal faces. The largest icosahedron cavity ($5^{12}6^8$) has 12 pentagonal faces, as well as a girdle of 6 hexagonal faces and a hexagonal face at both the cavity crown and foot.

The guest molecule and the host molecule only form a single crystal structure under a certain condition. However, as the conditions change, the crystal structure formed may also change. For example, when the temperature changes, the crystal structure of cyclopropane hydrate will change from sI to sII, or from sII to sI, and even sI and sII may coexist [1]. The crystal structure may also change due to the addition of another guest molecule. For example, pure CH_4 will form sI, but if a small amount of propane (C_3H_8) is added, it will form sII then.

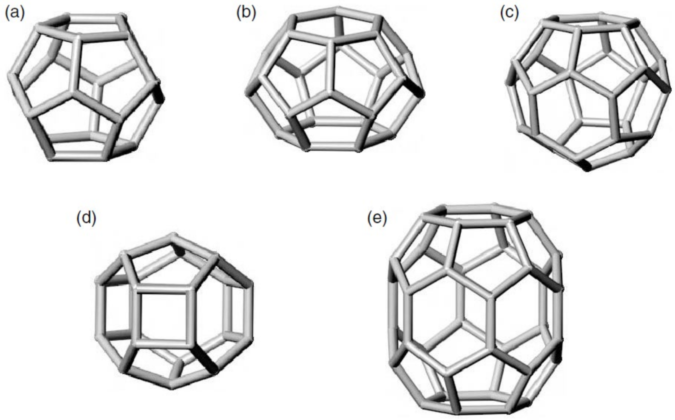

Figure 1.2. Three cavities in gas clathrate hydrates: (a) pentagonal dodecahedron (5^{12}), (b) tetrakaidecahedron ($5^{12}6^2$), (c) hexakaidecahedron ($5^{12}6^4$), (d) irregular dodecahedron ($4^35^66^3$), and (e) icosahedron ($5^{12}6^8$) [1].

Table 1.1. Geometry of cages.

Hydrate crystal structure	sI		sII		sH		
Cavity	Small	Large	Small	Large	Small	Medium	Large
Description	5^{12}	$5^{12}6^2$	5^{12}	$5^{12}6^4$	5^{12}	$4^35^66^3$	$5^{12}6^8$
No. of cavities/unit cell	2	6	16	8	3	2	1
Average cavity radius (Å)	3.95	4.33	3.91	4.73	3.94	4.04	5.79
No. of water molecules/cavity	20	24	20	28	20	20	36
Theoretical expression	$8M\cdot46H_2O$		$24M\cdot136H_2O$		$6M\cdot34H_2O$		

1.1.2 Properties of gas hydrate

Due to the disordered distribution of guest molecules among the cavities, the ratio of guest molecules to host molecules in the crystal is different under different conditions. So hydrate has no definite chemical formula and is a non-stoichiometric mixture. Therefore, we can understand hydrates in this way: the empty hydrate lattice is like a porous medium, and it becomes a hydrate when gas molecules are adsorbed in it. According to theoretical calculations, 1 m^3 gas hydrates can store 160–180 m^3 of the gas at standard pressure and temperature condition [2].

In addition, due to the certain structure of hydrate crystals, the distance between host molecules is greater than that between liquid water molecules. If no guest molecules enter the cavities, the crystal density must be less than 1 g cm^{-3}. In a hypothesis without guest molecules in the cavities, the densities of sI and sII hydrate are 0.796 g cm^{-3} and 0.786 g cm^{-3}, respectively. Generally, the hydrate density is 0.8–1.2 g cm^{-3}. The density of different hydrates can be calculated by the following equations

$$\rho_{\mathrm{I}} = \frac{46\times 18 + 2M\theta_{\mathrm{s}} + 6M\theta_{\mathrm{l}}}{N_0 a^3}, \tag{1.1}$$

$$\rho_{\mathrm{II}} = \frac{136\times 18 + 16M\theta_{\mathrm{s}} + 8M\theta_{\mathrm{l}}}{N_0 a^3}, \tag{1.2}$$

where M is the molecular mass of the guest molecule; θ_{s} and θ_{l} are the fractional occupation of small and large cavities by guest molecules; N_0 is the Avogadro constant; a is the volume of unit cell, for sI hydrate $a = 1.2\times 10^{-7}$ cm^3 mol^{-1}, for sII hydrate $a = 1.73\times 10^{-7}$ cm^3 mol^{-1}. The densities of common gas hydrates are listed in Table 1.2.

Table 1.2. Densities of common gas hydrates at 273.15 K.

Gas	CH_4	C_2H_6	C_3H_8	CO_2	N_2
Molecular mass (g mol^{-1})	16.04	30.07	44.09	44.01	28.04
Density (g cm^{-3})	0.910	0.959	0.866	1.117	0.995

Waite et al. [3] studied the thermal properties of methane hydrate and found that its thermal conductivity (λ) was very low. Basically, the thermal conductivity of CH_4 hydrate is only one-fifth of that of ice. Other thermal properties of gas hydrates are shown in Table 1.3.

Table 1.3. Thermal properties of gas hydrates.

Hydrate structure	sI	sII	Ice
CTE[a] at 220 K ($\times 10^{-5}$ K^{-1})	7.7	5.2	5.6
β_s[b] at 273 K ($\times 10^{-11}$ Pa)	14	14	12
λ at 263 K ($Wm^{-1}K^{-1}$)	0.49 ± 0.2	0.51 ± 0.2	2.23

[a] CET refers to the coefficient of linear thermal expansion;
[b] β_s is the adiabatic compressibility.

1.2 Hydrate formation kinetics

Gas hydrate formation is similar to the crystallization process and can be described by two steps: hydrate nucleation and hydrate growth. Hydrate nucleation is an intrinsically stochastic process that involves the formation and growth of gas–water clusters to critical-sized hydrate nuclei. During the hydrate nucleation process, small clusters of water and gas (hydrate nuclei) grow and disperse in water to achieve critical size for continued growth. The nucleation step is a microscopic phenomenon involving tens to thousands of molecules and is difficult to observe experimentally. Current hypotheses for hydrate nucleation are based upon the better known phenomena of water freezing, the dissolution of hydrocarbons in water, and computer simulations of both phenomena [1]. Evidence from experiments shows that nucleation is a statistically probable process [4].

In contrast, the hydrate growth process involves the continuous growth of stable hydrate nuclei to solid hydrates until reaching a stable condition. On the molecular level, hydrate growth can be considered to be a combination of three factors: (1) the kinetics of crystal growth at the hydrate surface, (2) mass transfer of components to the growing crystal surface, and (3) heat transfer of the exothermic heat of hydrate formation away from the growing crystal surface.

Here, we cite the hydrate formation theory of Sloan in 1994 [1]. A hypothesis picture of hydrate growth at a crystal is shown in Figure 1.3. This conceptual picture for crystal growth may be combined with either the labile cluster or local structuring hypotheses for nucleation. In the figure, step-growth of the hydrate crystal is depicted with the following components:

(i) A guest in a temporal water cluster is transported to the growing crystal surface. The cluster is driven to the surface by the lower Gibbs free energy provided at the crystal surface.

(ii) The cluster adsorbs on the crystal surface. The solid crystal exerts a force field into the fluid which results in the cluster adhering to the surface. Upon adsorption, some of the water molecules detach from the cluster and diffuse away.

(iii) The cluster diffuses over the surface to a step in the crystal. Since the solid force field is perpendicular to the crystal face, the adsorbed species can diffuse only in two dimensions along the surface.

(iv) The cluster attaches to a crystal step, releasing further solvent molecules. The step is an attractive site because two solid faces of the step exert a force (with two surface–reactant interactions) on the mobile species, in contrast to a single force field (with one surface–reactant interaction) on the flat surface.

(v) The cluster can now move only in a single dimension, along the step. The cluster diffuses along the step to a kink or defect point in the step.

(vi) The cluster adsorbs at the kink. The kink is an attractive site because three or more solid faces of the kink exert a larger force on the species than the two forces exerted by the step alone.

(vii) The cluster is now immobilized in three dimensions (not shown).

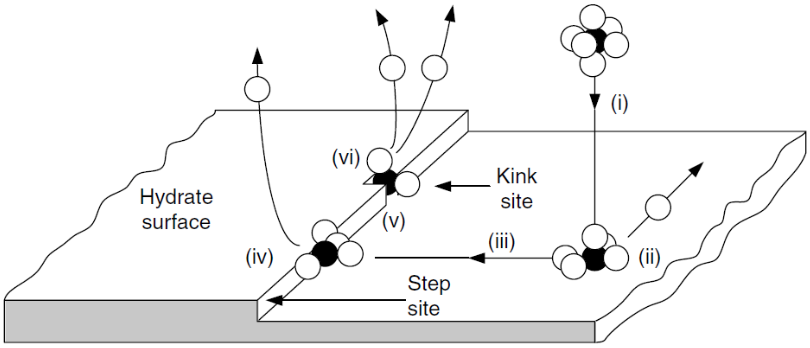

Figure 1.3. Hypothesis picture of hydrate growth at a crystal [1].

To illustrate the concept of hydrate formation more intuitively, Figure 1.4 shows a typical gas absorption curve for the hydrate formation process in a laboratory-scale stirred tank reactor [4]. The rate of gas consumption represents the hydrate formation rate which is controlled by the process of gas dissolution and induction, hydrate nucleation and growth processes. Gas dissolution and hydrate nucleation period is marked as Region 1 in Figure 1.4. This period includes the hydrate nucleation induction, which is the time taken from the attainment of super-saturation until the first hydrate crystal nuclei are visible or detected at the macroscopic level [5, 6]. In contrast, Regions 2, 3 and 4 denote the different stages during hydrate growth. In Region 2, a very rapid hydrate growth occurs and a significant increase in gas consumption can be observed. During the hydrate growth period, gas molecules are being transported from vapour phase to liquid phase and densely packed in the hydrate cages. As the water and gas molecules are consumed during hydrate formation, the rate of hydrate formation gradually decreases with time and finally flattens at the end of the hydrate formation process, which is denoted in Region 3. The attained steady-state in Region 4 could be due to the complete consumption of hydrate-forming components (i.e., water or gas) inside the reactor or the limitation of mass transfer or heat transfer, which results in small driving forces and slow hydrate formation rate. At the point E, the formed hydrate is deemed to be stable, and could be extracted for laboratory testing or used for dissociation experiments.

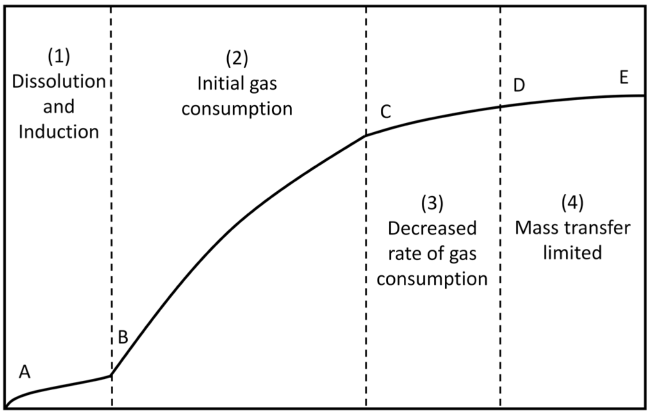

Figure 1.4. Typical gas uptake curve during hydrate formation in a stirred tank reactor [7].

1.3 Methods for promoting hydrate formation

The development of clathrate hydrate technology has been obstructed by its low formation rate and unsatisfied gas capacity. Studies have revealed that the relatively severe formation conditions of hydrate and low mass transfer rate are limitations of gas hydrate technology in practical applications [8]. Methods to enhance mass transfer by increasing gas–liquid contact area or reducing interfacial surface tension is frequently used. Common methods to increase the gas–water interfacial area include spraying, stirring, bubbling, or adding particles. The use of particles in gas hydrate formation provides an effective alternative to mechanical mixing for reduced energy consumption and improved safety. In addition, chemical additives act as hydrate promoters that may reduce the equilibrium hydrate formation pressure, shorten the induction time, increase the hydration rate, enhance gas uptake and improve the selectivity of gas in hydrate cages, which have been of great interest. Chemical promoters are generally divided into two classes: thermodynamic promoters and kinetic promoters. Therefore, the promotion of hydrate formation can also be divided into thermodynamic promotion and kinetic promotion.

1.3.1 Thermodynamic promotion

Thermodynamic promoters induce the formation of the targeted gas hydrates at milder conditions. The most widely investigated thermodynamic promoters include tetrahydrofuran (THF), tetra-*n*-butyl ammonium bromide (TBAB), cyclopentane (CP), and propane (C_3H_8) [9]. THF, CP, and C_3H_8 form hydrates without breaking the structure of the water cavities, while TBAB takes part in the formation of semiclathrate hydrate structures by joining in and changing the water cages. The cages of semiclathrate hydrates are able to encage small-sized gas molecules and have the potential for gas separation; at the same time, the formation of these hydrates promotes a dramatic reduction of formation pressure [7]. The chemical structures of common promoters are presented in Table 1.4 [9].

In recent years, thermal properties of TBAB semiclathrate hydrates such as phase equilibrium and enthalpy of dissociation have been studied extensively by Chazallon et al. [10, 11], especially in the formation of hydrates with CO_2. TBAB with TBA^+ occupies large cages, leaving small cages vacant for CO_2 molecules for stable occupation, and therefore the required formation pressure is reduced [12]. It was reported by Wang and Dennis [13] that the CO_2 hydrate equilibrium pressure was reduced from 4.4 MPa to 0.55 MPa with the addition of 10-wt% TBAB at 283 K. It shows excellent mitigation effects on CO_2 hydrate formation conditions.

Fan et al. [14] presented the CO_2 capture by semiclathrate hydrate formation in 32-wt% TBAB solution. The CO_2 recovery was about 50% by one-stage hydrate separation and can reach up to 90% by two-stage separation. Many papers studied the phase equilibrium conditions of CO_2–TBAB semiclathrate hydrates at different TBAB concentrations [15–17]. Recent literature on the kinetics of CO_2–TBAB semiclathrate hydrates revealed that the presence of TBAB prolonged the formation time and lowered the CO_2 gas uptake [18–20]. The reasons might be that (i) TBA^+ occupies large cages, reducing available cavities to entrap CO_2 [21], and (ii) at high TBAB concentrations, semiclathrate hydrates aggregate on the gas–liquid interface, which hinders further permeation of CO_2 [22, 23].

Table 1.4. The chemical structure of various chemical additives [9].

Chemical additives		Chemical structure
Thermodynamic promoters	Tetrahydrofuran (THF)	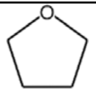
	Propane	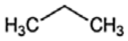
	Cyclopentane (CP)	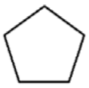
	Tetra-*n*-butyl ammonium bromide (TBAB)	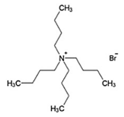
Kinetic promoters (Surfactants)	Tween-80 (T-80)	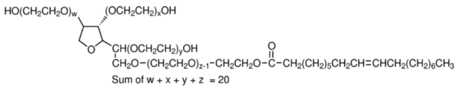
	Dodecyltrimethyl-ammonium chloride (DTAC)	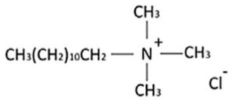 $CH_3(CH_2)_{10}CH_2 - \underset{CH_3}{\overset{CH_3}{\overset{+}{N}}} - CH_3 \quad Cl^-$
	Sodium dodecyl sulfate (SDS)	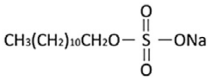 $CH_3(CH_2)_{10}CH_2O - \underset{O}{\overset{O}{S}} - ONa$

However, TBAB takes part in the hydrate structures by changing and jointly occupying the water cages, causing the formation of CO_2–TBAB semiclathrate hydrates [24]. Ye et al. [25] reported the phase equilibrium data of CO_2–TBAB hydrates in 5–55-wt% TBAB aqueous solutions. The promotion effect of TBAB was found to be enhanced with the rise of TBAB concentration until a peak at 32 wt%, after which the promotion effect started to reduce. The authors also reported that the TBAB semiclathrate hydrates tended to form inside the aqueous solution rather than on the gas–water interface and deposited at the bottom of the reactor due to the high density. Nguyen et al. [26] used TBAB as a promoter for hydrate-based carbon capture (HBCC) from CO_2/N_2 mixtures. In the experiment, a wide range of TBAB concentrations were investigated, and the formation conditions and gas storage capacity of hydrates were determined. The results showed a longer induction time of hydrate formation and a lower CO_2 gas uptake in the presence of TBAB [13]. A possible explanation is that TBA^+ occupies cages in semiclathrate hydrates, which reduces available cavities to entrap CO_2 [27]. In addition, TBAB nucleates into massive semiclathrate hydrates and blocks gas permeability [23]; that is, the formed dense hydrate layers may hinder gas diffusion [27].

1.3.2 Kinetic promotion

Kinetic promoters increase the hydrate formation rate without taking part in the hydrate structure itself. Surfactants can accelerate the formation rate by reducing surface tension and improving water activity [9, 28]. Widely used surfactants include anionic surfactant sodium dodecyl sulfate (SDS) [29], cationic surfactant dodecyltrimethylammonium chloride (DTAC) [30], and non-ionic surfactant, for example, Tween 20 and Tween 80 (T-80) [31, 32]. Their chemical structures are presented in Table 1.4. The presence of surfactant molecules reduces the surface tension, improves water-to-gas contact, and improves the water activity, thus enhancing the gas diffusion rate.

A small amount of anionic surfactant SDS is often added as a kinetic promoter to speed up hydrate crystal formation and increase gas uptake [33]. Li et al. [34] studied the semiclathrate hydrate formation for flue gas carbon capture in the presence of cationic surfactant DTAC. It was found that DTAC not only enhanced the gas uptake rate but also improved the separation performance of CO_2 from gas mixtures. CO_2 was purified from 17.0 mol% to 99.4 mol% after a two-stage hydrate-based separation process. The CO_2 concentration in typical flue gas is 15 mol% to 20 mol%, while it increases to around 70 mol% before getting into the second stage. Zhang et al. [35]

reported that the split fraction and separation factor of CO_2 were greatly improved in the presence of DTAC.

However, little is known about the effect of non-ionic surfactants on the thermodynamic promoter. T-80, as a low-cost and environmentally friendly non-ionic surfactant and emulsifier, is commonly used in the food and cosmetics industries [36]. It can be used to solubilize hydrophobic organic compounds from the soil due to its low polarity, low toxicity, and high solubilization capacity [37]. Zhang et al. [38] found that the solubilization of 1310-ppm T-80 produced supersaturated CH_4 molecules to promote the mass transfer and provided the complexation between water and CH_4, performing a reduction in induction time. Prah et al. [36] experimentally investigated the flow characteristics of CO_2 hydrate slurry in the presence of T-80 to elucidate the potential of CO_2 hydrate transportation in HBCC. The results showed that T-80 had a positive effect on the slurry stability, slurry temperature, and slurry density. Mohammadi et al. [32] studied the impact of T-80 on CO_2–TBAB hydrate formation. They used pure CO_2 in 0–15-wt% TBAB systems and concluded that 500-ppm T-80 presented a slight positive effect on the kinetics of hydrate formation in the presence and absence of TBAB, while 1500-ppm T-80 was found to inhibit the kinetics of hydrate formation.

1.3.3 Combined effects of thermodynamic and kinetic promotion

To form CO_2 hydrates in both moderate conditions and at a fast rate, thermodynamic and kinetic promoters were added jointly in some studies. For example, THF+SDS mixtures have been used in the work of Lirio et al. [33]. It was found that in the presence of SDS, the induction time was highly reduced. By adopting the recipe of 500-ppm SDS and 5-mol% THF, the largest CO_2 capture amount reached 91.9% with an induction time of 25 min. Torré et al. [39] also reported the CO_2 enclathration in the presence of THF and SDS. THF was found to increase the hydrate temperature and decrease the hydrate pressure, while SDS showed no influence on phase equilibrium conditions. The combination of THF and SDS significantly improved gas uptake. The optimal concentration in the experiments was 0.3 wt% SDS+4 wt% THF. However, these studies only focused on pure CO_2, or gas mixtures with a single promoter. The effects of binary promoters on the separation of CO_2 from gas mixtures are still unknown.

Most current studies focus on the combined effects of TBAB with ionic surfactants, which may influence the performance of TBAB through electrostatic interactions. Renault-Crispo and Servio [40] studied the combined effect of TBAB and anionic surfactant SDS on CH_4 hydrate formation and found initially reduced growth kinetics in 100–1250 ppm SDS with 5-wt% TBAB. The inhibition trend of 5-wt% and 20-wt% TBAB was also found with SDS. Wang et al. [41] studied the synergetic effect of SDS and TBAB on CO_2 separation. They found that the kinetics of hydrate growth were promoted by SDS, but the CO_2 separation efficiency was reduced. Zhang et al. [35] tested the effect of varied concentrations of SDS and DTAC with 10-wt% TBAB on CO_2 hydrate formation kinetics. The separation performance was also found to be reduced by SDS. The gas uptake yield was reduced by 39%–52% with DTAC concentrations higher than 1000 ppm due to the reduced water activities caused by intramolecular interactions. However, the mechanism of non-ionic T-80 on TBAB semiclathrates is still unclear; very few papers studied the T-80+TBAB pairs, and the effect of T-80 on CO_2 separation from gas mixtures is still unclear.

1.3.4 Hydrate formation in porous media

Porous materials are widely used on various occasions as a way to increase the contact area and improve mass transfer. The use of particles in gas hydrate formation provides an effective alternative to mechanical mixing for reduced energy consumption and improved safety. Water (or aqueous solution) is usually dispersed uniformly around or inside the small particles, so that the contact area between gas and water is significantly increased, and then hydrates can form in the pores. Widely used particles include hydrophilic silica gels [42, 43], silica sands [44, 45], activated carbons [46], commercial zeolite [47], aluminum foam [48], montmorillonite[49], polymers [50], hydrogels [51], and dry water [52]. The low-temperature (at 163 K) scanning electron microscopy (SEM) image for methane hydrates formed around porous silica gels is shown in Figure 1.5 [2].

Some experiments on CO_2 hydrate formation and dissociation in porous media, and even with the addition of some promoters, have been carried out. The formation mechanism of methane hydrate in porous materials like seafloor sediments has been reported [51, 53, 54], but information on the influence of porous materials on the formation of CO_2 hydrate is insufficient. Some reports showed that with the existence of porous media, more water will be converted to hydrate, and the CO_2 recovery rate can also be increased [45, 55–60]. However, some articles revealed that the equilibrium pressure of the corresponding gas hydrates in porous media were higher than those of bulk hydrates [2]. Uchida et al. [61, 62] experimentally determined the equilibrium pressures of CH_4, C_3H_8, and CO_2 hydrates in porous glass. Wilder et al. [63, 64], Seshadri et al. [65], Smith et al. [66], and Zhang et al. [67] used conceptual models to explain the hydrate equilibria in porous media adopting a pore size distribution. Some researchers [68, 69] have modified the thermodynamic model for bulk hydrates originally developed by van der Waals and Platteeuw to elucidate the effect of pore size on hydrate equilibrium conditions. The mechanism of porous media to effect the hydrate equilibriu, and formation kinetics is unknown.

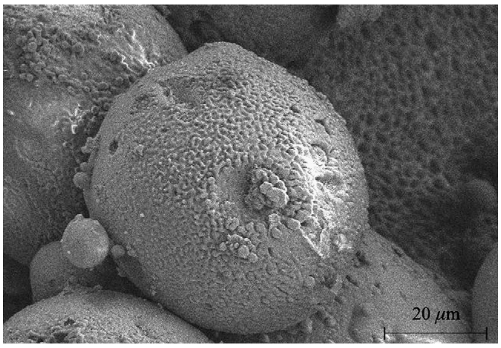

Figure 1.5. Low-temperature (at 163 K) SEM image for methane hydrates formed around porous silica gels [2].

1.4 Kinetics models of hydrate growth

The growth of gas hydrates practically takes place right after the nucleation, and is considered as a complicated interfacial phenomenon, which involves multicomponent (i.e., water, gas, and hydrate) distribution in multiphase (i.e., aqueous, gas and hydrate) at multiscale level (i.e., molecular-scale and macroscopic-scale). The analysis of this phenomenon requires the understanding of heat and mass transfer, fluid flow, and intrinsic kinetics of phase change. At the macroscopic level, the rate of gas hydrates growth was typically quantified according to the gas consumption rate calculated from the measurement of pressure and temperature, as well as other direct visualization techniques on the hydrate film thickness and morphology [70–72]. At the microscopic level, hydrates growth can be considered as a combination of three different factors:

(i) mass transfer of water and gas molecules to the growing hydrate surface;

(ii) the intrinsic kinetics of hydrate growth at the hydrate surface;

(iii) transport of the heat released from the exothermic hydrate formation reaction from the growing crystal surface.

Accordingly, the structure of a kinetic model can be based on the particular controlling mechanism: (i) mass transfer; (ii) intrinsic kinetics; (iii) heat transfer, or a combination of them. Since hydrate growth is generally considered as an interfacial phenomenon, the movement of guest gas molecules from one phase to another should be considered in the rate equation. Thus, the common rate expression typically incorporated mass transfer rate terms in addition to the commonly known "intrinsic kinetics" [73, 74]. In addition, heat transfer analysis stemming from classical nucleation theory also provided insight into the thickness and growth rate of the initial gas hydrate film [72, 75]. These mechanisms are often coupled and either one of them could be dominating during the process of hydrate growth, depending on the hydrate formation condition.

To better understand the formation kinetics, many modeling studies have been implemented since the early 1970s [76]. Vysniauskas and Bishnoi [77] first proposed a semiempirical Arrhenius-type rate equation in 1983. Englezos et al. [4] improved Vysniauskas' experimental setup and built a kinetic model to represent the physical and chemical insights into the process of hydrate growth. The model, with high prediction accuracy, considers clathrate hydrate formation in two consecutive steps: diffusion and adsorption. Further, Skovborg and Rasmussen simplified the model of Englezos [78]. Table 1.5 summarizes the different hydrate growth models that have been developed by various research groups.

The shrinking core model (SCM) was first used in hydrate formation of deepwater oil/gas blowouts systems [79]. It was further explored in water-in-condensate oil emulsions in a flow loop unit [80, 81]. Later, the SCM was modified to predict hydrate formation from ice powders [82] and CH_4 formation kinetics in the hydrogel particles [53, 83]. While these studies have demonstrated the high suitability of the SCMs to particles with well-defined geometries, the models developed so far have not yet completely reflected the chemical process. For instance, heat transfer and the effects of the porous structure of hydrates have not been clearly considered in the previously reported SCMs. Some assumptions, such that the hydrate nucleus is homogeneously distributed in all pores, conflict with the shrinking core concept that supports the growth and propagation of gas hydrate from the outer to the inner layers [28].

Table 1.5. Hydrate growth models.

Growth model based on	Driving force / model features	Researchers and references
Growth kinetics	$\left(f - f_{\mathrm{eq}}\right)$	Englezos et al., 1987 a,b [4, 74]
Growth kinetics	$\left(f - f_{\mathrm{eq}}\right)$ Minor modification to Englezos' model	Malegaonkar et al., 1997 [84]
Mass transfer	$\left(x_{\mathrm{int}}^{i} - x_{\mathrm{b}}^{i}\right)$ Simplification/modification to Englezos' model	Skovborg and Rasmussen, 1994 [78]
Mass transfer	Based on phase field theory	Svandal et al., 2005 [85]
Mass transfer	Based on Monte Carlo cellular automata	Buanes et al., 2006 [86]
Heat transfer	Curved film front growth on water–hydrate former interface	Uchida et al., 1999 a [87]
Heat transfer	Curved film front growth on water–hydrate former fluid interface	Mori, 2001 [88]
Heat transfer	Straight film front growth on water side of water–hydrate former interface	Freer et al., 2001; Mochizuki and Mori, 2006 [75, 89]

1.5 Hydrate-based carbon capture

In recent years, CO_2 emissions have increased year by year, and the resulting climate change issues, such as the greenhouse effect, have attracted widespread attention. Corresponding CO_2 emission reduction technologies have also been extensively studied. At present, carbon capture and storage (CCS) technology is one of the most effective ways to reduce CO_2 emissions in the short term [90]. The conventional CO_2 capture technologies include chemical absorption, physical adsorption and membrane separation, and so on. These technologies have been commercially available for over 50 years. However, some analyses have shown that such technologies increase the power plants' energy requirement by 25%–40% [91], with the capture part making up to two-thirds of the total CCS cost [92]. Consequently, the conventional capture methods are not cost-effective, and they also may produce a corresponding negative impact due to the solvent emission [93]. Therefore, different strategies and technologies need to be developed to decrease both the overall CCS cost and the environmental impact of conventional CO_2 absorbers or absorbers. Currently, gas hydrates are getting more significant attention as a potential CO_2 capture and storage technology [7].

The fact that gas can form solid hydrates in water has been known for many years [94], and has driven intensive investigation in recent years into its capability to separate and to store gas. Many researchers have unveiled the existence of gas hydrate in nature, like methane hydrate in deep oceans where the pressure is very high and the temperature is low. HBCC technology has been recognized as a potential method for CO_2 capture because each individual gas has different hydrate formation conditions; for example, CO_2 forms hydrate at 1.2 MPa and 273K, N_2 forms hydrate at 15.9 MPa and 273K, and H_2 forms hydrate at 200 MPa and 273K. The mechanism of HBCC is shown in Figure 1.6. Additionally, the advantage that per volume gas hydrate can contain hundreds of times that volume of gas makes it a promising application for CO_2 storage after CO_2 capture.

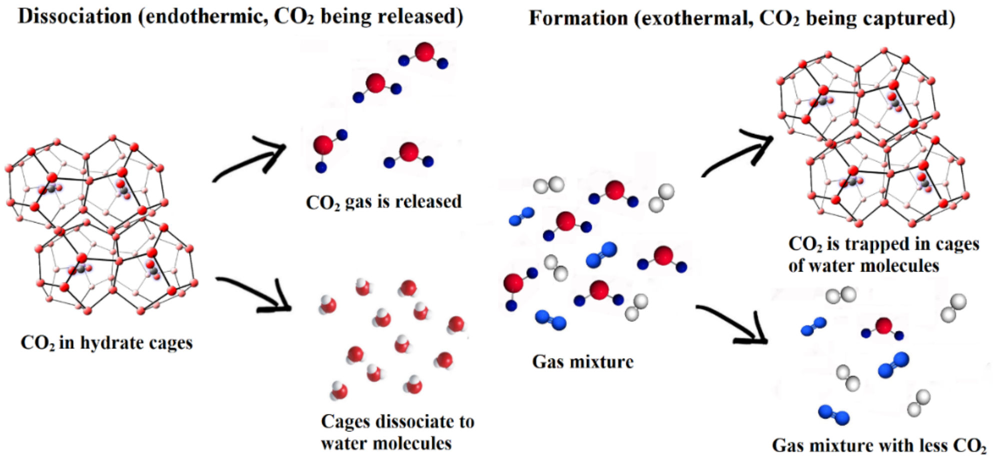
Dissociation (endothermic, CO₂ being released)
Formation (exothermal, CO₂ being captured)
CO₂ gas is released
CO₂ in hydrate cages
Cages dissociate to water molecules
Gas mixture
CO₂ is trapped in cages of water molecules
Gas mixture with less CO₂

Figure 1.6. Mechanism of hydrate-based CO_2 capture [21].

This HBCC technology involves no or very few chemical agents, but only uses cold water or lean aqueous solution as the working fluid. In most cases, the equilibrium temperature of hydrate is lower than the ambient temperature, hence the regeneration by raising the temperature can be easily achieved through heat exchange with the atmospheric environment, and the release of CO_2 at a high pressure which benefits the subsequent transportation and storage [95]. The cost of HBCC technology in an integrated gasification combined cycle (IGCC) plant was reported in 1999 by the US Department of Energy to be US$8.75 per ton of CO_2 captured, which is significantly lower than the cost of US$59 per ton of CO_2 captured using conventional amine-based absorption and US$64 per ton of CO_2 for adsorption by zeolite [9, 92, 96–98].

However, the practical application of this new technology is limited due to the low mass transfer between the gas phase and the liquid phase. In a common experiment of hydrate formation, the interface area between the gas and liquid is always just the cross-sectional area of the reactor, which is very limited for mass transfer and reaction. Although the addition of promoters to accelerate the rate of hydrate formation has been discussed in a large body of literature [99–102], the rate of hydrate formation has not yet been as rapid as in conventional absorption methods, such as chemical absorption. So it is essential to enhance the mass transfer between the gas and liquid and speed up the reaction duration to form hydrates rapidly under a relatively moderate pressure condition[103, 104].

1.6 Research objectives

This work aims to study the mechanism of promoting CO_2 hydrate formation for effective carbon capture. Both chemical promoters and porous material will be used to enhance the mass transfer. Except for the experimental study, kinetics models for hydrate growth will also be built to investigate the detailed theoretical basis for the improvement of kinetics. The whole thesis will be divided into two parts, the experiments and model strategies.

(1) Thermodynamic and kinetic promotion experiments

Unlike previous studies, in this work we try to find the optimal recipe for CO_2 hydrate formation considering both thermodynamic and kinetic properties with the help of TBAB and an anionic, a cationic, or a non-ionic surfactant—TBAB+SDS, TBAB+DTAC, and TBAB+T-80, and to investigate their practical applications for CO_2 separation from gas mixtures with high CO_2 proportion of CO_2/N_2. In order to moderate the CO_2 hydrate phase equilibrium conditions and accelerate their formation, TBAB was used as a primary promoter for thermodynamic enhancement. Secondary kinetic promoters, i.e., surfactants, were added to compensate for the lower gas uptake caused by TBAB. Anionic surfactant SDS, cationic surfactant DTAC, and non-ionic surfactant T-80 were chosen to prompt the performance of HBCC from CO_2/N_2 gas mixtures in the presence of TBAB. Experiments were conducted in TBAB systems at the concentration of 10 wt% in conjunction with varied surfactant concentrations. The effects of the concentration of SDS, DTAC and T-80 on induction time, CO_2 gas uptake, and separation performance in the TBAB systems were investigated and compared with those in the pure water system. The effect of temperature driving force on CO_2 separation was also studied.

CO_2/N_2 gas mixtures with a mole fraction ratio of 70:30 were used in this study. Although the concentration of CO_2 in power plants is generally in the range from 15 mol% to 20 mol%, it can be several tens of percent in steelmaking plants. This includes the tail gas in the FINEX® process with a concentration from 66 mol% to 80 mol%, or in natural gas production, for example, CH_4 replacement from natural gas hydrates by CO_2-rich gas mixtures (approx. $CO_2:N_2 = 3:1$) [105]. More importantly, the HBCC is suitable to integrate with other carbon capture processes, where the HBCC can be used in the later stage with the benefits of energy saving and storage in one step [34, 106]. Thus the CO_2/N_2 gas mixtures with 70-mol% CO_2 were used in this work. Our findings will fill the gap in knowledge of the effects of combined TBAB and surfactants for high-efficiency HBCC separation processes.

(2) Hydrate formation experiments in “dry water” and the shrinking core model

In this work, a comprehensive SCM was developed and validated to study the CO_2 hydrate formation kinetics in “dry water” particles. “Dry water” is the term for the isolated water drops encapsulated by hydrophobic silica [51, 52, 54, 107, 108]. It provides a suitable scattered structure within dispersed small spherical particles for the kinetic promotion of gas hydrate formation through enhancing mass transfer. CO_2 dissolved in water and the capillary effect of the porous hydrate shell were particularly considered in the model. The impact of heat released on the formation kinetics was determined by establishing a new heat transfer model. As a comparison, the model was also applied to the formation process of CH_4 hydrate, for which the experimental data was obtained from the previous work of Shi et al. [83]. The different volume expansion in CO_2 and CH_4 hydrate growth in “dry water” was also considered in this work. Key parameters during CO_2 and CH_4 hydrate formation, namely the effective diffusion coefficient, hydrate shell thickness, and water consumption in capillaries, were determined by the model. This work aims to propose a more accurate modeling strategy to describe the hydrate formation kinetics in particles, revealing the roles of critical parameters on hydrate formation kinetics, thus providing a detailed theoretical basis for the improvement of kinetics.

(3) Hydrate formation experiments in silica gels and the shrinking core model

Moreover, silica gels (SGs) in varied pore sizes were used as the base structure for hydrate formation. The effects of SG pores and surfactants on the hydrate formation kinetics were also investigated both experimentally and numerically. SDS or DTAC solutions at varied concentrations were used to further improve the water activity. An advanced SCM was used to simulate CO_2 hydrate formation kinetics in SGs, which is the first model considering pore size, capillary effect, CO_2 solubility, and the effects of surfactants. Key parameters of CO_2 hydrate formation were determined by the model, including the reaction rate constant, effective diffusion coefficient, water consumption by capillaries, and hydrate shell thickness in the pores. Specifically, it reveals four mechanisms: (a) the migration of hydrate–liquid interface in nanopores during CO_2 hydrate formation; (b) the variation of the effective diffusion coefficient during hydrate formation; (c) the effect of surfactants on the reaction rate constant, effective diffusion coefficient, and capillary effect; and (d) the possible changes in the capillary structure.

(4) Investigation of the effects of surfactants by shrinking core model

Furthermore, the SCM was also advanced to investigate the effects of surfactants on the CO_2 separation performance from CO_2/N_2 gas mixtures. The SCM especially considers the role of N_2 in the CO_2 separation of HBCC. The modeling strategies quantitatively analyze the binary effects of surfactants and nanopores, revealing the variations and roles of critical parameters of hydrate formation kinetics, thus contributing to a theoretical ground for gas hydrate kinetics improvement.

This work reveals the mechanism of mass transfer during gas hydrate formation in microparticles compared to that in bulk water. This work also enhances the understanding of the transport phenomena of gas molecules and helps to extend the knowledge of gas separation and surfactants in hydrate formation.

Chapter 2 Thermodynamic and kinetic promotions of CO_2 hydrate formation using chemical promoters[1]

2.1 Introduction

Tetra-*n*-butyl ammonium bromide (TBAB) takes part in the formation of semiclathrate hydrate structures by joining in and changing the water cages. The cages of semiclathrate hydrates are able to encage small-sized gas molecules and the formation of these hydrates promotes a dramatic reduction of formation pressure. This chapter presents experimental results of the CO_2–TBAB semiclathrate hydrate formation kinetics. The phase equilibrium and gas uptake yields of CO_2–TBAB semiclathrate hydrate formation are investigated under different TBAB concentrations with pure CO_2 to determine the optimal TBAB concentration. In order to maintain the high-temperature and low-pressure phase equilibrium while compensating for the reduced gas uptake caused by TBAB, surfactants are added to the system to increase the formation rate. The combined effects of TBAB and surfactants on CO_2–TBAB semiclathrate hydrate formation kinetics are investigated. The three kinds of surfactants used in this chapter are anionic surfactant sodium dodecyl sulfate (SDS), cationic surfactant dodecyltrimethyl-ammonium chloride (DTAC), and non-ionic surfactant Tween 80 (T-80). All the experiments are implemented under isothermal conditions. CO_2/N_2 (70:30 mol%) gas mixtures are used in this chapter to evaluate the separation performance of CO_2–TBAB semiclathrate hydrate. Key parameters, namely the induction time, CO_2 gas uptake yield, percentage water conversion, CO_2 recovery rate, and separation performance, are comprehensively evaluated in this chapter.

---

[1] The content of this chapter has been published in the following articles:

Zhang F, Wang X*, Lou X, Lipiński W*. The effect of sodium dodecyl sulfate and dodecyltrimethylammonium chloride on the kinetics of CO_2 hydrate formation in the presence of tetra-*n*-butyl ammonium bromide for carbon capture applications. Energy. 2021;227:120424.

Zhang F, Wang X*, Lou X, Lipiński W*. Effects of Tween 80 on clathrate and semiclathrate CO_2 hydrates formation kinetics for carbon capture from CO_2-rich gas mixtures. Carbon Capture Science & Technology. 2022;4:100053.

2.2 CO_2–TBAB semiclathrate hydrate formation

The phase equilibrium of CO_2–TBAB semiclathrate hydrate formation was investigated in a previous study of Wang et al. [13]. TBAB solutions were prepared with the various mass fractions of 10, 20 and 32 wt%, where the 32 wt% is the stoichiometric concentration for CO_2–TBAB semiclathrate formation. The hydrate formation is induced by stepwise cooling of the samples, and the equilibrium temperature is determined not only by the visibility of the solids formed but also by the variations in the cooling curve.

Figure 2.1 shows the dissociation equilibrium of CO_2–TBAB semiclathrate hydrate. In the dissociation, the required pressure at a certain temperature is considerably reduced by the rise in TBAB mass fraction. These data are also compared with those from other literature and show reliability [109–112]. This reveals that the addition of TBAB is helpful in increasing the hydrate formation temperature.

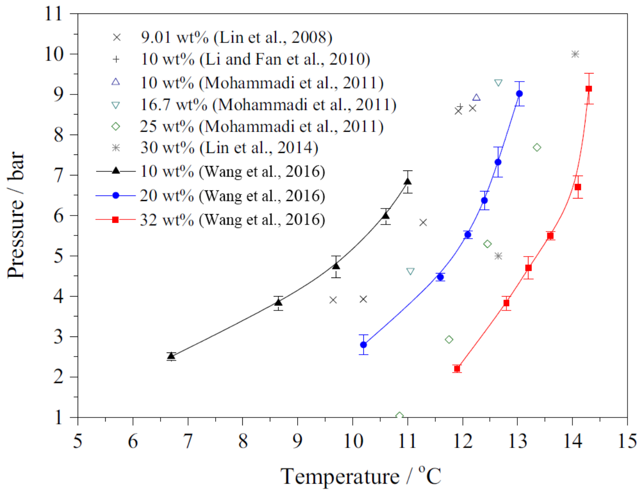

Figure 2.1. Phase equilibrium of CO_2–TBAB hydrate at various mass fraction [13].

However, the higher concentration of TBAB will also result in reduced CO_2 gas uptakes. The combined effect of feed pressure and TBAB mass fraction on the CO_2 gas uptake is presented in Figure 2.2. This analysis was conducted in a pressure range from 2.3 to 9.4 bar with the same TBAB mass fraction of 10, 20 and 32 wt% as mentioned above. The results show that higher feed pressure leads to larger CO_2 uptake quality and efficiency for all the TBAB mass fractions studied. However, a higher TBAB mass fraction results in lower CO_2 uptake quality and efficiency throughout the pressure range. It is assumed that with sufficient overpressure driving force the amount of CO_2 uptake mainly relies on the number of vacant cages (nucleation sites) in the hydrate structure, which is to some extent enhanced by high TBAB mass fractions. However, at a low feed pressure, the trapping of CO_2 is less dependent on the number of vacant cages; instead, the mass transfer becomes a major restraint on the hydrate formation. In this case, a lower TBAB mass fraction is more favorable since it provides more free water for CO_2 gas dissolution thus improving the mass transfer. This tendency is also attributed to the hydrate growth of 32 wt% TBAB not being sustainable, with its effect diminishing and finally this may result in an early stoppage of gas consumption [23].

A similar finding is also in the work of Fukumoto et al. [113], in which the CO_2 separation factor drops with increasing TBAB concentration, which was attributed to that when the pressure is lower and salt concentration is high, type A hydrate is more stable and the separation factors of type A hydrate are much smaller than those of type B hydrates.

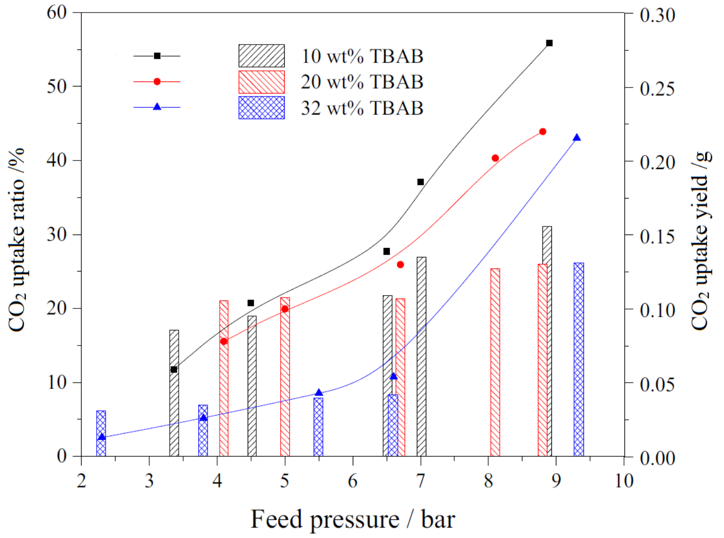

Figure 2.2. CO_2 gas uptake at various feed pressures and TBAB mass fractions [13].

Considering the trade-off of experimental conditions and gas uptake yields, 10-wt% TBAB will be used in the rest of this chapter to evaluate the combined effects of TBAB and surfactants.

2.3 Experimental study on combined effects of TBAB and ionic surfactants

To form CO_2 hydrates both in moderate conditions and at a fast rate, thermodynamic and kinetic promoters were added jointly in this study. Unlike previous studies, this work aims to find the optimal recipe for CO_2 hydrate formation considering both thermodynamic and kinetic properties with the help of an anionic and a cationic surfactant, respectively—TBAB+SDS and TBAB+DTAC, and their practical applications for CO_2 separation from gas mixtures with high CO_2 proportion of CO_2/N_2. TBAB was used as a primary promoter for thermodynamic enhancement. Anionic surfactant SDS and cationic surfactant DTAC were chosen to prompt the performance of HBCC from CO_2/N_2 gas mixtures in the presence of TBAB. Experiments were conducted in TBAB systems at the concentration of 10 wt% in conjunction with SDS at 500, 1000 and 1500 ppm, or DTAC at 1000, 2000 and 6000 ppm. The effects of the concentration of SDS and DTAC on induction time, CO_2 gas uptake, and separation performance in TBAB systems were investigated and compared with those in the pure water system. The effect of subcooling on CO_2 separation was also studied.

In addition to the promoters, previous studies of HBCC mainly focused on the CO_2 proportion of 17 mol% to 20 mol% for the flue gas [34, 114]. Although this proportion is approximately the gas composition after combustion, it is very intensive in energy consumption [7, 9]. In addition, the exhaust gas in the process is at a high temperature and not suitable for HBCC directly. In practical applications, it is applicable to use a cheap separation method for the first stage that generates a CO_2/N_2 gas mixture with a high CO_2 proportion, and then use the HBCC method in the following stage for separation and storage to produce CO_2 with a purity of >95 mol%. This multi-stage capture not only reduces energy consumption but also allows the high-temperature exhaust gas to cool down before reaching the capture unit for stable and continuous operations. To be applied in the second or third stage of separation/storage, HBCC for a gas mixture with a high CO_2 proportion (around 70 mol%) is of significance.

2.3.1 Experimental methods

CO_2/N_2 gas mixtures containing 70 mol% CO_2 and 30 mol% N_2 were used in this work, supplied by BOC Limited Australia. TBAB (CAS: 1643-19-2), SDS (CAS: 151-21-3), and DTAC (CAS: 112-00-5) were supplied by Sigma Aldrich with purity of 99%, 98.5%, and 99% respectively. The TBAB water solution with a concentration of 10 wt% was prepared in the lab with the deionized water.

The apparatus consisted of a 635-mL steel cylindrical reactor (maximum pressure 30 MPa) with a mechanical stirrer from the top, a low-temperature thermostatic bath, a water tank containing cooling fluid, a vacuum pump, as well as a data acquisition system, shown in Figure 2.3. The QMS 100 Series Gas Analyzer from Stanford Research Systems was used to measure the gas components. The QMS series gas analyzer had a fast response time of less than 0.5 seconds. The pressure and temperature variations in the reactor were recorded by a pressure transducer and thermocouples with accuracy of ±0.01 MPa and ±0.1°C, respectively. More details of the apparatus are shown in Table 2.1.

The kinetic experimental program was conducted under the condition of constant temperature and volume (batch mode). The solution volume used in each experiment was 100 mL. The reactor was first washed and rinsed with deionized water five times and allowed to dry. After the solution was charged into the reactor, the reactor was sealed and degassed using a vacuum pump. Then the reactor was cooled by the thermostatic bath. Once the reactor reached and further stabilized at the desired temperature for 60 min, it was pressured by CO_2/N_2 gas mixtures to 3.8 MPa. Meanwhile, the adjustable motor stirrer was set to 500 rpm. The gas composition in the reactor was sampled and characterized by the gas analyzer every 30 min instantaneously. The gas loss due to gas sampling, 0.1–0.3 mL, was negligible. Each experiment lasted for at least 6 hours after hydrates were formed, and was repeated twice under the same conditions with the same reaction system, referring to one “fresh” run and two “memory” runs, where the “memory” runs are—runs with water or TBAB solution that have formed CO_2 hydrates before. Throughout these processes, the pressure and temperature in the reactor were acquired every 10 seconds.

The temperatures in the experiments were chosen considering all the equilibrium temperatures of CO_2 hydrates, TBAB hydrates, and CO_2–TBAB semiclathrate hydrates. To form CO_2 hydrate in pure water, the temperature should not exceed 279.35 K, and should be higher than 262.65 K in case of CO_2 liquefaction at a global pressure of 3.8 MPa for 70% CO_2 gas mixtures. TBAB could form two types of salt hydrates in the absence of guest gas, which are type A and type B [115]. The minimum temperature to prevent TBAB from forming salt hydrates with water at the concentration of 10 wt% is 280 K, according to the data from the work of Oyama and Darbouret [116, 117]. On the other hand, based on the phase equilibrium data of CO_2–TBAB semiclathrate hydrates reported by Ye and Zhang in Figure 2.4 [25], the temperature should be lower than 287.84 K at a global pressure of 3.8 MPa for gas mixtures with 70 mol% CO_2. Thus, in this work, the experimental temperature was set in the range of 280.00–287.84 K for TBAB systems to form CO_2–TBAB semiclathrate hydrates. The experimental conditions for all experiments in this study are shown in Table 2.2.

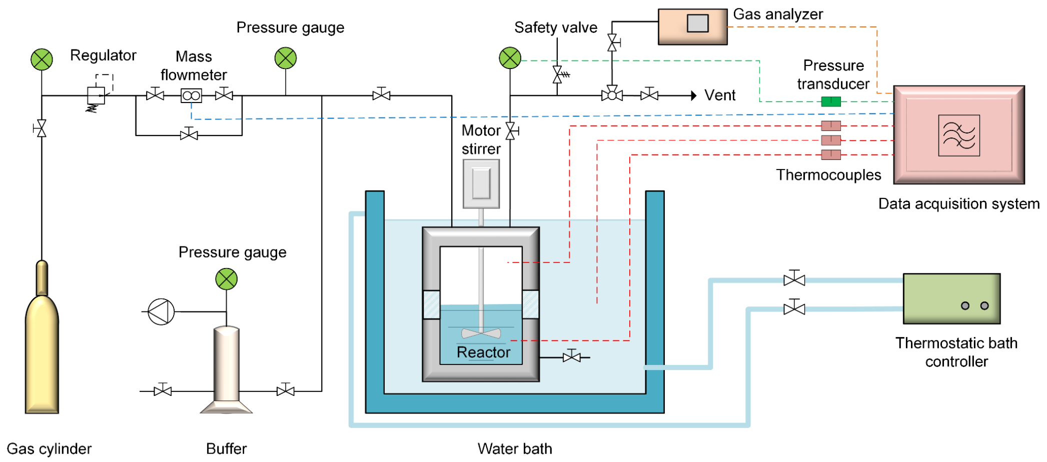
Gas analyzer
Pressure gauge
Safety valve
Regulator
Mass flowmeter
Pressure transducer
Vent
Motor stirrer
Thermocouples
Data acquisition system
Pressure gauge
Reactor
Thermostatic bath controller
Gas cylinder
Buffer
Water bath

Figure 2.3. Schematic diagram of the experimental apparatus.

Table 2.1. Apparatus and materials properties.

Apparatus	Model	Technical index	Supplier
Cylindrical reactor	316L steel	635 mL, 30 MPa	Hai'an Scientific Research Apparatus Co., Ltd, China
Adjustable motor stirrer	MY-358	200 W	Hai'an Scientific Research Apparatus Co., Ltd, China
Thermostatic bath	HX-1030	–10 to 99.99℃, 30 L, 16 L min^{-1}	TOPTION Group Co., Ltd, China
Vacuum pump	VP6DE	144 L min^{-1}	CPS Products Australia
Pressure transducer	PX790GW	40 ± 0.01 MPa	OMEGA Engineering Australia
Thermocouple	TJ36	–20 to 100℃, ±0.1℃	OMEGA Engineering Australia

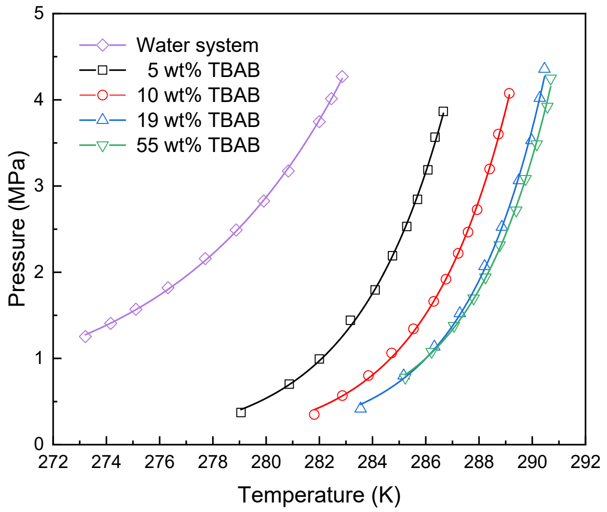

Figure 2.4. Phase diagram for CO_2 hydrate in the water system and CO_2–TBAB semiclathrate hydrate at different TBAB concentrations [25].

Table 2.2. Experimental conditions for the studied CO_2 hydrate formation systems.

Exp. no.	System	Kinetic promoters	Exp. state	T_{exp} (K)	ΔT[1] (K)
1	TBAB	–	Fresh	283.15	4.69
2			Memory 1	283.15	
3			Memory 2	283.15	
4	Water	–	Fresh	276.45	2.9
5			Memory 1	276.45	
6			Memory 2	276.45	
7	Water	SDS (500 ppm)	Fresh	276.45	2.9
8			Memory 1	276.45	
9			Memory 2	276.45	
10	Water	SDS (1000 ppm)	Fresh	276.45	2.9
11			Memory 1	276.45	
12			Memory 2	276.45	
13	Water	SDS (1500 ppm)	Fresh	276.45	2.9
14			Memory 1	276.45	
15			Memory 2	276.45	
16	TBAB	SDS (500 ppm)	Fresh	283.15	4.69
17			Memory 1	283.15	4.69
18			Memory 2	283.15	4.69
19			Fresh	285.15	2.69

Exp. no.	System	Kinetic promoters	Exp. state	T_{exp} (K)	ΔT [1] (K)
20			Fresh	286.15	1.69
21			Fresh	283.15	
22	TBAB	SDS (1000 ppm)	Memory 1	283.15	4.69
23			Memory 2	283.15	
24			Fresh	283.15	
25	TBAB	SDS (1500 ppm)	Memory 1	283.15	4.69
26			Memory 2	283.15	
27			Fresh	276.45	
28	Water	DTAC (0.1 wt%)	Memory 1	276.45	2.9
29			Memory 2	276.45	
30			Fresh	276.45	
31	Water	DTAC (0.2 wt%)	Memory 1	276.45	2.9
32			Memory 2	276.45	
33			Fresh	276.45	
34	Water	DTAC (0.6 wt%)	Memory 1	276.45	2.9
35			Memory 2	276.45	
36			Fresh	283.15	4.69
37			Memory 1	283.15	4.69
38	TBAB	DTAC (0.1 wt%)	Memory 2	283.15	4.69
39			Fresh	285.15	2.69
40			Fresh	286.15	1.69
41			Fresh	283.15	
42	TBAB	DTAC (0.2 wt%)	Memory 1	283.15	4.69
43			Memory 2	283.15	
44			Fresh	283.15	
45	TBAB	DTAC (0.6 wt%)	Memory 1	283.15	4.69
46			Memory 2	283.15	

[1] ΔT, subcooling, is defined as the difference between the phase equilibrium temperature and the experimental temperature at a given pressure.

2.3.2 Performance metrics

2.3.2.1 Gas uptake and normalized gas uptake

The initial amount of gas pressurized into the reactor is defined as

$$n_{\mathrm{g,0}} = \frac{P_0\left(V^{\mathrm{R}} - V^{\mathrm{S}}\right)}{Z_0 R T_{\mathrm{exp}}}, \tag{2.1}$$

where P_0 is the initial pressure in the reactor at the onset of an experiment ($t = 0$), V^{R} and V^{S} are the inner volume of the reactor and the volume of solution added into the reactor, respectively. R is the ideal gas constant, and T_{exp} is the temperature of the gas phase in the reactor. Z_0 is the gas compressibility factor at $t = 0$, calculated by Peng–Robinson equations of state [118]. The gas compressibility factor of gas mixtures can be obtained by solving the Peng–Robinson cubic equation with the binary interaction parameters for mixtures (see Appendix B). The value of the compressibility factor in this paper was compared with that obtained by Pitzer's correlation [119], which shows a good agreement with the present study with a small error of ±0.001.

The amount of gas in the reactor at any given time t is calculated as

$$n_{\mathrm{g,t}} = \frac{P_{\mathrm{t}}\left(V^{\mathrm{R}} - V^{\mathrm{S}}\right)}{Z_{\mathrm{t}} R T_{\mathrm{exp}}}, \tag{2.2}$$

where P_{t} and Z_{t} are the pressure in the reactor at time t and the gas compressibility factor at time t, respectively. Thus, the gas uptake $\Delta n_{\mathrm{g,t}}$ at time t can be expressed as follows

$$\Delta n_{\mathrm{g,t}} = n_{\mathrm{g,0}} - n_{\mathrm{g,t}}. \tag{2.3}$$

The normalized gas uptake $\mathrm{NG_t}$ at any given time t is calculated as [120]

$$\mathrm{NG_t} = \frac{\Delta n_{\mathrm{g,t}}}{n_{\mathrm{H_2O}}}, \tag{2.4}$$

where $n_{\mathrm{H_2O}}$ is the total number of moles of water initially in the reactor.

To calculate the gas uptake of CO_2 in a gas mixture, Eqs (2.1) and (2.2) are multiplied by the mole fraction of CO_2 measured by the gas analyzer.

2.3.2.2 Normalized rate of CO₂ hydrate growth

The normalized rate of CO_2 hydrate growth for the first 30 min after the CO_2 hydrate formation is calculated by using the following equation [121]

$$\mathrm{NR}_{30,\mathrm{CO_2}} = \frac{n_{\mathrm{CO_2},0} - n^{\mathrm{R}}_{\mathrm{CO_2},30}}{V_{\mathrm{H_2O}} \times t}, \tag{2.5}$$

where $\mathrm{NR}_{30,\mathrm{CO_2}}$ is the normalized rate of CO_2 hydrate growth for the first 30 min after the CO_2 hydrate formation, $n_{\mathrm{CO_2},0}$ is the initial moles of CO_2 in the reactor, $n^{\mathrm{R}}_{\mathrm{CO_2},30}$ is the moles of CO_2 in the reactor at 30 min after the CO_2 hydrate formation, and $V_{\mathrm{H_2O}}$ is the initial volume of water in the reactor.

2.3.2.3 Percent water conversion

The percent water conversion (PWC) is determined by Eq. (2.6) as

$$\mathrm{PWC} = \frac{\Delta n_{\mathrm{g},\,t} \times \text{hydration number}}{n_{\mathrm{H_2O}}} \times 100\%\,, \tag{2.6}$$

where the hydration number is the theoretical number of water molecules consumed per guest molecule [55]. The hydration numbers of clathrate hydrates and TBAB semiclathrate hydrates were chosen at 7.23 and 15.1 in this study based on the test results of Kang et al. [122] and Lin et al. [109], respectively.

2.3.2.4 Split fraction and separation factor

The split fraction of CO_2, also referred to as CO_2 recovery, was proposed by Linga to quantify the selectivity towards CO_2 of the gas hydrate reaction [114] as

$$\mathrm{S.Fr.} = \frac{n^{\mathrm{H}}_{\mathrm{CO_2}}}{n_{\mathrm{CO_2},0}}\,, \tag{2.7}$$

where $n_{\mathrm{CO_2},0}$ is defined as the number of moles of CO_2 at $t = 0$ and $n^{\mathrm{H}}_{\mathrm{CO_2}}$ is the number of moles of CO_2 in the hydrates phase at the end of the experiment.

The separation factor of CO_2 shows the relative capability to capture CO_2 gas rather than other gases in a gas mixture, which is determined by the following equation [114] as

$$\mathrm{S.F.} = \frac{n^{\mathrm{H}}_{\mathrm{CO_2}} n^{\mathrm{gas}}_{\mathrm{N_2}}}{n^{\mathrm{H}}_{\mathrm{N_2}} n^{\mathrm{gas}}_{\mathrm{CO_2}}}\,, \tag{2.8}$$

where $n^{\mathrm{gas}}_{\mathrm{CO_2}}$ and $n^{\mathrm{gas}}_{\mathrm{N_2}}$ are the number of moles of CO_2 and N_2 in the gas phase at the end of the experiment, respectively, and $n^{\mathrm{H}}_{\mathrm{CO_2}}$ and $n^{\mathrm{H}}_{\mathrm{N_2}}$ are the number of moles of CO_2 and N_2 in the hydrate phase at the end of the experiment, respectively.

2.4 Results and discussion of combined effects of TBAB and ionic surfactants

2.4.1 Induction time

The time interval between the establishment of the target pressure and temperature conditions to the moment when there is both a sudden pressure decrease and temperature increase is defined as the induction time [123]. The period onward is defined as the hydrate growth period. Figure 2.5 shows the experimentally determined induction times for the "fresh" runs and "memory" runs. It can be seen that the "memory" runs result in a remarkable reduction in the induction time for all sets of experiments. Exp. no. 1–3 and 4–6 (as marked in Table 2.2) are for the systems of 10 wt% TBAB solution and pure water without any kinetic promoter, respectively, acting as reference cases in the experiment. The induction time for the 10 wt% TBAB system at 283.15 K in the experiment is 15.2–20 min, and that for the water system at 276.45 K is 12.5–31 min. For the water system in the presence of SDS only, the induction time is significantly reduced from 12.5–31 min to 0.5–2 min in the presence of SDS at 500–1000 ppm. It is due to the fact that SDS as a surfactant can lower its surface tension and change the water activity [34]. However, it is found that for the SDS concentration of 1500 ppm (exp. no. 13–15 in Table 2.2), the induction time is 17.4–25.5 min, which is significantly longer than that of the SDS system at 500–1000 ppm. This is likely due to a reduced SDS activity for gas migration at high concentrations of SDS. SDS molecules tend to interact with each other and form micelles in water at its critical micelle concentration (CMC), which is 2450 ppm at 276.45 K, calculated by the method of Marcolongo and Mirenda [124]. The higher SDS concentration (1500 ppm) in this study may have resulted in stronger intramolecular interactions of SDS–SDS molecules, and reduced SDS–gas and/or SDS–water interactions, and therefore prolonged induction time. DTAC also shows a reduction effect on induction time in pure water systems. At 276.45 K, the induction time is shortened from 36 min to 4.6 min when DTAC concentration increases from 0.1 to 0.6 wt%.

As for the TBAB systems, with the addition of SDS or DTAC, the induction time is also reduced in general compared with the reference case of TBAB solution. As in the water system, SDS reduces the induction times at the two lower concentrations but increases the induction time at the high concentration (1500 ppm). For DTAC, just as in pure water, a positive correlation between the increase of the concentration and the induction time reduction is observed. Furthermore, DTAC has an overall better effect on induction time reduction than SDS in the TBAB system for the concentrations studied. This is different from what occurs in the water system, in which a low concentration of SDS results in a stronger effect on induction time reduction than DTAC. One possible reason is that TBAB itself is a cationic surfactant [22]. The TBAB molecules may interact with the anionic molecules of SDS, reducing its capacity to reduce the induction time. It has been reported that formulas containing cationic surfactants and oppositely charged anionic surfactants tend to produce a gooey mess that falls out of solution due to the molecular interactions of the two types of surfactants [125, 126]. Therefore, where TBAB is present, the effect of the anionic surfactant SDS is impaired.

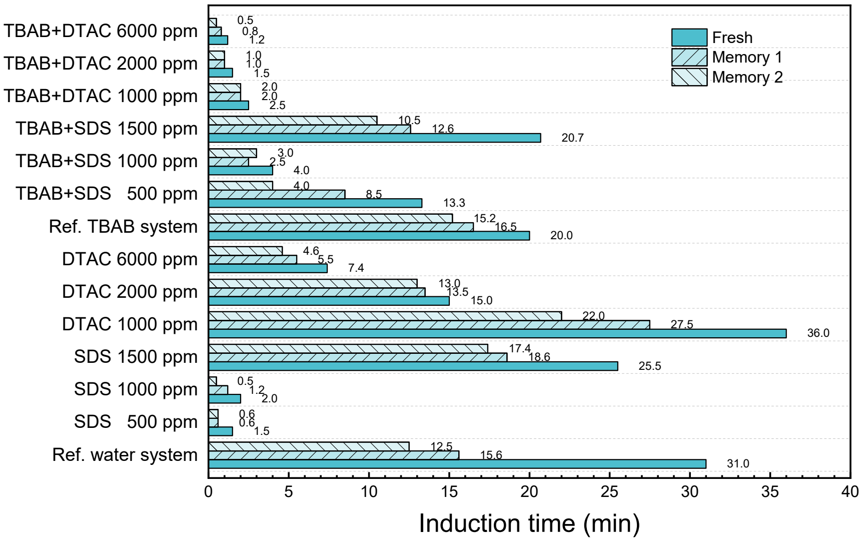

Figure 2.5. Induction time for the experimental runs investigated in this study. For the water system, the experimental temperature is 276.45 K; for the TBAB system, the experimental temperature is 283.15 K.

2.4.2 Gas uptake during hydrate formation

In addition to the induction time, normalized CO_2 gas uptake is used to evaluate the performance of different kinetic promoters. Figure 2.6 and Figure 2.7 show the normalized CO_2 gas uptake in experimental runs of SDS and DTAC promoters in water systems at 276.45 K at the same initial pressure of 3.8 MPa. The points in the lines of the figures represent the mean normalized gas uptake of three repeated runs. The vertical error bars correspond to 95% confidence intervals based on a student's *t*-test (see Appendix C). The errors in the methods come from both random errors and systematic errors. Because the hydrate nucleation is random in the solution [127], there are bound to be discrepancies in the results of different runs, although operated in the same condition. In addition, the cooling temperature is slightly affected by the change of room temperature during the long experimental duration. The thermostatic bath temperature also fluctuates within a small temperature range of ±0.05 K. Moreover, the gas analyzer also bring measurement errors, including the operation of testing gas samples and the precision of the gas analyzer. It can be seen that the normalized CO_2 uptake increases with the increase of SDS and DTAC concentrations. Variations in CO_2 uptake rate, that is, the slope of the curves, are observed in the first half of the experiments. The uptake rates in the DTAC system are closer to each other (Figure 2.7), while those in the SDS system are further apart (Figure 2.6). With DTAC, the final CO_2 uptake yields within 6 hours are also close to each other, and are in general double that in pure water. Comparing all the runs, 6000-ppm DTAC achieves the largest amount of normalized CO_2 uptake of 0.0825 $mol_{(gas)}/mol_{(water)}$, which is 2.17 times that of the reference water system. Although the gas uptake is still gradually increasing at around 6 hours for some runs without TBAB, the results are all compared in a unique 6 hours in this work because of the practical operation needs and the intensive uptake periods.

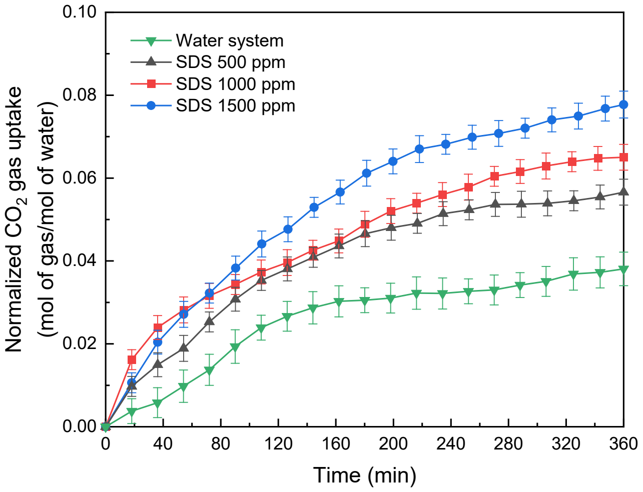

Figure 2.6. Normalized CO_2 gas uptake with SDS at 276.45 K. Vertical error bars correspond to 95% confidence intervals.

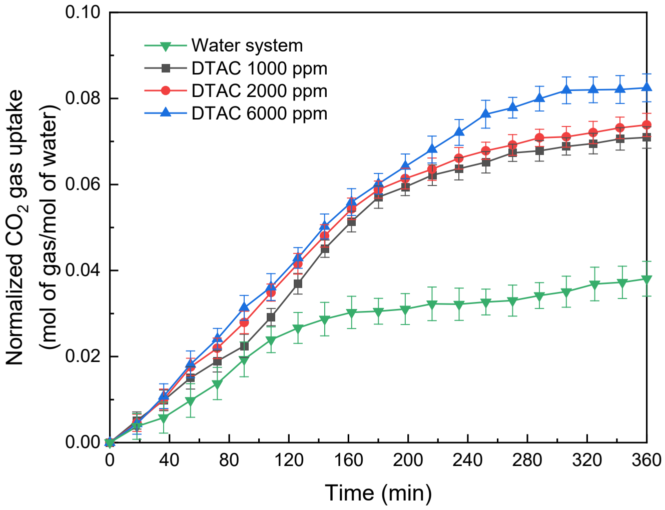

Figure 2.7. Normalized CO_2 gas uptake with DTAC at 276.45 K. Vertical error bars correspond to 95% confidence intervals.

Figure 2.8 and Figure 2.9 present the normalized CO_2 gas uptake for CO_2–TBAB semiclathrate hydrates formed in the presence of SDS and DTAC at 283.15 K and 3.8 MPa at the same TBAB concentration of 10 wt%. It can be seen in Figure 2.8 that the normalized CO_2 gas uptake decreases with increased SDS concentration, which is different from the trend found in the pure water systems (Figure 2.6). Overall, only SDS at 500 ppm presents a slightly higher normalized CO_2 uptake than that of the reference case of the TBAB system. The normalized CO_2 gas uptake in the reference case of the TBAB system reaches 0.025 $mol_{(gas)}/mol_{(water)}$ in 120 min, but in other studies, it was only 0.0104 $mol_{(gas)}/mol_{(water)}$ in 5 wt% TBAB solution without other promoters at 6 MPa and 279.2 K [23]. This reflects that the gas uptake can vary widely under different experimental conditions and setups. The higher concentration of SDS results in lower CO_2 uptake after exceeding 500 ppm, indicating an inhibitory effect of SDS in TBAB solutions. In the water system (Figure 2.6), there is no inhibitory effect of gas uptake found for all SDS concentrations studied, while the inhibitory effect appears in the TBAB solution for SDS concentrations of 1000 and 1500 ppm (Figure 2.8). The inhibitory effect of SDS in CO_2 recovery has been reported by others where it can also be used as an inhibitor for hydrate formation with thermodynamic promoters at certain concentrations [128]. The addition of the SDS may in turn cancel some thermodynamic effects of TBAB due to the opposite charge of SDS, especially at higher concentrations of 1000 and 1500 ppm. As can be seen in Figure 2.4, a higher driving force is required for CO_2 hydrate formation at reduced TBAB concentrations.

In other words, the presence of the anionic kinetic promoter SDS, alleviating the thermodynamic effects of TBAB, reduces the driving force for CO_2 hydrates formation when compared with the TBAB system without SDS, and thus results in reduced CO_2 uptake. The opposite charge of TBAB also in turn alleviates the kinetic effects of SDS, as discussed, which is another reason for the lower uptake in the SDS–TBAB system than in the SDS–water system.

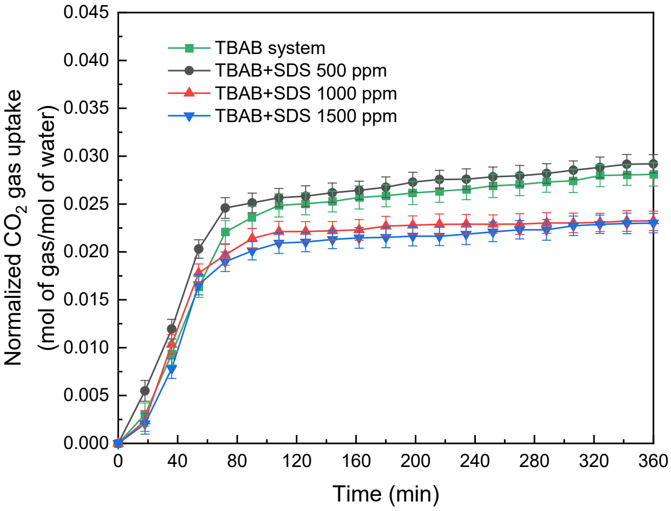

Figure 2.8. Normalized CO_2 gas uptake in TBAB+SDS solution at 283.15 K. Vertical error bars correspond to 95% confidence intervals.

Figure 2.9 illustrates a similar dependence of CO_2 uptake on DTAC concentration. At the concentration of 1000 ppm, a much higher CO_2 uptake than that of the TBAB system is observed during the entire 6 hours, and it keeps growing even at the end of experiment. At 2000 ppm, the results are very close to those of the reference case (system with only TBAB). A further increase in DTAC concentration to 6000 ppm results in a dramatic reduction in CO_2 uptake compared to the TBAB system. The CMC of DTAC in water at the experimental temperature is 6600 ppm as reported in the work of Mehta et al. [129], and the investigated concentration of 6000 ppm, in the present study is very close to the reported CMC. The presence of TBAB may further reduce its CMC due to the impact of the ionic strength on the surfactant [129]. Therefore in the presence of TBAB, the increased DTAC concentration may predominantly strengthen the DTAC–DTAC intramolecular interactions and reduce DTAC–gas and/or DTAC–water interactions, resulting in reduced water activities and therefore reduced gas uptake. In addition, TBAB is a strong polar and acidic compound. The TBAB semiclathrate crystals can rapidly form a dense hydrate layer due to the effect of dispersive forces, induction forces, orientation forces and ionic polarization [130]. In the present work, the hydrates formed from TBAB solutions are only observed at the water–gas interface. It is believed that as the surface tension is lowered by surfactants, CO_2–TBAB hydrate forms more intensively on the water–gas interface, which however, blocks CO_2 permeability into bulk water in an earlier stage for further hydrate formation [23], resulting in a low gas uptake. Besides, as is shown in Figure 2.9, with the addition of DTAC, the CO_2 uptake continuously rises until the end of the experiment, but in Figure 2.8, with the addition of SDS, it rises more rapidly and plateaues in a short time (around 75 min). This may be due to the higher density and lower porosity of semiclathrate hydrates formed with SDS than those with DTAC. Morphology studies of the CO_2–TBAB semiclathrate hydrates in the presence of SDS or DTAC are needed to understand the mechanisms. Overall, within 6-hour hydrate formation, the highest uptake (0.0412 $mol_{(gas)}/mol_{(water)}$) is achieved by DTAC at 1000 ppm, which is close to that of the pure water system at 276.45 K.

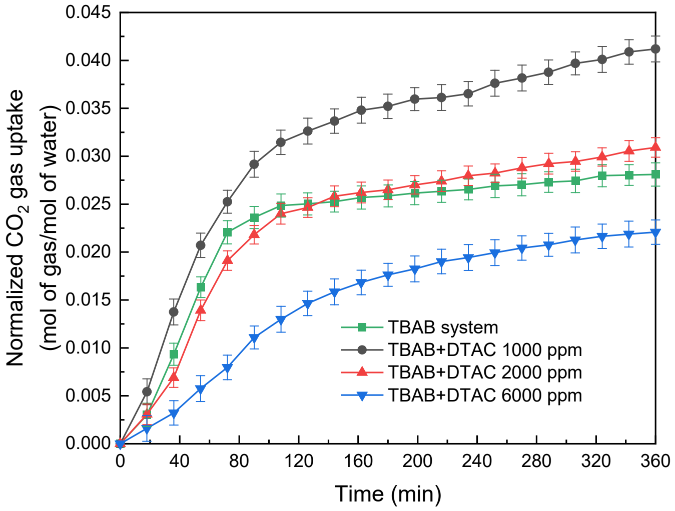

Figure 2.9. Normalized CO_2 gas uptake in TBAB+DTAC solution at 283.15 K. Vertical error bars correspond to 95% confidence intervals.

Figure 2.10 shows a comparison of the rate of CO_2 hydrate growth in all the experimental runs in the first 30 min after hydrate nucleation, which is denoted by NR_{30,CO_2}. It can be seen clearly that CO_2 hydrates in the SDS and TBAB+SDS systems grow faster than those in the DTAC and TBAB+DTAC systems. In the water system with SDS, the highest CO_2 hydrate growth rate is achieved. In the case of SDS at 1500 ppm in water system, the normalized rate of CO_2 hydrate growth is 30 mol $min^{-1}m^{-3}$, and the normalized gas uptake reaches up to 0.08 $mol_{(gas)}/mol_{(water)}$ in Figure 2.6. Interestingly, in the work of Linga et al. [131, 132], the CO_2 hydrate formation in the silica sand was reported to have a similar gas uptake of 0.09 $mol_{(gas)}/mol_{(water)}$ and the normalized hydrate growth rate of 32 mol $min^{-1}m^{-3}$. This is a surprising result that the SDS 1500 ppm has a close promotion effect to the silica sand with an average diameter of 329 μm (specific surface area of 0.3499 cm^2g^{-1}). In the water system with DTAC, CO_2 hydrate growth rates in the three runs are similar, which is consistent with the results shown in Figure 2.7. In TBAB solutions, SDS also performs better than DTAC to accelerate hydrate growth. However, the overall effects of both SDS and DTAC on the acceleration of hydrate growth are weakened as the surfactant concentrations increased in TBAB systems.

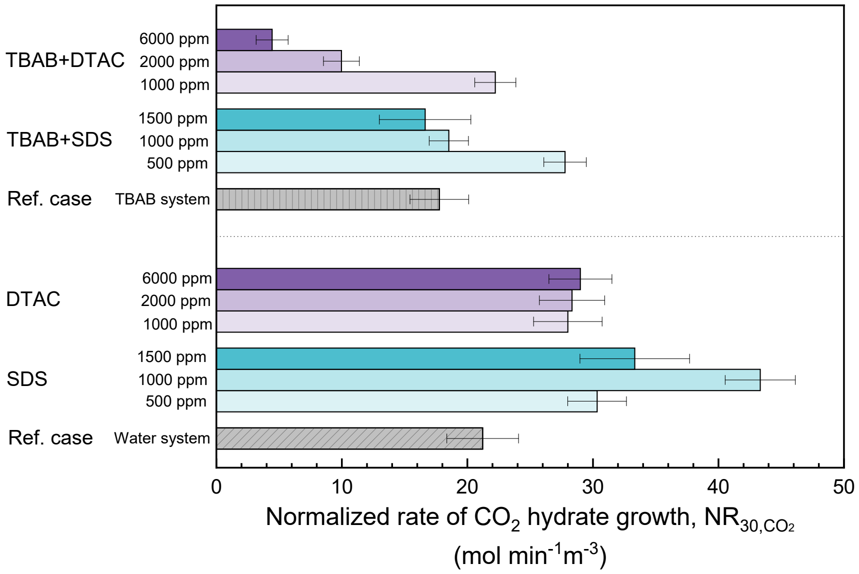

Figure 2.10. Normalized rate of CO_2 hydrate growth, NR_{30,CO_2} . For DTAC and SDS in water system, T_{exp} = 276.45 K. For TBAB+DTAC and TBAB+SDS, T_{exp} = 283.15 K. Horizontal error bars correspond to 95% confidence intervals.

2.4.3 CO_2 recovery during hydrate formation

The separation efficiency of the combined effect of TBAB and kinetic promoters is evaluated using split fraction (S.Fr.) and separation factor (S.F.). Figure 2.11

compares S.Fr. for experiment runs at the end of 6 hours. All the experiments, both in the water system and TBAB system are conducted at the same initial pressure of 3.8 MPa. What stands out in the figure is that S.Fr. in systems with DTAC is in general larger than that in systems with SDS. In the water system, S.Fr. ranges from 0.37 to 0.46 with the addition of DTAC and from 0.32 to 0.39 with the addition of SDS, and it is seen that S.Fr. increases continuously with the rise of surfactant concentration throughout the concentration range studied. Compared with the work in a previous study [114], the S.Fr. was only 0.32 for CO_2/N_2 gas mixtures in the water system without any kinetic promoters. In the TBAB system, S.Fr. is lower than that in water, that is, 0.18–0.23 for the TBAB+SDS system and 0.13–0.29 for the TBAB+DTAC system. It was reported that in 5 wt% TBAB and 4000 ppm DTAC solution, the S.Fr. was 0.54 [34], almost double the result in the present work. So it is also considered that although a high concentration of TBAB (e.g., the present work in comparison to [34]) can raise the phase equilibrium temperature, the CO_2 recovery performance is reduced. It is also noted that in TBAB systems, SDS at 1000 and 1500 ppm and DTAC at 6000 ppm demonstrate inhibitory effects in S.Fr. compared with the reference case, which is also in agreement with the inhibitory effect shown in Figure 2.8 and Figure 2.9.

The results of the separation factor for 6-hour hydrate formation are summarized in Figure 2.12. S.F. is an indicator that reflects the ability to separate CO_2 selectively from other gases. It is apparent that DTAC performed better selectivity than SDS in both water and TBAB systems. The S.F. of DTAC in the water system varies from 6.79 to 10.20, and the S.F. of SDS in the water system ranges from 5.57 to 8.09. Similarly, S.F. in TBAB systems is also lower than that in water systems. In general, the trends of S.F. is consistent with that of S.Fr. in Figure 2.11. It can be concluded that DTAC performs better than SDS in CO_2 recovery and selectivity from gas mixtures of CO_2 and N_2 at given concentrations.

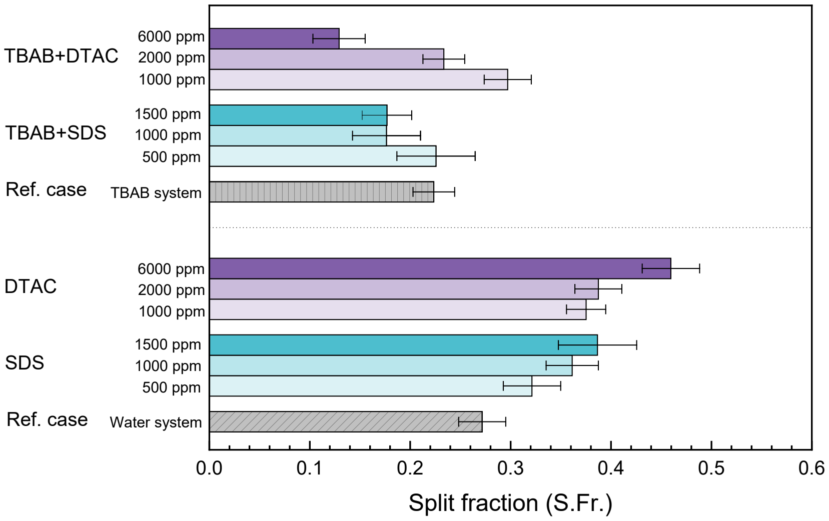

Figure 2.11. Split fraction after hydrate formed for 6 hours. For DTAC and SDS in water systems, T_{exp} = 276.45 K; for DTAC and SDS in TBAB systems T_{exp} = 283.15 K. Horizontal error bars correspond to 95% confidence intervals.

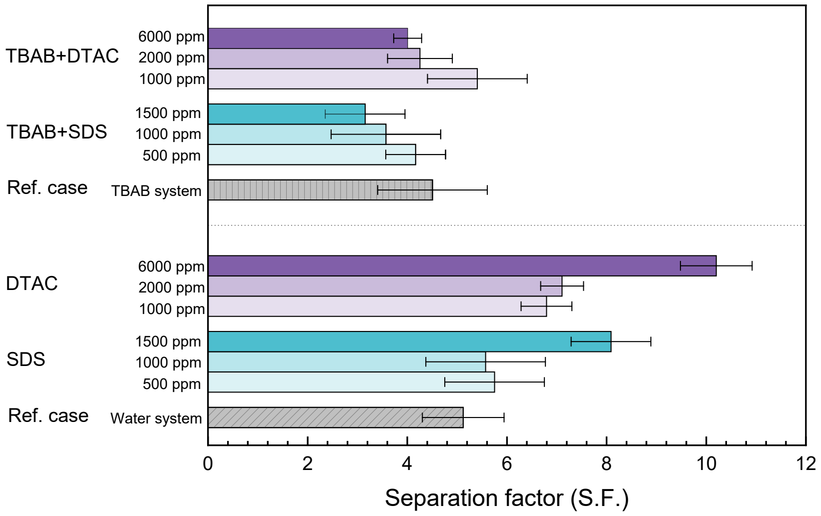

Figure 2.12. Separation factor after hydrate formed for 6 hours. For DTAC and SDS in water systems, T_{exp} = 276.45 K; for DTAC and SDS in TBAB systems, T_{exp} = 283.15 K. Horizontal error bars correspond to 95% confidence intervals.

2.4.4 Effect of subcooling on CO_2 hydrate formation

Subcooling (ΔT) is defined as the difference between the phase equilibrium temperature and the experimental temperature at a given pressure. Figure 2.13 and Figure 2.14 show the normalized CO_2 gas uptake for the SDS concentration of 500 ppm and DTAC concentration of 1000 ppm (the optimal concentrations considering induction time, gas uptake and separation factor) in the 10-wt% TBAB system at three different subcooling degrees (4.69, 2.69 and 1.69 K). As shown in the results of SDS in Figure 2.13, in the case of subcooling at 4.69 K, the gas uptake reaches at peak at around 75 min after the formation starts, and similarly, the gas uptake with subcooling at 2.69 and 1.69 K approaches the peak at about 125 and 170 min, respectively, and then flattened out. The greater the degree of subcooling, the earlier the peak point appears. For the results of DTAC in Figure 2.14, the normalized CO_2 gas uptake rises continuously even at the end of 6 hours for all subcooling conditions. No obvious plateau is seen, although the increase of gas uptake becomes slower after a turning point. In both cases, the overall CO_2 gas uptake increases with increased subcooling. It can be concluded when kinetic promoters have a promotion effect on gas uptake, a larger subcooling will also enhance this promotion effect.

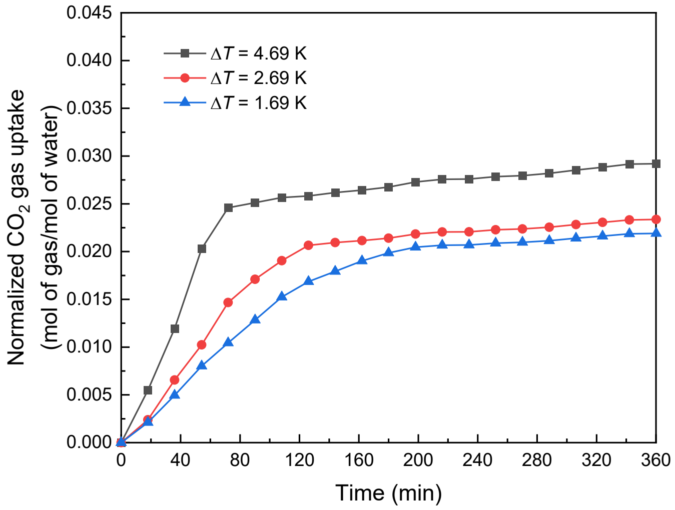

Figure 2.13. Effect of subcooling for TBAB+SDS system with SDS of 500 ppm.

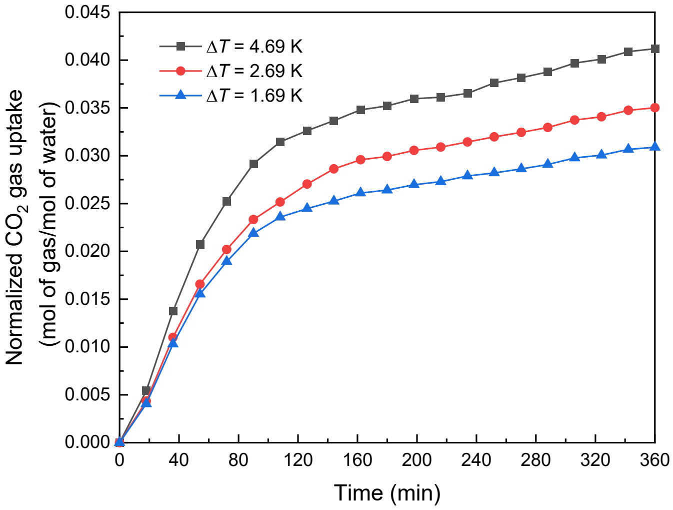

Figure 2.14. Effect of subcooling for TBAB+DTAC with DTAC of 1000 ppm.

Figure 2.15 and Figure 2.16 present the split fraction and separation factor for the TBAB+SDS (SDS at 500 ppm) and TBAB+DTAC (DTAC at 0.1 wt%) systems at three different subcooling degrees. For each experiment, the time duration is 6 hours after hydrate formation. As shown in Figure 2.15, the split fraction increases with the increase in subcooling for both TBAB+SDS and TBAB+DTAC systems. DTAC shows a higher split fraction than SDS at all the three subcooling conditions. The effect of subcooling on the split fraction of systems with DTAC is more obvious. The split fraction of the TBAB+SDS system ranges from 0.16 to 0.23, and the split fraction of the TBAB+DTAC system varies from 0.19 to 0.30 at the subcooling of 1.69–4.69 K. It can be seen in Figure 2.16 that the separation factor also increases with the rise of subcooling, and DTAC presents better separation performance than SDS at all three subcooling conditions. In addition, subcooling affects the separation factor of DTAC systems more significantly. The separation factor of the TBAB+SDS system varies from 2.65 to 4.17, and the separation factor of the TBAB+DTAC system changes from 3.03 to 5.41 at subcooling of 1.69–4.69 K.

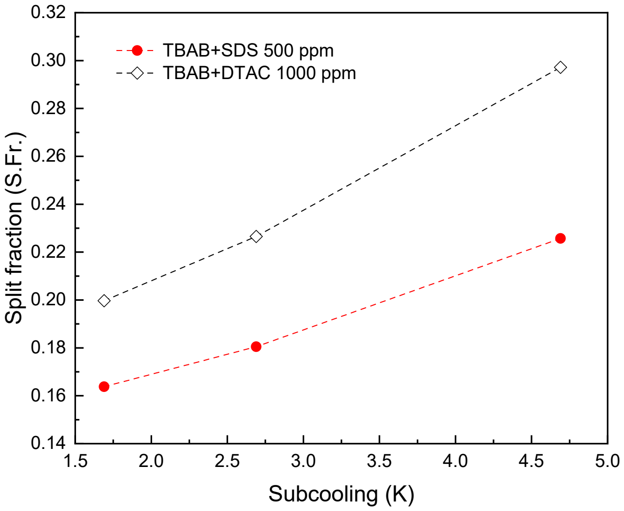

Figure 2.15. Effect of subcooling on split fraction.

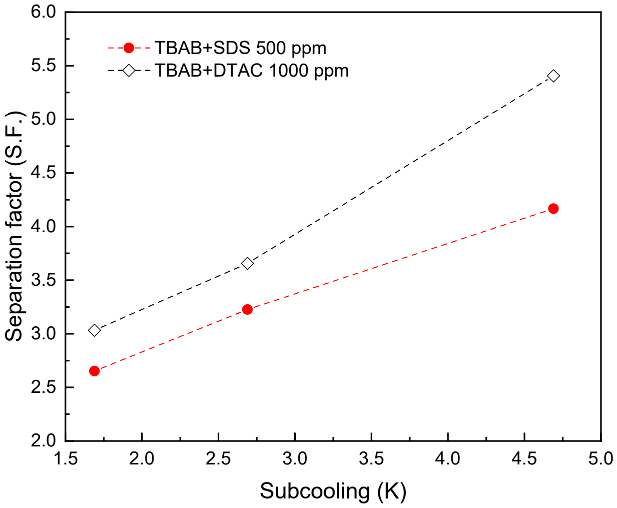

Figure 2.16. Effect of subcooling on separation factor.

2.4.5 CO_2 uptake rate and intensive uptake period of hydrate formation

The normalized CO_2 uptake rate (1st derivative of normalized CO_2 uptake), shown as the dashed lines in Figure 2.17, is used to evaluate the kinetics of the TBAB+SDS (SDS at 500 ppm) system and the TBAB+DTAC (DTAC at 0.1 wt%) system at a unique subcooling of 2.69 K. A green demarcation line of CO_2 uptake rate is defined as 5×10^{-5} $mol_{(gas)}/mol_{(water)}/min$ for effective CO_2 uptake. The period with CO_2 uptake rate higher than this value is identified as an intensive uptake period, while the one with lower uptake rate than this value is taken as a weak uptake period, as is illustrated in Figure 2.17. It can be seen that the TBAB+DTAC system has a longer intensive uptake period of 154 min than the TBAB+SDS system of 126 min.

Based on this definition, the intensive uptake periods of the two systems at three subcooling degrees (1.69, 2.69 and 4.69 K) are summarized in Table 2.3. As can be found in Table 2.3, the duration of the intensive uptake period of TBAB+SDS (SDS at 500 ppm) system decreases with the increment of subcooling, indicating that the system completes effective uptake more rapidly with higher driving force, probably due to the early blockage of hydrate film on the gas–water interface. In contrast, the intensive uptake periods of the TBAB+DTAC (DTAC at 1000 ppm) system are extended with higher subcooling, which is also a result of a lower blockage effect on CO_2 permeability of the hydrates formed with DTAC, and this is to be verified in subsequent studies. The aim of proposing this intensive uptake period based on the normalized gas uptake rate is to understand the optimal duration of hydrate-based carbon capture (HBCC) processes. It is noted that in different systems and conditions, the normalized gas uptake rate of a benchmark will vary. The intensive uptake period is another metric of promoter selection and can be used to recommend practical applications for energy saving.

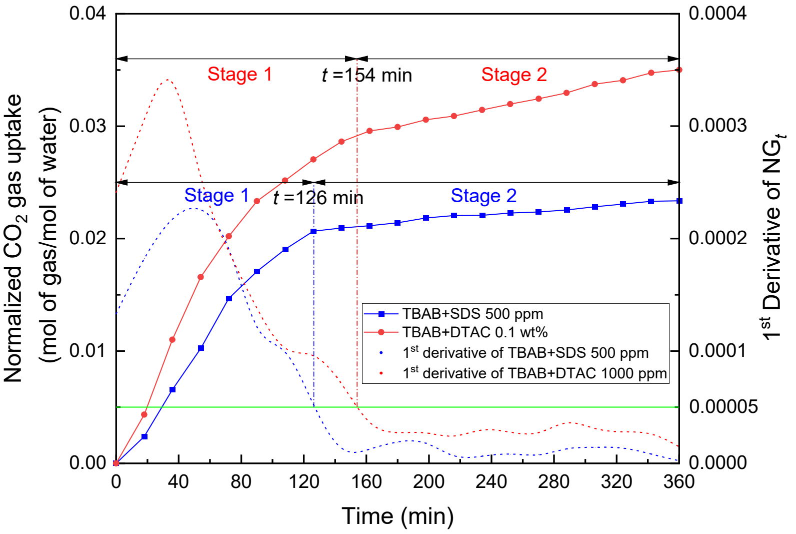

Figure 2.17. Normalized CO_2 gas uptake rate for TBAB+SDS (SDS at 500 ppm) and TBAB+DTAC (DTAC at 1000 ppm) systems at subcooling of 2.69 K. The scatter lines represent the normalized CO_2 gas uptake, and the dash lines are the 1st derivatives of the normalized CO_2 uptake.

Table 2.3. The intensive uptake periods of TBAB+SDS (SDS at 500 ppm) and TBAB+DTAC (DTAC at 0.1 wt%) systems at three subcooling degrees.

Exp. no.	System	Kinetic promoters	T_{exp} (K)	ΔT (K)	Intensive uptake period (min)
16	TBAB	SDS (500 ppm)	283.15	4.69	82
19	TBAB	SDS (500 ppm)	285.15	2.69	126
20	TBAB	SDS (500 ppm)	286.15	1.69	165
36	TBAB	DTAC (1000 ppm)	283.15	4.69	159
39	TBAB	DTAC (1000 ppm)	285.15	2.69	154
40	TBAB	DTAC (1000 ppm)	286.15	1.69	121

Figure 2.18 is the illustration of CO_2 and surfactants movement during hydrate formation with/without TBAB considering the aforesaid hydrate film blockage mechanism in a stationary hydrate formation. DTAC 2000 ppm solutions with/without TBAB (runs no. 30 and 41) are used as examples to show the difference in the presence and absence of TBAB. N_2 is not included in this diagram for simplification. As shown in Figure 2.18 (a1) and (b1), before hydrates form, the surfactants improve CO_2 transport into the liquid phase both in the system with/without TBAB. In Figure 2.18 (a2) and (b2), as hydrate film is formed, CO_2 will need to cross the hydrate film to reach water to form further hydrate. With the help of surfactants in the water system, effective CO_2 transportation is maintained; however, as CO_2–TBAB double hydrate is more compact than CO_2 hydrate [23, 130], CO_2 transportation through the hydrate film requires more driving force, and therefore less CO_2 permeates in this stage in Figure 2.18 (b2) with TBAB. As the thickness of hydrate film reaches the critical hydrate film thickness (CHFT), as shown in Figure 2.18 (a3) and (b3), no CO_2 can be transported to water anymore (i.e., the CO_2 transportation path is entirely blocked), and the onward hydrate formation only makes use of CO_2 that is already in the bulk water until the end of hydrate formation, as shown in Figure 2.18 (a4) and (b4). The CHFT is defined in this work. It is believed that the turning point of normalized CO_2 uptake curves and the end of the intensive uptake period are very likely to coincide with the time when the hydrate film reaches the CHFT, that is, the period before CHFT represents the intensive uptake period. It is also noted that the CHFT with TBAB is thinner than that without TBAB, as shown in Figure 2.18 (a3) and (b3), due to the compact CO_2–TBAB double hydrate. Comparing Figure 2.18 (a4) and (b4), it can be seen that for the above reasons the gas uptake is bound to be less in the system with

TBAB and the effect of surfactant is weakened, which is consistent with the findings in Section 2.4.2. In the present study, due to the stationary formation process, small reactor size and low TBAB concentrations, deposition of hydrate to the bottom of the reactor is not observed. However, in large reactors with continuous agitation, the blockage effect of hydrate film may not be dominant. It is noted that the semiclathrate hydrate formation can happen synchronously inside the aqueous solution and be deposited at the bottom of the reactor due to the high density, as reported in an experimental study under continuous stirring [25]. In this case, the hydrate nucleation is more likely to occur inside the solution due to the prompted CO_2 permeation in water and the homogeneity of the solution. However, in this present study, the stirrer is stopped after hydrates started to form, and in the stationary system the semiclathrate hydrates formed in the gas–liquid interface preferentially.

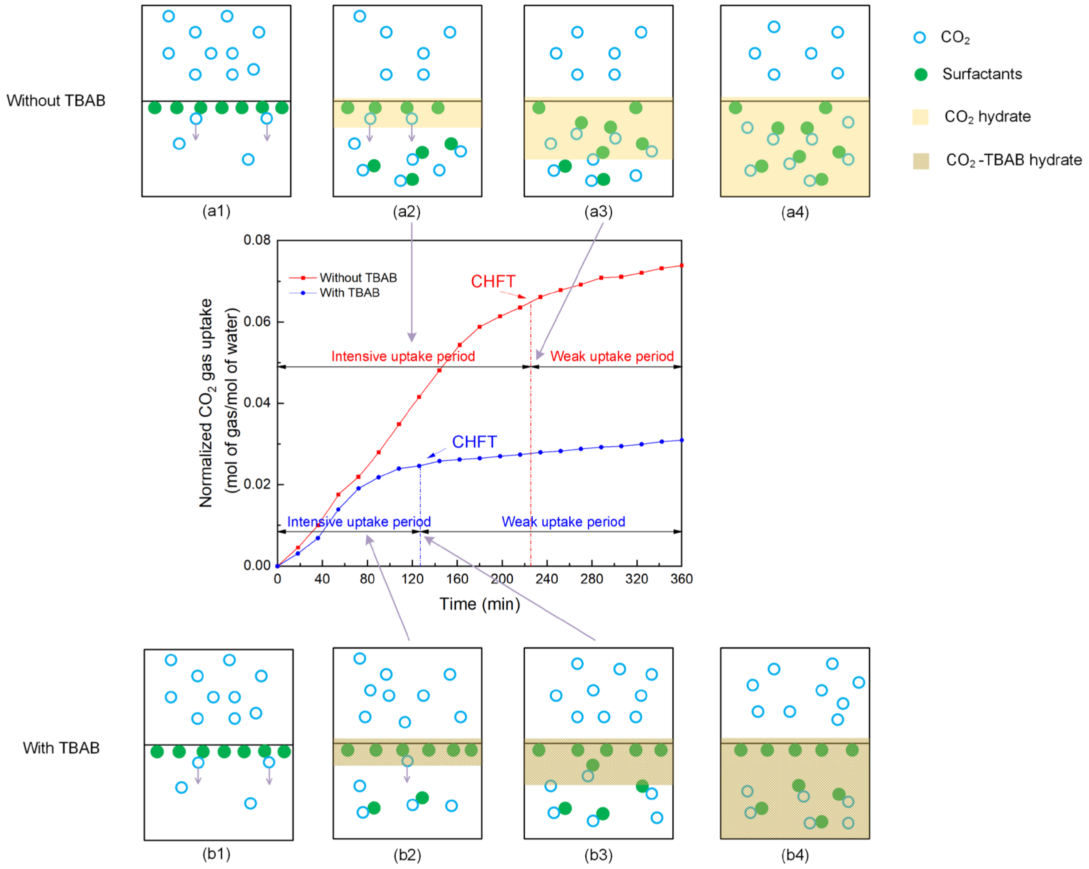

Figure 2.18. CO_2 hydrates formation with 2000-ppm DTAC with/without TBAB in the hydrate reactor: (a1) and (b1) before hydrate formation; (a2) and (b2) hydrate film thickness less than CHFT; (a3) and (b3) hydrate film thickness reaches CHFT; (a4) and (b4) end of hydrate formation.

2.5 Experimental study on combined effects of TBAB and non-ionic surfactant

The combined effects of thermodynamic promoters and ionic surfactants have been studied for years. However, little is known about the effect of non-ionic surfactants on the thermodynamic promoter. T-80, as a low-cost and environmentally friendly non-ionic surfactant and emulsifier, is commonly used in the food and cosmetics industries [36]. Currently, the mechanism of non-ionic T-80 on TBAB semiclathrates is still unclear; very few papers studied the T-80+TBAB pairs, and the effect of T-80 on CO_2 separation from gas mixtures is still unknown. This section aims to experimentally explain the influence of the non-ionic T-80 on the CO_2 hydrates formation conditions in TBAB semiclathrate hydrates and to improve the gas uptake yields that may not be possible with TBAB alone. CO_2/N_2 gas mixtures with 70-mol% CO_2 were also used in this section. The kinetic experiments were conducted in TBAB solutions (0 and 10 wt%) containing varied T-80 concentrations of 0, 1000, 2000 and 3000 ppm. The effects of T-80 on CO_2 hydrate kinetic performance were comprehensively evaluated, including induction time, CO_2 gas uptake yield, hydrate growth rate, percent water conversion, and separation performance. The pressure change on selected systems was also examined. Photos of hydrates formed in different systems were analyzed.

2.5.1 Experimental procedure

The experimental apparatus used in this section was the same as that in Section 2.3. The reactor was first cleaned and rinsed five times before the solution was poured in. Then, the reactor was closed tightly and degassed by a vacuum pump. The thermostatic bath was turned on to provide a thermostatic condition for hydrate formation. Once it has been maintained at the target temperature for 30 min, the reactor was charged with the gas mixtures, and the motor stirrer on top was set to run at 500 rpm. This is the onset of the kinetic experiment. During the experiments, the gas composition was analyzed by the gas analyzer. The amount of gas taken for sampling was ~0.1 mL, <0.2‰ of the total charged gas volume, and negligible. Each experimental run lasted for at least 360 min and was repeated twice under the same conditions. Since the repeated runs were conducted in solutions that have experienced hydrate formation, the memory effect may occur; therefore, the experimental runs were named as “Fresh”, “Memory 1” and “Memory 2” respectively. The volume of solution used in each run is 100 mL. The initial experimental pressures (P_{exp}) and temperatures (T_{exp}) in this work are shown in Table 2.4.

2.5.2 Experimental conditions

Although 15–25-mol% CO_2 with N_2 are approximately the actual composition of flue gas [27, 114], HBCC is perfectly employed in the latter stage of multi-stage carbon capture [7–9] with approximately 70-mol% CO_2 to achieve high CO_2 purity of >95 mol% after separation [35]. The TBAB concentration used in this work was 10-wt%, unique for all the runs, for both a suitable phase equilibrium condition and a large gas uptake yield of the hydrate formation, based on the findings of our previous studies [13, 35]. For the experimental conditions in this work, they are also carefully chosen. As is found in literature, TBAB itself can form hydrates in water without guest gas [116]. To form CO_2–TBAB semiclathrate hydrates and prevent TBAB itself from hydration, the pressure and temperature setting should be carefully determined. In water system (clathrate hydrates), T_{exp} was set to 276.45 K (the corresponding equilibrium data can be found in [133]). To prevent CO_2 from liquefaction at 276.45 K, the pressure should be lower than 5.48 MPa. In the 10-wt% TBAB solution, TBAB itself can form hydrate below 280 K, so the T_{exp} was set to 283.15 K (the corresponding equilibrium data of CO_2–TBAB semiclathrate hydrates can be found in [134]). The subcooling, defined as the difference between T_{eq} and T_{exp} at given pressure for each experiment, is listed in Table 2.4.

Table 2.4. Summary of experimental conditions and measured data.

Exp. no.	Solution	Kinetic promoters	Exp. state	P_{exp} (MPa)	T_{exp} (K)	ΔT (K)	x_{CO2}^*
1	Water	–	Fresh	3.8	276.45	2.90	64.12
2			Memory 1				63.84
3			Memory 2				63.69
4	Water	T-80 (1000 ppm)	Fresh	3.8	276.45	2.90	53.22
5			Memory 1				52.11
6			Memory 2				52.09
7			Fresh	3.0	276.45	0.91	54.70
8			Memory 1				54.35

Exp. no.	Solution	Kinetic promoters	Exp. state	P_{exp} (MPa)	T_{exp} (K)	ΔT (K)	x_{CO2}[*]
9			Memory 2				54.13
10			Fresh	4.5	276.45	5.25	51.10
11			Memory 1				51.25
12			Memory 2				50.86
13	Water	T-80 (2000 ppm)	Fresh	3.8	276.45	2.90	56.05
14			Memory 1				55.92
15			Memory 2				55.61
16	Water	T-80 (3000 ppm)	Fresh	3.8	276.45	2.90	59.71
17			Memory 1				57.78
18			Memory 2				57.50
19	TBAB (10 wt%)	–	Fresh	3.8	283.15	4.69	66.35
20			Memory 1				66.12
21			Memory 2				65.89
22	TBAB (10 wt%)	T-80 (1000 ppm)	Fresh	3.8	283.15	4.69	55.65
23			Memory 1				55.41
24			Memory 2				54.12
25			Fresh	3.0	283.15	4.10	56.32
26			Memory 1				56.24
27			Memory 2				56.18
28			Fresh	4.5	283.15	5.65	53.28
29			Memory 1				53.03
30			Memory 2				52.65
31	TBAB (10 wt%)	T-80 (2000 ppm)	Fresh	3.8	283.15	4.69	54.12
32			Memory 1				53.98
33			Memory 2				53.77
34	TBAB (10 wt%)	T-80 (3000 ppm)	Fresh	3.8	283.15	4.69	60.59
35			Memory 1				60.14
36			Memory 2				59.87

[*] x_{CO2} represents the final CO_2 concentration in the gas phase.

2.6 Results and discussion of combined effects of TBAB and non-ionic surfactant

2.6.1 Induction time

Induction time is determined as the time period between the onset of the experiment and the moment when an abrupt pressure decrease and a temperature increase occur simultaneously, as shown in Figure 2.19 [123]. Figure 2.20 shows the induction time for different experimental runs. "Ref. clathrate hydrates" or "Ref. semiclathrate hydrates" represents the reference runs in water or TBAB solution without adding T-80, corresponding to exp. no. 1–3 and 19–21 in Table 2.4, respectively. As can be seen, the induction time is lower in "memory" runs than in "fresh" runs in both systems, especially in the clathrate hydrates. The induction time is overall shorter in semiclathrate hydrates (2–20 min) than that in clathrate hydrates (13–31 min). The diffusion of CO_2 into the liquid phase is thus believed vital for hydrate formation kinetics. Moreover, for both systems, the greater the concentration of T-80, the shorter the induction time. It is also found from Figure 2.20 that in semiclathrate hydrates, the induction time is more significantly reduced by T-80 than for clathrate hydrates. For instance, in the "fresh" runs, the induction time of the TBAB+T-80 systems has a 67.5%–85.0% reduction compared to that of the "Ref. semiclathrate system", whereas it is only 14.5%–32.2% reduced in clathrate hydrates compared to the "Ref. clathrate hydrates". The induction time in "memory" runs is also dramatically reduced compared with "fresh" runs. For example, the induction time is reduced by 31%–50% in clathrate hydrates, and reduced by 18%–38% in semiclathrate hydrates from "fresh" runs to "memory" runs. However, the induction time reduces very little from "memory 1" to "memory 2" runs.

2.6.2 CO_2 gas uptake

The CO_2 gas uptake is a key metric for kinetic performance. This work measures all the gas uptakes under the normalized gas uptake. Figure 2.21 shows the CO_2 gas uptake in clathrate hydrates with T-80 at 276.45 K. The data presented in the figure are the average values of the three runs, and the error bars are the 95% confidence intervals based on the Student's *t*-distribution. It can be found that the CO_2 gas uptake of three systems with T-80 is all higher than that of the "Ref. clathrate hydrates". At the end of experiments ($t = 360$ min), T-80 at 1000 ppm presents the highest gas uptake among all the systems studied. It is also noted that although the gas uptake is still gradually increasing at around 360 min, the increasing rates of gas uptake are getting slower after 200 min. Thus, the results are all compared within a unique 360-minute time frame, taking into account the energy-saving requirements in practical CO_2 capture operations.

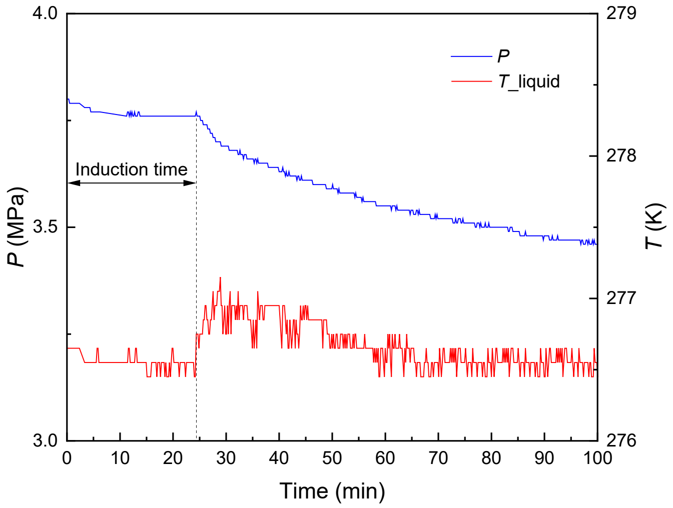

Figure 2.19. A typical temperature and pressure curve (For exp. no. 4).

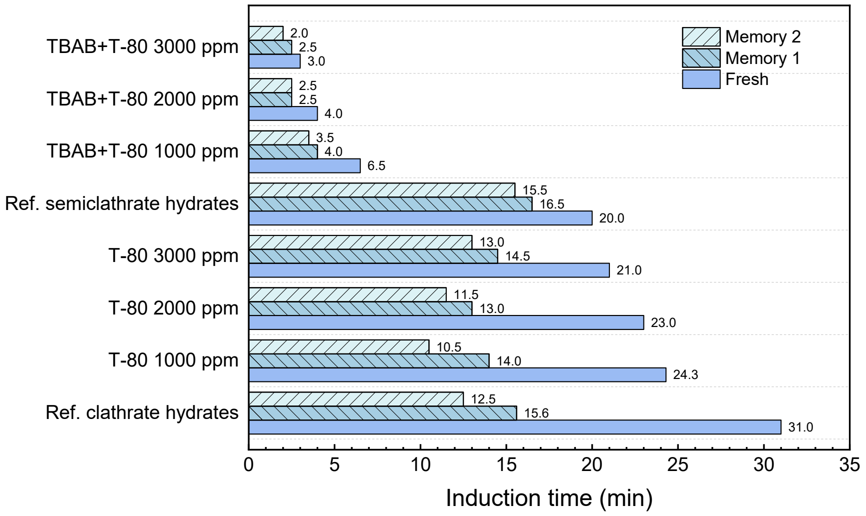

Figure 2.20. Induction time in the experimental runs of different systems at $P_{exp} = 3.8$ MPa. For clathrate hydrates, $T_{exp} = 276.45$ K; for semiclathrate hydrates, $T_{exp} = 283.15$ K.

Due to the overlap of the error bars and the stochasticity of gas hydrate formation, an analysis of variance (ANOVA) [135] (see Appendix C) is conducted to determine the magnitude of discrepancy in the results of different runs in the first 180 min. Only the time period before 180 min is studied by ANOVA as the difference in gas uptake after 180 min can be viewed apparently from the curves. Figure 2.22 shows the calculated probability (*p*-value) of the statistical significance of the systems studied containing T-80 at 1000, 2000 and 3000 ppm. Based on the theory of ANOVA, if the *p*-value is greater than 0.05, the difference of data is statistically insignificant, which means the data can be recognized as no difference. As can be seen, within 80–140 min at which error bars overlap severely, the *p*-value is greater than 0.05, indicating that the difference of gas uptakes is statistically insignificant; however, beyond this range, the differences in the results are convincing. This indicates that the gas uptakes can be recognized as different from 0–80 min and 140–360 min although the error bars are partly overlapped. Considering both Figure 2.21 and Figure 2.22, an initial positive correlation between the T-80 concentration and the gas uptakes (before t = 80 min) becomes inversely correlated afterward (after t = 140 min). The initial positive correlation is attributed to the fact that more micelles form at higher T-80 concentrations. Previous studies have reported that the critical micelle concentration (CMC) of T-80 is around 0.015 mM (20 ppm) at 298 K and depends weakly on temperature [136, 137]. Although the optimal concentration of anionic surfactants as efficient promoters is generally lower than its CMC, the T-80 concentrations in this work are far beyond its CMC. When exceeding CMC, the surface area is significantly increased by micelles formed in water, therefore enhancing CO_2 transport and uptake, which is prompted at higher concentrations of surfactants [138]. Zhang et al. [38] also reported that 1310 ppm T-80 produced supersaturated CH_4 molecules to promote the mass transfer and provide the complexation between water and CH_4. The inverse correlation between T-80 concentration and gas uptake later on can be caused by the increased viscosity of T-80 solution at higher concentrations. It is known that the viscosity of T-80 is 375 times that of water [32]. The viscosity of the solution might be increased at higher T-80 concentrations, which hinders the gas diffusion in the liquid phase.

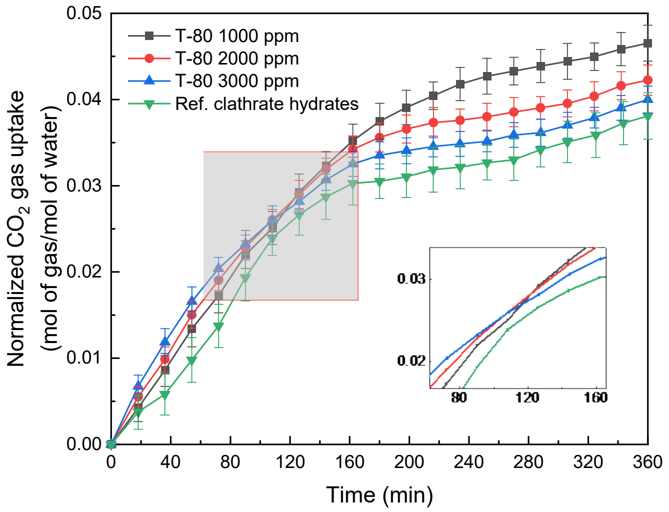

Figure 2.21. Normalized CO_2 uptake in clathrate hydrates with T-80 at 276.45 K, 3.8 MPa.

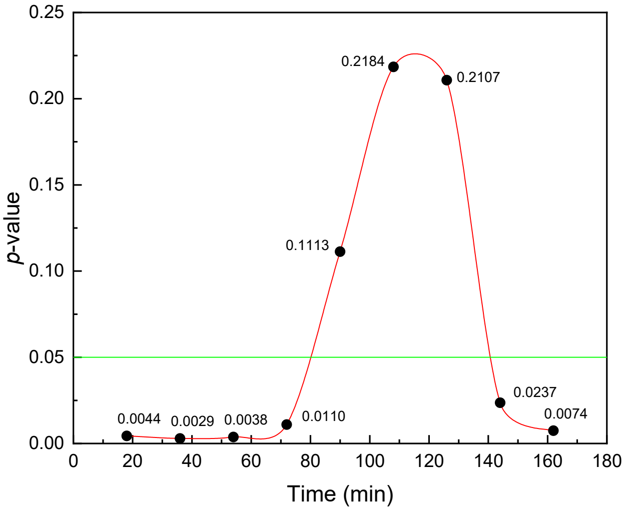

Figure 2.22. The *p*-value of the normalized CO_2 uptakes in clathrate hydrates.

Figure 2.23 presents the CO_2 gas uptake in TBAB systems with T-80 at 283.15 K. An ANOVA analysis of the four systems studied, as shown in Figure 2.24, is conducted within the first 100 min, during which overlaps of curves were noticed. It reveals that the gas uptake of the four systems is significantly different ($p < 0.05$). The initial gas uptake is in positive correlation to the concentration of T-80, similar to the tendency of pure water systems. Except for T-80 at 3000 ppm, the gas uptakes of the other three systems continue rising with increased concentration of T-80 until reaching plateaus at around 126 min, due to the "block effect" of the CO_2–TBAB semiclathrate formed. It is known that TBAB is a strong polar compound. The CO_2–TBAB hydrates can rapidly build a compact layer on the gas–water interface due to the effect of dispersive forces, induction forces, and ionic polarization of TBAB [130], causing a “block effect” that slows down further CO_2 transport. Such a characteristic of CO_2–TBAB semiclathrates is observed in Figure 2.25, which compares the morphology of CO_2 hydrate formation in clathrate hydrates and semiclathrate hydrates at 360 min. It can be seen that in clathrate hydrates with T-80 (Figure 2.25 a1–a3), hydrates tend to be uniformly suspend in the bulk solution, showing no apparent hydrate layer. However, in semiclathrate hydrates with T-80 (Figure 2.25 b1–b3), the hydrates formed mostly aggregate on the gas–liquid interface, while the lower solution remained clear. The uniform hydrate distribution in clathrate hydrates allows for continuing hydrate formation for a longer time and increased gas uptake (Figure 2.21), while the compact hydrate layers and blockage in semiclathrate hydrates lead to ceased hydrates growth at 80–120 min (Figure 2.23). A similar phenomenon was reported in previous studies by Daniel-David et al. [139]. They used a CCD camera to investigate the CO_2 hydrate formation in a water droplet in the presence of different surfactants including T-80, and crusts can be observed in most of the cases, except in the presence of some anionic surfactants (SDS). For 3000-ppm of T-80 in TBAB, the hydrate growth ceases as early as 80 min, and shows an obvious inhibition effect compared with “Ref. semiclathrate hydrates”. It is therefore suggested that for practical applications, it is essential to promptly separate the hydrate slurries formed from the solution. In addition, identifying the intensive gas uptake period for each specified system is vital to determine a proper operation duration for energy-efficient carbon capture.

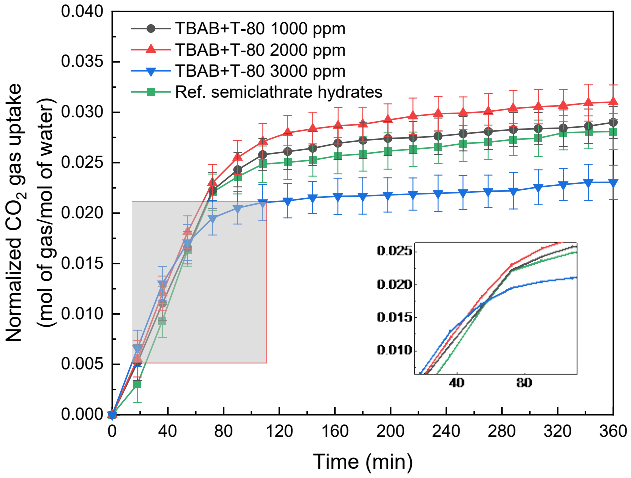

Figure 2.23. Normalized CO_2 uptake in semiclathrate hydrates at 283.15 K, 3.8 MPa.

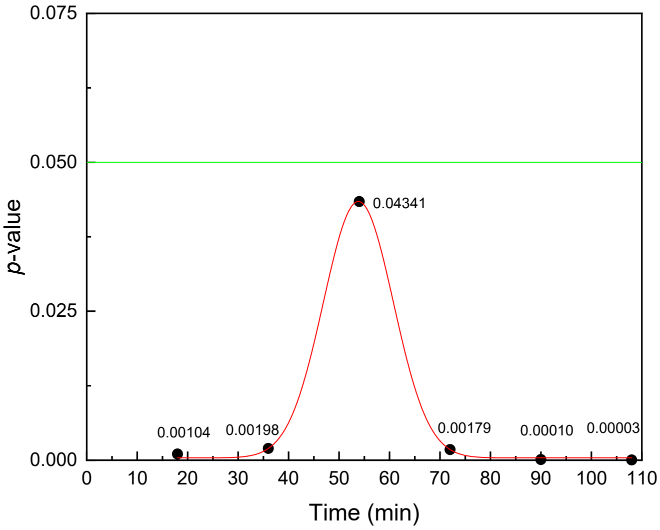

Figure 2.24. The *p*-value of the normalized CO_2 uptakes in semiclathrate hydrates.

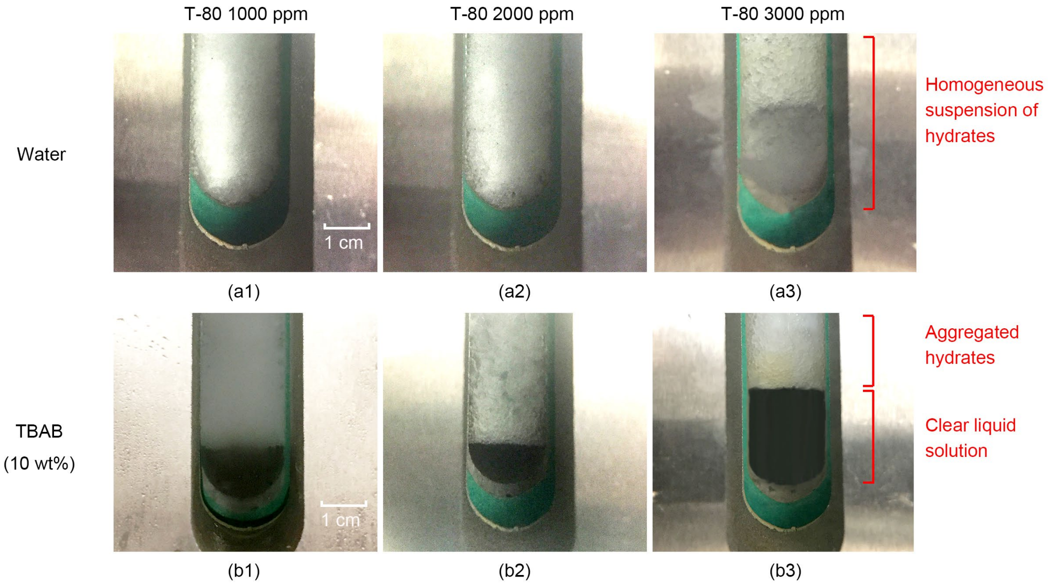
T-80 1000 ppm
T-80 2000 ppm
T-80 3000 ppm
Water
1 cm
Homogeneous suspension of hydrates
(a1)
(a2)
(a3)
TBAB
(10 wt%)
1 cm
Aggregated hydrates
Clear liquid solution
(b1)
(b2)
(b3)

Figure 2.25. Photographs of hydrate formation at t = 360 min. For clathrate hydrates, T_{exp} = 276.45 K, P_{exp} = 3.8 MPa; for semiclathrate hydrates, T_{exp} = 283.15 K, P_{exp} = 3.8 MPa. (a1) T-80 at 1000 ppm, (a2) T-80 at 2000 ppm, (a3) T-80 at 3000 ppm; (b1) TBAB with 1000-ppm T-80, (b2) TBAB with 2000-ppm T-80, (b3) TBAB with 3000-ppm T-80.

In this work, the effect of initial pressure is also studied. The initial pressure varies between 3.0, 3.8 and 4.5 MPa to investigate the effect of initial pressure on total gas uptake of systems with T-80 at 1000 ppm at 360 min, as shown in Figure 2.26. The corresponding driving force is 1.2 MPa, 2.0 MPa and 2.7 MPa for clathrate hydrates, and 2.4 MPa, 3.2 MPa and 3.9 MPa for semiclathrate hydrates. It can be seen that the CO_2 gas uptake increases with elevated initial pressure for both systems. This is because there is more driving force for gas diffusion at a higher pressure. The effect of initial pressure is more dominant in clathrate hydrates because the "block effect" in semiclathrate hydrates is developed faster with a higher driving force [140].

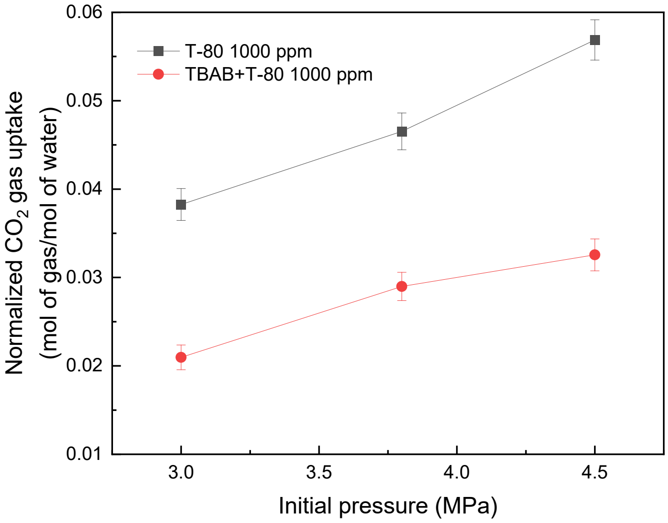

Figure 2.26. Effect of initial pressure on CO_2 gas uptake in clathrate and semiclathrate hydrates with 1000-ppm T-80.

2.6.3 Percent water conversion

The percent water conversion is usually used to quantify the process of reaction. Figure 2.27 shows the percent water conversion at 126 and 360 min for all studied systems. It can be found that at 360 min, the percent water conversion of the water system is 11.75%–17.22%, while in semiclathrate hydrates, it varies from 10.69% to 22.71%. Except for the inhibition effect observed in the system of TBAB with 3000-ppm T-80, the water conversion rate in semiclathrate hydrates is generally higher than that in the water system at the same T-80 concentration. This is because CO_2–TBAB semiclathrate hydrates consume more water than clathrate hydrates to capture the same amount of CO_2. The results also show that the percent water conversions in semiclathrate hydrates at 126 min are very close to those at 360 min, accounting for 72.23%, 77.73%, 79.78% and 73.90% in semiclathrate hydrates with T-80 at 0, 1000, 2000 and 3000 ppm, respectively. By contrast, only 36.85%, 35.02 %, 40.05% and 40.88% of the hydrate formation are completed in the corresponding water systems in the first third of the experimental durations. The findings suggest that, although none of the semiclathrate hydrates have achieved a comparable gas uptake to the pure water system (0.038 mol$_{(gas)}$/mol$_{(water)}$), TBAB with T-80 demonstrates higher conservation of water to hydrate in a shorter period of time.

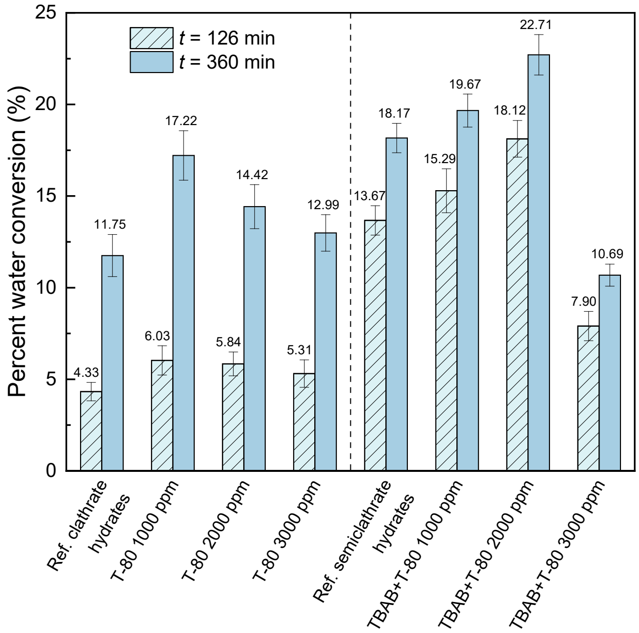

Figure 2.27. Percent water conversion for all the studied runs at 126 min and 360 min, $P_{\mathrm{exp}} = 3.8$ MPa.

2.6.4 CO_2 hydrate growth rate

Figure 2.28 illustrates the CO_2 hydrate growth rate of all the experimental runs. It is observed that with the addition of T-80, the CO_2 hydrate growth rate increases in both systems. In each system, the increment of growth rate is in positive correlation to the concentration of T-80, that is, T-80 of 3000-ppm results in the highest growth rate in two systems within the first 30 min. In clathrate hydrates, the $\mathrm{NR}_{30,\,\mathrm{CO}_2}$ is 28.57 mol min^{-1}m^{-3} for T-80 at 3000 ppm, which is improved by 34.7% compared with the "Ref. clathrate hydrates", whereas in semiclathrate hydrates, it is increased by 59.6% by T-80 at 3000 ppm. It can also be noted that the CO_2 hydrate growth rates are close in the two systems at the same concentration of T-80 for the initial 30 min. This indicates that the effect of TBAB is less dominant within the initial stage of hydrate formation when there is T-80 in the solution. It can be seen that the $\mathrm{NR}_{30,\,\mathrm{CO}_2}$ in the first 30 min is lower in "Ref. semiclathrate hydrates" than that in "Ref. clathrate hydrates". We consider the hydrate formation as two consecutive steps of diffusion and reaction. Because the TBAB solution is a viscous liquid, the gas diffusion through the TBAB solution is harder than that in clathrate hydrates. Although the subcooling in semiclathrate hydrates is higher than that in clathrate hydrates, the gas diffusion is primarily hindered by the viscous liquid.

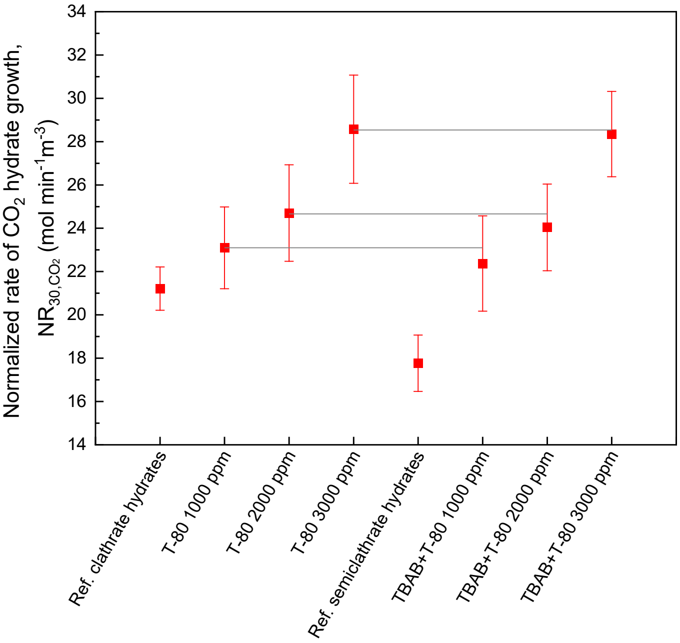

Figure 2.28. CO_2 hydrate growth rate of all experimental runs at $P_{\mathrm{exp}} = 3.8$ MPa. In clathrate hydrates, $T_{\mathrm{exp}} = 276.45$ K. In semiclathrate hydrates, $T_{\mathrm{exp}} = 283.15$ K.

2.6.5 CO_2 recovery and separation

The CO_2 recovery and separation efficiency are evaluated by the split fraction and separation factor at 126 min and 360 min in this work. It can be seen from Figure 2.29 that, in the presence of T-80, the split fraction of CO_2 increases in both systems. In clathrate hydrates, the split fraction of CO_2 drops with the rise in T-80 concentration, while in semiclathrate hydrates, the split fraction of CO_2 achieves at peak of 0.32 in the system of TBAB+T-80 at 2000 ppm, which is similar to the trends of their gas uptakes in Figure 2.21 and Figure 2.23. Although the system of TBAB+T-80 at 3000 ppm shows an inhibition effect on the total gas uptake, its split fraction is still higher than that of the "Ref. semiclathrate hydrates".

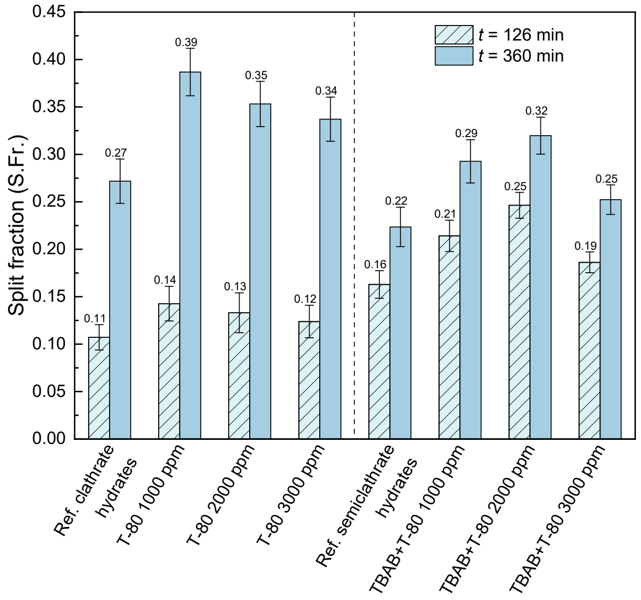

Figure 2.29. CO_2 split fraction of all experiment runs (P_{exp} = 3.8 MPa).

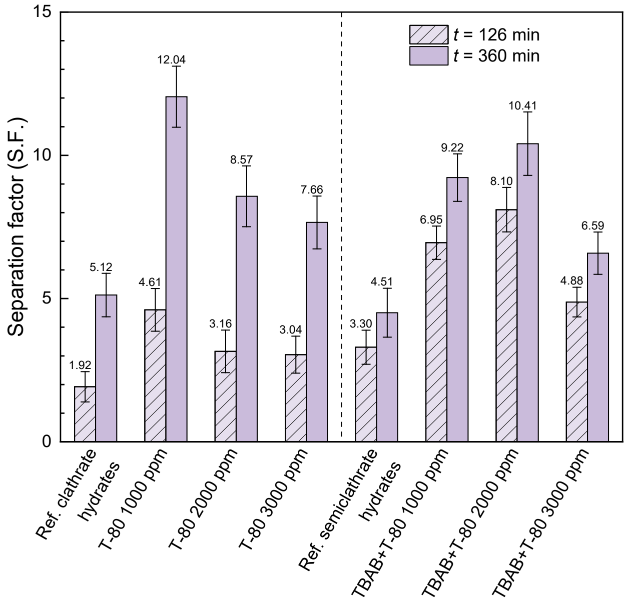

Figure 2.30. CO_2 separation factor of all experiment runs (P_{exp} = 3.8 MPa).

The separation factor varies from 5.12 to 12.04 at 360 min in clathrate hydrate, 2.35 times higher than that of the “Ref. clathrate hydrates”, as shown in Figure 2.30. It is apparent that the separation factor of CO_2 surges up with the addition of 1000-ppm T-80 in clathrate hydrates. In semiclathrate hydrates, the separation factor ranges from 4.51 to 10.41 at 360 min, and the highest value appears with TBAB with T-80 of 2000 ppm, which is 2.31 times that of the “Ref. semiclathrate hydrates”. Based on the work of Rodriguez et al. [11], the average separation factor for 10-mol% CO_2/90-mol% N_2 was 7.5 at 282 K in 35-wt% TBAB solution. The higher separation factor in this work may be attributed to the addition of Tween 80 and a higher concentration of CO_2 in gas mixtures.

The separation performance of TBAB+Tween 80 pairs is also compared with the tetrahydrofuran (THF) in similar CO_2-rich gas mixtures. Tang et al. [128] tested the separation performance in THF solutions with 59-mol% CO_2/41-mol% N_2 and 80-mol% CO_2/20-mol% CH_4 gas mixtures. The separation factors were 4–6 with different THF concentrations in CO_2/N_2 gas mixtures. In CO_2/CH_4 gas mixtures, the separation factors were as low as 2 with varied THF concentrations. THF has a similar hydrate formation mechanism to TBAB, that is, THF generates type II hydrate and occupies the large cavities while CO_2, N_2, and CH_4 occupy the small cavities. However, the overall separation performance of THF in CO_2-rich gases is not as good as that of TBAB.

Further investigation is carried out on the effect of the initial pressure on S.Fr. and S.F. with the addition of T-80. Figure 2.31 presents the S.Fr. of CO_2 for clathrate and semiclathrate hydrates with 1000-ppm T-80. The experimental conditions are the same as those mentioned in Section 2.5.2. In clathrate hydrates, the S.Fr. for T-80 at 1000 ppm rises from 0.33 to 0.47 (increased by 42.4%), for an increment of initial pressure from 3.0 to 4.5 MPa. It rises from 0.25 to 0.32 in semiclathrate hydrates (increased by 28%) for the same pressure increment. It can be concluded that the higher driving force has a positive effect on the split fraction in both hydrates; however, the dense CO_2–TBAB hydrates layers formed may weaken the favorable effect of the driving force.

Figure 2.32 shows the S.F. of CO_2 in two hydrates with 1000-ppm T-80. The trends of S.F. in Figure 2.32 are similar to those in Figure 2.31. In both hydrates, the S.F. is found to rise with larger initial pressures. The increment of S.F. from 3.0 to 4.5 MPa in clathrate hydrates is approximately double (55.2%) that in clathrate hydrates (28.2%). Compared with other kinetic promoters, such as SDS and DTAC [34, 35, 128] in clathrate hydrates, T-80 presents a higher S.F. of CO_2 from gas mixtures. The initial pressure affects the S.F. of CO_2 in clathrate hydrates more significantly than that in semiclathrate hydrates. All the key data of the studied experiments are listed in Table 2.5.

The effects of TBAB+T-80 pairs on the selectivity and separation performance of CO_2 hydrate are compared to ionic surfactants in Figure 2.33. From the literature [35], in 10-wt% TBAB water solutions, the systems with the optimal concentrations, that is, 500-ppm anionic surfactant SDS and 1000-ppm cationic surfactant DTAC, showed an S.Fr. of 0.23 and 0.30, respectively, and an S.F. of 4.17 and 5.41, respectively. They are lower than the S.Fr of TBAB with 2000-ppm T-80 by 28.13% and 6.25%, respectively, and lower than the S.F. of TBAB with 2000-ppm T-80 by 59.94% and 48.03%, respectively. This comparison indicates the superior effects of non-ionic T-80 in CO_2–TBAB semiclathrate hydrate formation. In addition, in the results of Li et al. [34], the optimum system of 4.95-wt% TBAB and 4000-ppm DTAC was most favorable for CO_2 separation from CO_2/N_2 (17:83 mole fraction) gas mixtures with an S.Fr. of 0.54 and S.F. of 9.6. This implies the optimum surfactant concentration may vary with the TBAB concentrations, and the separation performance can also be affected by gas mixture components.

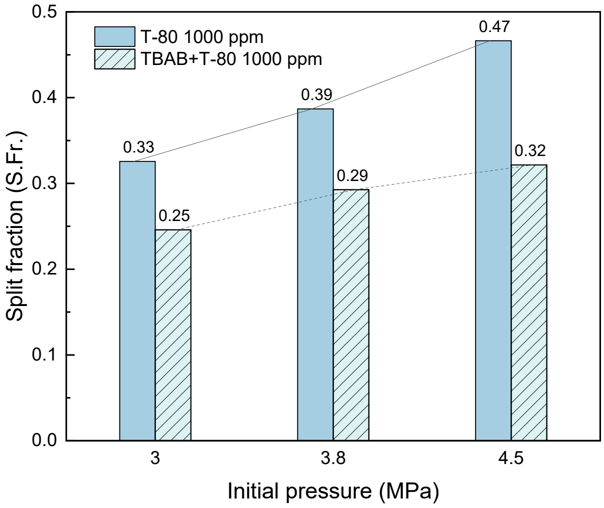

Figure 2.31. Effect of initial pressure on CO_2 split fraction.

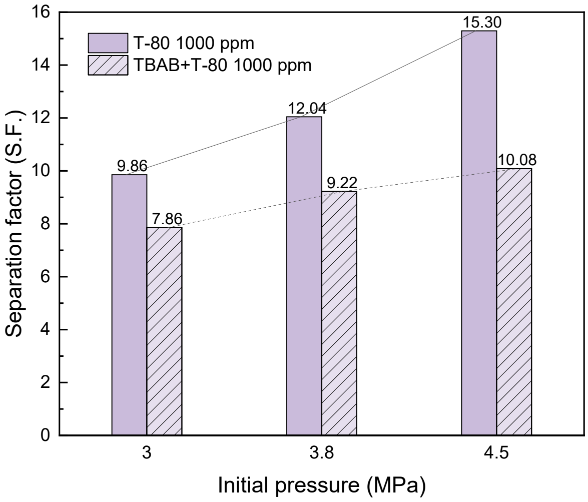

Figure 2.32. Effect of initial pressure on CO_2 separation factor.

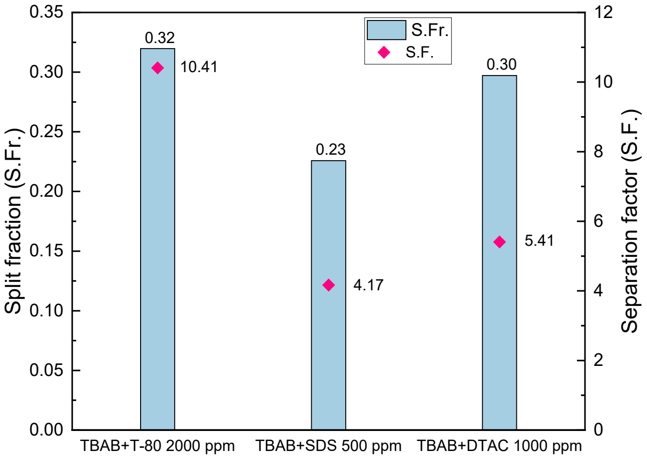

Figure 2.33. Comparison of the kinetic promotion performance of the optimal concentration of three surfactants—T-80, SDS and DTAC in 10-wt% TBAB solutions.

Table 2.1. Summary of experimental findings.

Solution	T-80 concentration (ppm)	Induction time [a] (min)	$NR_{30,\,CO_2}$ (mol min^{-1} m^{-3})	NG_t (mol$_{(gas)}$/mol$_{(water)}$)		Percent water conversion (%)		S.Fr.		S.F.	
				t=126 min	t=360 min	t=126 min	t=360 min	t=126 min	t=360 min	t=126 min	t=360 min
Water	0	19.7	21.21	0.0267	0.0381	4.33	11.75	0.11	0.27	1.92	5.12
	1000	16.3	23.10	0.0293	0.0465	6.03	17.22	0.14	0.39	4.61	12.04
	2000	15.8	24.70	0.0290	0.0423	5.84	14.42	0.13	0.35	3.16	8.57
	3000	16.2	28.57	0.0282	0.0400	5.31	12.99	0.12	0.34	3.04	7.66
TBAB (10 wt%)	0	17.3	17.77	0.0250	0.0281	13.67	18.17	0.16	0.22	3.30	4.51
	1000	4.7	22.37	0.0261	0.0289	15.29	19.67	0.21	0.29	6.95	9.22
	2000	3.0	24.04	0.0279	0.0310	18.12	22.71	0.25	0.32	8.10	10.41
	3000	2.5	28.35	0.0212	0.0231	7.90	10.69	0.19	0.25	4.88	6.59

[a] Induction time in this table reports the average induction time of three runs.

2.7 Decision box for optimal systems

In order to select optimal systems for fast hydrate formation with considerable gas uptake, we introduce the “Eisenhower Decision Box” to evaluate the performances of systems. Figure 2.34 shows the decision box of all the systems studied in this work. The evaluation of the performances of the different systems studied are based on two criteria—induction time and percent water conversion. It is divided into four boxes by lines intersecting at the point of “Ref. semiclathrate hydrates”. The two systems within the highlighted parts represent the TBAB+T-80 pairs having shorter induction time and higher percent water conversions than those of the reference semiclathrate hydrates, which are both desirable. The systems studied, TBAB+T-80 2000 ppm, at the very upper left corner manifests the best performance among all the studied systems. In contrast, the TBAB+T-80 3000 ppm, which shows the inhibition effect in percent water conversion compared to Ref. semiclathrate hydrates, is outside the highlighted part for systems selection, although it has a shorter induction time.

Overall, it is seen that the three systems studied with the presence of TBAB all achieved better performances than the three without TBAB and “Ref. clathrate hydrates” in both criteria. In the present work, induction time and percent water conversion were chosen for evaluation; however, these metrics can be varied according to the requirements of practical systems.

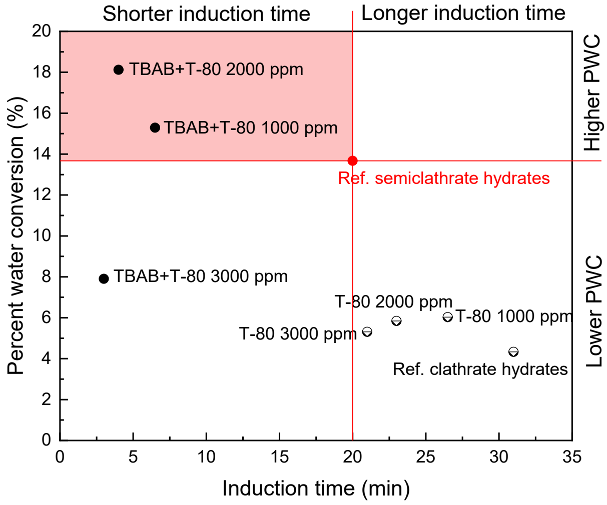

Figure 2.34. Eisenhower Decision Box for optimal systems. The vertical axis shows the percent water conversion of samples at the end of intensive uptake period ($t = 126$ min).

2.8 Summary

In this chapter, the kinetics of CO_2 semiclathrate hydrate formation have been studied in a batch reactor for carbon capture from CO_2/N_2 mixtures in the presence of various concentrations of surfactants with tetra-*n*-butyl ammonium bromide (TBAB). TBAB is known as a thermodynamics promoter to moderate the CO_2 semiclathrate hydrates formation conditions, but it reduces the gas uptake. Considering the trade-off of phase equilibrium temperature and gas uptake yield, 10-wt% TBAB was used as a thermodynamic promoter for CO_2 hydrates formation at constant temperature. In order to maintain the high-temperature and low-pressure phase equilibrium while compensating for the reduced gas uptake caused by TBAB, anionic surfactant sodium dodecyl sulfate (SDS), cationic surfactant dodecyltrimethylammonium chloride (DTAC), and non-ionic surfactant Tween 80 (T-80) were added. Their synthetic effects with TBAB on the induction time, gas uptake, split fraction and separation factor were investigated experimentally.

(1) Synthetic effects of TBAB and SDS/DTAC

The results showed that in 10-wt% TBAB systems, DTAC at 1000–6000 ppm overall had better reduction effects on induction time than SDS at 500–1500 ppm; while SDS performed better than DTAC to accelerate hydrate growth. Within a 6-hour hydrate formation, the CO_2 uptake of the TBAB system with 0.1-wt% DTAC at 283.15 K approached the same amount of gas uptake as that of the pure water system at 276.45 K under the same initial pressure of 3.8 MPa, revealing this recipe to be the optimal among all those studied in terms of both thermodynamic and kinetic promotion. The system of TBAB with 6000-ppm DTAC showed the highest split fraction and separation factor of CO_2. In both TBAB systems with SDS at 500 ppm or DTAC at 1000 ppm, the CO_2 uptake increased overall with increased subcooling. In addition, to shorten the process duration for energy saving, an intensive uptake period was defined to recommend a reasonable practical operation time of hydrate-based carbon capture. The blockage effect that was intensified by the presence of TBAB may be an important selection criterion of thermodynamic promoters when used in stationary reactors.

(2) Synthetic effects of TBAB and T-80

The results also showed that the induction time was significantly reduced by T-80 in semiclathrate hydrates and clathrate hydrates (with or without TBAB). The initial gas uptake rate increases with the increased concentration of T-80, which resulted in a higher gas uptake in the early formation period for both hydrates. After the initial growth period, CO_2 uptakes increased continuously in clathrate hydrates. However, in semiclathrate hydrates, gas uptake became constant at the end of the intensive gas uptake period. Both 1000-ppm and 2000-ppm T-80 improved the gas uptake in semiclathrate hydrates, while 3000-ppm T-80 showed an inhibition effect. In addition, the percent water conversion of the TBAB+T-80 2000 ppm system reached 80% of the total value within one-third of the entire test period, whilst that of the best water system (T-80 1000 ppm) only achieved 35% over the same test period.

Based on the above conclusions, a thermodynamic promoter alone cannot achieve a satisfactory CO_2 gas uptake by HBCC. With the addition of surfactants, the gas uptake yield and rate can be improved. In the following chapters, the kinetic promotion in porous materials, and the combined effect of surfactant and porous material, will be investigated.

Chapter 3 Kinetic promotion of CO_2 hydrate formation in microparticles[2]

3.1 Introduction

The development of clathrate hydrate technology is mainly impeded by its low formation rate and unsatisfied gas capacity. Except for the common methods of spraying, stirring, and bubbling, porous material can increase the gas–liquid contact area, and thus kinetically promote the hydrate formation. The use of particles in gas hydrate formation provides an effective alternative to mechanical mixing for reduced energy consumption and improved safety. In this chapter, the kinetic promotion of CO_2 hydrate formation in microparticles is studied experimentally. Two microparticles, namely "dry water" and silica gels, are used. Both materials are microparticles. Water (or aqueous solution) is dispersed uniformly throughout the small particles, so that the contact area between gas and water is markedly increased. It provides a suitable structure within dispersed small spherical particles for the kinetic promotion of gas hydrate formation through enhancing mass transfer. CO_2 hydrate formation using various particle sizes is experimentally investigated.

---

[2] Part of the content of this chapter has been published in the following article:

Zhang F, Wang X*, Wang B, Lou X*, Lipiński W*. Experimental and numerical analysis of CO_2 and CH_4 hydrate formation kinetics in microparticles: A comparative study based on shrinking core model. Chemical Engineering Journal. 2022;446:137247.

3.2 Experimental study of hydrate formation in dry water

3.2.1 Preparation of dry water

“Dry water” refers to free-flowing particles formed by high-speed mixing of the hydrophobic silica and dispersed water, as proposed by Wang and Cooper [52]. During high-speed mixing in the air, the water was scattered into small drops surrounded by hydrophobic silica nanoparticles, which prevented the coalescence of the water drops. The pyrogenic silica HDK® H18 (hydrophobic grades) was provided by Wacker Chemie AG. It is a loose, bulky, white and chemically inert powder with a low order of toxicity and a high grade of purity. The Breville blender (BBL620SIL) used in this work had five-speed settings from 17,000 to 23,000 rpm with a glass jug of 2.0 L.

In this work, “dry water” particles with 3-, 5- and 8-wt% H18 silica were prepared. The “dry water” with 3-wt% silica was prepared using 97-mL deionized water and 3-g silica at a blending speed of 19,000 rpm for 90 seconds. The higher concentration of H18 requires the water to be broken into smaller droplets at a higher blend speed. The preparation conditions of the other sizes of “dry water” particles are shown in Table 3.1. The blender was paused for 10 seconds every 30 seconds to avoid the evaporation of water caused by heat generated while blending. The photograph of prepared “dry water” is shown in Figure 3.1. The microscope photos of the three concentrations of “dry water” are shown in Figure 3.2. It can be seen that the “dry water” particles were basically spherical and scattered, but some inevitably aggregated with each other. The average radius of prepared “dry water” is also tabulated in Table 3.1.

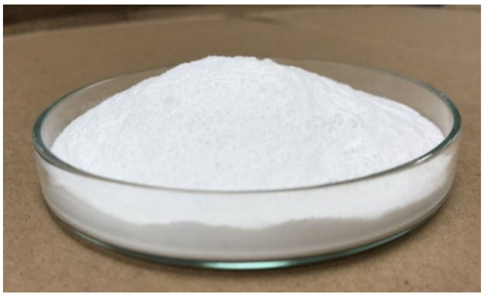

Figure 3.1. Appearance of “dry water” synthesized from hydrophobic silica “H18” and deionized water.

Table 3.1. The preparation process and the average measured sizes of "dry water".

	Amount of H18 (g)	Amount of deionized water (g)	Blending speed (rpm)	Blending time (seconds)	Average radius/standard error[a] (μm)
"dry water" with 3-wt% silica	3.0	97.0	19,000	90	26.3/1.95
"dry water" with 5-wt% silica	5.0	95.0	21,000	90	8.1/0.82
"dry water" with 8-wt% silica	8.0	92.0	23,000	90	6.4/0.71

[a] Standard error $= \sqrt{\dfrac{\sum(x_i - \bar{x})^2}{N(N-1)}}$, where x_i is of measurement value, $\bar{x}$ is the mean value of measurements, and N is the number of measurements, $N = 20$.

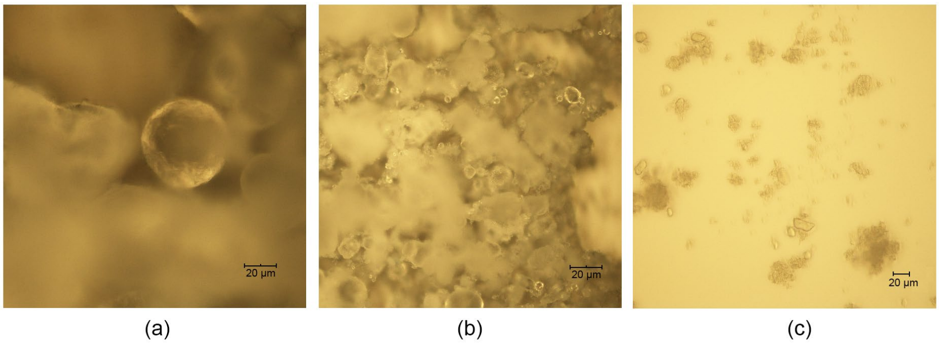

Figure 3.2. Micrographs of "dry water" particles: (a) with 3-wt% silica; (b) with 5-wt% silica; and (c) with 8-wt% silica.

3.2.2 Apparatus and procedures

The experimental apparatus, shown in Figure 3.3, mainly consisted of a 635.53-mL cylindrical reactor, a thermostatic bath, a data acquisition system, and a CO_2 gas cylinder. The cooling fluid (30 L) in the thermostatic bath was 30-vol% propylene glycol aqueous solution with a freezing point of –13.3°C. The data acquisition system logged the temperature and pressure every 10 seconds via a pressure transducer and a thermocouple, respectively.

The experiments were conducted at a constant temperature in a closed system. The reactor was cleaned and rinsed three times before the "dry water" particles were poured in. Then the reactor was filled with "dry water" and closed tightly. The thermostatic bath was turned on to provide a thermostatic cooling condition for hydrate formation. Once it was maintained at the target temperature for 30 min, the reactor was purged by CO_2 gas and vented three times to remove the residual air in the reactor. Then CO_2 gas was charged into the reactor slowly to the target pressure. The gas valve closure marked the onset of the experiment. Each run was terminated when the pressure remained unchanged for half an hour, and runs were repeated twice under the same conditions. Memory effect may have occurred when the repeated runs were conducted on the same particles that experienced hydrate formation. Therefore, the three experimental runs were named "Fresh cycle", "Repeat 1" and "Repeat 2", respectively. The initial experimental pressures (P_{ini}) and temperatures (T_{exp}) for both CH_4 and CO_2 hydrate formation in "dry water" are shown in Table 3.2. More details of CO_2 hydrate formation experimental apparatus and procedures can be found in a previous study [35]. For the CH_4 hydrate experimental setups and procedures, details can be found in Shi et al. [83].

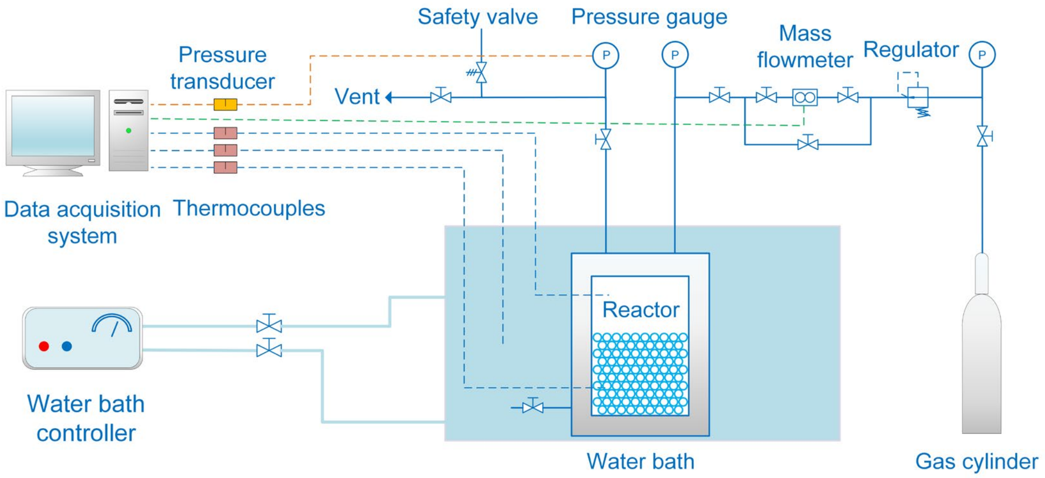
Safety valve
Pressure gauge
Mass flowmeter
Regulator
Pressure transducer
Vent
P
P
P
Data acquisition system
Thermocouples
Reactor
Water bath controller
Water bath
Gas cylinder

Figure 3.3. Schematic diagram of the experimental setup.

Table 3.2. Experimental conditions and measured induction time of hydrate formation in “dry water”.

Exp. no.	Gas	Exp. state	H18 concentration	P_{ini} (MPa)	T_{exp} (K)	Induction time (min)
1		Fresh				24.0
2	CO_2	Repeat 1	3 wt%	3.5	277.15	18.2
3		Repeat 2				12.5
4		Fresh				18.6
5	CO_2	Repeat 1	5 wt%	3.5	277.15	16.0
6		Repeat 2				10.8
7		Fresh				17.5
8	CO_2	Repeat 1	8 wt%	3.5	277.15	5.0
9		Repeat 2				3.3
10	CO_2	Bulk	0	3.5	277.15	34.5
11*	CH_4	Fresh	5 wt%	4.5	273.65	–

3.3 CO_2 hydrate formation kinetics in dry water

3.3.1 Pressure and temperature profile of hydrate formation in dry water

Figure 3.4 shows the pressure and temperature profile of CO_2 hydrate formation in 5-wt% “dry water” at a constant temperature of 277.15 K. It shows the initial stage only to illustrate the typical temperature peak and pressure drop that indicates the beginning of hydrate formation. From an initial pressure of 3.5 MPa, the pressure first decreases slowly as CO_2 dissolved in water and a supersaturated state is gradually formed [4]. There is a noticeable increase in temperature and a sudden pressure drop at 18.6 min. The surge in temperature is caused by the exothermic hydrate formation. The period before formation (18.6 min) is defined as the induction time.

The induction time for all experiments is shown in Table 3.2. It can be seen that for each formula, the induction time is shorter in repeat runs than in the fresh cycle due to the memory effect [141] (from 24 to 12.5 min for “dry water” with 3-wt% silica; from 18.6 to 10.8 min for “dry water” with 5-wt% silica; and from 17.5 to 3.3 min for “dry water” with 8-wt% silica). Overall, the induction time for “dry water” with 3-

wt% silica is the longest (24 min), while that for 8-wt% is the shortest (17.5 min). This is due to the largest gas–water contact area of "dry water" with 8-wt% silica for its smallest particle size. It was reported that with a larger contact area, there tended to be more hydrate crystallizing during nucleation, thus taking a shorter induction time [5].

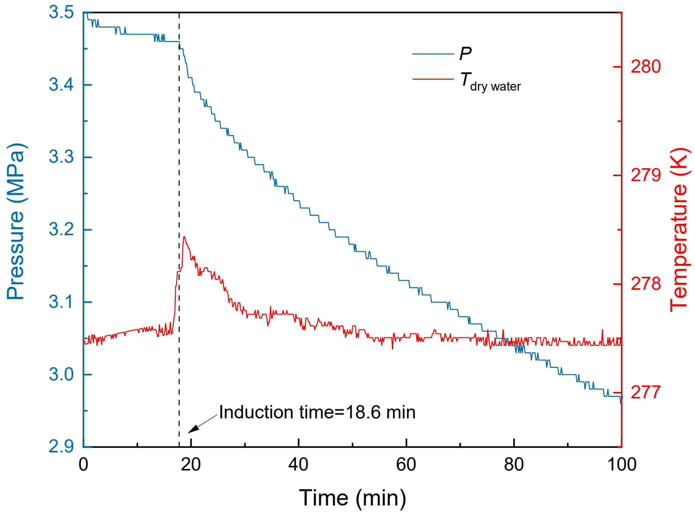

Figure 3.4. *P*-*t* and *T*-*t* profiles at the start of CO_2 hydrate formation in "dry water" with 5-wt% silica at $T_{\text{exp}} = 277.15$ K.

3.3.2 Normalized gas uptake of hydrate formation in dry water

The normalized gas uptake NG_t ($\text{mol}_{(\text{gas})}/\text{mol}_{(\text{water})}$) at the time *t* (min) is calculated by the following equation [120]:

$$\text{NG}_t = \frac{\Delta n_{\text{g},\,t}}{n_{\text{H}_2\text{O}}} = \frac{n_{\text{g},0} - n_{\text{g},\,t}}{n_{\text{H}_2\text{O}}}, \tag{3.1}$$

where $n_{\text{H}_2\text{O}}$ is the initial amount of water (mol), $\Delta n_{\text{g},\,t}$ is the CO_2 gas uptake yield (mol) at time *t*. $n_{\text{g},0}$ and $n_{\text{g},\,t}$ are the amounts of CO_2 in the reactor (mol) at the onset and time *t* of experiment, which can be calculated by Eqs. (3.2) and (3.3), respectively,

$$n_{\text{g},0} = \frac{P_{\text{exp}} V}{Z_0 R T_{\text{exp}}}, \tag{3.2}$$

$$n_{g,t} = \frac{P_t V}{Z_t R T_{exp}}, \tag{3.3}$$

where V is the volume of gas (m^3), and R is the ideal gas constant ($J\ mol^{-1}K^{-1}$). Z_0 and Z_t are the gas compressibility factors at the onset and the time t of experiments, calculated by Pitzer's correlation [119].

Figure 3.5 shows the normalized CO_2 gas uptake in the fresh cycle of hydrate formation in different "dry water" samples compared to that in bulk water. All the experiments of CO_2 hydrate formation were conducted at the same P_{ini} and T_{exp}. It can be seen that the gas uptake increases with the increase in silica concentrations (i.e., the decrease in particle size and the increase in the overall gas–water interface area). "Dry water" with the 8-wt% silica sample has the highest CO_2 uptake. The increment in gas uptake from 5-wt% to 8-wt% silica (5.5%) is much smaller than the increment from 3-wt% to 5-wt% silica (76.5%) in 1000 min. The gas uptakes when using "dry water" in all sizes are dramatically higher than that in the bulk water without any stirring or additives.

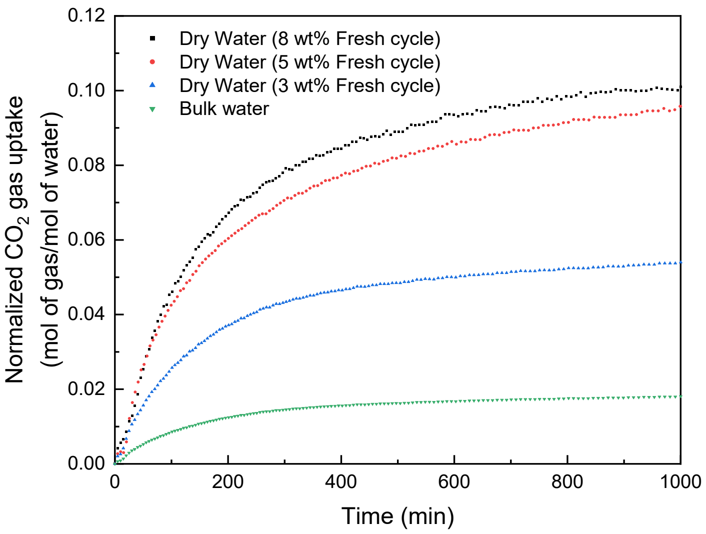

Figure 3.5. Normalized CO_2 gas uptake in the fresh cycle of different sizes of "dry water" particles.

3.3.3 Cyclic performance of dry water in hydrate formation

Figure 3.6 shows the gas uptake of three repeated experiments in different “dry water” samples. It can be seen that the gas uptake yield decreases markedly in all sizes of “dry water” as experiments are repeated. The percentage of reduction of gas uptake yield in 1000 min for the three “dry water” samples in the repeated cycles is summarized in Table 3.3. From the fresh cycle to Repeat 1, the gas uptake yield is reduced by 29.0%–59.3%; a further reduction from the fresh cycle to Repeat 2 is by nearly 70%. Similar observations were reported for repeated CH_4 hydrate formations in “dry water”; as a result, the “dry water” structure is not stable for repeated hydrate formations [142].

Figure 3.7 shows the reactor window before “Repeat 2” experiment of 3-wt% silica. A clear layer of bulk water above the “dry water” can be seen, indicating that the “dry water” structures were broken after the cycles, and the water previously inside is released and aggregated into bulk water. It is also noted that the gas uptake yields in 1000 min of the two repeated runs in “dry water” with 3-wt% silica and in bulk water are almost the same (0.022, 0.021 and 0.018 $mol_{(gas)}/mol_{(water)}$, respectively), indicating that after the fresh run the majority of water had turned to bulk water.

Table 3.3. Gas uptake yield in 1000 min and percent reduction of yield for repeat runs.

“Dry water” sample		8-wt% silica	5-wt% silica	3-wt% silica
Fresh–Repeat 1	Yield*	0.100–0.071	0.094–0.059	0.054–0.022
	Reduction	29.0%	37.2%	59.3%
Fresh–Repeat 2	Yield	0.100–0.036	0.094–0.025	0.054–0.021
	Reduction	64.0%	73.4%	61.1%

*unit: $mol_{(gas)}/mol_{(water)}$.

Figure 3.8 illustrates the percent water conversion (PWC) of all the studied “dry water” experiments in 1000 min. The PWC increases along with the rise of H18 concentration as a larger gas–water contact area is favorable to mass transfer and the water conversion to hydrate. The PWC has a similar trend to that of the gas uptake yield, that is, the value of PWC decreases as the experiments are repeated. As can be seen from Figure 3.8, the highest PWC of 77.16% appears at the fresh cycle of 8-wt% “dry water”, whereas the lowest PWC is only 13.21% in 3-wt% “dry water” after the second repeat.

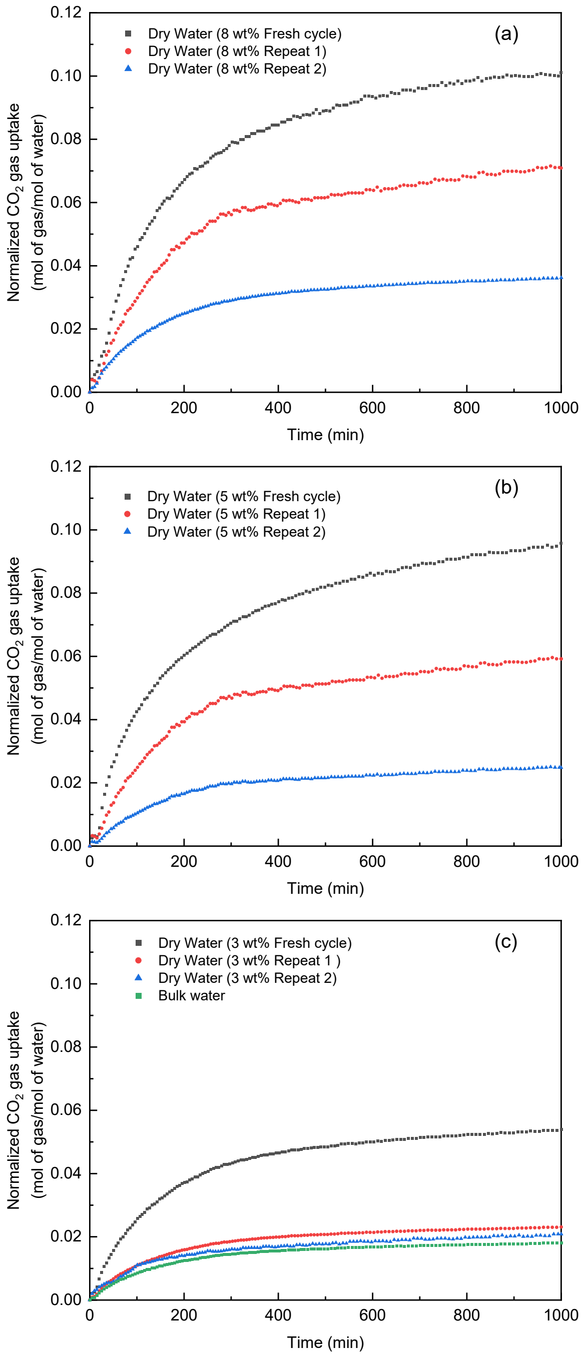

Figure 3.6. CO_2 uptake in fresh and repeat hydrate formations in “dry water” at a constant temperature of 277.15 K: (a) with 8-wt% silica, (b) with 5-wt% silica, and (c) with 3-wt% silica.

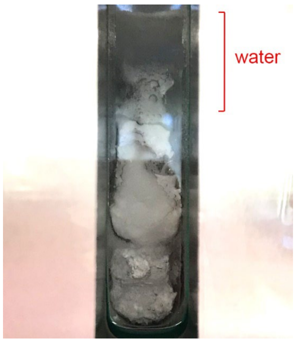

Figure 3.7. “Dry water” with 3-wt% silica in the reactor after two cycles of CO_2 hydrate formation.

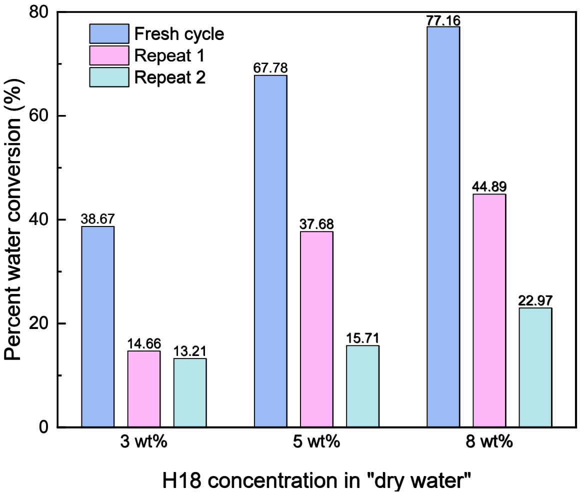

Figure 3.8. Percent water conversion after 1000 min of CO_2 hydrate formation.

3.4 Experimental study of hydrate formation in silica gels

3.4.1 Preparation of saturated silica gels

CO_2 gas cylinders supplied by BOC Australia were used in this work. Deionized water with a resistivity of 18.2 MΩ·cm, produced by ELGA® PURELAB, was used. Spherical silica gels (SGs) were provided by SiliCycle® Inc. (Canada). The SGs used in this work were hydrophilic, with silanol groups on the entire surface and pores inside and were not burned, as shown in Figure 3.9. In such a structure, water can be absorbed inside the pores by hydrogen bonds. Micromeritics® TriStar II 3020 was used to measure the properties of the SGs. The structural properties of SGs of three different sizes are listed in Table 3.4.

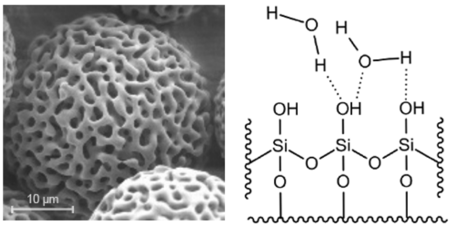

Figure 3.9. Structure of the spherical hydrophilic silica gel used in this work. (Copyright Nouryon–image used with permission)

Table 3.4. Structural properties of silica gels.

Property name	100-nm SG	50-nm SG	30-nm SG
Mean diameter (μm)	75–200	75–200	75–200
Average pore diameter (Å)	951	485	311
Pore volume (mL g^{-1})	0.9	0.78	0.78
Specific surface area (m^2g^{-1})	30.09	58.39	82.06

3.4.2 Experimental procedures

The experiments were carried out in the same apparatus as those with dry water. The SGs were first dried at 373.15 K for at least 24 hrs to get rid of all the moisture. At this temperature, the silanol groups were not burned, so the SGs were still hydrophilic. The prepared solution with a volume equal to the pore volume of the SG was added into the SG to obtain the saturated SG. Saturated SG ensures the pores are completely filled with water, in order to make sure that the SG pores do not result in any prominent capillary effect before hydrate formation. To make sure the solution was evenly distributed in the SG pores, they were placed in the centrifuge at 3000 rpm for 3 min and then transferred to the ultrasonic bath at ambient temperature for another 6 hrs. The ultrasonic bath was paused periodically to prevent the evaporation of water from pores caused by the accumulated heat generated by the ultrasound. The SGs were found to be evenly dispersed with water from observation.

It was reported that the hydrate formation in SGs presented higher equilibrium pressure (P_{eq}) than that in the bulk water [2, 55]. In this work, the experiments were conducted under a constant-temperature and constant-pressure condition with excess gas and a constant pressure driving force (ΔP = 1.4 MPa, i.e., the pressure difference between P_{exp} and P_{eq}). The phase equilibrium data of CO_2 hydrate formation in SGs were obtained from previous studies [42, 62]. After the saturated SGs were placed in the reactor, the thermostatic bath was turned on to provide a thermostatic condition for hydrate formation. Meanwhile, the reactor was purged with pure CO_2 gas and vented three times to remove the residual air inside. When the temperature of the gas phase in the reactor was maintained at the target temperature (T_{exp}), CO_2 was charged slowly into the reactor to reach and maintain the target pressure (P_{exp}). The gas consumptions were measured by the mass flowmeter. The experimental conditions are shown in Table 3.5.

Table 3.5. Summary of experimental conditions.

Exp. no.	Gas	Solution	SG type (nm)	T_{exp} (K)	P_{exp} (MPa)	P_{eq} at T_{exp} (MPa)	ΔP (MPa)
1	CO_2	Pure water	100	275.15	3.01	1.61[a]	1.4
2	CO_2	Pure water	50	275.15	3.04	1.64[a]	1.4
3	CO_2	Pure water	30	275.15	3.13	1.73[b]	1.4

[a] Data obtained from Uchida et al. [62].
[b] Data obtained from Seo et al. [42].

3.5 CO_2 hydrate formation kinetics in silica gels

3.5.1 Normalized gas uptake of hydrate formation in silica gels

The effects of SG pore size and surfactant concentration on CO_2 gas uptake are investigated through a comprehensive experimental program. Figure 3.10 shows the normalized CO_2 gas uptake in SG of different pore sizes. The calculation method of normalized gas uptake can be found in a previous work [35]. The vertical error bars show the 95% confidence intervals based on student's *t*-distribution. The errors come from both the thermal couples and the pressure sensors of ±0.1°C and ±0.01 MPa, respectively. The results show a marked increase in gas uptake in larger pores. At 600 min, the gas uptake in 50-nm and 100-nm SGs are 1.71 times and 3.50 times that in 30-nm SG, respectively. As can be seen in Figure 3.10, although the 30-nm SG has the largest overall specific surface area, the largest pore diameter of the 100-nm SG is more favorable for gas hydrate formation. It seems that the overall surface area is not a dominant factor, as all the pores are fully of water. Figure 3.10 also shows the CO_2 gas uptake rate in the systems studied. It can be seen that the overall gas uptake yield and rate were higher in larger pore SGs, and the highest were with 100-nm SGs. In general, the gas uptake rate was high in the beginning, but it slowly decreased to near zero at around 300 min. This is due to the thick hydrate layer formed in the pores hindering further gas diffusion. Therefore, it is recommended that the experiment be finished early (at about 300 min) in practical applications.

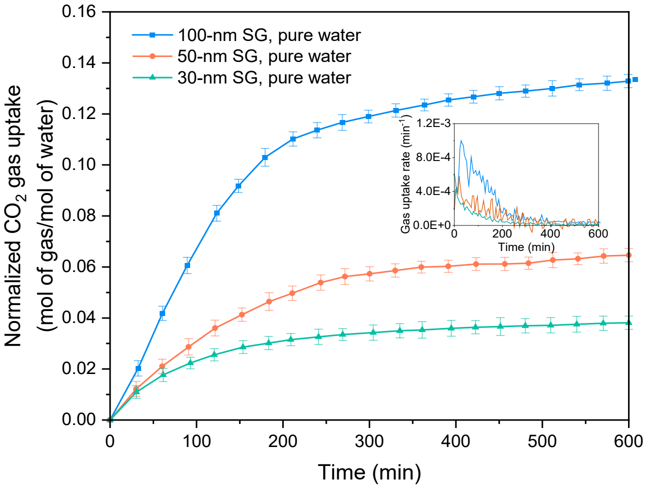

Figure 3.10. Normalized CO_2 gas uptake in SGs of different pore sizes.

3.5.2 Percent water conversion

The percent water conversion (PWC) is a metric to evaluate the amount of water consumed in the hydrate formation compared to the initial total amount of water, and is defined as

$$\mathrm{PWC} = \frac{\Delta n_{\mathrm{g},\,t} \times \text{hydration number}}{n_{\mathrm{H_2O}}} \times 100\% , \tag{3.4}$$

where the hydration number is the theoretical number of water molecules consumed per guest molecule [55].

Table 3.6 shows the final PWC of all the systems at 600 min. It can be clearly seen that the 100-nm SG has an absolute advantage in enhancing the PWC over the 50-nm SG. The PWC in 100-nm SG cases is above 86%, while they are only approximately 43% in the 50-nm SG cases. Compared with CO_2 hydrate formation in “dry water” particles, both the CO_2 gas uptake yield and rate in silica gels are much higher. In addition, based on observation, the water in the silica gel pores does not aggregate into bulk water as in the “dry water” experiment.

Table 3.6. Percent water conversion at the end of CO_2 hydrate formation (600 min).

System	100-nm SG, pure water	50-nm SG, pure water	100-nm SG, 300-ppm SDS
PWC (%)	86.6	42.8	89.4

3.6 Summary

In this chapter, the hydrate formation kinetics of CO_2 have been studied in microparticles of “dry water” and silica gels (SGs). “Dry water” particles prepared by mixing hydrophobically modified silica and water were used to create micro-size droplets of water. The experimental results showed that the hydrate formation in “dry water” with 8-wt% silica representd the highest normalized gas uptake due to its smallest particle size. A clear layer of bulk water above the “dry water” can be seen, indicating that “dry water” structures are broken after cycles. From the fresh cycle to Repeat 1, the gas uptake yield was reduced by 29.0–59.3%; a further reduction from the fresh cycle to Repeat 2 was by nearly 70%. SGs with 30-, 50- and 100-nm pore sizes were used as frameworks for hydrate formation. The experimental results showed a marked increase in both gas uptake yield and gas uptake rate in SGs with larger pores. No obvious fragmentation of SGs was found. Overall, SGs showed a better stability and promotion effect on CO_2 hydrate formation kinetics. In the next chapter, SGs will be chosen as the framework of CO_2 hydrate formation in porous material to further investigate the combined effect of surfactants and SGs in kinetic promotion.

Chapter 4 CO_2 hydrate formation in silica gel pores in the presence of surfactants[3]

4.1 Introduction

Currently, most of previous studies have mainly focused on gas uptake enhancement in SGs; little work has been done to interpret the physics of hydrate formation in SGs and the effect of the porous structure and surfactants on the hydrate formation kinetics. In this chapter, the effects of the SG porous framework and surfactants on hydrate formation kinetics have been investigated experimentally. Both CO_2 hydrates and CO_2/N_2 hydrate formation experiments are implemented in an SG column with pore diameters of 100, 50 or 30 nm. Sodium dodecyl sulfate (SDS) or dodecyl-trimethylammonium chloride (DTAC) solutions at different concentrations are added to improve the water activity. The kinetic metrics, including the induction time, gas uptake yield, gas uptake rate, and separation performance, are analyzed from the experimental results. This chapter aims to quantitatively analyze the binary effects of surfactants and nanopores, revealing the variations and roles of critical parameters on hydrate formation kinetics, and thus contributing to a theoretical ground for gas hydrate kinetics improvement.

---

[3] The content of this chapter has been submitted in the following article:

Zhang F, Wang X*, Wang B, Lou X, Lipiński W*. The effect of silica gel nanopores and surfactants on CO_2 hydrate formation kinetics: An experimental and modeling study based on shrinking core model. Chemical Engineering Science. 2022;262:118002.

4.2 Experimental study

4.2.1 Experimental materials

Pure CO_2 and CO_2/N_2 (70:30 mol%) gas cylinders supplied by BOC Australia were used in this work. SDS (CAS: 151-21-3) and DTAC (CAS: 112-00-5) were supplied by Sigma Aldrich with the purity of 98.5% and 99.0%, respectively. Deionized water with a resistivity of 18.2 MΩ·cm produced by ELGA® PURELAB was used. Spherical SGs were provided by SiliCycle® Inc. (Canada). The SGs used in this chapter were hydrophilic with silanol groups on the entire surface and pores inside and were not burned. Its chemical structure has been shown in Chapter 3.

4.2.2 Apparatus and procedures

The experiments were carried out in a previously reported apparatus as shown in Figure 4.1. It was reported that the hydrate formation in SGs presented higher equilibrium pressure (P_{eq}) than that in the bulk water [2, 55]. In this study, the experiments were conducted under constant-temperature and constant-pressure conditions with excess gas and a constant pressure driving force (ΔP = 1.4 MPa, i.e., the pressure difference between P_{exp} and P_{eq}). The phase equilibrium data of CO_2 hydrate formation in SGs were obtained from previous studies [42, 62]. The phase equilibrium conditions are not obviously affected by surfactants but can be affected by both the SG pore sizes and gas mixture components [2, 33]. After the saturated SGs were placed in the reactor, the thermostatic bath was turned on to provide a thermostatic condition for hydrate formation. Meanwhile, the reactor was purged with gases and vented three times to remove the residual air inside. When the temperature of the gas phase in the reactor was maintained the target temperature (T_{exp}), the gas was charged slowly into the reactor to reach and maintain at the target pressure (P_{exp}). The gas consumption was measured by the mass flowmeter. The experimental conditions are shown in Table 4.1; this ensured that CO_2 was not liquefied at the experimental temperature (T_{exp}) and pressure (P_{exp}).

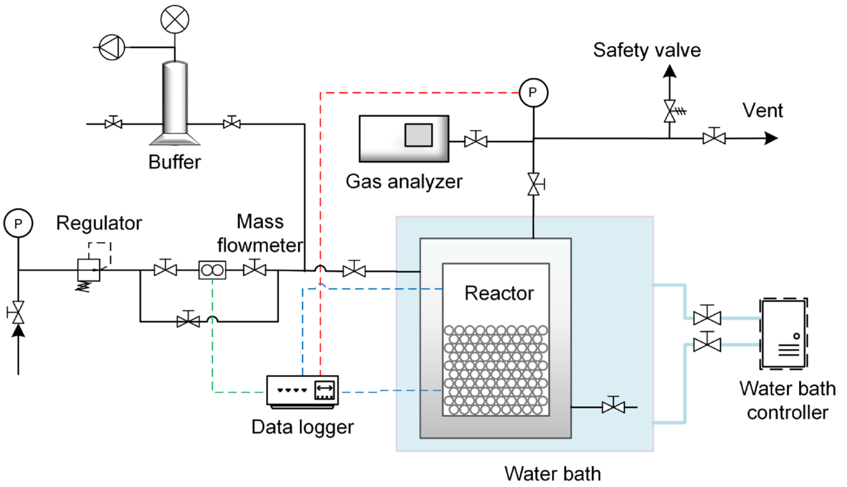
Safety valve
Vent
Buffer
Gas analyzer
Regulator
Mass flowmeter
Reactor
Water bath controller
Data logger
Water bath
P

Figure 4.1. Schematic diagram of the experimental system.

Table 4.1. Summary of experimental conditions.

Exp. no.	Gas	Solution	SG type (nm)	T_{exp} (K)	P_{exp} (MPa)	P_{eq} (MPa)	ΔP (MPa)
1	CO_2	Pure water	100	275.15	3.01	1.61	1.4
2	CO_2	Pure water	50	275.15	3.04	1.64	1.4
3	CO_2	Pure water	30	275.15	3.13	1.73	1.4
4	CO_2	SDS 300 ppm	100	275.15	3.01	1.61	1.4
5	CO_2	SDS 500 ppm	100	275.15	3.01	1.61	1.4
6	CO_2	SDS 500 ppm	50	275.15	3.04	1.64	1.4
7	CO_2	SDS 500 ppm	30	275.15	3.13	1.73	1.4
8	CO_2	DTAC 1000 ppm	100	275.15	3.01	1.61	1.4
9	CO_2	DTAC 2000 ppm	100	275.15	3.01	1.61	1.4
10	CO_2/N_2	Pure water	100	275.15	3.70	2.30	1.4
11	CO_2/N_2	Pure water	50	275.15	3.75	2.35	1.4
12	CO_2/N_2	Pure water	30	275.15	3.87	2.47	1.4
13	CO_2/N_2	DTAC 1000 ppm	100	275.15	3.70	2.30	1.4
14	CO_2/N_2	DTAC 2000 ppm	100	275.15	3.70	2.30	1.4
15	CO_2/N_2	DTAC 6000 ppm	100	275.15	3.70	2.30	1.4
16	CO_2/N_2	DTAC 1000 ppm	50	275.15	3.75	2.35	1.4

4.3 Results and discussion

4.3.1 Effect of surfactants concentration

Based on the results in Chapter 3, the CO_2 gas uptake yield is much advanced in the larger SG pores. In this section, the 100-nm SG was chosen to study the binary effect of SG and surfactants on hydrate formation kinetics. Water solutions of SDS at 300 and 500-ppm and DTAC at 1000 and 2000-ppm were added to 100-nm SG particles. These surfactants and concentrations all present good promotion effects of the bulk water systems, as discussed in Chapter 2 [35].

Figure 4.2 shows the normalized gas uptake in CO_2 hydrate formation in 100-nm SG with different SDS concentrations in pure CO_2 systems (Exp. no. 1, 4 and 5). Both 300- and 500-ppm SDS solutions lead to increased gas uptake rates. At 600 min, the normalized gas uptake yield in 300 and 500-ppm SDS systems are 0.139 and 0.142 $mol_{(gas)}/mol_{(water)}$, respectively, higher than that in the pure water system (0.133 $mol_{(gas)}/mol_{(water)}$) by 4.44% and 6.85%, respectively. The rapid increments in gas uptake rate by adding SDS mostly appeares in the first 150 min. Therefore, ceasing the CO_2 capture process at an early stage is also recommended in the presence of surfactants. To achieve the same gas uptake yield of 0.119 $mol_{(gas)}/mol_{(water)}$, the 300-ppm SDS system take 229 min while the 500-ppm one only took 152 min, saving 23.7% and 49.3% of the total time, respectively.

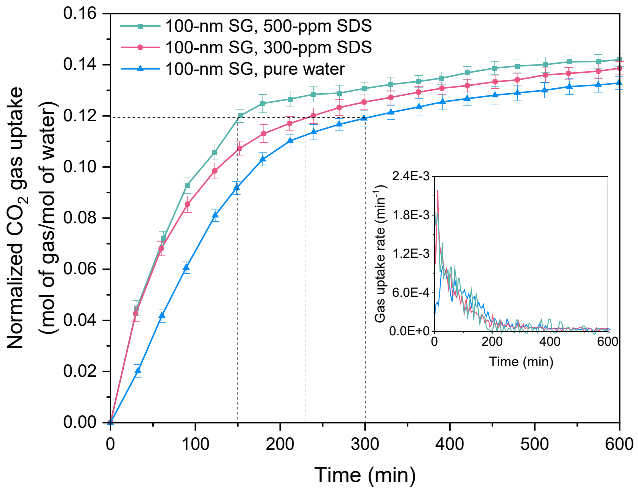

Figure 4.2. Normalized CO_2 gas uptake in 100-nm SGs with different SDS concentrations in pure CO_2 systems (Exp. no. 1, 4 and 5).

Figure 4.3 shows the normalized CO_2 gas uptake in 100-nm SG with DTAC of 1000- and 2000-ppm compared with the pure water 100-nm SG system (Exp. no. 1, 8 and 9). Overall, DTAC in 100-nm SG only promotes the gas uptake rate in the early stage, that is, <200 min, but fails to increase the final uptake yield compared to that with pure water. An early end can also bring slight time- and energy-saving benefits without compromising too much CO_2 uptake yield. Time-saving from 300 min to 252 min (16% time saved) is achieved by using DTAC at the two concentrations for an uptake yield of 0.119 $mol_{(gas)}/mol_{(water)}$. Overall, SDS can save more time than DTAC to obtain the same gas uptakes at the concentrations studied in the first 250 min. This is the same as the results in bulk water systems in Chapter 2.

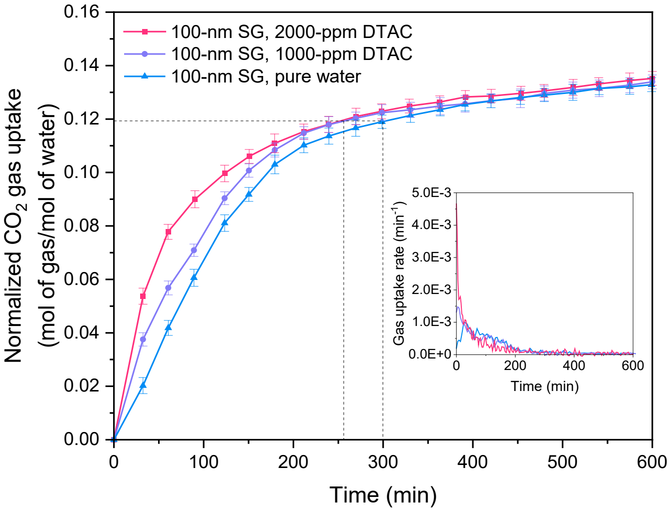

Figure 4.3. Normalized CO_2 gas uptake in 100-nm SGs with varied DTAC concentrations in pure CO_2 systems (Exp. no. 1, 8 and 9).

Figure 4.4 presents the effect of DTAC on CO_2 gas uptake in 100-nm SGs in CO_2/N_2 systems (Exp. no. 10, 13, 14 and 15). In general, a marked improvement in gas uptake is found in the presence of DTAC. A higher concentration of DTAC results in a considerable increase in the amount of CO_2 captured. At the end of the experiment, the normalized CO_2 gas uptake is 0.10, 0.13 and 0.15 $mol_{(gas)}/mol_{(water)}$ for 1000-, 2000- and 6000-ppm DTAC systems, respectively, which are higher than that in the pure water system by 17.6%, 52.9% and 76.5%, respectively. Furthermore, the intensive uptake period of 200 min is shortened in the presence of DTAC.

4.3.2 Effect of silica gel pore size

Based on the above discussion, 500-ppm SDS is found to have the greatest enhancement in both gas uptake yield and rate in 100-nm SGs. However, the promotion effect of 500-ppm SDS in SGs with smaller pores (30 nm and 50 nm) is unknown, which is revealed in Figure 4.5 (Exp. no. 2, 3, 6 and 7). It can be seen that 500-ppm SDS produces a marked enhancement in 50-nm SGs in the first 250 min, and the later gas uptake rates are similar. The final gas uptake also increases from 0.0651 to 0.0668 $mol_{(gas)}/mol_{(water)}$, indicating a similar promotion effect to that of 500-ppm SDS in 100-nm SGs in Figure 4.2. However, the gas uptake for the system of 500-ppm SDS in 30-nm SGs is even slightly lower than that of pure water in 30-nm SGs. The reason may be that the effects of surface tension and/or water activity on hydrate formation kinetics in very small pores are insignificant.

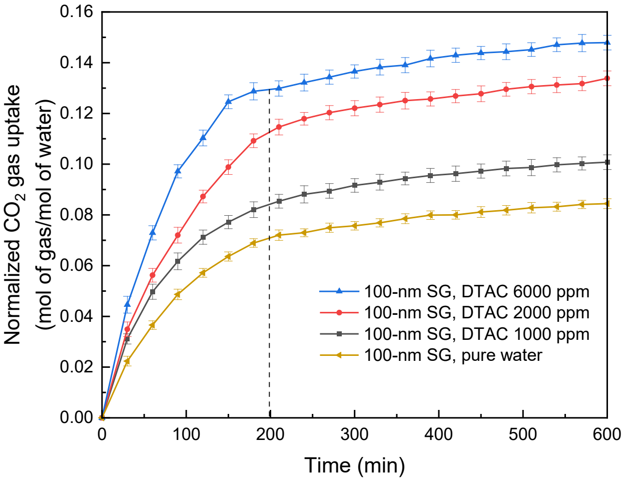

Figure 4.4. Effect of DTAC concentration on the normalized CO_2 gas uptake in 100-nm SGs (CO_2/N_2 systems, Exp. no. 10, 13, 14 and 15).

Figure 4.6 shows the effect of SG pore size on the normalized CO_2 gas uptake for CO_2/N_2 gas mixture systems in the absence of DTAC (Exp. no. 10, 11 and 12). The normalized CO_2 gas uptake is defined as the CO_2 gas uptake yield per mole of initial water. The error bars in the figure correspond to 95% confidence intervals. As can be seen, a higher CO_2 gas uptake is obtained with larger SG pores. It is believed that with the same particle size, in saturated SGs with larger pore size, CO_2 has a larger contact area with water. Before 270 min (left of the dashed line in the figure), the gas uptakes grows rapidly, especially in the cases with larger pores, while after 270 min, the normalized gas uptake lines are flat and almost parallel, indicating no obvious effect of the pore size. The time period from the onset of the experiment to the time when intensive gas uptake ends (around 270 min in this study) can be defined as the “intensive uptake period” [35].

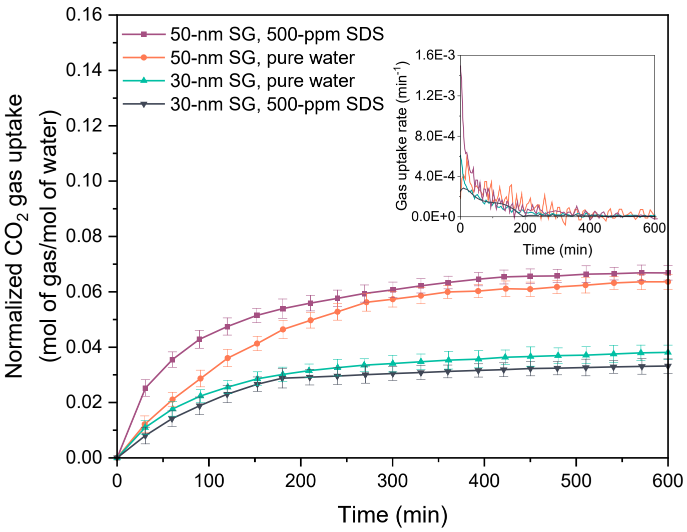

Figure 4.5. Effects of 500-ppm SDS on CO_2 hydrate formation in 30-nm SGs and 50-nm SGs in pure CO_2 systems (Exp. no. 2, 3, 6 and 7).

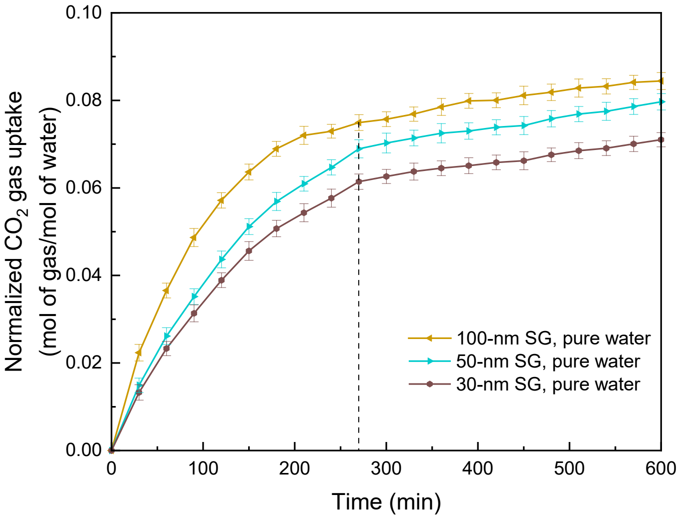

Figure 4.6. Effect of silica gel pore size on the normalized CO_2 gas uptake for CO_2/N_2 gas mixture systems (Exp. no. 10, 11 and 12).

4.3.3 CO_2 recovery and separation performance

Table 4.2 summarizes the split fraction, separation factor and final gaseous CO_2 concentration at the end of each study (600 min) of all the CO_2/N_2 cases. In the pure water system, the final CO_2 concentration in the gas phase decreases from the initial 70 mol% to 46.2–52.3 mol%, with the split fractions of CO_2 varying from 0.61 to 0.69 and the CO_2 separation factor from 25.54 to 32.61. SGs with larger pores present a better promotion effect in CO_2/N_2 separation than those with smaller pores. When DTAC is added to the systems, the final CO_2 concentration in the gas phase decreases, showing a significant improvement in both split fraction and separation factor. For example, in 100-nm SGs, with the addition of 1000, 2000 and 6000-ppm DTAC, the CO_2 split fractions increase by 13.0%, 18.8% and 20.3%, respectively, and the CO_2 separation factors even rise by 36.6%, 65.9% and 77.5%, respectively. Compared with the work of Zhang et al. [35] that reported the split fraction of CO_2 from the same gas mixtures was 0.32–0.39 with the addition of SDS, and 0.37–0.46 with the addition of DTAC in the pure water system without SGs, the results of this study indicate that the combination of SGs and DTAC leads to a much improved CO_2 separation performance with the split fraction of CO_2 up to 0.83.

Table 4.2. Separation performance for CO_2/N_2 hydrates formation with DTAC.

Exp. no.	SG type (nm)	System	Split fraction	Separation factor	Final gaseous CO_2 concentration (mol%)
10	100	Pure water	0.69	32.61	46.2
11	50	Pure water	0.65	28.22	49.8
12	30	Pure water	0.61	25.54	52.3
13	100	DTAC 1000 ppm	0.78	44.54	38.6
14	100	DTAC 2000 ppm	0.82	54.11	34.1
15	100	DTAC 6000 ppm	0.83	57.89	32.6
16	50	DTAC 1000 ppm	0.77	42.53	39.7

4.3.4 Induction time

Induction time is defined as the time period between the onset when the desired experimental condition is reached and the moment when a sudden pressure decrease and temperature rise both take place [123, 143]. After the induction, as a certain number of crystals are formed exceeding the critical size, the gas hydrate growth starts. Figure 4.7 shows the average induction time of all the systems studied. In pure water systems without DTAC, it can be seen that the induction time was much shorter in larger pore SGs. In the 100-nm SG pure water system, the induction time is only 20.5 min, while it increases by a factor of 2 and 5 to 41.3 and 102.2 min in 50- and 30-nm SGs, respectively. With the addition of DTAC, the induction time is reduced markedly. In 100-nm SGs, the induction time is in a range of 10.6–13.8 min with DTAC at 0.1–0.6 wt%, and a shorter induction time appears at higher DTAC concentrations. This is because DTAC surfactant lowers the surface tension and changes the water activity, and thus gases diffuse into the liquid phase more efficiently [34]. The shortest induction time appears at 0.6-wt% DTAC in 100-nm SG (10.6 min). In 50-nm SG systems, DTAC is also found to shorten the induction time compared with the pure water case.

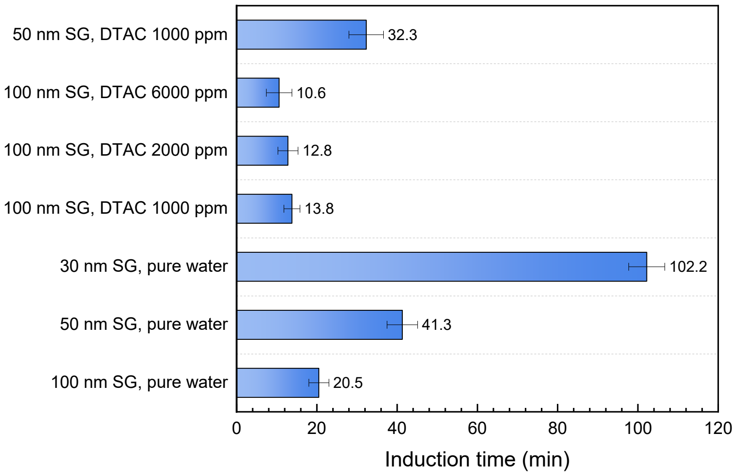

Figure 4.7. Induction time of CO_2/N_2 hydrates formation with DTAC.

4.3.5 Percent water conversion

The percent water conversion (PWC) of all the CO_2/N_2 gas mixture systems at the end of the experiment is shown in Figure 4.8. It can be seen that the PWC increased in larger pores or in higher DTAC concentrations. In the pure water cases, the PWC increases from 44.3% to 53.5% in large pores. In the presence of 1000-, 2000- and 6000-ppm DATC, the PWC increases by 19.3%, 57.6% and 76.6%, respectively, compared with the pure water system in 100-nm SG. With the addition of 6000-ppm DTAC, PWC grows even higher to 94.5%, showing a dramatic improvement in water conversion ratio.

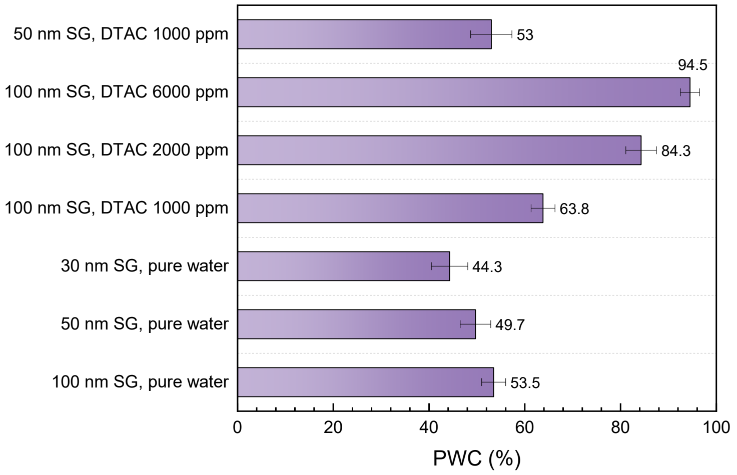

Figure 4.8. Percent water conversion at the end of each experiment (600 min).

4.4 Summary

In this chapter, the effects of surfactants on CO_2 hydrate formation kinetics in silica gels (SGs) have been studied in both pure CO_2 systems and CO_2/N_2 gas mixture systems. SGs with 30-, 50- and 100-nm pore sizes were used as frameworks for hydrate formation. Sodium dodecyl sulfate (SDS) and dodecyltrimethylammonium chloride (DTAC) surfactants were added as kinetic promoters and their effects on kinetic parameters were experimentally analyzed.

The experimental results in pure CO_2 systems showed a marked increase in both gas uptake yield and gas uptake rate in SGs with larger pores. With the addition of surfactants in 100-nm SGs, SDS systems saved 23.7%–49.3% of the time to achieve the same amount of gas uptake, while DTAC systems save 16% of the time.

The experimental results in CO_2/N_2 gas mixture systems revealed that the induction time was much shorter in larger pores of SGs, and was markedly reduced with higher DTAC concentrations. The CO_2 gas uptakes increased considerably in the initial 200–270 min but tended to change little later, indicating the finish of the intensive uptake period. When DTAC was added to the systems, the final CO_2

concentration in the gas phase decreased from 70 mol% to 32.6 mol%, showing a significant improvement in both split fraction and separation factor. Overall, the combined effect of surfactants SDS and DTAC on CO_2 hydrate formation in SGs pores improved CO_2 gas uptake yield and rate while maintaining high separation performance.

Chapter 5 Modeling study of CO_2 hydrate formation kinetics in microparticles[4]

5.1 Introduction

To better understand the formation kinetics, many modeling studies have been implemented since the early 1970s [76]. The shrinking core model (SCM) is commonly used in simulating the gas–water reactions where the diffusion rate is lower than the reaction rate. It was first applied in hydrate formation in deepwater oil/gas blowouts [79], and developed in water-in-condensate oil emulsions in the flow loop unit [80, 81]. Later, the SCM was modified to predict hydrate formation from ice powders [82] and CH_4 formation kinetics in the hydrogel particles [53, 83]. While these studies have demonstrated the high suitability of the SCMs to particles with well-defined geometries, the models developed so far have not yet completely reflected the chemical process. For instance, heat transfer and the effects of the porous structure of hydrates have not been clearly considered in the previously reported SCMs. Some assumptions such as the hydrate nucleus being homogeneously distributed in all pores conflict with the shrinking core concept that supports the growth and propagation of hydrate from the outer to the inner layers.

---

[4] The content of this chapter has been published in the following article:

Zhang F, Wang X[*], Wang B, Lou X[*], Lipiński W[*]. Experimental and numerical analysis of CO_2 and CH_4 hydrate formation kinetics in microparticles: A comparative study based on shrinking core model. Chemical Engineering Journal. 2022;446:137247.

Zhang F, Bhatia SK, Wang B, Chalermsinsuwan B, Wang X[*]. Experimental and numerical study on the kinetics of CO2–N2 clathrate hydrates formation in silica gel column with dodecyltrimethylammonium chloride for effective carbon capture. Journal of Molecular Liquids. 2022;363:119764.

In this chapter, a comprehensive SCM is developed and validated to study the CO_2 hydrate formation kinetics in “dry water” and silica gel (SG) pores. The CO_2 dissolved in water and the capillary effect of the porous hydrate shell are particularly considered in the model. The impact of heat released on formation kinetics is determined by establishing a new heat transfer model. As a comparison, the model is also applied to the formation process of CH_4 hydrate, for which the experimental data is obtained from a previous work of Shi et al. [83]. The different volume expansion in CO_2 and CH_4 hydrate growth in “dry water” is also considered in this work. Key parameters during CO_2 and CH_4 hydrate formation, namely the reaction rate constant, effective diffusion coefficient, and hydrate shell thickness, are determined by the model. This chapter aims to propose a more accurate modeling strategy to describe the hydrate formation kinetics in particles.

5.2 System description and assumptions

5.2.1 Hydrate formation in dry water particles

To better understand the formation kinetics and the key parameters that dominate the hydrate formation in small particles, a model was developed with modification based on the SCM reported in a previous study [80, 83]. The model of the hydrate growth mechanism was based on the work of Englezos et al. [4], where the hydrate growth consists of two consecutive steps: diffusion of dissolved gas to the hydrate–water interface and “reaction” at the interface (actually gas encaged by water cages). The hydrate formation in the SCM can be described as follows. Once nucleation starts, the initial hydrate film forms at the outer surface of the water droplets inside the silica shell, that is, the water surface where the CO_2 concentration is the highest. The hydrate grows inwards to the center of the water droplet. The schematic diagram for hydrate growth in “dry water” is shown in Figure 5.1. Assumptions made for the modeling study are:

1. “Dry water” particles are assumed to be spherical.
2. The system is assumed to be in a quasi-steady state where gas concentration in the system will not change during a small time interval.
3. The solution of CH_4 in water is neglected because of its low value at experimental conditions (approx. 0.10 mol L^{-1}) [144].

4. The solution of CO_2 in water is based on Henry's law for solubility at P_{exp} and T_{exp}.
5. The fugacity difference between the gas phase and the three-phase equilibrium condition at T_{exp} is considered as the driving force, since the latter is the minimum fugacity for hydrate to exist.
6. Capillaries spread all over the porous hydrate shell for the permeation of water, according to the study of Mori [145]. Only the hydrate growth in the radius direction of capillaries is considered.
7. The hydrate density is considered as a constant of 0.91 g cm^{-3} for CH_4 hydrate and 1.117 g cm^{-3} for CO_2 hydrate at the studied experimental conditions, according to the analytical expression of Sloan and Koh [1].
8. Although the theoretical hydration number for sI hydrate is 5.75, in reality the water cages cannot be fully occupied by gas molecules [1]. The actual hydration number varies with the occupancy rate of the cages. We choose 6.0 and 6.4 as the CH_4 and CO_2 hydration numbers based on the reported data of previous studies in the studied experimental conditions [146, 147].

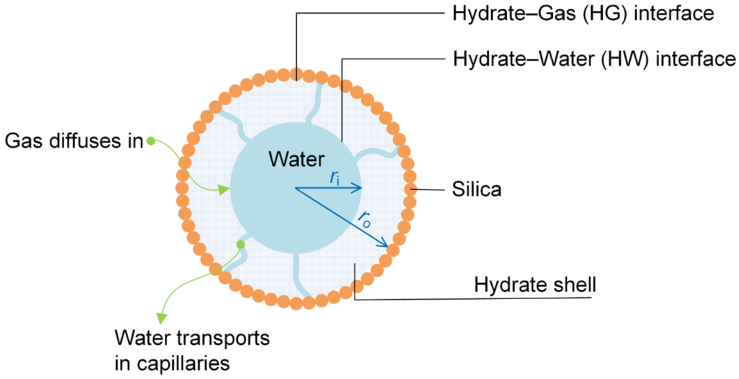
Hydrate–Gas (HG) interface
Hydrate–Water (HW) interface
Gas diffuses in
Water
r_i
r_o
Silica
Hydrate shell
Water transports in capillaries

Figure 5.1. Schematic diagram of the physical model for hydrate growth in "dry water".

5.2.2 Hydrate formation in silica gel pores

The schematic diagram of CO_2 hydrate formation in an SG is shown in Figure 5.2. The SCM of CO_2 hydrate formation in an SG is described as: the initial hydrate film forms at the outer surface of the water in the SG pores once the nucleus appears, and the hydrate grows inwards to the center of the SG. The formed porous hydrate layer is assumed as capillaries that are permeated with the water. More assumptions are given below.

1. The diameter of SG is calculated as the mean value of the particle size distribution because the particles number is large.
2. The driving force is also defined as the fugacity difference between the gas phase and the three-phase equilibrium condition since the latter is the minimum fugacity for hydrate to exist.
3. The hydrate formation is also considered a quasi-steady state in each calculation step.
4. The gas can only diffuse towards the core through the SG pores rather than the SG skeletons.
5. Capillaries distribute themselves randomly in all directions in the formed hydrates. In the SCM, only the capillaries in the radial direction are considered valid for inward mass transport.

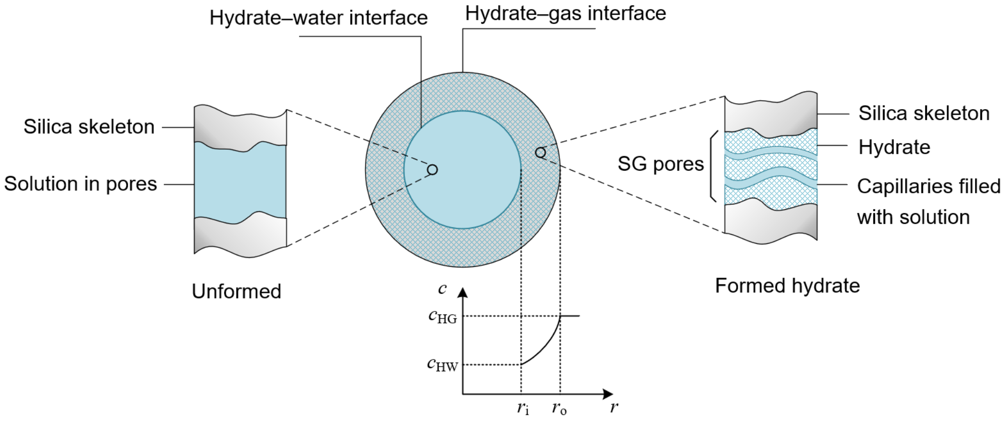
Hydrate–water interface
Hydrate–gas interface
Silica skeleton
Solution in pores
Unformed
SG pores
Silica skeleton
Hydrate
Capillaries filled with solution
Formed hydrate
c
c_{HG}
c_{HW}
r_i
r_o
r

Figure 5.2. Physical model for CO_2 hydrate formation within a SG particle.

5.3 Hydrate growth at the hydrate–water interface

5.3.1 Diffusion-controlled functions

The gas molecules diffuse to the hydrate–water interface through the hydrate shell. Fick’s second law can be used to describe the spherical symmetric diffusion

$$\frac{\partial c}{\partial t} = D_\mathrm{s} \frac{1}{r^2} \frac{\partial}{\partial r}\left(r^2 \frac{\partial c}{\partial r} \right) , \tag{5.1}$$

where D_s is the effective diffusion coefficient of gas through the hydrate shell, c is the gas concentration, and r is the particle radius. The system is assumed to be in a quasi-steady state where gas concentration in the system will not change during a small time interval, so that the following governing function of diffusion can be obtained

$$\frac{\mathrm{d}}{\mathrm{d}r}\left(r^2 \frac{\mathrm{d}c}{\mathrm{d}r} \right) = 0, \ \left(r_\mathrm{i} < r < r_\mathrm{o} \right), \tag{5.2}$$

where r_i and r_o are the inner and outer radius of the hydrate shell, respectively.

The boundary conditions of Eq. (5.2) are

$$\begin{cases} c = c_\mathrm{HW}, & r = r_\mathrm{i} \\ c = c_\mathrm{HG}, & r = r_\mathrm{o} \end{cases} , \tag{5.3}$$

where c_HW and c_HG are the gas concentration at the hydrate–water interface and hydrate–gas interface, respectively. The analytical solution of Eq. (5.3) can be obtained, and the gas diffusion rate at the hydrate–water interface can be expressed as

$$\Phi_\mathrm{g,\,d} = \frac{\mathrm{d}n}{\mathrm{d}t} = \alpha 4\pi r_\mathrm{i}^2 D_\mathrm{s} \left.\frac{\mathrm{d}c}{\mathrm{d}r}\right|_{r=r_\mathrm{i}} = \alpha 4\pi D_\mathrm{s} \frac{c_\mathrm{HG} - c_\mathrm{HW}}{\frac{1}{r_\mathrm{i}} - \frac{1}{r_\mathrm{o}}} , \tag{5.4}$$

where α is the volume fraction of the pores for porous material. In this thesis, $\alpha = 1$ for “dry water” particles.

5.3.2 Reaction-controlled functions

The gas diffusing through the hydrate shell may join the reaction of hydrate growth at the hydrate–water interface. The reaction is described as an adsorption process, including the trapping of gas molecules in water cages and the subsequent stabilization of cage frameworks [4]. From the perspective of reaction kinetics, the gas consumption rate in the reaction of a single “dry water” particle can be expressed as

$$\Phi_\mathrm{g,\,r} = \alpha K^* 4\pi r_\mathrm{i}^2 \left(f_\mathrm{HW} - f_\mathrm{eq} \right), \tag{5.5}$$

where K^* is the combined reaction rate constant for the entire diffusion and adsorption process, f_{HW} is the fugacity of gas at the hydrate–water interface, and f_{eq} is the fugacity of gas at the three-phase equilibrium condition at T_{exp}.

The definition of K^* is followed by the crystal growth theory of Karpiński and Englezos [4, 148], where the hydrate growth consists of two consecutive steps: gas diffusion to the nuclei at the hydrate–water interface (K_{d}) and gas adsorption into the structured water ("reaction") at the interface (K_{r}). K^*, K_{d} and K_{r} are related by the following equation

$$\frac{1}{K^*}=\frac{1}{K_{\mathrm{d}}}+\frac{1}{K_{\mathrm{r}}}. \tag{5.6}$$

Since the concentration of the gas can be written in terms of its fugacity, assuming that the number of moles of water remains practically constant, we have

$$f_{\mathrm{j}}=k_{\mathrm{H,j}}\frac{c_{\mathrm{j}}}{c_{\mathrm{j}}+c_{\mathrm{w0}}}, \tag{5.7}$$

where $k_{\mathrm{H,j}}$ is Henry's law constant. The $c_{\mathrm{w0}}=55.6\ \mathrm{mol/L}\gg c_{\mathrm{j}}$, so the fugacity can be written as

$$f_{\mathrm{j}}\approx k_{\mathrm{H,j}}\frac{c_{\mathrm{j}}}{c_{\mathrm{w0}}}. \tag{5.8}$$

The Henry's law constant is not easy to decide, especially in a gas mixture system. Here we define a concentration parameter to describe the degree of gas dissolution, the ratio of the fugacity to the concentration

$$\Omega_{\mathrm{j}}=\frac{f_{\mathrm{j}}}{c_{\mathrm{j}}}\left(=\frac{k_{\mathrm{H,j}}}{c_{\mathrm{w0}}}\right), \tag{5.9}$$

where Ω_{j} is a constant that only depends on gas species and temperature. Thus, Eq. (5.5) is written as

$$\Phi_{\mathrm{g,\,r}}=\alpha K^* 4\pi r_{\mathrm{i}}^2\left(\Omega_{\mathrm{HW}}c_{\mathrm{HW}}-\Omega_{\mathrm{eq}}c_{\mathrm{eq}}\right). \tag{5.10}$$

5.3.3 Mass balance of gas

Before the hydrates formed, CO_2 gas had already dissolved in the water. The gas molecules pre-dissolved in water also participate in hydrate formation. In the growth stage, the gas consumption rate resulting from pre-dissolved gas is expressed as

$$\Phi_{\mathrm{g,\,s}} = \frac{\mathrm{d}}{\mathrm{d}t}\left(\alpha \frac{4}{3}\pi r_{\mathrm{i}}^{3} c\right) \approx \alpha 4\pi r_{\mathrm{i}}^{2} \frac{\mathrm{d}r_{\mathrm{i}}}{\mathrm{d}t} c\,. \tag{5.11}$$

The above approximation holds for the quasi-steady state where concentration does not change in a small time interval. We assume that the water is saturated with CO_2 around the hydrate–water interface as the CO_2 in the reactor is in excess so that the solubility of gas, s, at T_{exp} and P_{exp} is used to represent the pre-dissolved gas concentration. The solubility of gas is calculated using Henry's law at the studied temperature and pressure.

When water is consumed for hydrate formation, the gas pre-dissolved in the amount of hydrated water will separate out and also participate in hydrate formation together with the gas diffused through the hydrate shell. The mass balance for gas diffusion and reaction can be written as

$$\Phi_{\mathrm{g,\,d}} + \Phi_{\mathrm{g,\,s}} = \Phi_{\mathrm{g,\,r}}\,. \tag{5.12}$$

5.4 Capillary effect of the hydrate shell

According to hydrate morphology studies, the formed hydrate shell is porous [2, 13, 149–151]. We assumed that the water permeated from the water droplet was instantaneously converted into hydrates, because the gas concentration at the hydrate–gas interface was sufficient for hydrate formation and growth. Thus, it is considered the hydrate shell a "water-permeable solid plate" within which the transport capillaries were distributed. Permeated water from the water droplet was totally converted into gas hydrates. The degree of hydrate formation and growth at the hydrate–gas interface depended on the amount of water permeated. This made the outside of the hydrate shell dry and inert.

In this work, the assumptions to describe the permeation of water have referred to the model developed by Mori and Mochizuki (1997) [152] with the incorporation of some alterations. Micro perforations and tortuous capillaries with the same radius and length were evenly distributed over the shell. The driving force for sucking the water was the capillary pressure induced by the water and outside interface, which was located near the gas-side mouth of each capillary and was strongly concave towards the gas side due to the hydrophilic nature of the hydrate surface.

The driving force for water to be transported through the capillaries is the surface tension, and the water transport can be considered as a Hagen–Poiseuille flow [145], which is given by

$$v_{\mathrm{water}} = \frac{\pi r_{\mathrm{c}}^4}{8\mu_{\mathrm{w}}} \frac{\Delta P}{L} \left(\mathrm{m}^3/\mathrm{s}\right), \tag{5.13}$$

$$\Delta P = \frac{2\sigma \cos\theta}{r_{\mathrm{c}}}, \tag{5.14}$$

$$L = \left(r_{\mathrm{o}} - r_{\mathrm{i}}\right)\tau, \tag{5.15}$$

where ΔP is the pressure difference between the two ends of the capillary tube, L is the length of capillary tube, r_{c} is the radius of capillary tubes, $\tau\left(\geq 1\right)$ denotes the tortuosity of the capillary, so the $\tau\left(r_{\mathrm{o}} - r_{\mathrm{i}}\right)$ is the length of capillary tubes, θ is the water-side contact angle on the capillary wall, σ is the water–gas interfacial tension, μ_{w} is the viscosity of water, and n_{c} is the number of capillary tubes. So, the water consumption in capillaries is given by

$$\begin{aligned} v_{\mathrm{w,\,cap}} &= \frac{\pi r_{\mathrm{c}}^4}{8\mu_{\mathrm{w}}} \frac{2\sigma\cos\theta}{r_{\mathrm{c}}} \frac{1}{\left(r_{\mathrm{o}} - r_{\mathrm{i}}\right)\tau} n_{\mathrm{c}} \\ &= \frac{n_{\mathrm{c}} r_{\mathrm{c}}^3 \cos\theta}{\tau} \frac{\pi\sigma}{4\mu_{\mathrm{w}}\left(r_{\mathrm{o}} - r_{\mathrm{i}}\right)}. \end{aligned} \tag{5.16}$$

We assume the water sucked out by the capillaries is totally converted into hydrate continuously and instantly due to sufficient gas on the outer surface. However, the water transport rate by the capillaries will decrease due to the blockage of capillaries or the increase in tortuosity of the capillaries as the hydrate grows [153]. Here, we use $\varepsilon_{\mathrm{cap}}$ as the capillary structure parameter to describe the change of all unknown parameters including the number and radius of capillaries, and the tortuosity of the capillary, and so on. ($\varepsilon_{\mathrm{cap}} = n_{\mathrm{c}} r_{\mathrm{c}}^3 \cos\theta / \tau$). The water consumption rate resulting from the capillary effect is given by [81, 145]

$$\Phi_{\mathrm{w,\,cap}} = \varepsilon_{\mathrm{cap}} \frac{\pi\sigma}{4\mu_{\mathrm{w}}\left(r_{\mathrm{o}} - r_{\mathrm{i}}\right)} \frac{\rho_{\mathrm{w}}}{M_{\mathrm{w}}}, \tag{5.17}$$

where σ is the surface tension of water at T_{exp}, and μ_{w} is the dynamic viscosity of water at T_{exp}, ρ_{w} is the water density and M_{w} is the molar mass of water.

5.5 Mass balance of water

The total water consumption rate related to the radius of water droplets can be expressed as

$$\Phi_{\mathrm{w,\,total}} = \frac{\mathrm{d}}{\mathrm{d}t}\left(\alpha \frac{4}{3}\pi r_{\mathrm{i}}^{3} \frac{\rho_{\mathrm{w}}}{M_{\mathrm{w}}}\right) = \alpha 4\pi r_{\mathrm{i}}^{2} \frac{\rho_{\mathrm{w}}}{M_{\mathrm{w}}} \frac{\mathrm{d}r_{\mathrm{i}}}{\mathrm{d}t}. \tag{5.18}$$

The total water consumption by hydrate formation is divided into that at the hydrate–water interface inward the particle ($\Phi_{\mathrm{w,\,HW}}$) and the one in the capillaries ($\Phi_{\mathrm{w,\,cap}}$). Thus, the mass balance for the water consumption rate is given by

$$\Phi_{\mathrm{w,\,HW}} = \Phi_{\mathrm{w,\,total}} - \Phi_{\mathrm{w,\,cap}}. \tag{5.19}$$

In addition, the gas consumption rate is proportional to the water consumption rate

$$\beta\,\Phi_{\mathrm{g,\,r}} = -\Phi_{\mathrm{w,\,HW}}, \tag{5.20}$$

where β is the hydration number. So the following equation can be obtained

$$\alpha 4\pi\beta D_{\mathrm{s}} \frac{c_{\mathrm{HG}} - c_{\mathrm{HW}}}{\frac{1}{r_{\mathrm{i}}} - \frac{1}{r_{\mathrm{o}}}} + \alpha 4\pi r_{\mathrm{i}}^{2} \frac{\mathrm{d}r_{\mathrm{i}}}{\mathrm{d}t}\beta s = \alpha 4\pi r_{\mathrm{i}}^{2} K^{*} \beta\left(\Omega_{\mathrm{HW}} c_{\mathrm{HW}} - \Omega_{\mathrm{eq}} c_{\mathrm{eq}}\right) = -\alpha 4\pi r_{\mathrm{i}}^{2} \frac{\rho_{\mathrm{w}}}{M_{\mathrm{w}}} \frac{\mathrm{d}r_{\mathrm{i}}}{\mathrm{d}t} + \Phi_{\mathrm{w,\,cap}}. \tag{5.21}$$

Coupling the first two terms of Eq. (5.21) to solve c_{HW}, we can obtain

$$c_{\mathrm{HW}} = \frac{\frac{D}{\frac{1}{r_{\mathrm{i}}} - \frac{1}{r_{\mathrm{o}}}} c_{\mathrm{HG}} + r_{\mathrm{i}}^{2} \frac{\mathrm{d}r_{\mathrm{i}}}{\mathrm{d}t} s + K^{*} r_{\mathrm{i}}^{2} \Omega_{\mathrm{eq}} c_{\mathrm{eq}}}{K^{*} r_{\mathrm{i}}^{2} \Omega_{\mathrm{HW}} + \frac{D}{\frac{1}{r_{\mathrm{i}}} - \frac{1}{r_{\mathrm{o}}}}}. \tag{5.22}$$

Then taking c_{HW} to the first and third items of Eq. (5.21), $\frac{\mathrm{d}r_{\mathrm{i}}}{\mathrm{d}t}$ can be solved:

$$\beta 4\pi D_{\mathrm{s}} \frac{c_{\mathrm{HG}} - \dfrac{\dfrac{D_{\mathrm{s}}}{\frac{1}{r_{\mathrm{i}}}-\frac{1}{r_{\mathrm{o}}}} c_{\mathrm{HG}} + r_{\mathrm{i}}^2 \dfrac{\mathrm{d}r_{\mathrm{i}}}{\mathrm{d}t} s + K^* r_{\mathrm{i}}^2 \Omega_{\mathrm{eq}} c_{\mathrm{eq}}}{K^* r_{\mathrm{i}}^2 \Omega_{\mathrm{HW}} + \dfrac{D_{\mathrm{s}}}{\frac{1}{r_{\mathrm{i}}}-\frac{1}{r_{\mathrm{o}}}}}}{\dfrac{1}{r_{\mathrm{i}}}-\dfrac{1}{r_{\mathrm{o}}}} - \frac{\Phi_{\mathrm{w,\,cap}}}{\alpha} = -4\pi r_{\mathrm{i}}^2 \frac{\mathrm{d}r_{\mathrm{i}}}{\mathrm{d}t}\left(\beta s + \frac{\rho_{\mathrm{w}}}{M_{\mathrm{w}}}\right), \tag{5.23}$$

$$\beta 4\pi D_{\mathrm{s}} \frac{c_{\mathrm{HG}} K r_{\mathrm{i}}^2 \Omega_{\mathrm{HW}} - r_{\mathrm{i}}^2 \dfrac{\mathrm{d}r_{\mathrm{i}}}{\mathrm{d}t} s - K r_{\mathrm{i}}^2 \Omega_{\mathrm{eq}} c_{\mathrm{eq}}}{K r_{\mathrm{i}}^2 \Omega_{\mathrm{HW}}\left(\dfrac{1}{r_{\mathrm{i}}}-\dfrac{1}{r_{\mathrm{o}}}\right) + D_{\mathrm{s}}} - \frac{\Phi_{\mathrm{w,\,cap}}}{\alpha} = -4\pi r_{\mathrm{i}}^2 \frac{\mathrm{d}r_{\mathrm{i}}}{\mathrm{d}t}\left(\beta s + \frac{\rho_{\mathrm{w}}}{M_{\mathrm{w}}}\right), \tag{5.24}$$

$$\left[-4\pi r_{\mathrm{i}}^2\left(\beta S + \frac{\rho_{\mathrm{w}}}{M_{\mathrm{w}}}\right) + \frac{\beta 4\pi D r_{\mathrm{i}}^2 S}{K r_{\mathrm{i}}^2 \Omega_{\mathrm{HW}}\left(\dfrac{1}{r_{\mathrm{i}}}-\dfrac{1}{r_{\mathrm{o}}}\right) + D}\right]\frac{\mathrm{d}r_{\mathrm{i}}}{\mathrm{d}t} = \frac{\beta 4\pi K r_{\mathrm{i}}^2\left(c_{\mathrm{HG}}\Omega_{\mathrm{HW}} - \Omega_{\mathrm{eq}} c_{\mathrm{eq}}\right)}{K r_{\mathrm{i}}^2 \dfrac{\Omega_{\mathrm{HW}}}{D}\left(\dfrac{1}{r_{\mathrm{i}}}-\dfrac{1}{r_{\mathrm{o}}}\right) + 1} - \frac{\Phi_{\mathrm{w,\,cap}}}{\alpha}, \tag{5.25}$$

where $\Phi_{\mathrm{w,\,cap}} = \dfrac{\varepsilon_{\mathrm{cap}} \pi \sigma \rho_{\mathrm{w}}}{4\mu_{\mathrm{w}}\left(r_{\mathrm{o}} - r_{\mathrm{i}}\right) M_{\mathrm{w}}}$.

So the inner radius change rate is expressed as

$$\frac{\mathrm{d}r_{\mathrm{i}}}{\mathrm{d}t} = \frac{K\left(f_{\mathrm{HW}} - f_{\mathrm{eq}}\right) - \dfrac{\varepsilon_{\mathrm{cap}} \sigma \rho_{\mathrm{w}}}{16\alpha\mu_{\mathrm{w}}\beta M_{\mathrm{w}} r_{\mathrm{i}}^2\left(r_{\mathrm{o}} - r_{\mathrm{i}}\right)}\left[K r_{\mathrm{i}}^2 \dfrac{f_{\mathrm{HW}}}{D_{\mathrm{s}} c_{\mathrm{HW}}}\left(\dfrac{1}{r_{\mathrm{i}}}-\dfrac{1}{r_{\mathrm{o}}}\right) + 1\right]}{-\left(s + \dfrac{\rho_{\mathrm{w}}}{\beta M_{\mathrm{w}}}\right)\left[K r_{\mathrm{i}}^2 \dfrac{f_{\mathrm{HW}}}{D_{\mathrm{s}} c_{\mathrm{HW}}}\left(\dfrac{1}{r_{\mathrm{i}}}-\dfrac{1}{r_{\mathrm{o}}}\right) + 1\right] + s}. \tag{5.26}$$

Equation (5.26) is a nonlinear ordinary differential equation (ODE), which can be rearranged into

$$\Delta r_i^{(t_n)} = \left[\frac{K\left(r_{\mathrm{i}}^{(t_{n-1})}\right)^2\left(f_{\mathrm{HW}} - f_{\mathrm{eq}}\right) - \dfrac{\varepsilon_{\mathrm{cap}}^{(t_{n-1})} \sigma \rho_{\mathrm{w}}\left[K\left(r_{\mathrm{i}}^{(t_{n-1})}\right)^2 \dfrac{f_{\mathrm{HW}}}{D^{(t_{n-1})} c_{\mathrm{HW}}}\left(\dfrac{1}{r_{\mathrm{i}}^{(t_{n-1})}} - \dfrac{1}{r_{\mathrm{o}}^{(t_{n-1})}}\right) + 1\right]}{16\alpha\beta\mu_{\mathrm{w}}\left(r_{\mathrm{o}}^{(t_{n-1})} - r_{\mathrm{i}}^{(t_{n-1})}\right) M_{\mathrm{w}}}}{-\left(r_{\mathrm{i}}^{(t_{n-1})}\right)^2\left(s + \dfrac{\rho_{\mathrm{w}}}{\beta M_{\mathrm{w}}}\right)\left[K\left(r_{\mathrm{i}}^{(t_{n-1})}\right)^2 \dfrac{f_{\mathrm{HW}}}{D^{(t_{n-1})} c_{\mathrm{HW}}}\left(\dfrac{1}{r_{\mathrm{i}}^{(t_{n-1})}} - \dfrac{1}{r_{\mathrm{o}}^{(t_{n-1})}}\right) + 1\right] + \left(r_{\mathrm{i}}^{(t_{n-1})}\right)^2 s}\right]\Delta t\,. \tag{5.27}$$

Equation (5.27) is the explicit form of finite differences, where the Euler forward integration is used to give a straightforward calculation of the hydrate shell inner radius change Δr_{i} at time t_{n} directly from the previous time step $t_{\mathrm{n-1}}$.

In addition, the percent water conversion (PWC) is a metric to evaluate the amount of water consumed in the hydrate formation compared to the initial total amount of water, defined as

$$\frac{\mathrm{dPWC}}{\mathrm{d}t}=\frac{\Phi_{\mathrm{w,\,total}}}{n_{\mathrm{w,\,ini}}}, \tag{5.28}$$

where $n_{\mathrm{w,\,ini}}$ is the initial number of moles of the water in a single microparticle.

5.6 Effective diffusion coefficient and capillary structure parameter

Along with the hydrate growth, the hydrate shell becomes thicker and more compact, which however, hinders the mass transfer. The diffusion coefficient becomes a function of the shell thickness decreasing along with hydrate growth. The PWC is a metric to evaluate the amount of water consumed in the hydrate formation compared to the initial total amount of water. Thus, the boundary conditions for the diffusion coefficient can be expressed as:

$$\begin{cases} D=D_0, & \mathrm{PWC}=0 \\ D>0, & \mathrm{PWC}=1 \end{cases}. \tag{5.29}$$

The diffusion coefficient of gas through the hydrate shell is a vital parameter for hydrate formation; it is affected by the gas composition and temperature/pressure conditions, and is difficult to measure. Although the diffusion coefficient is a physical parameter, it varies with the shell density and compactness as hydrate grows. Thus we believe the diffusion coefficient is a function of the amount of water consumed. In the work of Shi et al. [81], the decreasing trend of the diffusion coefficient was described by a logarithmic function; when the calculated diffusion coefficient value becomes less than zero, it is taken as equal to zero. It conflicts, however, with the fact that the diffusion coefficient can never be zero since even when all water forms hydrate, the gas molecules can still diffuse into the hydrate phase. Thus, here we propose an exponential function to present the variation of the effective diffusion coefficient,

$$D_{\mathrm{s}}=D_{\mathrm{s},0}\exp\left(-\xi\,\mathrm{PWC}\right),\ \xi\in\left(0,+\infty\right), \tag{5.30}$$

where $D_{s,0}$ is the initial effective diffusion coefficient of gas through the hydrate layer at $t = 0$, that is, the end of nucleation and the onset of hydrate growth, and ξ is the reduction factor of the diffusion coefficient.

Similarly, for the capillary structure parameter ε_{cap}, when the water in the capillary is being consumed, the capillary will become thinner, and both the number of capillaries and the amount of water in the capillaries will decrease. Therefore, the capillary structural parameter is also a gradually decreasing function. But even if all the water is consumed, the porous structure of the hydrate still exists, and the capillary structural parameter will not drop to zero. Therefore, the exponential function is also used to construct the capillary structural parameter as follows:

$$\varepsilon_{\text{cap}} = \varepsilon_{\text{cap},0} \exp\left(-\varsigma\, \text{PWC}\right),\ \varsigma \in \left(0, +\infty\right), \tag{5.31}$$

where $\varepsilon_{cap,0}$ is the initial capillary structure parameter and ς is the reduction factor of the capillary structure parameter. It is noted that there are many kinds of construction functions to describe the diffusion coefficient and capillary structural parameters such as those in Eqs. (5.30) and (5.31). The simple expression chosen in this work is intended to reduce the computational load.

Thus far, all the mass transfer models of hydrate growth in a single “dry water” particle have been established. The numerical calculation is implemented by a nonlinear curve-fitting function “lsqcurvefit” of MATLAB to obtain the optimal parameters.

5.7 Model validation and extraction of kinetic constants

Based on the modeling strategies established above, this section validates the models through experimental data of CO_2 hydrate formation in “dry water” and silica gels (SGs) presented in Chapters 3 and 4. Basically, the models are suitable for both “dry water” and SGs; however, the practical calculation and parameter selection may vary in different systems. This chapter discusses the model validation and simulation results for “dry water” and SGs separately. Both CO_2 hydrate and CO_2/N_2 hydrates formation are included. Key parameters, including effective diffusion coefficient, water consumption in capillaries, hydrate shell thickness in CO_2 and CH_4 hydrate formation were found. The heat transfer models are further established for CO_2

hydrate formation in “dry water” particles. The effects of surfactants sodium dodecyl sulfate (SDS) and dodecyltrimethylammonium chloride (DTAC) on hydrate formation in SG pores are also investigated. Furthermore, the models are applied to CO_2/N_2 hydrate formation in SG pores to investigate the roles of N_2 in hydrate formation and to reveal the effects of DTAC in CO_2 separation, due to the better separation performance of DTAC over SDS, as mentioned in Chapter 4.

5.7.1 CO_2 hydrate formation in dry water

The simulated gas consumptions of CO_2 and CH_4 in the gas hydrate growth in “dry water” particles are shown in Figure 5.3. It can be seen that the simulation results are in good agreement with the experimental data. The data of CH_4 hydrate formation in 5-wt% “dry water” particles was obtained from Shi et al. [83] at $T_{\mathrm{exp}} = 273.65$ K and $P_{\mathrm{exp}} = 4.5$ MPa. The reaction rate constant, K^*, is in the range of $6.9 - 7.1 \times 10^{-6}$ mol m^{-2}MPa^{-1}s^{-1} for CO_2 hydrate formation, and $5.5–6.5\times10^{-6}$ mol m^{-2}MPa^{-1}s^{-1} for CH_4 hydrate formation, according to the measured data used in Englezos’ modeling that took fugacity as the driving force, as is done in this work [4, 154]. Shi et al. [83] reported that K^* of CH_4 hydrate formation was in the range of $5.49 - 6.05 \times 10^{-6}$ mol m^{-2}MPa^{-1}s^{-1}. The K^* value regressed in a preliminary modeling work under the same P_{exp} and T_{exp} also had a magnitude of 10^{-6} mol m^{-2}MPa^{-1}s^{-1}. Since K^* should be a constant under the same experimental conditions, it is reasonable to use a known K^* as a constant of 7.0×10^{-6} mol m^{-2}MPa^{-1}s^{-1} for CO_2 and 6.05×10^{-6} mol m^{-2}MPa^{-1}s^{-1} for CH_4 from references with similar experimental conditions.

The fitting results are evaluated by the mean absolute percentage error (MAPE), expressed in Eq. (5.32). The MAPE of CH_4 hydrate formation is 2.11%, which is lower than that of a previous simulation work [83]. The values of MAPE of CO_2 hydrate formation are below 5%, showing the accuracy of the modified model. Table 5.1 summarizes these optimal parameters.

$$\mathrm{MAPE} = \frac{1}{N}\sum_{i=1}^{N}\left|\frac{x_{\mathrm{sim},i} - x_{\mathrm{exp},i}}{x_{\mathrm{exp},i}}\right| \times 100\% \tag{5.32}$$

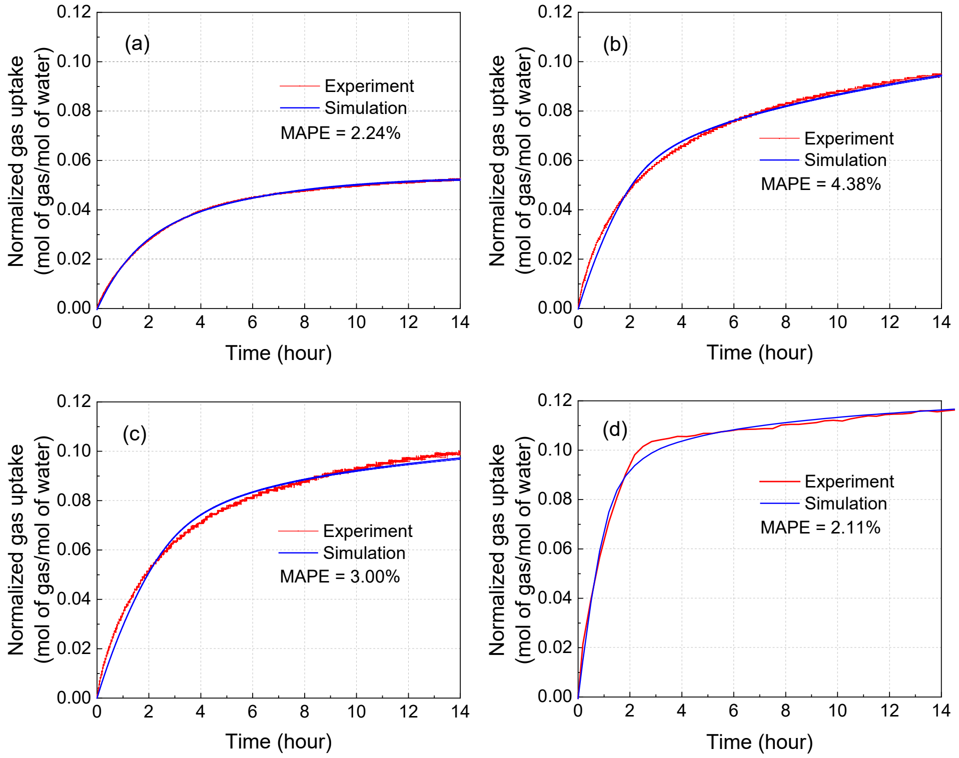

Figure 5.3. Simulated gas consumptions during hydrate formation in "dry water" using the SCM: (a) CO_2 with 3-wt% silica; (b) CO_2 with 5-wt% silica; (c) CO_2 with 8-wt% silica; and (d) CH_4 with 5-wt% silica.

5.7.2 CO_2 hydrate formation in silica gels

The CO_2 hydrate formation experiments in SG pores were implemented in surfactant solutions. To determine the constant parameter (Ω) and CO_2 solubility (s) in the solutions with surfactants, Henry's law constants (k_H) should first be determined. There are several ways to determine k_H. In this work, a flash column (Flash 2 block) with components of gas and solutions in the feed stream was run in Aspen Plus to obtain the values of components at equilibrium. Then k_H can be calculated by the ratio of components after the flash calculation. The calculated k_H values are 0.93 and 1.29 mol $L^{-1}MPa^{-1}$ for CO_2 in 300-ppm and 500-ppm SDS solutions at T_{exp}, and 1.10 and 1.84 mol $L^{-1}MPa^{-1}$ in 1000-ppm and 2000-ppm DTAC solutions at T_{exp}. The k_H values calculated by Aspen Plus are also validated with the reported data of CO_2 dissolution experiments in SDS [155] and DTAC [156] solutions with high accuracy. Then **Ω** and *s* can be calculated.

Figure 5.4 shows the fitting of the experimental gas consumption results in SGs with the results from the revised SCM. As can be seen, the simulation results are in good agreement with the experimental data. The fitting results are evaluated by the MAPE. It can be seen that the MAPEs of all the simulation results are in the range of 1.58%–3.11%, proving the high accuracy of the modified models.

Table 5.1. Summary of optimal parameters of CO_2 hydrate formation in "dry water".

Parameters	Notation	"Dry water" system			
		CO_2 in 3-wt% silica	CO_2 in 5-wt% silica	CO_2 in 8-wt% silica	CH_4 in 5-wt% silica
Initial effective diffusion coefficient	$D_{s,0}$ ($\times10^{-14}$ m^2s^{-1})	6.41	6.44	6.50	6.83
Reduction factor of diffusion coefficient	ξ	7.86	6.77	2.64	8.82
Initial capillary structure parameter	$\varepsilon_{cap,0}$ ($\times10^{-27}$ m^3)	1.15	1.34	1.82	1.37
Reduction factor of the capillary structure	ς ($\times10^{-11}$)	6.90	3.58	1.02	1.04
Mean absolute percentage error	MAPE	2.24%	4.74%	3.00%	2.11%

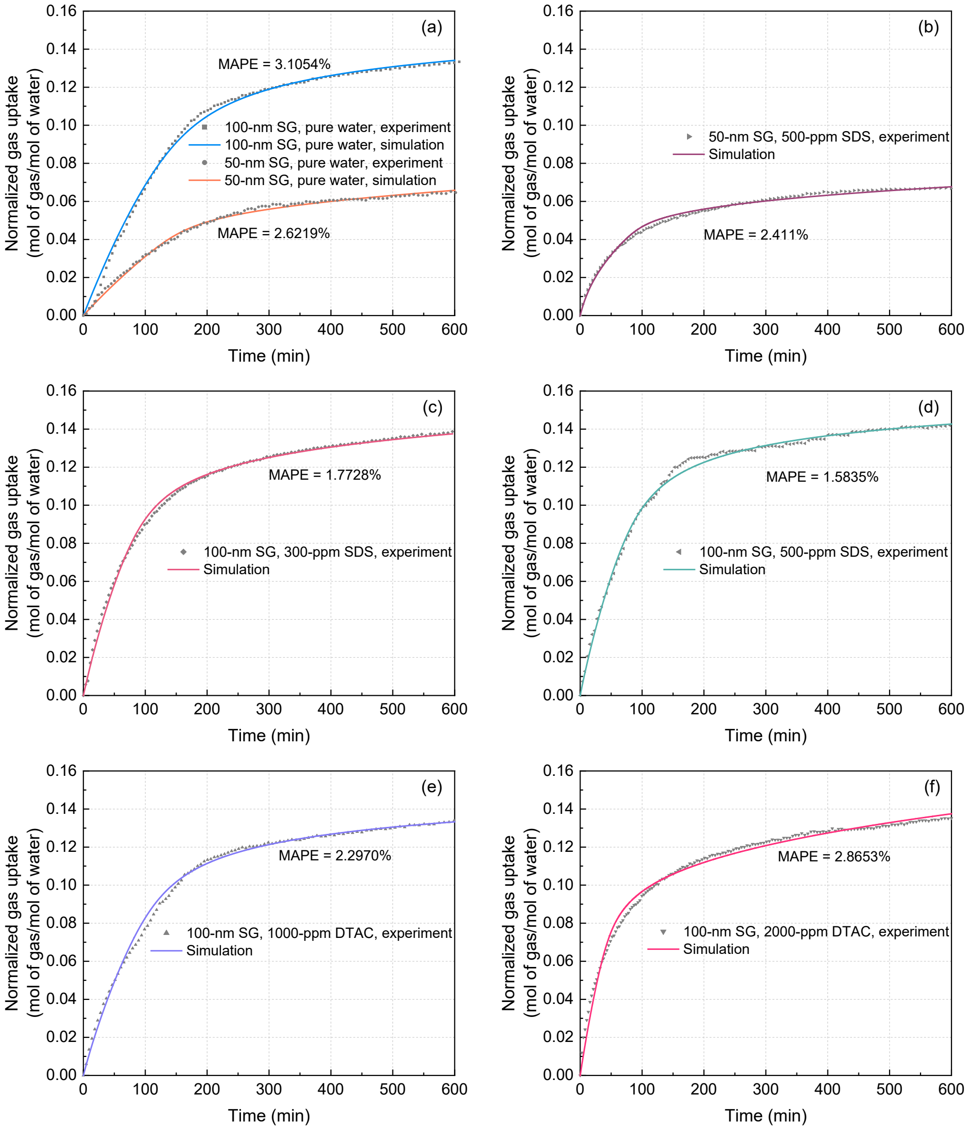

Figure 5.4. Experimental and simulation results of gas consumption in CO_2 hydrate formation in SGs.

Based on the optimal simulation results, all of the $D_{s,0}$ regress within a small range of 4.7–4.9×10^{-12} m^2s^{-1}. $D_{s,0}$ refers to the initial effective diffusion coefficient of CO_2 that is transported through the initially formed gas hydrate shell when the nucleation ceases and hydrate growth begins. The very close results of $D_{s,0}$ reveal that $D_{s,0}$ is an inherent property of hydrate, which is only related to the type of hydrate and is not affected by surfactants. Thus, it's reasonable to choose $D_{s,0}$ as a constant of 4.8×10^{-12} m^2s^{-1} in simulation to reduce the freedom of the modeling. For comparison, the reported effective diffusion coefficient of CO_2 through the hydrate shell varied from 10^{-15} to 10^{-12} m^2s^{-1} during hydrate formation under similar experimental conditions [157]. The other simulated optimal parameters are summarized in Table 5.2.

Table 5.2. Summary of optimal parameters of CO_2 hydrate formation in silica gels.

System	Exp. no.[a]	K^* ($\times10^{-6}$)	ξ	$\varepsilon_{cap,0}$ ($\times10^{-23}$)	ς	MAPE (%)
100-nm SG, pure water	1	17.20	9.73	5.65	3.91	3.11
50-nm SG, pure water	2	5.38	37.16	14.26	4.22	2.62
100-nm SG, 300-ppm SDS	4	23.52	10.08	145.07	4.44	1.77
100-nm SG, 500-ppm SDS	5	28.87	11.84	165.83	4.66	1.58
100-nm SG, 1000-ppm DTAC	8	20.70	10.94	151.27	4.44	2.30
100-nm SG, 2000-ppm DTAC	9	33.32	15.20	190.73	4.58	2.87
50-nm SG, 500-ppm SDS	6	6.45	59.96	174.90	4.69	2.41

[a] Experiment numbers refer to those in Table 4.1.

5.7.3 CO_2/N_2 hydrate formation in silica gels

Figure 5.5 shows the experimental results and the simulation results from the modified SCM. The SCM has three unknown parameters to be fitted, namely the combined reaction rate constant K^*, the initial effective diffusion coefficient $D_{s,0}$, and the reduction rate of the effective diffusion coefficient ξ. The total gas uptake yields shown in Figure 5.5 include those for CO_2 and N_2. The errors between the simulation results and the experimental data are evaluated using the MAPE in gas mixtures, as expressed in Eq. (5.33) below. The simulation results are in very good agreement with the experimental data, showing evidence of the high accuracy of the SCM.

$$\text{MAPE} = \frac{1}{N}\sum\left|\frac{x_{\text{sim, CO}_2\text{,i}} + x_{\text{sim, N}_2\text{,i}} - x_{\text{exp,total,i}}}{x_{\text{exp,total,i}}}\right| \times 100\% \tag{5.33}$$

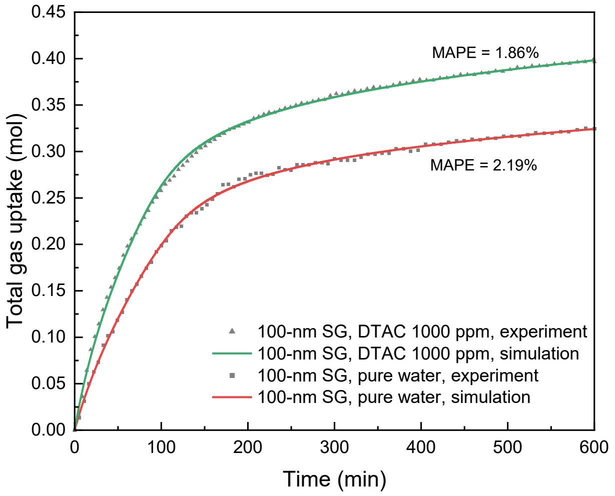

Figure 5.5. Experimental and simulation results of CO_2/N_2 hydrate formation in silica gels.

The parameters of CO_2 and N_2 of all studied cases from the simulation are shown in Table 5.3. The data obtained were based on the mean values of the three repeated runs. All of the MAPEs are within the range of 1.52%–2.42%. Other simulation results can be obtained in the following sections.

Table 5.3. Summary of optimal parameters of CO_2/N_2 hydrate formation in silica gels.

Systems	Exp. no.[a]	$K^*_{CO_2}$ $(\times 10^{-5})$	ξ_{CO_2}	$K^*_{N_2}$ $(\times 10^{-6})$	ξ_{N_2}	MAPE (%)
100-nm SG, pure water	10	1.66	24.13	0.46	23.16	2.26
50-nm SG, pure water	11	1.32	27.24	0.44	25.27	1.52
30-nm SG, pure water	12	1.07	30.15	0.40	29.88	1.56
100-nm SG, 1000-ppm DTAC	13	2.27	23.68	0.65	24.66	1.84
100-nm SG, 2000-ppm DTAC	14	3.42	10.19	1.15	14.28	2.11
100-nm SG, 6000-ppm DTAC	15	5.24	8.52	1.69	11.89	2.42
50-nm SG, 1000-ppm DTAC	16	1.80	22.51	0.56	24.38	2.29

[a] Experiment numbers refer to those in Table 4.1.

5.8 Simulation results of CO_2 hydrate formation in dry water

5.8.1 Volume change as hydrate forms

The hydrate formation will lead to a volume change around the microparticle due to the density change from water to gas hydrate. It is known that the density of CH_4 and CO_2 hydrate are 0.91 g cm^{-3} and 1.117 g cm^{-3} at the experimental conditions, respectively [158]. According to the density change from water to hydrate and the hydration number of CH_4 and CO_2 hydrates, it can be calculated that the volume in the hydrate growth will expand by a factor of 1.260 for CH_4 hydrate and 1.234 for CO_2 hydrate. The schematic diagrams of CH_4 and CO_2 hydrate formation in "dry water" particles are illustrated in Figure 5.6.

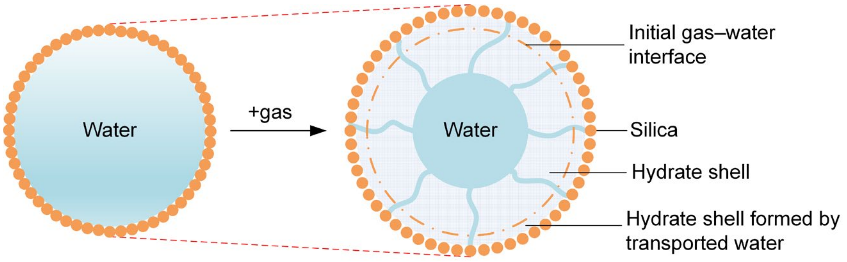
Water
+gas
Water
Initial gas–water interface
Silica
Hydrate shell
Hydrate shell formed by transported water

Figure 5.6. Schematic diagrams of hydrate formation in a "dry water" particle.

It is believed that the initially formed hydrate layer starts from the outer surface of the droplet and the formed shell is rigid. The expansion mentioned above at the hydrate–water interface due to CH_4 and CO_2 hydrate formation keeps driving water to move outside the hydrate shell through the capillaries in the hydrate shell. The water transported through capillaries then forms hydrates on the outer surface of the hydrate shell, which causes continuous growth of the outer radius of the particle (Figure 5.6). The volume expansion in the CH_4 and CO_2 hydrate growth can be written as

$$1.260\Phi_{\mathrm{w,\,total}}=\frac{\mathrm{d}}{\mathrm{d}t}\left[\frac{4}{3}\pi\left(r_{\mathrm{o}}^{3}-r_{\mathrm{i}}^{3}\right)\frac{\rho_{\mathrm{w}}}{M_{\mathrm{w}}}\right]\ \text{for } CH_4 \tag{5.34}$$

$$1.234\Phi_{\mathrm{w,\,total}}=\frac{\mathrm{d}}{\mathrm{d}t}\left[\frac{4}{3}\pi\left(r_{\mathrm{o}}^{3}-r_{\mathrm{i}}^{3}\right)\frac{\rho_{\mathrm{w}}}{M_{\mathrm{w}}}\right]\ \text{for } CO_2 \tag{5.35}$$

Figure 5.7 shows the inner and outer radius change of the hydrate shells (i.e., the hydrate–water interface and the hydrate–gas interface, respectively) during the hydrate formation in a "dry water" particle. It can be seen that in all the cases, the thickness of the hydrate shell increases with time. The inner hydrate radius in the figure indicates the amount of unconverted water remaining inside the hydrate shell. The dashed lines in the figures represent the initial "dry water" radius. In Figure 5.7 (a), for CO_2 hydrate formation in "dry water" with 3-wt% silica, the initial "dry water" radius is 26.3 μm, and the radius of the sphere of unconverted water at the end of the experiment changes very slightly to 23.1 μm, resulting in the lowest percent water conversion (PWC). In contrast, although the hydrate shell of 8-wt% silica is the thinnest among all CO_2 studies (Figure 5.7 (c)), its PWC is the highest, revealing that the proportion of remaining water is the lowest. The changes in the outer radius show the volume expansion from water to hydrate. It can be seen that in Figure 5.7 (b) and (d), for "dry water" of 5-wt% silica, CH_4 hydrate formation has a larger volumetric expansion than that of CO_2 hydrates, which is consistent with the expansion factors used in Eqs. (5.34) and (5.35).

5.8.2 Effective diffusion coefficient

It can be seen in Table 5.1 that the values for the initial effective diffusion coefficient, $D_{s,0}$, of gas through hydrate shell in this work are in a small range of $6.41–6.50\times10^{-14}$ m^2s^{-1} for CO_2 at 277.15 K and 6.83×10^{-14} m^2s^{-1} for CH_4 at 273.65 K. To be compared, the reported effective diffusion coefficient was in range of 1×10^{-16} to 2×10^{-14} m^2s^{-1} for CO_2 diffusion through CO_2 hydrate at 270 K [159], and varied from 10^{-15} to 10^{-12} m^2s^{-1} for CH_4 diffusion through CH_4 hydrate at temperatures of 264.85–270.45 K [157].

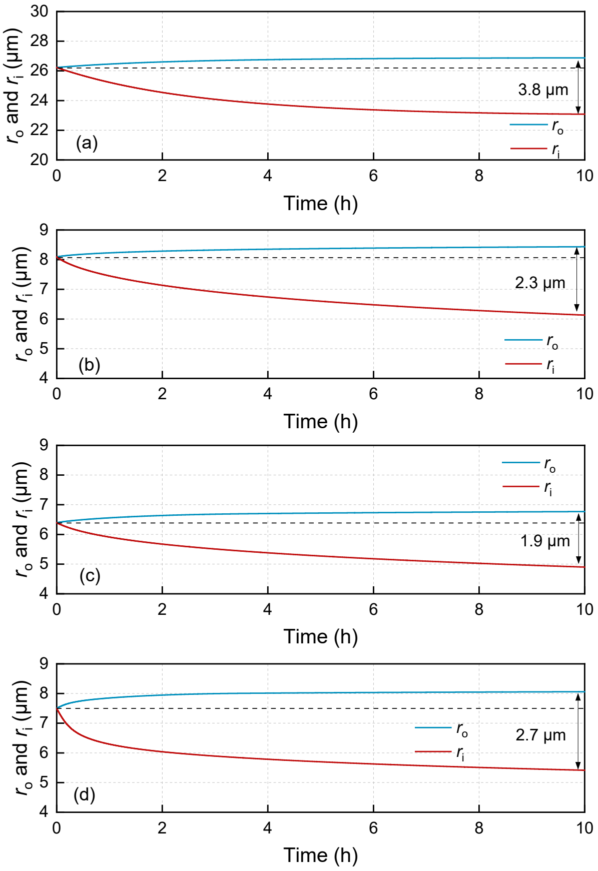

Figure 5.7. The variation of radius of hydrate shell and inner water droplets during hydrate formation in "dry water": (a) CO_2 with 3-wt% silica; (b) CO_2 with 5-wt% silica; (c) CO_2 with 8-wt% silica; and (d) CH_4 with 5-wt% silica.

In further evidence that the effective diffusion coefficient should not be taken as a constant in the model, this work introduces a simple calculation based on the water consumption and gas consumption in hydrate in the 3-wt% silica and 8-wt% silica "dry water" particles. The initial average radii of larger 3-wt% and the smaller 8-wt% silica "dry water" particles are 26.3 μm and 6.4 μm, respectively. It is found that the water consumption of a single large particle is 35.9 times that of a single small particle, while the gas consumption of a single large particle is 38.6 times that a single small particle. This indicates the gas occupancy in the hydrate shell in the two types of particles differs, with a slightly higher rate of gas occupancy in the large particle. This may be attributed to the large initial gas–water interface area of a single large particle that allows better gas transport and occupancy. The diffusion coefficient in a larger particle is lower due to the denser state of the hydrate shell with a higher rate of gas occupancy.

Figure 5.8 shows the variations of effective diffusion coefficient with time during the CO_2 hydrate formation in a "dry water" particle. The dashed lines represent the average effective diffusion coefficient for the three sizes of "dry water" particles, which are 1.27×10^{-14}, 1.83×10^{-14}, and 3.46×10^{-14} m^2s^{-1} for 3-wt%, 5-wt% and 8-wt%, respectively. That is to say, the average effective diffusion coefficient is higher in a smaller particle. It can be seen that the initial effective diffusion coefficients, $D_{s,0}$, are very similar for all the CO_2 hydrate cases. The effective diffusion coefficient decreases with time as the hydrate shell grows. The decrease in the first 4 h is rather rapid and becomes slower afterwards. It decreases most rapidly in the largest 3-wt% silica "dry water" particles than in the other two sizes. The reason is that the larger particle has a larger initial gas–water interface area in a single particle, allowing a better mass transfer of gas from the beginning and thus a higher rate of gas occupancy, and as a result, the denser hydrate shell is formed within the same time, so lowering the diffusion coefficient. In the model, the decreasing rate of the effective diffusion coefficient, D_s, is controlled by the reduction factor, ξ. For 3-wt% silica particles, ξ is 7.86, which is higher than the factor of 6.77 for 5-wt% silica and 2.64 for 8-wt% silica, that is, ξ is higher in a larger particle. For CO_2 hydrate formation in 3-wt% silica "dry water" particles, the diffusion coefficient tends to be very low after 4 h, indicating the end of the gas hydrate formation at an earlier time. This is consistent with the result of PWC in Chapter 3.

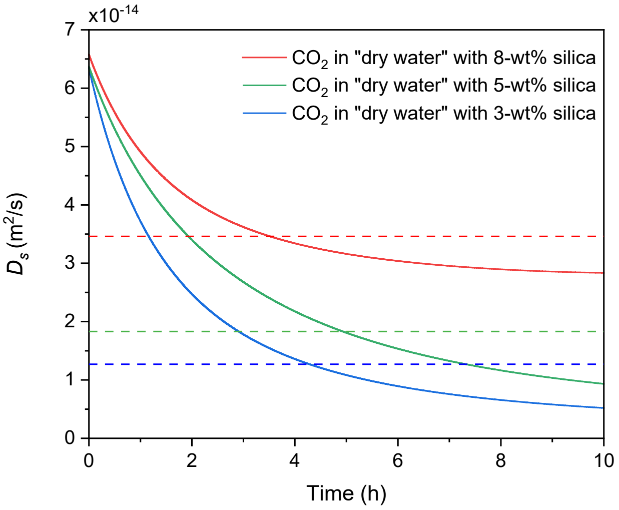

Figure 5.8. Effective diffusion coefficient of CO_2 through formed hydrate in "dry water" particles of different sizes.

5.8.3 Water consumption and capillary effect

Figure 5.9 presents the water consumption during the hydrate formation in a "dry water" particle. The left four figures (a1)–(d1) show the water consumption at the hydrate–water interface, $V_{\mathrm{w,HW}}$, for CO_2 and CH_4 hydrate formation at different silica concentrations; and the right four figures (a2)–(d2) show the water consumption by the capillary effect of the hydrate shell, $V_{\mathrm{w,cap}}$. It can be seen that both $V_{\mathrm{w,HW}}$ and $V_{\mathrm{w,cap}}$ decrease with time. For hydrate formation in "dry water" particle with 3-wt% silica, $V_{\mathrm{w,cap}}$ accounts only for 1% of $V_{\mathrm{w,HW}}$; however, in "dry water" particles with 5-wt% and 8-wt% silica, $V_{\mathrm{w,cap}}$ is about 10% of $V_{\mathrm{w,HW}}$. These small percentages reveal that the inward hydrate growth was faster than the outward growth, indicating that the gas diffusion through the hydrate shell was easier than the water permeation through the capillaries. It also indicates that for smaller particles, the capillary effect is more significant to the reaction kinetics.

The consideration of capillary effect, which is a novelty of this work, has the following importance: (1) many studies have assumed that each particle is expanding from water to gas hydrate for different gases; however they failed to explain how water is transported to the outer surface [160, 161]; in considering the capillary effect, we are able to explain how water is squeezed out through the hydrate shell. (2) if the capillary effect is ignored, all the water consumed will contribute to the hydrate formation at the hydrate–water interface, which will lead to a much higher value of diffusion coefficient in the modeling result. This is contradictory to the fact. For example, if the capillary effect in 8-wt% silica "dry water" is ignored, the calculated average effective diffusion coefficient will be 1.13×10^{-14} m^2s^{-1}, much lower than 3.46×10^{-14} m^2s^{-1} with the capillary effect considered. This reveals the importance of the inclusion of the capillary effect in the kinetic model. It should be noted that the actual hydrate growth does not proceed only in the radius direction. Inter-crosslinking of capillaries may cause water consumption in other directions, and the actual water consumption by the capillary effect may be higher.

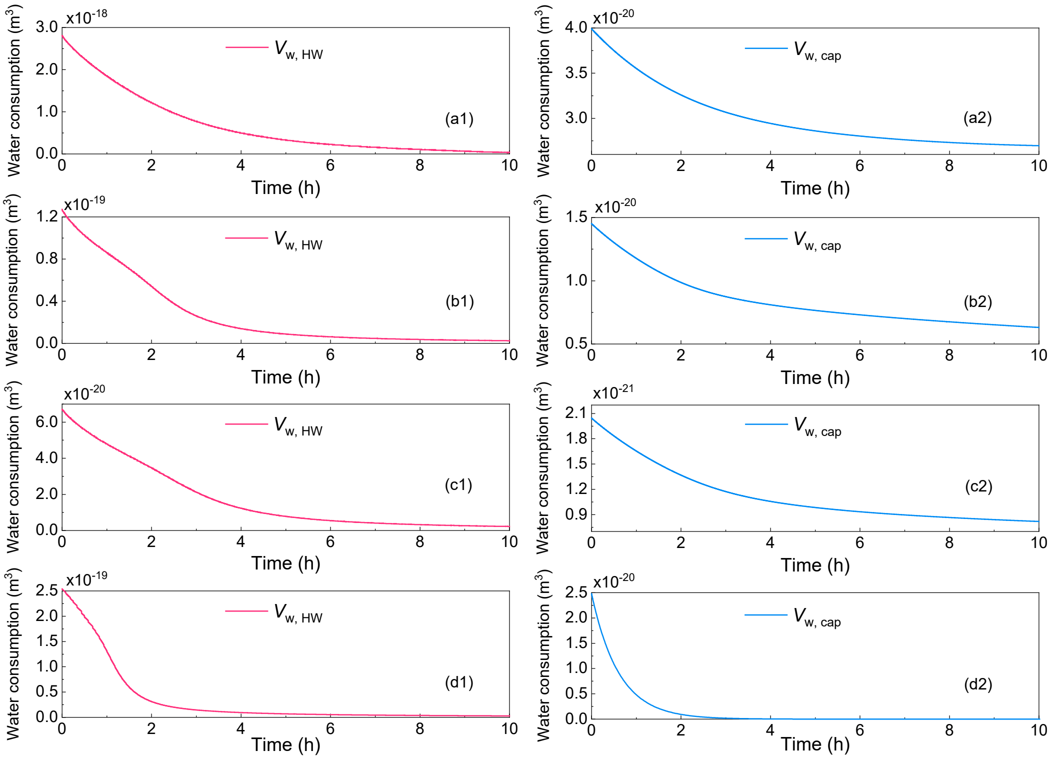

Figure 5.9. Water consumption at hydrate–water interface and by capillary effect in hydrate formation in "dry water": (a) CO_2 with 3-wt% silica; (b) CO_2 with 5-wt% silica; (c) CO_2 with 8-wt% silica; and (d) CH_4 with 5-wt% silica.

5.8.4 Heat transfer of hydrate formation in dry water

Since hydrate formation is an exothermic reaction, the heat release will cause a temperature gradient in the particle. A decoupled quasi-steady-state heat transfer model was developed to predict the temperature profile of the hydrate shell by processing the data from the aforesaid mass transfer models. The schematic diagram for heat transfer is shown in Figure 5.10. The heat released at the hydrate–water interface will be transferred to both the water phase and hydrate phase (indicated by the arrows). The other heat released at the hydrate–gas interface is instantaneously conducted to the gas phase and cooled by the water bath. The control volume of the heat transfer model is defined as the hydrate shell.

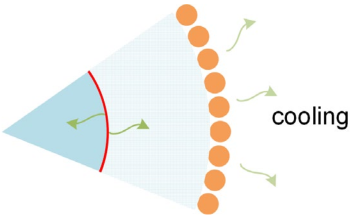

Figure 5.10. The schematic diagram for heat transfer at the hydrate–water interface.

The basic energy balance equation can be written in the form [162]

$$\frac{\partial\left(\rho c_{\mathrm{p}} T\right)}{\partial t}+\nabla\cdot\left(\rho \vec{\mathbf{u}} c_{\mathrm{p}} T\right)=-\nabla\cdot\vec{\mathbf{q}}_{\mathrm{cond}}+E\,, \tag{5.36}$$

where c_{P} is the specific heat capacity, T is the temperature profile of the control volume, t is time, $\vec{\mathbf{u}}$ is the velocity vector, $\nabla\cdot\vec{\mathbf{q}}_{\mathrm{cond}}$ is the heat conduction term and E is the heat source term.

The hydrate formation is considered as a quasi-steady state within each time step, and there is no heat convection in the particle. As hydrate formation occurs only on the hydrate–water interface, there is no heat generation within the control volume. Thus, Eq. (5.36) can be written as

$$\nabla\cdot\vec{\mathbf{q}}_{\mathrm{cond}}=0\,. \tag{5.37}$$

For the uniform growth of hydrate, the one-dimensional form of the heat conduction equation in spherical coordinates is written as

$$\frac{1}{r^2}\frac{\partial}{\partial r}\left(r^2\frac{\partial T}{\partial r}\right)=0\,, \tag{5.38}$$

where r is the radius.

Because heat released at the hydrate–water interface was conducted to the inner water phase and hydrate shell simultaneously, ignoring the convective heat transfer of inner water, we assume the temperature of inner water is uniform. Hence, the boundary conditions for both sides of the control volume at time t are expressed as

$$\begin{cases}\dfrac{\mathrm{d}Q}{\mathrm{d}t}=-\lambda_{\mathrm{H}}\dfrac{\partial T}{\partial r}4\pi r^2+\dfrac{4}{3}\pi r^3\rho_{\mathrm{w}}c_{\mathrm{p,w}}\dfrac{\partial T}{\partial t}, & r=r_{\mathrm{i}}\\ T=T_{\mathrm{exp}}, & r=r_{\mathrm{o}}\end{cases}\,, \tag{5.39}$$

where Q is the heat released at the hydrate–water interface, and λ_{H} is the thermal conductivity of the hydrate shell. The hydrate formation reaction is expressed as

$$\mathrm{M} + \beta\mathrm{H_2O} \longrightarrow \mathrm{M}\cdot\beta\mathrm{H_2O}\,,\ \Delta H_\mathrm{f} < 0\,, \tag{5.40}$$

where M is the gas, ΔH_f represents the enthalpy change during hydrate formation ($\Delta H_\mathrm{f} < 0$ for the exothermic process). The rate of heat released at the hydrate–water interface is thus expressed as

$$\frac{\mathrm{d}Q}{\mathrm{d}t} = -\Phi_{\mathrm{w,\,HW}}\frac{\Delta H_\mathrm{f}}{\beta}\,. \tag{5.41}$$

The analytical solution of Eq. (5.38) at time t can be obtained and coupled with Eqs. (5.39)–(5.41), and the temperature contours of the hydrate shell can be plotted.

After the optimal parameters of hydrate formation are obtained, the temperature profile in the hydrate shell can be calculated. Figure 5.11 presents the temperature contour in the CO_2 hydrate shell in an 8-wt% silica "dry water" particle at $t = 100$, 300 and 500 min. It can be seen that along with the formation, the temperature at the hydrate–water interface decreases due to the reduced heat released that results from the lowered gas uptake rate with time. The temperature at the hydrate–water interface represents the mean temperature of the inner water droplet in our models. The calculation results show that the temperature gradient at the initial 10 min just after the nucleation can be 10^{-1} K m^{-1}. After that, with the effective cooling by water bath, the temperature gradient is only 10^{-2} K m^{-1}, and the temperature increase in the hydrate shell is as low as 10^{-8} K in the stable hydrate growth period. In addition, the thermal conductivity of the hydrate shell (λ_H) is 0.584 W m^{-1}K^{-1} [163], almost the same as that of water (0.582 W m^{-1}K^{-1}) under experimental conditions. This proves that both our decoupled processing of the heat transfer model and the assumption of the homogenous temperature of inner water are reasonable. It also implies that the effect of heat released by the hydrate formation on kinetics is negligible in the presence of effective cooling.

As the temperature gradient is small during the hydrate formation in microparticles, and the heat released caused minor impacts, the heat transfer in silica gel particles will not be considered in the following discussions.

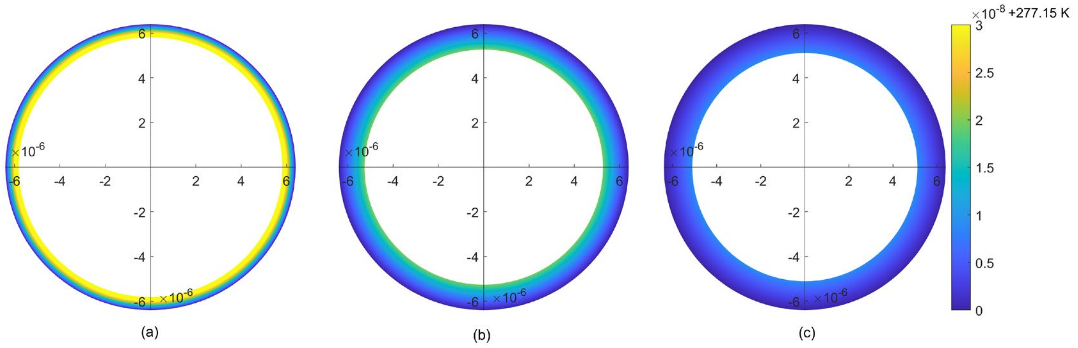

Figure 5.11. Temperature profile of CO_2 hydrate shell in "dry water" particle with 8-wt% silica at (a) $t = 100$ min; (b) $t = 300$ min; and (c) $t = 500$ min.

5.9 Simulation results of CO_2 hydrate formation in silica gels

5.9.1 Combined reaction rate constant

The simulated combined reaction rate constant, K^*, was in the range of 5.38–17.20×10^{-6} mol $m^{-2}MPa^{-1}s^{-1}$ for CO_2 hydrate formation in SGs in pure water systems in Table 5.2. The value of K^* is verified by a previous study reporting that the K^* of CO_2 hydrate formation in a bulk water system was 6.9–7.1×10^{-6} mol $m^{-2}MPa^{-1}s^{-1}$ with a stirring speed of 500 rpm based on the fugacity driving force [154]. It should be noted that both the unit and the value of K^* can be different when using another driving force in the model (e.g., concentration difference). The K^* of 100-nm SGs in this work is much higher than that in the literature, indicating a strong promotion effect in large SG pores.

With surfactant added to the system, K^* is much higher. When adding surfactants to 100-nm SG, K^* rises to 2.07–3.33×10^{-5} mol $m^{-2}MPa^{-1}s^{-1}$, over 1.9 times that without surfactants. The results of K^* show a great improvement effect by surfactants. As is mentioned in the above Chapters, the surfactants increase the mass transfer by reducing the surface tension; thus gas molecules quickly dissolve into the water, causing the improvement of K^*. In this work, it can be seen in Table 5.2 that for both SDS and DTAC, the higher the concentration of surfactants, the higher the value of K^*.

Furthermore, it is also found that K^* is lower in smaller pore sizes. As mentioned in the modeling strategies, the combined reaction rate constant K^* is a comprehensive performance of K_d and K_r. In this way, K_r relates to the rate when gas is encaged by water cages. The water–silica interactions will slow down the water–CO_2 interactions due to the hydrophilicity of the silica. This retardation will be more significant in smaller pores with more specific surface areas (58.39 m^2g^{-1} for 50-nm SG and 30.01 m^2g^{-1} for 100-nm SG), so that the limitation effect of K_r is stronger in smaller pores.

5.9.2 Effective diffusion coefficient

Figure 5.12 compares the effective diffusion coefficient of CO_2 through the hydrate shell (D_s) in SG pores, which is obtained from the constructed exponential function in Eq. (18). For all the studied cases, D_s decreases dramatically with time. The decrease in the first 200 min is rather rapid and becomes slower afterwards, indicating hindered gas–water mass transfer. The initial effective diffusion coefficients, $D_{s,0}$, of all the cases are very similar regardless of surfactants; however, the decreasing rates are different with varied surfactant concentrations. The decreasing rate of D_s is controlled by the reduction factor ξ. From both Table 5.2 and Figure 5.12, the reduction factor ξ is larger in the presence of surfactants, and the higher the concentration of surfactants, the higher value of ξ. This is evidenced by the fact that, when the water activity is extremely increased by more surfactants, the CO_2 hydrate shell forms more intensively, which, in turn, hinders CO_2 permeability to water in an earlier stage and thus slows down further hydrate formation [23]. In addition, ξ is also found higher in SGs with smaller pores, showing a more significant blockage in smaller pores.

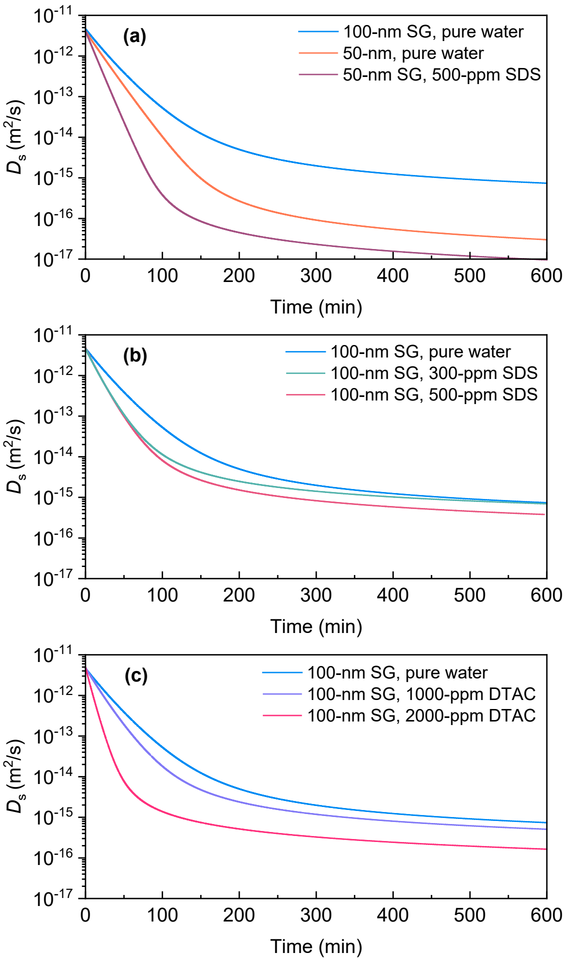

Figure 5.12. Effective diffusion coefficient of CO_2 through hydrate shell in SG pores.

5.9.3 Variation of hydrate shell radius

The hydrate shell thickness during CO_2 hydrate formation in a single SG is presented in Figure 5.13. It can be found in Figure 5.13 (a) that the hydrate shell thicknesses in 100-nm SGs grow rapidly at the beginning, and the growth rate gradually slows down. The radius of the inner water sphere does not change obviously after ~200 min in 50-nm SGs, indicating the end of hydrate formation. This is consistent with the gas uptake rate growth pattern found in Chapter 4. The results in Figure 5.13 (b) also show the further increase in the hydrate shell thickness in the presence of 300 and 500-ppm SDS in 100-nm SGs. SDS shows a rapid increase of hydrate shell thickness in the first 200 min.

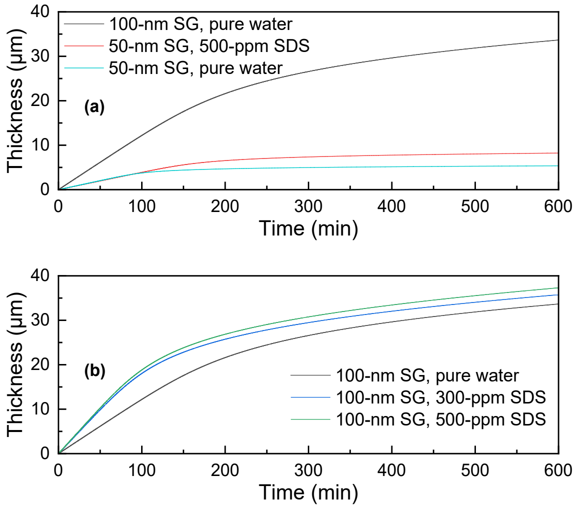

Figure 5.13. Hydrate shell thickness during CO_2 hydrate formation.

5.9.4 Water consumption by capillary effect

Figure 5.14 shows the water consumption by capillary effect in the porous hydrate shell formed ($V_{w,cap}$ in the left seven figures) and the total water consumption ($V_{w,total}$ in the right seven figures) at every moment during the CO_2 hydrate formation in the SG pores. It can be seen that both $V_{w,cap}$ and $V_{w,total}$ decrease with time in all systems. However, the ratio of $V_{w,cap}$ to $V_{w,total}$ is very small.

The proportion of water consumed by capillary effect to the total water consumption can be calculated from $V_{w,cap}/V_{w,total}$. Figure 5.15 shows the initial proportion of water consumed by capillaries at $t = 0$. For the 100-nm SG pure water system, the water consumed by capillary effect accounts for only ~1% of the total water consumed. With the addition of surfactants, the proportion increases to 19.8%–24.6% in 100-nm SGs. The proportion is higher in the SDS systems studied than that in DTAC systems, but it is not obviously affected by surfactant concentration. What stands out in the figure is that in the smaller pores of the 50-nm SG pure water system, the proportion is about 26.6%, and it increases to almost 74.9% in the presence of 500-ppm SDS. These results reveal that the capillary effect is more prominent in both smaller pores and in the presence of surfactants.

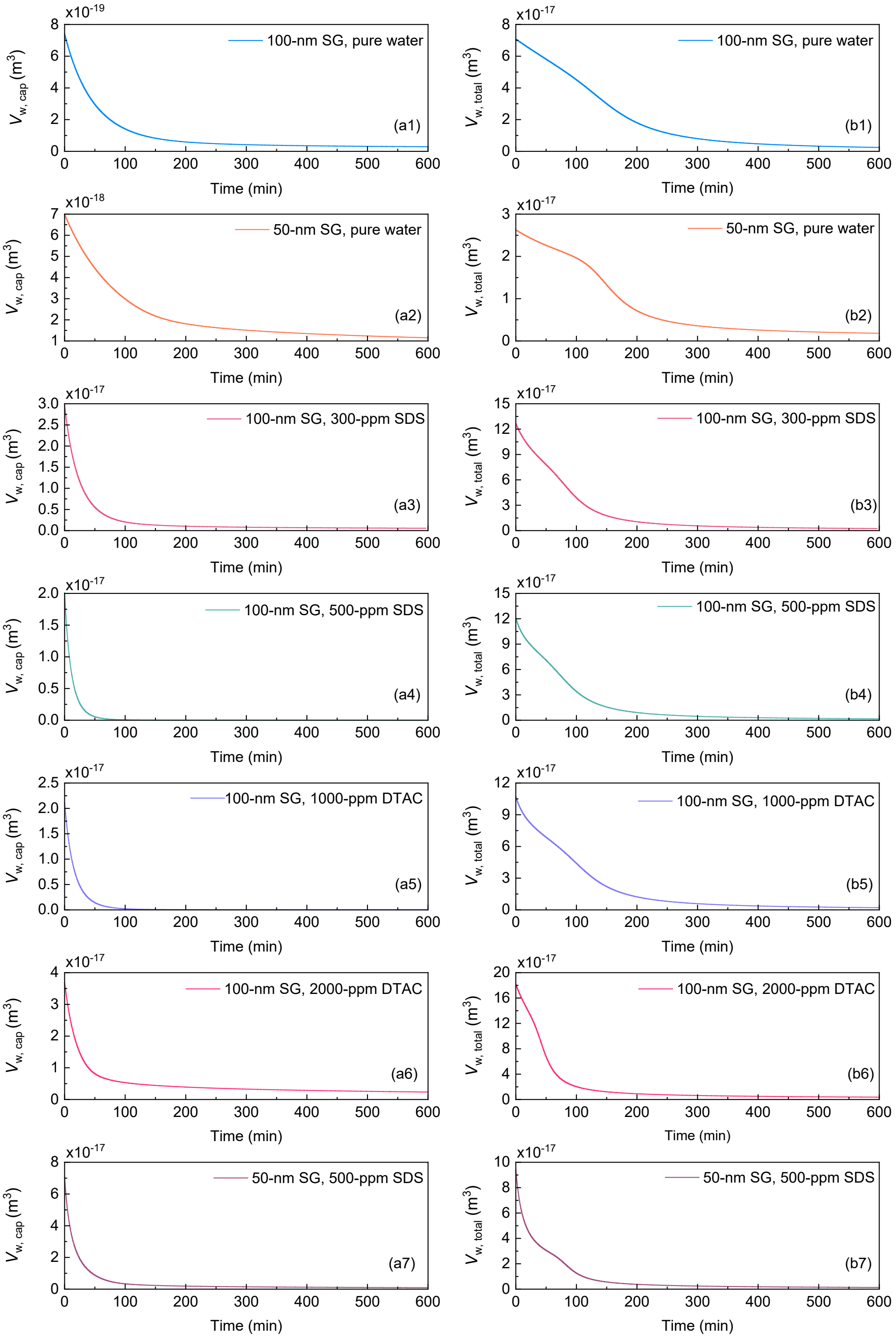

Figure 5.14. Water consumption during CO_2 hydrate formation in SG pores. (a1)–(a7) water consumed by capillary effect; (b1)–(b7) total water consumption.

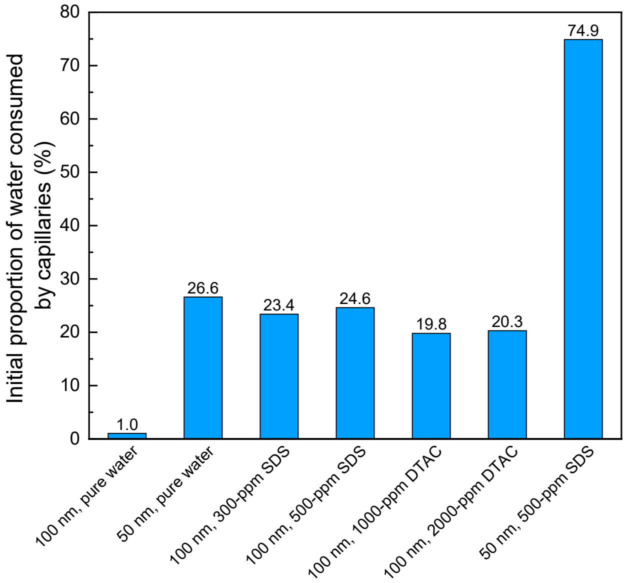

Figure 5.15. Initial proportion of water consumed by capillaries.

As can be seen in Table 5.2, the initial capillary structure parameter ($\varepsilon_{\text{cap},0}$) also increases over 30 times for both SDS or DTAC systems. The capillary structure parameter (ε_{cap}) is defined as

$$\varepsilon_{\text{cap}} = \frac{n_c r_c^3}{\tau} \frac{\sigma \cos\theta}{\mu_w}. \tag{5.42}$$

From Table 5.2, $\varepsilon_{\text{cap},0}$ is higher in the presence of surfactants, and the reduction factors ς are similar in all the cases, revealing a much higher ε_{cap} in surfactant cases than those in pure water cases. Compared with the pure water systems, when the surfactant is added, the surface tension (σ) will be reduced substantially, the viscosity (μ_w) will also be slightly increased, but the contact angle (θ) is reported to change little [164]. This means the term $\sigma \cos\theta / \mu_w$ is reduced when the surfactant is added. Thus, based on Eq. (6.11), the higher ε_{cap} in surfactant cases must be caused by an increased number of tubes (n_c) or radius of capillary tubes (r_c), or a reduced tortuosity of capillary tubes (τ) along with hydrate formation, as shown in Figure 5.16. It should be noted that Figure 5.16 is only indicative and the real distribution of capillaries in hydrates is random.

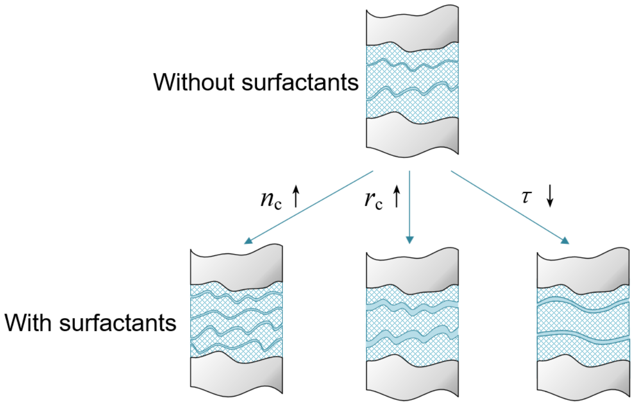

Figure 5.16. Indicative illustration of initial changes of capillaries with the addition of surfactants.

During the hydrate formation, although all of the three factors—the number, radius and tortuosity of the capillaries—are considered in Figure 5.16, it is speculated that the facts most likely to change are the number and radius of capillaries. The tortuosity of capillaries in the hydrate shell is unlikely to change much once an initial configuration is formed, as hydrate grows continuously and the hydrate shell is rigid. At a later stage, as the further formed hydrate in the capillary tubes becomes a blockage, the number and/or radius of capillaries will decrease dramatically and finally maintain a status similar to that of the systems without surfactants.

5.10 Simulation results of CO_2/N_2 hydrate formation in silica gels

5.10.1 Combined reaction rate constant

The combined reaction rate constant, K^*, quantifies the direction and rate of a chemical reaction. It is determined by the type of reaction and the experimental conditions. The definition of K^* is followed by the crystal growth theory of Karpiński and Englezos [4, 148], where the hydrate growth consists of two consecutive steps: Step 1, gas diffusion to the hydrate–liquid interface, and Step 2, gas adsorption into the structured water ("reaction") at the interface. The rate constants of the two steps are represented as K_d and K_r, respectively, and are related by the following equation

$$\frac{1}{K^*}=\frac{1}{K_\mathrm{d}}+\frac{1}{K_\mathrm{r}}. \tag{5.43}$$

In this case, the K_r relates to the rate at which encapsulating cages form. From Table 5.3, it can be seen that in pure water systems, the $K^*_{\mathrm{CO_2}}$ varies in a small range of 1.07–1.66×10^{-5} mol m^{-2}MPa^{-1}s^{-1} due to similar experimental conditions. However, it is also found that $K^*_{\mathrm{CO_2}}$ is lower in smaller pore sizes. This is because the water–silica interactions will slow down the process of water–CO_2 interactions due to the hydrophilicity of the silica. This retardation will be stronger in smaller pores with more specific surface areas where the confinement effect is stronger. Zhang et al. [160] also reported that the hydrate formation rate was controlled by the gas diffusion process (K_d) in smaller pores and was controlled by the reaction process (K_r) in larger pores. This implies that the diffusion is very fast in the larger pores, so K_d is more significantly affected by the pore size than is K_r.

Moreover, when DTAC is added to the system, $K^*_{\mathrm{CO_2}}$ increases to 1.80–5.24×10^{-5} mol m^{-2}MPa^{-1}s^{-1}. With a higher concentration of DTAC, a higher $K^*_{\mathrm{CO_2}}$ is obtained, indicating that DTAC, as a surfactant, increases the reaction rate by allowing CO_2 molecules to be transported in water more efficiently. Moreover, the addition of DTAC improves $K^*_{\mathrm{N_2}}$, which is more obvious with DTAC at a higher concentration, as in the case for CO_2. It should be noted that the calculation of K^* is based on a certain driving force in the model, and both the unit and the value of it can be different when using another driving force in the model. The driving force can be the difference of pressures, concentrations, and fugacities. Fugacity difference is used as the driving force in this work. The K^* in this work is much higher than that in the literature based on the same driving force, where CO_2 hydrate was formed in bulk water without any surfactant (6.9–7.1×10^{-6} mol m^{-2}MPa^{-1}s^{-1}) [154]. This proves that the reaction rate constant is greatly improved by DTAC.

5.10.2 Effective diffusion coefficient

As the hydrate shell grows thicker with time, it becomes more and more difficult for gases to diffuse through the hydrate shell, so the effective diffusion coefficient is controlled by a constructed function in this work. $D_{\mathrm{s},0}$ refers to the effective diffusion coefficient of gas molecules that are transported through the initially formed gas hydrate shell right after the induction period. Based on the optimal simulation results, the D_{s0,CO_2} regresses in the range of 4.6–4.8×10^{-10} m^2s^{-1} and D_{s0,N_2} regresses in the range of 7.6–8.4×10^{-12} m^2s^{-1}. It is considered that the formed hydrate shell at $t = 0$ has little difference under the same experimental temperature and pressure. Thus, it is reasonable to choose D_{s0,CO_2} and D_{s0,N_2} as constants of 4.7×10^{-10} m^2s^{-1} and 8.0×10^{-12} m^2s^{-1} in simulation, respectively, to reduce the freedom of the modeling. For comparison, the reported gas diffusion coefficient through the hydrate can be in a wide range of 10^{-12}–10^{-8} m^2s^{-1} under experimental conditions close to this work [157, 165]. The lower value of D_{s0,N_2} than for D_{s0,CO_2} in this work is due to the very low solubility of N_2 in water.

The initial effective diffusion coefficient D_{s0} and reduction factor ξ together control the gas diffusion through the hydrate shell. As defined, a larger ξ value results in a faster decrease in the diffusion coefficient. It can be seen in Table 6.3 that in the pure water systems, smaller SG pores lead to a higher ξ_{CO_2} and ξ_{N_2}. This means that in smaller pores, the diffusion coefficient of gas drops more rapidly. ξ is reduced with more DTAC added, which also shows that DTAC can help gas molecules diffuse into the water through the hydrate shell more efficiently.

Figure 5.17 shows the change of D_{s,CO_2} with PWC in 100-nm SGs. It is found that the D_{s,CO_2} decreases dramatically with an increased PWC, and the decreasing rate drops as the PWC value increases. PWC represents how much water is hydrated, reflecting the progress of the hydration reaction. D_{s,CO_2} is a fixed value for a certain material if its density does not change. It decreases when the proportion of the hydrate in the shell region increases and the shell becomes more compact, with more water being converted into hydrates during the hydrate formation. This is because that the hydrate shell is composed of solid hydrate and a small amount of liquid water. Mori and Mochizuki [145] considered the shell a permeable plate, where capillaries provided transport channels for water so that the outer surface could always be wet. The water in these capillaries also participates in the hydrate formation, resulting in thinner or more tortuous capillaries or fewer capillaries with increased PWC [166]. Therefore, D_{s,CO_2} decreases with an increased PWC, indicating that gas molecules diffuse through the shell less easily. This is also the reason we use the effective diffusion coefficient rather than the bulk diffusion coefficient for the porous hydrate shell. Considering the shape and size of the capillaries are not homogeneous, the effective diffusion coefficient and the bulk diffusion coefficient have the following relationship with the porosity and tortuosity in hydrates [167, 168]:

$$\frac{D_s}{D_{\mathrm{s,bulk}}} = \frac{\varphi}{\tau}, \tag{5.44}$$

where D_{s} is the effective diffusion coefficient, $D_{\mathrm{s,bulk}}$ is the bulk diffusion coefficient, φ is the porosity of the hydrate shell, and τ is the tortuosity of capillaries in the hydrate shell. On the other hand, it can be seen from Figure 6.15 that $D_{\mathrm{s,CO_2}}$ is higher with a higher DTAC concentration. This may be because the porosity of the hydrate shell φ is higher and/or the tortuosity of capillaries τ is lower since there is more DTAC in the system.

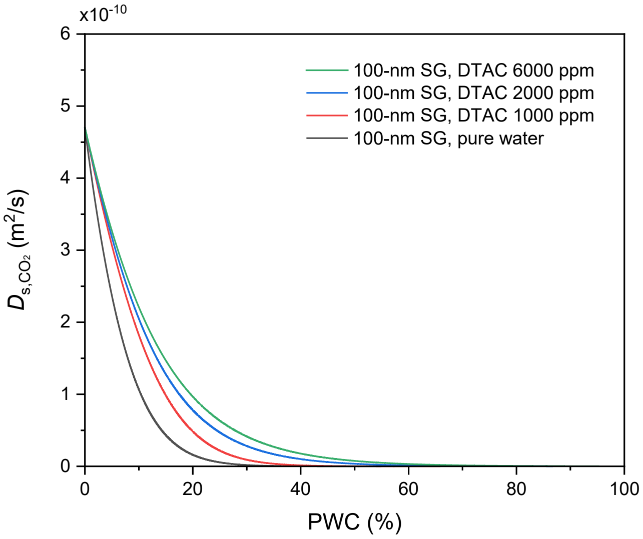

Figure 5.17. Effective diffusion coefficient of CO_2 through the hydrate shell with percent water conversion.

5.10.3 Variation of hydrate shell radius

Figure 5.18 shows the radius change during the hydrate formation in 600 min. The dashed lines indicate the initial radius of the SG particle. The lines above the dashed lines represent the outer radius (r_{o}), and the ones below indicate the inner radius (r_{i}) of the spherical SG particle after hydrate growth. It can be seen in all the systems of Figure 5.18 that the hydrate shell thicknesses grow rapidly at the beginning and the growth rate gradually slow down later on. In Figure 5.18 (a), the hydrate shell grows thicker in SGs with larger pores but tends to remain unchanged after 300 min, indicating that the hydrate growth has almost ceased. In Figure 5.18 (b), a higher concentration of DTAC results in a thicker hydrate shell, showing the same trend of gas uptake in Chapter 4. Moreover, the hydrate shell thickness in the 6000-ppm DTAC was more than double that in the 1000-ppm DTAC, showing a significant promotion by DTAC on the PWC.

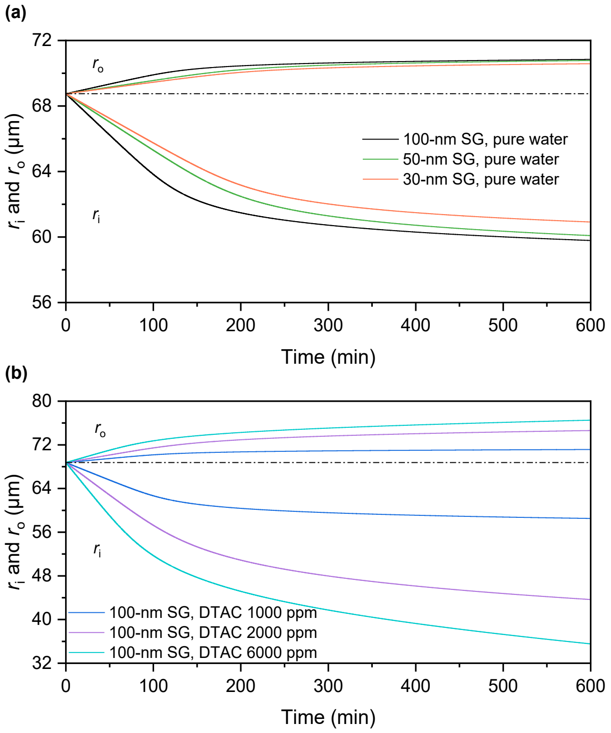

Figure 5.18. Radius change of hydrate shell during the gas hydrate formation. (a) in pure water systems; (b) in 100-nm SGs.

5.11 Summary

In this chapter, numerical studies of CO_2 and CO_2/N_2 hydrates formation kinetics in "dry water" microparticles and silica gel (SG) pores have been implemented based on the advanced shrinking core model (SCM). The model of the hydrate growth mechanism was based on the work of Englezos, in which the hydrate growth consisted of two consecutive steps: diffusion of dissolved gas to the hydrate–water interface and "reaction" at the interface (actually gas encaged by water cages). Compared with previous models, the dissolved CO_2 and capillary effect of the porous hydrate shell were specially considered in this model. Key parameters, including the effective diffusion coefficient, water consumption in capillaries, and hydrate shell thickness, were found. For the CO_2 hydrate formation in "dry water" particles, the modeling results fit the experimental data well with a high agreement, evidenced by the small mean absolute percentage error in the range of 2.11%–4.74%. During the gas hydrate formation, the thickness of the hydrate shell increased quickly at first and then slowed down. The effective gas diffusion coefficient through the shell decreased more dramatically in larger particles, with the average value in a range of $1.27–3.46\times10^{-14}$ m^2s^{-1}. The water consumed in the capillaries was less than 10% of the water consumed at the hydrate–water interface, and it was found to be more dominant in smaller particles. In addition, a decoupled quasi-steady-state heat transfer model was developed to quantify the effect of heat released on kinetics. The results showed that the temperature gradient in the hydrate shell is only 10^{-2} K m^{-1}, revealing that the impact of heat transfer on gas hydrate formation kinetics in microparticles was negligible.

For the CO_2 hydrate formation in SG pores, the surfactants SDS and DTAC were added as kinetic promoters. The simulation results revealed that when surfactants or larger pores exist, the combined reaction rate constant increases. The effective diffusion coefficient dropped dramatically in all cases, but the initial diffusion coefficients were very close. The reduction factor of the diffusion coefficient was higher in small pores or in the presence of surfactants, which resulted in a more marked decrease in the diffusion coefficient. The initial water consumed by the capillary effect was more prominent in smaller pores, that is, about 1% and 26.6% in 100-nm and 50-nm SGs, respectively. In the presence of surfactants, the initial proportion of water consumed by the capillary effect even rose up to 74.9% in smaller pores. Based on the modeling of capillary structure, it was likely to be due to the increased number of capillaries with larger radii formed in the presence of surfactants.

For the CO_2/N_2 hydrates formation in SG pores in the presence of DTAC, the SCM was established to investigate the roles of CO_2 and N_2 in hydrate formation and to reveal the effects of DTAC in hydrate formation. Based on the simulation results, the higher concentration of DTAC, the higher the reaction rate constant, indicating that DTAC increased the reaction rate by allowing both CO_2 and N_2 molecules to be transported in water more efficiently. The lower reaction rate constant in smaller pores indicated that the diffusion rate constant changed with pore size more rapidly than the reaction rate constant. The dramatic decreasing trend of the effective diffusion coefficient reflected the higher porosity of the hydrate shell with more DTAC added. The establishment of SCM for hydrate formation in microparticles provided a detailed analysis of the complex hydrate formation mechanism in nanopores. These findings contributed to the understanding of the roles of pores, DTAC, and N_2 in hydrate formation kinetics, and provided a basis for the improvement of the kinetics and separation performance of hydrate-based carbon capture. This chapter is of great value in developing hydrate formation mechanisms in other porous materials.

Chapter 6 Conclusions and outlook

6.1 Summary and conclusions

This thesis aims at investigating mechanisms of promoting carbon dioxide (CO_2) hydrate formation for effective carbon capture application. Both experimental work and a numerical study on mass transfer enhancement have been implemented in this thesis. Chemical promoters and porous materials were used to enhance the mass transfer. Comprehensive kinetics models for hydrate growth were built to investigate the detailed theoretical basis for the improvement of kinetics. The simulation results further analyzed the factors affecting the rapid formation of hydrates, which guided the practical application of hydrate-based carbon capture (HBCC).

The promotion experiments of CO_2 hydrate formation were divided into thermodynamic and kinetic promotion in the presence of tetra-*n*-butyl ammonium bromide (TBAB) and kinetic promotion in microparticles. In Chapter 2, the thermodynamic promotion of CO_2–TBAB semiclathrate hydrate formation was investigated. Three kinds of surfactants, namely anionic surfactant sodium dodecyl sulfate (SDS), cationic surfactant dodecyltrimethylammonium chloride (DTAC), and non-ionic surfactant Tween 80 (T-80), were added in the system to offset the low gas uptake yields of semiclathrate hydrates. The kinetic promotion experiments on CO_2 hydrate formation in “dry water” microparticles and silica gel (SG) pores were described in Chapter 3, and the combined effects of surfactants and SG pores were studied in Chapter 4. Later in Chapter 5, an advanced shrinking core model (SCM) was established to study the gas hydrates formation kinetics in microparticles. The detailed simulation results of CO_2 hydrate formation kinetics are also summarized in Chapter 5.

The thermodynamic promotion experiments on CO_2 hydrate formation were studied in TBAB solution. TBAB is known as a thermodynamic promoter to moderate the CO_2 semiclathrate hydrates formation conditions, but it reduces the gas uptake. The kinetics of CO_2 semiclathrate hydrate formation was studied in a batch reactor for carbon capture from CO_2/N_2 mixtures in the presence of various concentrations of surfactants with TBAB. Considering the trade-off of phase equilibrium temperature and gas uptake yield, 10-wt% TBAB was used as a thermodynamic promoter for CO_2 hydrates formation at constant temperature. The combined effects of surfactants and TBAB on the induction time, gas uptake, split fraction and separation factor were investigated experimentally. The results showed that in 10-wt% TBAB systems, DTAC at 1000–6000 ppm overall had better reduction effects on induction time than SDS at 500–1500 ppm; while SDS performed better than DTAC to accelerate hydrate growth. The system of TBAB with 6000-ppm DTAC showed the highest split fraction and separation factor of CO_2. In both TBAB systems with SDS at 500 ppm and DTAC at 1000 ppm, the CO_2 uptake increased overall with increased subcooling.

The results also showed that the induction time is significantly reduced by T-80 in semiclathrate hydrates and clathrate hydrates (with or without TBAB). The initial gas uptake rate increased with the increased concentration of T-80, which resulted in a higher gas uptake in the early formation period for both hydrates. After the initial growth period, CO_2 uptakes increased continuously in clathrate hydrates. However, in semiclathrate hydrates, gas uptake became constant at the end of the intensive gas uptake period. Both 1000-ppm and 2000-ppm T-80 can improve the gas uptakes in semiclathrate hydrates, while 3000-ppm T-80 produced an inhibition effect. In addition, the percent water conversion of TBAB+T-80 2000-ppm system reached 80% of the total value within one-third of the entire test period, while that of the best water system (T-80 1000 ppm) only achieved 35% over the same test period.

In addition, to shorten the process duration for energy saving, the intensive uptake period was defined to recommend a reasonable practical operation time of HBCC. Based on the above conclusions, thermodynamic promoters alone cannot achieve a satisfactory CO_2 gas uptake by HBCC. The kinetic promotion effects of "dry water" and SG on CO_2 hydrate formation were further studied experimentally. “Dry water” particles prepared by mixing hydrophobically modified silica and water were used to create micro-size droplets of water. The hydrate formation in “dry water” with 8-wt% silica represented the highest normalized gas uptake due to its smallest particle size. A clear layer of bulk water above the “dry water” can be seen, indicating that “dry water” structures were broken after cycles. From the fresh cycle to Repeat 1, the gas uptake yield was reduced by 29.0%–59.3%; a further reduction from the fresh cycle to Repeat 2 was by nearly 70%. However, no obvious fragmentation of SGs was found. Overall, SGs showed better stability and promotion effect than “dry water” on CO_2 hydrate formation kinetics.

The effects of surfactants on CO_2 hydrate formation kinetics in SGs were studied in both pure CO_2 systems and CO_2/N_2 gas mixture systems. SGs with 30, 50 and 100-nm pore sizes were used as frameworks for hydrate formation. SDS and DTAC surfactants were added as kinetic promoters. Both gas uptake yield and gas uptake rate were greatly improved in SGs with larger pores. With the addition of surfactants in 100-nm SGs, SDS systems saved up to 23.7%–49.3% time to achieve the same amount of gas uptake, while DTAC systems saved 16% of the time. In CO_2/N_2 gas mixture systems, DTAC was used to improve the CO_2 separation performance. The final CO_2 concentration in gas phase decreased from 70 mol% to 32.6 mol%, showing a significant improvement in both split fraction and separation factor. Overall, the combined effects of surfactants SDS and DTAC on CO_2 hydrate formation in SG pores improved CO_2 gas uptake yield and rate while maintaining high separation performance.

To further investigate the intrinsic formation kinetics, an SCM was established to study the gas hydrates formation kinetics in microparticles. The model of the hydrate growth mechanism was based on the work of Englezos, in which the hydrate growth consists of two consecutive steps: diffusion of dissolved gas to the hydrate–liquid interface and "reaction" at the interface. Compared with previous models, the dissolved CO_2 and capillary effect of the porous hydrate shell were specially considered in this model. Key parameters, including effective diffusion coefficient, water consumption in capillaries, hydrate shell thickness in CO_2 hydrate formation were included in the model. The establishment of this SCM for hydrate formation in microparticles provided a detailed analysis of the complex hydrate formation mechanism, and was of great value in developing hydrate formation mechanisms in other porous materials.

For the CO_2 hydrate formation in "dry water" particles, the modeling results fit the experimental data well with a high agreement, evidenced by the small mean absolute percentage error in the range of 2.11%–4.74%. During the gas hydrate formation, the thickness of the hydrate shell increased quickly at first and then slowed down. The effective gas diffusion coefficient through the shell decreased more dramatically in larger particles, with the average value in a range of $1.27–3.46\times10^{-14}$ m^2s^{-1}. The water consumed in capillaries was less than 10% of the water consumed at the hydrate–water interface, and it was found to be more dominant in smaller particles. In addition, a decoupled quasi-steady-state heat transfer model was developed to quantify the impact of heat released on kinetics. The results showed that the temperature gradient in the hydrate shell was only 10^{-2} K m^{-1}, revealing that the impact of heat transfer on gas hydrate formation kinetics in microparticles is negligible.

For the CO_2 hydrate formation in SG pores, the simulation results revealed that when surfactants or larger pores exist, the combined reaction rate constant increased. The effective diffusion coefficient dropped dramatically in pores, but the initial diffusion coefficients were very close. The reduction factor of the diffusion coefficient was higher in small pores or in the presence of surfactants, which will result in a more marked decrease in the diffusion coefficient. The initial water consumed by capillary effect was more prominent in smaller pores, that is, about 1% and 26.6% in 100-nm and 50-nm SGs, respectively. In the presence of surfactants, the initial proportion of water consumed by capillary effect even rose up to 74.9% in smaller pores. Based on the modeling of capillary structure, it was likely to be due to the increased number of capillaries with larger radii formed in the presence of surfactants.

The roles of N_2 in CO_2/N_2 hydrates formation and the effects of DTAC in CO_2 separation were further investigated by SCM. CO_2 and N_2 were found to compete in occupying 5^{12} cages. Based on the simulation results, the higher the concentration of DTAC, the higher the reaction rate constant, indicating that DTAC increased the reaction rate by allowing both CO_2 and N_2 molecules to diffuse in water more efficiently. The lower reaction rate constant in smaller pores indicated that the diffusion rate constant changed with pore size more strongly than the reaction rate constant. The dramatic decreasing trend of the effective diffusion coefficient reflected the higher porosity of the hydrate shell with more DTAC added.

This work enhanced the understanding of the transport phenomena of gas molecules and helped to extend the knowledge of gas separation and surfactants in hydrate formation. The findings in this work mathematically described the complex gas hydrate formation, contributed to understanding the mechanism of the roles of pores, surfactants, and N_2 in hydrate formation kinetics, and provided a basis for the improvement of the kinetics and separation performance in HBCC.

6.2 Outlook

In the experiments of CO_2 hydrate formation in TBAB solutions, the low gas consumption was due to the blockage of rapid formation of CO_2–TBAB semiclathrate hydrates. However, the difference between the actual macroscopic structure of semiclathrate and clathrate hydrates is still unclear. The influence of semiclathrate hydrate structure on diffusion coefficient is hard to determine. This brings the challenge of applying SCM to the CO_2–TBAB semiclathrate hydrate formation. So, future work is suggested on the mechanism of the blockage through morphology studies and the comparison of TBAB with other thermodynamic promoters in their blockage effects in the absence of agitation. In addition, the interactions between the surfactant micelles and semiclathrate hydrates are also unclear. Although this work tried to reveal the effects of surfactants on hydrate formation, the intrinsic interactions of different ionic surfactants and CO_2 should also be studied. Further studies are needed to identify the effects of surfactant micelles on the kinetics of CO_2–TBAB hydrate formation.

The SCM in this work was well applied to the hydrate formation in “dry water” and SG pores, but it can also be applied to other porous materials where the water geometry is spherical, for example, the hydrate formation in silica sands or even in bulk water. The corresponding gas diffusion and capillary effect should consider the effect of porous materials on gas and water. Future SCM is also suggested to distinguish and compare the capillary effect caused by SG pores and hydrate shell capillaries. Future work is also suggested to simulate the repeated runs to interpret the reason for degradation and apply the models to gas hydrate formation in other porous particles.

The SG used in this work was hydrophilic, but the effect of the hydrophilic group on CO_2 and water moleculars was ignored in this SCM. Whether the porous characteristic and hydrophilic group will affect the CO_2 dissolution and water conversion should be further studied. This complex interaction can not be simply revealed by SCM. It may need more observation of experiments on the nano scale. Thus, future work is also suggested to involve the porous characteristic of hydrate shells and the interactions between water–CO_2 and water–silica through molecular dynamics simulations.

From the perspective of practical application of HBCC, the CO_2 recovery rates in these experiments were only about 50%, which was lower than that of the traditional CCS method. Multi-stage HBCC separation can effectively increase the recovery rate to over 90%. Combined with other traditional separation methods or solar-driven cooling methods, the economics and energy efficiency of HBCC can be significantly improved.

Appendix A Two-film theory and population balance

A.1 Introduction

The two-file theory and population balance were introduced and developed in the previous classic kinetic modeling of Englezos et al. [4]. From the available models to describe the phenomena occurring when a gas phase is brought into contact with a liquid phase, the two-film theory was also adopted in this work. Assuming quasi-steady-state conditions, the accumulation term in the liquid film can be neglected, and hence the mass balance for the gas in the film in a slice of thickness and unit cross-sectional area is produced [169]. The two-film theory and population balance are important components of Englezos' models. This appendix provides a detailed derivation of the models.

A.2 Homogeneous reaction rate and two-film theory

The homogeneous reaction rate is used to formulate a global reaction rate for all the nuclei particles in the hydrate formation. The reaction rate per nucleation particle for all nuclei particles of any size is integrated as

$$\begin{aligned} R_y(t) &= \int_0^\infty \left(\frac{\mathrm{d}n}{\mathrm{d}t}\right)_\mathrm{P} \phi(r,t)\,\mathrm{d}r \\ &= \int_0^\infty K^* A_\mathrm{P}\left(f - f_\mathrm{eq}\right)\phi(r,t)\,\mathrm{d}r \\ &= 4\pi K^* \mu_2 \left(f - f_\mathrm{eq}\right) \\ &= K\left(f - f_\mathrm{eq}\right) \end{aligned} \tag{A.1}$$

where $\phi(r,t)$ is the crystal size distribution (m^{-4}), μ_2 is the second moment of particle size distribution (PSD) given by

$$\mu_2=\int_0^\infty r^2\phi(r,t)\mathrm{d}r\,. \tag{A.2}$$

Here the n-th moment of PSD is defined as

$$\mu_n=\int_0^\infty r^n\phi(r,t)\mathrm{d}r\ (\mathrm{m^n/m^3}). \tag{A.3}$$

Figure A.1 shows the schematic diagram of the gas diffusing through the water film. Based on Fick's first law, the diffusion flux is expressed as

$$J_\mathrm{A}=-D_\mathrm{AB}\cdot\frac{\mathrm{d}c}{\mathrm{d}y}\,. \tag{A.4}$$

The difference of diffusion flux is

$$J_\mathrm{in}-J_\mathrm{out}=R_y(t)\cdot\mathrm{d}y\,. \tag{A.5}$$

Couple Eqs. (A.1) to (A.5),

$$J_\mathrm{in}-J_\mathrm{out}=J_\mathrm{in}-\left(J_\mathrm{in}+\frac{\partial J}{\partial y}\cdot\mathrm{d}y\right)=-\frac{\partial J}{\partial y}\cdot\mathrm{d}y=D_\mathrm{AB}\frac{\mathrm{d}^2c}{\mathrm{d}y^2}\cdot\mathrm{d}y\,. \tag{A.6}$$

Thus, the relation between concentration and fugacity is obtained

$$D\frac{\mathrm{d}^2c}{\mathrm{d}y^2}=K\left(f-f_\mathrm{eq}\right). \tag{A.7}$$

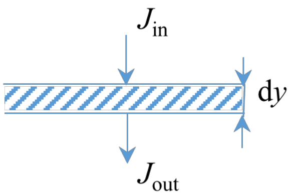

Figure A.1. Schematic diagram of gas dissolved through the film.

Based on Henry's law, the fugacity can be written as a function of gas concentration

$$f = H\frac{c}{c_{\mathrm{w0}}}, \tag{A.8}$$

And thus, we can get

$$D^*\frac{\mathrm{d}^2Y}{\mathrm{d}y^2} = KY, \tag{A.9}$$

where $Y = f - f_{\mathrm{eq}}$ and $D^* = \dfrac{Dc_{\mathrm{w0}}}{H} = \dfrac{Dc}{f}$.

Figure A.2 shows the schematic diagram of the two-film theory. The boundary condition of Eq. (A.9) are

$$\begin{cases} Y = f_{\mathrm{g}} - f_{\mathrm{eq}}, & y = 0 \\ Y = f_{\mathrm{b}} - f_{\mathrm{eq}}, & y = y_{\mathrm{L}} \end{cases}, \tag{A.10}$$

and Eq. (A.9) can also be reformed as

$$\frac{\mathrm{d}^2Y}{\mathrm{d}y^2} = \frac{K}{D^*}Y. \tag{A.11}$$

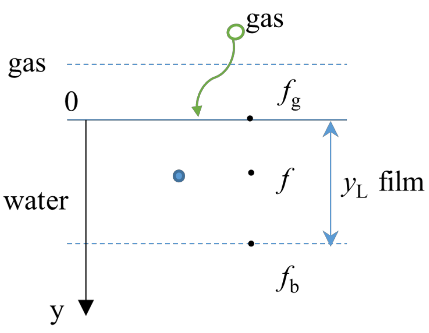

Figure A.2. Schematic diagram of two-film theory.

The characteristic equation of Eq. (A.11) is

$$Y'' - \frac{K}{D^*}Y = 0, \tag{A.12}$$

$$r^2 - \frac{K}{D^*} = 0. \tag{A.13}$$

The roots are $r = \pm\sqrt{\dfrac{K}{D^*}}$. The general solution of (A.13) is

$$Y = c_1 e^{\sqrt{K/D^*}y} + c_2 e^{-\sqrt{K/D^*}y}. \tag{A.14}$$

With boundary conditions, we can obtain

$$\begin{cases} c_1 + c_2 = Y_1 \\ c_1 e^{\sqrt{K/D^*}y_\mathrm{L}} + c_2 e^{-\sqrt{K/D^*}y_\mathrm{L}} = Y_2 \end{cases}, \tag{A.15}$$

$$c_1 e^{\sqrt{K/D^*}y_\mathrm{L}} + c_2 e^{\sqrt{K/D^*}y_\mathrm{L}} = Y_1 e^{\sqrt{K/D^*}y_\mathrm{L}}, \tag{A.16}$$

$$c_2\left(e^{\sqrt{K/D^*}y_\mathrm{L}} - e^{-\sqrt{K/D^*}y_\mathrm{L}}\right) = Y_1 e^{\sqrt{K/D^*}y_\mathrm{L}} - Y_2, \tag{A.17}$$

Thus we can derive

$$c_2 = \frac{Y_1 e^{\sqrt{K/D^*}y_\mathrm{L}} - Y_2}{e^{\sqrt{K/D^*}y_\mathrm{L}} - e^{-\sqrt{K/D^*}y_\mathrm{L}}} = \frac{2}{\sinh\left(\sqrt{K/D^*}\,y_\mathrm{L}\right)}\left(Y_1 e^{\sqrt{K/D^*}y_\mathrm{L}} - Y_2\right), \tag{A.18}$$

$$c_1 = Y_1 - c_2 = \frac{Y_2 - Y_1 e^{-\sqrt{K/D^*}y_\mathrm{L}}}{e^{\sqrt{K/D^*}y_\mathrm{L}} - e^{-\sqrt{K/D^*}y_\mathrm{L}}} = \frac{2}{\sinh\left(\sqrt{K/D^*}\,y_\mathrm{L}\right)}\left(Y_2 - Y_1 e^{-\sqrt{K/D^*}y_\mathrm{L}}\right). \tag{A.19}$$

The Hatta number is defined as reaction rate over diffusion rate, written as

$$\gamma = y_\mathrm{L}\sqrt{\frac{K}{D^*}} = \sqrt{\frac{4\pi K^* \mu_2}{D^*}}, \tag{A.20}$$

so that c_1 and c_2 can be written as

$$c_1 = \frac{2}{\sinh\gamma}\left(f_\mathrm{b} - f_\mathrm{eq} - f_\mathrm{g} e^{-\gamma} + f_\mathrm{eq} e^{-\gamma}\right), \tag{A.21}$$

$$c_2 = \frac{2}{\sinh\gamma}\left(f_\mathrm{g} e^{\gamma} - f_\mathrm{eq} e^{\gamma} - f_\mathrm{b} + f_\mathrm{eq}\right). \tag{A.22}$$

The solution of the characteristic equation is

$$\begin{aligned}
Y &= c_1 e^{\sqrt{K/D^*}\, y_{\mathrm{L}} \frac{y}{y_{\mathrm{L}}}} + c_2 e^{-\sqrt{K/D^*}\, y_{\mathrm{L}} \frac{y}{y_{\mathrm{L}}}} \\
&= c_1 e^{\gamma \frac{y}{y_{\mathrm{L}}}} + c_2 e^{-\gamma \frac{y}{y_{\mathrm{L}}}} \\
&= \frac{2}{\sinh \gamma}\left(f_{\mathrm{b}} e^{\gamma \frac{y}{y_{\mathrm{L}}}} - f_{\mathrm{eq}} e^{\gamma \frac{y}{y_{\mathrm{L}}}} - f_{\mathrm{g}} e^{\gamma\left(\frac{y}{y_{\mathrm{L}}}-1\right)} + f_{\mathrm{eq}} e^{\gamma\left(\frac{y}{y_{\mathrm{L}}}-1\right)} + f_{\mathrm{g}} e^{\gamma\left(1-\frac{y}{y_{\mathrm{L}}}\right)} - f_{\mathrm{eq}} e^{\gamma\left(1-\frac{y}{y_{\mathrm{L}}}\right)} - f_{\mathrm{b}} e^{-\gamma \frac{y}{y_{\mathrm{L}}}} + f_{\mathrm{eq}} e^{-\gamma \frac{y}{y_{\mathrm{L}}}} \right) \\
&= \frac{1}{\sinh \gamma}\left[f_{\mathrm{g}} \sinh\left(\gamma\left(1-\frac{y}{y_{\mathrm{L}}}\right)\right) - f_{\mathrm{eq}} \sinh\left(\gamma\left(1-\frac{y}{y_{\mathrm{L}}}\right)\right) + f_{\mathrm{b}} \sinh\left(\gamma \frac{y}{y_{\mathrm{L}}}\right) - f_{\mathrm{eq}} \sinh\left(\gamma \frac{y}{y_{\mathrm{L}}}\right) \right] \\
&= \frac{1}{\sinh \gamma}\left[\left(f_{\mathrm{g}} - f_{\mathrm{eq}}\right) \sinh\left(\gamma\left(1-\frac{y}{y_{\mathrm{L}}}\right)\right) + \left(f_{\mathrm{b}} - f_{\mathrm{eq}}\right) \sinh\left(\gamma \frac{y}{y_{\mathrm{L}}}\right) \right]
\end{aligned} \tag{A.23}$$

Thus, we can write

$$f = f_{\mathrm{eq}} + \left[\left(f_{\mathrm{g}} - f_{\mathrm{eq}}\right) \sinh\left(\gamma\left(1-\frac{y}{y_{\mathrm{L}}}\right)\right) + \left(f_{\mathrm{b}} - f_{\mathrm{eq}}\right) \sinh\left(\gamma \frac{y}{y_{\mathrm{L}}}\right) \right]\left(\frac{1}{\sinh \gamma}\right). \tag{A.24}$$

The rate of the number of moles of gas is expressed as

$$\frac{\mathrm{d}n}{\mathrm{d}t} = J\big|_{y=0} \cdot A_{(\mathrm{g-l})} = -D\left(\frac{\mathrm{d}c}{\mathrm{d}y}\right)\bigg|_{y=0} \cdot A_{(\mathrm{g-l})} = -D^*\left(\frac{\mathrm{d}f}{\mathrm{d}y}\right)\bigg|_{y=0} \cdot A_{(\mathrm{g-l})}, \tag{A.25}$$

Substitution of Eq. (A.24) into Eq. (A.25) yields

$$\frac{\mathrm{d}f}{\mathrm{d}y} = \left[-\left(f_{\mathrm{g}} - f_{\mathrm{eq}}\right) \cosh\left(\gamma\left(1-\frac{y}{y_{\mathrm{L}}}\right)\right)\frac{\gamma}{y_{\mathrm{L}}} + \left(f_{\mathrm{b}} - f_{\mathrm{eq}}\right) \cosh\left(\gamma \frac{y}{y_{\mathrm{L}}}\right)\frac{\gamma}{y_{\mathrm{L}}} \right]\left(\frac{1}{\sinh \gamma}\right) \tag{A.26}$$

and

$$\frac{\mathrm{d}f}{\mathrm{d}y}\bigg|_{y=0} = \left[-\left(f_{\mathrm{g}} - f_{\mathrm{eq}}\right) \cosh \gamma \frac{\gamma}{y_{\mathrm{L}}} + \left(f_{\mathrm{b}} - f_{\mathrm{eq}}\right) \frac{\gamma}{y_{\mathrm{L}}} \right]\left(\frac{1}{\sinh \gamma}\right), \tag{A.27}$$

Thus, we can obtain

$$\frac{\mathrm{d}n}{\mathrm{d}t} = \left(\frac{D^* \gamma A_{(\mathrm{g-l})}}{y_{\mathrm{L}}}\right) \frac{\left[\left(f_{\mathrm{g}} - f_{\mathrm{eq}}\right)\cosh \gamma - \left(f_{\mathrm{b}} - f_{\mathrm{eq}}\right)\right]}{\sinh \gamma}, \tag{A.28}$$

The initial condition of Eq. (A.28) is the turbidity point. The value of f_{b} in Eq. (A.28) should be determined using the following equations.

In order to determine f_{b} as a function of time, we do a mass balance in the bulk water:

$$\left.\frac{\mathrm{d}c}{\mathrm{d}t}\right|_{\mathrm{bulk}}\cdot V=J\big|_{y=y_{\mathrm{L}}}\cdot A_{(\mathrm{g}-1)}-R_y(t)\big|_{\mathrm{bulk}}\cdot V\,, \tag{A.29}$$

where $\left.\frac{\mathrm{d}c}{\mathrm{d}t}\right|_{\mathrm{bulk}}=\frac{c_{\mathrm{w0}}}{H}\cdot\left.\frac{\mathrm{d}f}{\mathrm{d}t}\right|_{\mathrm{bulk}}$, which means $\frac{\mathrm{d}c_{\mathrm{b}}}{\mathrm{d}t}=\frac{c_{\mathrm{w0}}}{H}\cdot\frac{\mathrm{d}f_{\mathrm{b}}}{\mathrm{d}t}$.

The flux at $y=y_{\mathrm{L}}$ is

$$\begin{aligned}
J\big|_{y=y_{\mathrm{L}}}&=-D\left.\left(\frac{\mathrm{d}c}{\mathrm{d}y}\right)\right|_{y=y_{\mathrm{L}}}\cdot A_{(\mathrm{g}-1)}=-D^*\left.\left(\frac{\mathrm{d}f}{\mathrm{d}y}\right)\right|_{y=y_{\mathrm{L}}}\cdot A_{(\mathrm{g}-1)}\\
&=-D^*\left.\left\{\left(\frac{1}{\sinh\gamma}\right)\left[-\left(f_{\mathrm{g}}-f_{\mathrm{eq}}\right)\cosh\left(\gamma\left(1-\frac{y}{y_{\mathrm{L}}}\right)\right)\frac{\gamma}{y_{\mathrm{L}}}+\left(f_{\mathrm{b}}-f_{\mathrm{eq}}\right)\cosh\left(\gamma\frac{y}{y_{\mathrm{L}}}\right)\frac{\gamma}{y_{\mathrm{L}}}\right]\right\}\right|_{y=y_{\mathrm{L}}}\\
&=-D^*\left\{\left(\frac{1}{\sinh\gamma}\right)\left[-\left(f_{\mathrm{g}}-f_{\mathrm{eq}}\right)\right]\cdot\frac{\gamma}{y_{\mathrm{L}}}+\left(f_{\mathrm{b}}-f_{\mathrm{eq}}\right)\cosh\gamma\cdot\frac{\gamma}{y_{\mathrm{L}}}\right\}\\
&=\frac{D^*\gamma}{\sinh\gamma\cdot y_{\mathrm{L}}}\left[f_{\mathrm{g}}-f_{\mathrm{eq}}+\left(f_{\mathrm{eq}}-f_{\mathrm{b}}\right)\cosh\gamma\right]
\end{aligned} \tag{A.30}$$

So that,

$$\begin{aligned}
\frac{\mathrm{d}f_{\mathrm{b}}}{\mathrm{d}t}&=\frac{H}{c_{\mathrm{w0}}}\cdot a\cdot\frac{D^*\gamma}{\sinh\gamma\cdot y_{\mathrm{L}}}\left[\left(f_{\mathrm{g}}-f_{\mathrm{eq}}\right)+\left(f_{\mathrm{eq}}-f_{\mathrm{b}}\right)\cosh\gamma\right]-\frac{H}{c_{\mathrm{w0}}}\cdot R_{\mathrm{y}}(t)\big|_{\mathrm{bulk}}\\
&=\frac{HD^*\gamma a}{c_{\mathrm{w0}}y_{\mathrm{L}}\sinh\gamma}\left[\left(f_{\mathrm{g}}-f_{\mathrm{eq}}\right)+\left(f_{\mathrm{eq}}-f_{\mathrm{b}}\right)\cosh\gamma\right]-\frac{4\pi K^*\mu_2 H\left(f_{\mathrm{b}}-f_{\mathrm{eq}}\right)}{c_{\mathrm{w0}}}
\end{aligned} \tag{A.31}$$

where $a=\frac{A_{(\mathrm{g}-1)}}{V}$.

A.3 Population balance

To determine μ_2 as a function of time in Eq. (A.31), a population balance is needed. Some crystals are new born during the formation process, and some existing ones are growing bigger. The population balance is based on the change in the number of crystals in the size range from r to r+dr:

Change in the number of crystals = New born + Net change

$$\frac{\partial}{\partial t}\left(\phi\mathrm{d}r\right)+\frac{\partial}{\partial r}\left(G\phi\mathrm{d}r\right)=\theta\psi(r)\mathrm{d}r\,, \tag{A.32}$$

where ϕdr is the number of crystals per unit volume in the size range *r* to *r*+d*r*, *G* is the growth rate ($\partial r/\partial t$), θ is the nucleation rate per unit volume, and $\psi(r)\mathrm{d}r$ is the fraction of new born in the size range *r* to *r+dr*. $\frac{\partial}{\partial t}(\phi \mathrm{d}r)$ represents the change in the number of crystals in the size range *r* to *r*+d*r* as a function of time. $\frac{\partial}{\partial r}(G\phi \mathrm{d}r)$ is the number of crystals growing out of the size range minus those growing into the size range (transport item). $\theta\psi(r)\mathrm{d}r$ expresses the number of new crystals nucleated into the size range.

Simplifying the equation, the population balance can be obtained:

$$\frac{\partial \phi}{\partial t}+\frac{\partial}{\partial r}(G\phi)=\theta\psi(r). \tag{A.33}$$

It is assumed that:

1. Growth rate *G* is independent of crystal size *r*
2. New crystals are nucleated at near zero size
3. Nucleation rate is proportional to the *n*-th moment of particle size distribution, that is

$$\theta=\alpha_n\int_0^{\infty} r^n\phi \mathrm{d}r \equiv \alpha_n\mu_n. \tag{A.34}$$

Here we cite the Dirac delta function $\psi(r)=\delta(r-0)=\begin{cases}\infty & r=0\\ 0 & r\neq 0\end{cases}$, the characteristic of which is

$$\int_{-\infty}^{+\infty}\delta(r-0)=1. \tag{A.35}$$

Applying the assumption to the population balance results in the following equation

$$\frac{\partial \phi}{\partial t}+G\frac{\partial \phi}{\partial r}=\alpha_n\mu_n\delta(r-0). \tag{A.36}$$

Multiplying Eq. (A.36) by r^m and integrating with respect to *r* between the limits 0 to ∞ produces

$$\int_0^{\infty}\frac{\partial \phi}{\partial t}r^m\mathrm{d}r+G\int_0^{\infty}\frac{\partial \phi}{\partial r}r^m\mathrm{d}r=\int_0^{\infty}\alpha_n\mu_n\delta(r-0)r^m\mathrm{d}r, \tag{A.37}$$

and

$$\frac{\partial}{\partial t}\left(\int_0^\infty \phi r^m \mathrm{d}r\right)+G\int_0^\infty \frac{\partial \phi}{\partial r} r^m \mathrm{d}r=\alpha_n \mu_n \int_0^\infty \delta(r-0) r^m \mathrm{d}r, \tag{A.38}$$

where

$$\int_0^\infty \phi r^m \mathrm{d}r=\mu_m . \tag{A.39}$$

Since ϕ is the function of r and t, as $\phi=\phi(r,t)$ so that $\mathrm{d}\phi=\frac{\partial \phi}{\partial r}\mathrm{d}r+\frac{\partial \phi}{\partial t}\mathrm{d}t$, and combined with $\mathrm{d}\left(r^m \phi\right)=r^m \mathrm{d}\phi+\phi \mathrm{d}\left(r^m\right)$, we can obtain

$$\begin{aligned} G\int_0^\infty \frac{\partial \phi}{\partial r} r^m \mathrm{d}r &= G\int_{\phi(0,t_0)}^{\phi(\infty,t_\infty)} r^m \mathrm{d}\phi-G\int_{t_0(r=0)}^{t_\infty(r=\infty)} r^m \frac{\partial \phi}{\partial t}\mathrm{d}t \\ &= G\, r^m \phi\Big|_{\phi(0,t_0)}^{\phi(\infty,t_\infty)}-G\int_0^\infty m r^{m-1}\phi \mathrm{d}r-G\int_{t_0(r=0)}^{t_\infty(r=\infty)} r^m \frac{\partial \phi}{\partial t}\mathrm{d}t \\ &= -G\int_0^\infty m r^{m-1}\phi \mathrm{d}r \\ &= -Gm\mu_{m-1}. \end{aligned} \tag{A.40}$$

For $\int_0^\infty \delta(r-0) r^m \mathrm{d}r$, it meets

$$\int_0^\infty \delta(r-0) r^m \mathrm{d}r=\begin{cases}1 & m=0 \\ 0 & m\neq 0, r=0 \\ 0 & m\neq 0, r\neq 0\end{cases} \tag{A.41}$$

Thus,

$$\alpha_n \mu_n \int_0^\infty \delta(r-0) r^m \mathrm{d}r=\alpha_n \mu_n \delta_{0m}, \tag{A.42}$$

where δ_{0m} is the Kronecker delta, defined as $\delta_{ij}=\begin{cases}1 & i=j \\ 0 & i\neq j\end{cases}$.

And Eq. (A.38) can be formed as

$$\frac{\mathrm{d}\mu_m}{\mathrm{d}t}=mG\mu_{m-1}+\delta_{0m}\alpha_n \mu_n \tag{A.43}$$

For any integer value of *n*, Eq. (A.43) can be rewritten as a set of (*n*+1) ordinary differential equations

$$\begin{aligned}
\frac{\mathrm{d}\mu_0}{\mathrm{d}t} &= \alpha_n \mu_n \\
\frac{\mathrm{d}\mu_1}{\mathrm{d}t} &= G\mu_0 \\
\cdot \quad & \quad \cdot \\
\cdot \quad & \quad \cdot \\
\cdot \quad & \quad \cdot \\
\frac{\mathrm{d}\mu_n}{\mathrm{d}t} &= nG\mu_{n-1}
\end{aligned} \tag{A.44}$$

This set of equations can be combined to yield

$$\frac{\mathrm{d}^{n+1}\mu_0}{\mathrm{d}t^{n+1}} - \beta^{n+1}\mu_0 = 0 \tag{A.45}$$

where $\beta = \left(n!\alpha_n G^n\right)^{1/(n+1)}$.

Here we only take total 2nd moment of PSD into consideration. The secondary nucleation rate is proportional to the second moment of the PSD, namely

$$\theta = \alpha_2 \int_0^{\infty} r^2 \phi \mathrm{d}r \equiv \alpha_2 \mu_2 \tag{A.46}$$

This equation implies that the nucleation rate is proportional to the total surface of the particles. Under the above assumption, it is not necessary to solve Eq. (A.46) to obtain $\mu_2(t)$. Instead, only the following three ordinary differential equations need to be solved:

$$\frac{\mathrm{d}\mu_0}{\mathrm{d}t} = \alpha_2 \mu_2 , \quad \mu_0(0) = \mu_0^0 , \tag{A.47}$$

$$\frac{\mathrm{d}\mu_1}{\mathrm{d}t} = G\mu_0 , \quad \mu_1(0) = \mu_1^0 , \tag{A.48}$$

$$\frac{\mathrm{d}\mu_2}{\mathrm{d}t} = 2G\mu_1 , \quad \mu_2(0) = \mu_2^0 . \tag{A.49}$$

The growth rate G is the function of time and distance from the gas-liquid interface but it is independent of the crystal size, $G = G(t, y)$. An average rate can be defined as follows

$$G_{avg}=\left(\frac{1}{L}\right)\left[\int_0^{y_L}\left(\frac{\mathrm{d}r}{\mathrm{d}t}\right)\mathrm{d}y+\left(\frac{\mathrm{d}r}{\mathrm{d}t}\right)_{\mathrm{b}}\left(L-y_L\right)\right], \tag{A.50}$$

where the linear growth rate is given by

$$\frac{\mathrm{d}r}{\mathrm{d}t}=\frac{K^{*}M\left(f-f_{\mathrm{eq}}\right)}{\rho}. \tag{A.51}$$

Thus the average rate can be obtained

$$\begin{aligned}
G_{\mathrm{avg}}&=\left(\frac{K^{*}M}{\rho L}\right)\left[\int_0^{y_{\mathrm{L}}}\left(f-f_{\mathrm{eq}}\right)\mathrm{d}y+\left(f_{\mathrm{b}}-f_{\mathrm{eq}}\right)\left(L-y_{\mathrm{L}}\right)\right]\\
&=\left(\frac{K^{*}M}{\rho L}\right)\left[\int_0^{y_{\mathrm{L}}}\frac{\left(f_{\mathrm{g}}-f_{\mathrm{eq}}\right)\sinh\left(\gamma\left(1-\frac{y}{y_{\mathrm{L}}}\right)\right)+\left(f_{\mathrm{b}}-f_{\mathrm{eq}}\right)\sinh\left(\gamma\frac{y}{y_{\mathrm{L}}}\right)}{\sinh\gamma}\mathrm{d}y+\left(f_{\mathrm{b}}-f_{\mathrm{eq}}\right)\left(L-y_{\mathrm{L}}\right)\right]\\
&=\left(\frac{K^{*}M}{\rho L}\right)\left[\frac{\left(f_{\mathrm{g}}-f_{\mathrm{eq}}\right)\left(-\frac{y_{\mathrm{L}}}{\gamma}(1-\cosh\gamma)\right)+\left(f_{\mathrm{b}}-f_{\mathrm{eq}}\right)\left(\frac{y_{\mathrm{L}}}{\gamma}(\cosh\gamma-1)\right)}{\sinh\gamma}+\left(f_{\mathrm{b}}-f_{\mathrm{eq}}\right)\left(L-y_{\mathrm{L}}\right)\right]\\
&=\left(\frac{K^{*}M}{\rho L}\right)\left[\frac{y_{\mathrm{L}}}{\gamma\sinh\gamma}(\cosh\gamma-1)\left(f_{\mathrm{b}}+f_{\mathrm{g}}-2f_{\mathrm{eq}}\right)+\left(f_{\mathrm{b}}-f_{\mathrm{eq}}\right)\left(L-y_{\mathrm{L}}\right)\right].
\end{aligned} \tag{A.52}$$

Finally, we obtain

$$G_{\mathrm{avg}}=\left(\frac{K^{*}M}{\rho L}\right)\left[y_{\mathrm{L}}\frac{\left(f_{\mathrm{b}}+f_{\mathrm{g}}-2f_{\mathrm{eq}}\right)(\cosh\gamma-1)}{\gamma\sinh\gamma}+\left(L-y_{\mathrm{L}}\right)\left(f_{\mathrm{b}}-f_{\mathrm{eq}}\right)\right]. \tag{A.53}$$

Appendix B Calculation of fugacity by Peng–Robinson equation of state

B.1 Introduction

There are many ways to calculate the fugacity of gas. In this work, the Peng–Robinson equation of state (PR EoS) is used. It has many advantages, such as stable performance, few parameters required, simple form, wide application, and higher accuracy. In this appendix, the calculation of fugacity by PR EoS is simply introduced, and other applications of PR EoS are also involved. More details of the derivation of PR EoS can be found in [118], and the properties of gases and liquids can be found in [144].

B.2 PR cubic expression

First we define the contrast temperature of gas as

$$T_{\mathrm{r}} = \frac{T}{T_{\mathrm{c}}}, \tag{B.1}$$

where T_{c} is the critical temperature. And the contrast pressure is similarly defined as

$$P_{\mathrm{r}} = \frac{P}{P_{\mathrm{c}}}, \tag{B.2}$$

where P_{c} is the critical pressure.

The actual gas law is expressed as

$$P = \frac{RT}{V_{\mathrm{m}} - b} - \frac{a}{V_{\mathrm{m}}^2 + 2bV_{\mathrm{m}} - b^2}, \tag{B.3}$$

where a is the van der Waals force factor, given by

$$a = \frac{0.45724 R^2 T_\mathrm{c}^{\ 2}}{P_\mathrm{c}} \alpha \,, \tag{B.4}$$

$$\alpha = \left[1 + \left(0.37464 + 1.54226\omega - 0.26992\omega^2 \right) \left(1 - \sqrt{T_\mathrm{r}} \right) \right]^2 , \tag{B.5}$$

where ω is the Pitzer acentric factor.

The minimum volume of gas b is given by

$$b = \frac{0.0778 R T_\mathrm{c}}{P_\mathrm{c}} . \tag{B.6}$$

For a single gas, we define

$$A = \frac{aP}{R^2 T^2} , \tag{B.7}$$

$$B = \frac{bP}{RT} . \tag{B.8}$$

For gas mixtures, the mixing rules are

$$a_\mathrm{m} = \sum_\mathrm{i} \sum_\mathrm{j} y_\mathrm{i} y_\mathrm{j} \left(1 - k_\mathrm{ij} \right) \sqrt{a_\mathrm{i} a_\mathrm{j}} \,, \tag{B.9}$$

$$b_\mathrm{m} = \sum_\mathrm{i} y_\mathrm{i} b_\mathrm{i} \,, \tag{B.10}$$

$$A_\mathrm{m} = \frac{a_\mathrm{m} P}{R^2 T^2} , \tag{B.11}$$

$$B_\mathrm{m} = \frac{b_\mathrm{m} P}{RT} , \tag{B.12}$$

where k_ij is the binary interaction parameters of mixtures, whose value can be found in [170, 171].

The PR cubic expression in the compressibility factor Z becomes

$$Z^3 - \left(1 - B \right) Z^2 + \left(A - 2B - 3B^2 \right) Z - \left(AB - B^2 - B^3 \right) = 0 . \tag{B.13}$$

All parameters of PR EoS are calculated by Z.

B.3 Fugacity coefficient

For a single gas, the fugacity coefficient φ is calculated by

$$\ln\left(\varphi\right) = Z - 1 - \ln\left(Z - B\right) - \frac{A}{2\sqrt{2}B}\ln\left(\frac{Z + 2.414B}{Z - 0.414B}\right). \tag{B.14}$$

For gas mixtures, β_{i} and α_{m} are used

$$\beta_{\mathrm{i}} = \frac{b_{\mathrm{i}}P}{RT}, \tag{B.15}$$

$$\alpha_{\mathrm{m}} = \sum_{\mathrm{i}}\sum_{\mathrm{j}} y_{\mathrm{i}}(1 - ki_{\mathrm{j}})\sqrt{a_{\mathrm{i}}a_{\mathrm{j}}}\,. \tag{B.16}$$

So the fugacity coefficient of component i (φ_{i}) is calculated by

$$\ln\left(\varphi_{\mathrm{i}}\right) = \frac{\beta_{\mathrm{i}}}{B_{\mathrm{m}}}\left(Z - 1\right) - \ln(Z - B_{\mathrm{m}}) + \frac{A_{\mathrm{m}}}{2\sqrt{2}B_{\mathrm{m}}}\left(\frac{\beta_{\mathrm{i}}}{B_{\mathrm{m}}} - \frac{2\alpha_{\mathrm{m}}}{a_{\mathrm{m}}}\right)\ln\left(\frac{Z + 2.414B_{\mathrm{m}}}{Z - 0.414B_{\mathrm{m}}}\right) \tag{B.17}$$

B.4 Calculation of other parameters

B.4.1 Density and molar volume of gas mixtures

The total molar mass of gas mixtures is calculated by

$$M_{\mathrm{w,mixtures}} = \sum y_{\mathrm{i}}M_{\mathrm{w,i}}\,, \tag{B.18}$$

where $M_{\mathrm{w,i}}$ is the molar mass of component i (kg mol^{-1}).

The density of gas mixtures is given by

$$\rho = \frac{M_{\mathrm{w,mixtures}}P}{ZRT}\ (\mathrm{kg\ m^{-3}}), \tag{B.19}$$

and the molar volume of gas mixtures is given by

$$V_{\mathrm{m}} = \frac{V}{n} = \frac{ZRT}{P} = \frac{M_{\mathrm{w,mixtures}}}{\rho}\,(\mathrm{m^3mol^{-1}})\,. \tag{B.20}$$

B.4.2 Departure internal energy, departure enthalpy and departure entropy

For a single gas, the departure factor should be calculated first

$$d = \left(0.37464 + 1.54226\omega - 0.26992\omega^2\right) a \sqrt{\frac{T_\mathrm{r}}{\alpha}} . \tag{B.21}$$

Then the departure internal energy (ΔU), departure enthalpy (ΔH) and departure entropy (ΔS) are given by

$$\Delta U = \frac{ART}{2\sqrt{2}B}\left(1 + \frac{d}{a}\right)\ln\left(\frac{Z + 2.414B}{Z - 0.414B}\right), \tag{B.22}$$

$$\Delta H = \Delta U + RT\left(1 - Z\right), \tag{B.23}$$

$$\Delta S = R\left[-\ln\left(Z - B\right) + \frac{Ad}{2\sqrt{2}aB}\ln\left(\frac{Z + 2.414B}{Z - 0.414B}\right)\right]. \tag{B.24}$$

For gas mixtures:

$$d_\mathrm{m} = \sum_\mathrm{i}\sum_\mathrm{j}\left(0.37464 + 1.54226\omega_\mathrm{j} - 0.26992\omega_\mathrm{j}^{\,2}\right) y_\mathrm{i} y_\mathrm{j} (1 - k_\mathrm{ij}) \sqrt{\frac{a_\mathrm{i} a_\mathrm{j} T_\mathrm{r,j}}{\alpha_\mathrm{j}}} , \tag{B.25}$$

$$\Delta U = \frac{A_\mathrm{m} RT}{2\sqrt{2}B_\mathrm{m}}\left(1 + \frac{d_\mathrm{m}}{a_\mathrm{m}}\right)\ln\left(\frac{Z + 2.414B_\mathrm{m}}{Z - 0.414B_\mathrm{m}}\right), \tag{B.26}$$

$$\Delta H = \Delta U + RT\left(1 - Z\right), \tag{B.27}$$

$$\Delta S = R\left[-\ln\left(Z - B_\mathrm{m}\right) + \frac{A_\mathrm{m} d_\mathrm{m}}{2\sqrt{2}a_\mathrm{m} B_\mathrm{m}}\ln\left(\frac{Z + 2.414B_\mathrm{m}}{Z - 0.414B_\mathrm{m}}\right)\right]. \tag{B.28}$$

It should be noted that the units of ΔU, ΔH and ΔS are all J mol^{-1}, to transfer their units to J kg^{-1}, they should be divided by their respective molar masses $M_\mathrm{w,mixtures}$, kg mol^{-1}.

Appendix C Student's *t*-distribution and Analysis of Variance

C.1 Introduction

The student's *t*-distribution is a probability distribution that is used to estimate population parameters when the sample size is small ($N < 30$) and/or when the population variance is unknown.

The confidence interval of the student's *t*-distribution is calculated as

$$\bar{x} \pm t\frac{s}{\sqrt{N}}, \tag{C.1}$$

where $\bar{x}$ is the mean of the sample, s is the standard deviation, N is the sample size, t is the critical value for student's *t*-distribution, shown in Table C.1. The value of t is affected by the degree of freedom ($df = N–1$) and the percent of confidence, and it can be found in tables or calculated by the cumulative distribution function. For example, if the sample size is 11 (df =10), and we want to calculate the 90% confidence intervals, then from Table C.1, $t = 1.372$.

Table C.1. Critical values for student's *t*-distribution.

One-tail	0.250	0.125	0.100	0.075	0.050	0.025	0.010	0.005	0.0005
Two-tail	0.500	0.250	0.200	0.150	0.100	0.050	0.020	0.010	0.0010
d*f*									
1	1.000	2.414	3.078	4.165	6.314	12.706	31.821	63.657	636.619
2	0.816	1.604	1.886	2.282	2.920	4.303	60965	9.925	31.599
3	0.765	1.423	1.638	1.924	2.353	3.182	4.541	5.841	12.924
4	0.741	1.344	1.533	1.778	2.132	2.776	3.747	4.604	8.610
5	0.727	1.301	1.476	1.699	2.015	2.571	3.365	4.032	6.869

One-tail	0.250	0.125	0.100	0.075	0.050	0.025	0.010	0.005	0.0005
Two-tail	0.500	0.250	0.200	0.150	0.100	0.050	0.020	0.010	0.0010
d*f*									
6	0.718	1.273	1.440	1.650	1.943	2.447	3.142	3.707	5.959
7	0.711	1.254	1.415	1.617	1.895	2.365	2.998	3.499	5.408
8	0.706	1.240	1.397	1.592	1.860	2.306	2.896	3.355	5.041
9	0.703	1.230	1.383	1.574	1.833	2.262	2.821	3.250	4.781
10	0.700	1.221	1.372	1.559	1.812	2.228	2.764	3.169	4.587

C.2 Analysis of Variance

Analysis of Variance (ANOVA) is a statistical formula used to compare variances across the means (or average) of different groups. A range of scenarios use it to determine if there is any difference between the means of different groups. It is the extension of the student's *t*-distribution.

The *F*-statistic is first calculated in ANOVA. It is used for comparing the factors of the total deviation. The formula of the *F*-statistic is

$$F\text{-statistic} = \frac{\text{MSG}}{\text{MSE}}, \tag{C.2}$$

where MSG is the mean sum of squares due to the group, and MSE is the mean sum of squares due to the error. The calculation of the *F*-statistic is listed in Table C.2.

Table C.2. Calculation of *F*-statistic.

	Degree of freedom	Sum Square	Mean Square	*F*-statistic
Group	df_G	SSG	MSG	*F*-value
Error	df_E	SSE = SST– SSG	MSE	
Total	df_T	SST		

C.3 The *p*-value analysis

The *p*-value is a measure of the probability that an observed difference could have occurred just by random chance. The lower the *p*-value, the greater the statistical significance of the observed difference. The p-value can serve as an alternative to or in addition to preselected confidence levels for hypothesis testing. The p-value is calculated by the F-statistic. Many software tools can implement the calculation. For example, in Microsoft Excel, the "fdist" function can calculate the p-value as

$$p\text{-value} = fdist\left(F\text{-statistic},\ \mathrm{d}f_{\mathrm{G}},\ \mathrm{d}f_{\mathrm{E}}\right). \tag{C.3}$$

The p-value reports the results of the observed difference. The smaller the p-value, the stronger the evidence that you should reject the null hypothesis. A p-value less than 0.05 (typically ≤ 0.05) is statistically significant. It indicates strong evidence against the null hypothesis, as there is less than a 5% probability the null is correct (and the results are random). A p-value less than 0.01 is highly statistically significant. A p-value less than 0.001 is very strongly statistically significant.

Bibliography

[1] Sloan Jr ED, Koh CA. Clathrate hydrates of natural gases: CRC press, 2007.

[2] Kang S-P, Lee J-W, Ryu H-J. Phase behavior of methane and carbon dioxide hydrates in meso- and macro-sized porous media. Fluid Phase Equilibria. 2008;274(1–2):68–72.

[3] Waite WF, Stern LA, Kirby SH, Winters WJ, Mason DH. Simultaneous determination of thermal conductivity, thermal diffusivity and specific heat in sI methane hydrate. Geophysical Journal International. 2007;169(2):767–74.

[4] Englezos P, Kalogerakis N, Dholabhai PD, Bishnoi PR. Kinetics of formation of methane and ethane gas hydrates. Chemical Engineering Science. 1987;42(11):2647–58.

[5] Kashchiev D, Firoozabadi A. Induction time in crystallization of gas hydrates. Journal of Crystal Growth. 2003;250(3):499–515.

[6] Kashchiev D, Verdoes D, van Rosmalen GM. Induction time and metastability limit in new phase formation. Journal of Crystal Growth. 1991;110(3):373–80.

[7] Ma ZW, Zhang P, Bao HS, Deng S. Review of fundamental properties of CO_2 hydrates and CO_2 capture and separation using hydration method. Renewable and Sustainable Energy Reviews. 2016;53:1273–302.

[8] Babu P, Linga P, Kumar R, Englezos P. A review of the hydrate based gas separation (HBGS) process for carbon dioxide pre-combustion capture. Energy. 2015;85:261–79.

[9] Dashti H, Zhehao Yew L, Lou X. Recent advances in gas hydrate-based CO_2 capture. Journal of Natural Gas Science and Engineering. 2015;23:195–207.

[10] Hashimoto H, Yamaguchi T, Kinoshita T, Muromachi S. Gas separation of flue gas by tetra-n-butylammonium bromide hydrates under moderate pressure conditions. Energy. 2017;129:292–8.

[11] Rodriguez CT, Le QD, Focsa C, Pirim C, Chazallon B. Influence of crystallization parameters on guest selectivity and structures in a CO_2-based

separation process using TBAB semi-clathrate hydrates. Chemical Engineering Journal. 2020;382:122867.

[12] Wang X, Zhang F, Lipiński W. Carbon dioxide hydrates for cold thermal energy storage: A review. Solar Energy. 2020;211:11–30.

[13] Wang X, Dennis M. Phase equilibrium and formation behaviour of CO_2-TBAB semi-clathrate hydrate at low pressures for cold storage air conditioning applications. Chemical Engineering Science. 2016;155:294–305.

[14] Fan S, Li S, Wang J, Lang X, Wang Y. Efficient Capture of CO_2 from Simulated Flue Gas by Formation of TBAB or TBAF Semiclathrate Hydrates. Energy & Fuels. 2009;23(8):4202–8.

[15] Xu C-G, Zhang S-H, Cai J, Chen Z-Y, Li X-S. CO_2 (carbon dioxide) separation from CO_2–H_2 (hydrogen) gas mixtures by gas hydrates in TBAB (tetra-n-butyl ammonium bromide) solution and Raman spectroscopic analysis. Energy. 2013;59:719–25.

[16] Lin W, Delahaye A, Fournaison L. Phase equilibrium and dissociation enthalpy for semi-clathrate hydrate of CO_2+TBAB. Fluid Phase Equilibria. 2008;264(1):220–7.

[17] Joshi A, Sangwai JS, Das K, Sami NA. Experimental investigations on the phase equilibrium of semiclathrate hydrates of carbon dioxide in TBAB with small amount of surfactant. International Journal of Energy and Environmental Engineering. 2013;4(1):11.

[18] Wang Y, Zhong D-L, Englezos P, Yan J, Ge B-B. Kinetic study of semiclathrate hydrates formed with CO_2 in the presence of tetra-n-butyl ammonium bromide and tetra-n-butyl phosphonium bromide. Energy. 2020;212:118697.

[19] Li X-S, Zhan H, Xu C-G, Zeng Z-Y, Lv Q-N, Yan K-F. Effects of Tetrabutyl-(ammonium/phosphonium) Salts on Clathrate Hydrate Capture of CO_2 from Simulated Flue Gas. Energy & Fuels. 2012;26(4):2518–27.

[20] Ye N, Zhang P, Liu QS. Kinetics of Hydrate Formation in the CO_2+TBAB+H_2O System at Low Mass Fractions. Industrial & Engineering Chemistry Research. 2014;53(24):10249–55.

[21] Wang X, Zhang F, Lipiński W. Research progress and challenges in hydrate-based carbon dioxide capture applications. Applied Energy. 2020;269:114928.

[22] Gupta RD, Raghav N. Differential effect of surfactants tetra-n-butyl ammonium bromide and N-Cetyl-N, N, N-trimethyl ammonium bromide bound to nano-cellulose on binding and sustained release of some non-steroidal anti-inflammatory drugs. International Journal of Biological Macromolecules. 2020;164:2745–52.

[23] Babu P, Chin WI, Kumar R, Linga P. Systematic Evaluation of Tetra-n-butyl Ammonium Bromide (TBAB) for Carbon Dioxide Capture Employing the Clathrate Process. Industrial & Engineering Chemistry Research. 2014;53(12):4878–87.

[24] Lee S, Park S, Lee Y, Lee J, Lee H, Seo Y. Guest Gas Enclathration in Semiclathrates of Tetra-n-butylammonium Bromide: Stability Condition and Spectroscopic Analysis. Langmuir. 2011;27(17):10597–603.

[25] Ye N, Zhang P. Equilibrium data and morphology of tetra-n-butyl ammonium bromide semiclathrate hydrate with carbon dioxide. Journal of Chemical & Engineering Data. 2012;57(5):1557–62.

[26] Duc NH, Chauvy F, Herri J-M. CO_2 capture by hydrate crystallization – A potential solution for gas emission of steelmaking industry. Energy Conversion and Management. 2007;48(4):1313–22.

[27] Xu C-G, Chen Z-Y, Cai J, Li X-S. Study on Pilot-Scale CO_2 Separation from Flue Gas by the Hydrate Method. Energy & Fuels. 2014;28(2):1242–8.

[28] Nasir Q, Suleman H, Elsheikh YA. A review on the role and impact of various additives as promoters/ inhibitors for gas hydrate formation. Journal of Natural Gas Science and Engineering. 2020;76:103211.

[29] Zhang JS, Lee S, Lee JW. Kinetics of Methane Hydrate Formation from SDS Solution. Industrial & Engineering Chemistry Research. 2007;46(19):6353–9.

[30] Viseu MI, Correia RF, Fernandes AC. Time evolution of the thermotropic behavior of spontaneous liposomes and disks of the DMPC–DTAC aqueous system. Journal of Colloid and Interface Science. 2010;351(1):156–65.

[31] Liu Z, Song Y, Liu W, Liu R, Lang C, Li Y. Rheology of methane hydrate slurries formed from water-in-oil emulsion with different surfactants concentrations. Fuel. 2020;275:117961.

[32] Mohammadi A, Jodat A. Investigation of the kinetics of TBAB + carbon dioxide semiclathrate hydrate in presence of tween 80 as a cold storage material. Journal of Molecular Liquids. 2019;293:111433.

[33] Lirio CFdS, Pessoa FLP, Uller AMC. Storage capacity of carbon dioxide hydrates in the presence of sodium dodecyl sulfate (SDS) and tetrahydrofuran (THF). Chemical Engineering Science. 2013;96:118–23.

[34] Li X-S, Xu C-G, Chen Z-Y, Wu H-J. Tetra-n-butyl ammonium bromide semi-clathrate hydrate process for post-combustion capture of carbon dioxide in the presence of dodecyl trimethyl ammonium chloride. Energy. 2010;35(9):3902–8.

[35] Zhang F, Wang X, Lou X, Lipiński W. The effect of sodium dodecyl sulfate and dodecyltrimethylammonium chloride on the kinetics of CO_2 hydrate

formation in the presence of tetra-n-butyl ammonium bromide for carbon capture applications. Energy. 2021;227:120424.

[36] Prah B, Yun R. Investigations on CO_2 hydrate slurry for transportation in carbon capture and storage. Journal of Mechanical Science and Technology. 2019;33(10):5085–92.

[37] Cheng M, Zeng G, Huang D, Yang C, Lai C, Zhang C, et al. Advantages and challenges of Tween 80 surfactant-enhanced technologies for the remediation of soils contaminated with hydrophobic organic compounds. Chemical Engineering Journal. 2017;314:98–113.

[38] Zhang B-y, Wu Q, Sun D-l. Effect of surfactant Tween on induction time of gas hydrate formation. Journal of China University of Mining and Technology. 2008;18(1):18–21.

[39] Torré J-P, Ricaurte M, Dicharry C, Broseta D. CO_2 enclathration in the presence of water-soluble hydrate promoters: Hydrate phase equilibria and kinetic studies in quiescent conditions. Chemical Engineering Science. 2012;82:1–13.

[40] Renault-Crispo J-S, Servio P. Methane gas hydrate kinetics with mixtures of sodium dodecyl sulphate and tetrabutylammonium bromide. The Canadian Journal of Chemical Engineering. 2018;96(7):1620–6.

[41] Wang Y, Zhong D-L, Li Z, Li J-B. Application of tetra-n-butyl ammonium bromide semi-clathrate hydrate for CO_2 capture from unconventional natural gases. Energy. 2020;197:117209.

[42] Seo Y-T, Moudrakovski IL, Ripmeester JA, Lee J-W, Lee H. Efficient Recovery of CO_2 from Flue Gas by Clathrate Hydrate Formation in Porous Silica Gels. Environmental Science & Technology. 2005;39(7):2315–9.

[43] Adeyemo A. Post combustion capture of carbon dioxide through hydrate formation in silica gel column: The University of British Columbia, 2008.

[44] Yin Z, Moridis G, Tan HK, Linga P. Numerical analysis of experimental studies of methane hydrate formation in a sandy porous medium. Applied Energy. 2018;220:681–704.

[45] Zhang B, Zheng J, Yin Z, Liu C, Wu Q, Wu Q, et al. Methane hydrate formation in mixed-size porous media with gas circulation: Effects of sediment properties on gas consumption, hydrate saturation and rate constant. Fuel. 2018;233:94–102.

[46] Perrin A, Celzard A, Marêché JF, Furdin G. Methane Storage within Dry and Wet Active Carbons: A Comparative Study. Energy & Fuels. 2003;17(5):1283–91.

[47] Zhao Y, Zhao J, Liang W, Gao Q, Yang D. Semi-clathrate hydrate process of methane in porous media-microporous materials of 5A-type zeolites. Fuel. 2018;220:185–91.

[48] Fan S, Yang L, Lang X, Wang Y, Xie D. Kinetics and thermal analysis of methane hydrate formation in aluminum foam. Chemical Engineering Science. 2012;82:185–93.

[49] Yan K, Li X, Chen Z, Zhang Y, Xu C, Xia Z. Methane hydrate formation and dissociation behaviors in montmorillonite. Chinese Journal of Chemical Engineering. 2019;27(5):1212–8.

[50] Su F, Bray CL, Tan B, Cooper AI. Rapid and Reversible Hydrogen Storage in Clathrate Hydrates Using Emulsion-Templated Polymers. Advanced Materials. 2008;20(14):2663–6.

[51] Ding A, Yang L, Fan S, Lou X. Reversible methane storage in porous hydrogel supported clathrates. Chemical Engineering Science. 2013;96:124–30.

[52] Wang W, Bray CL, Adams DJ, Cooper AI. Methane Storage in Dry Water Gas Hydrates. Journal of the American Chemical Society. 2008;130(35):11608–9.

[53] Shi B-H, Yang L, Fan S-S, Lou X. An investigation on repeated methane hydrates formation in porous hydrogel particles. Fuel. 2017;194:395–405.

[54] Fan S, Yang L, Wang Y, Lang X, Wen Y, Lou X. Rapid and high capacity methane storage in clathrate hydrates using surfactant dry solution. Chemical Engineering Science. 2014;106:53–9.

[55] Adeyemo A, Kumar R, Linga P, Ripmeester J, Englezos P. Capture of carbon dioxide from flue or fuel gas mixtures by clathrate crystallization in a silica gel column. International Journal of Greenhouse Gas Control. 2010;4(3):478–85.

[56] Anderson R, Llamedo M, Tohidi B, Burgass RW. Experimental Measurement of Methane and Carbon Dioxide Clathrate Hydrate Equilibria in Mesoporous Silica. The Journal of Physical Chemistry B. 2003;107(15):3507–14.

[57] Anderson R, Llamedo M, Tohidi B, Burgass RW. Characteristics of Clathrate Hydrate Equilibria in Mesopores and Interpretation of Experimental Data. The Journal of Physical Chemistry B. 2003;107(15):3500–6.

[58] Clennell MB, Hovland M, Booth JS, Henry P, Winters WJ. Formation of natural gas hydrates in marine sediments 1. Conceptual model of gas hydrate growth conditioned by host sediment properties. Journal of Geophysical Research B: Solid Earth. 1999;104(B10):22985–3003.

[59] Hou J, Ji Y, Zhou K, Liu Y, Wei B. Effect of hydrate on permeability in porous media: Pore-scale micro-simulation. International Journal of Heat and Mass Transfer. 2018;126:416–24.

[60] Park S, Lee S, Lee Y, Lee Y, Seo Y. Hydrate-based pre-combustion capture of carbon dioxide in the presence of a thermodynamic promoter and porous silica gels. International Journal of Greenhouse Gas Control. 2013;14:193–9.

[61] Uchida T, Ebinuma T, Ishizaki T. Dissociation Condition Measurements of Methane Hydrate in Confined Small Pores of Porous Glass. The Journal of Physical Chemistry B. 1999;103(18):3659–62.

[62] Uchida T, Ebinuma T, Takeya S, Nagao J, Narita H. Effects of Pore Sizes on Dissociation Temperatures and Pressures of Methane, Carbon Dioxide, and Propane Hydrates in Porous Media. The Journal of Physical Chemistry B. 2002;106(4):820–6.

[63] Wilder JW, Seshadri K, Smith DH. Modeling hydrate formation in media with broad pore size distributions. Langmuir. 2001;17(21):6729–35.

[64] Wilder JW, Seshadri K, Smith DH. Resolving apparent contradictions in equilibrium measurements for clathrate hydrates in porous media. The Journal of Physical Chemistry B. 2001;105(41):9970–2.

[65] Seshadri K, Wilder JW, Smith DH. Measurements of equilibrium pressures and temperatures for propane hydrate in silica gels with different pore-size distributions. The Journal of Physical Chemistry B. 2001;105(13):2627–31.

[66] Smith DH, Wilder JW, Seshadri K. Methane hydrate equilibria in silica gels with broad pore ‐ size distributions. AIChE Journal. 2002;48(2):393 ‐ 400.

[67] Zhang W, Wilder JW, Smith DH. Interpretation of ethane hydrate equilibrium data for porous media involving hydrate-ice equilibria. AIChE Journal. 2002;48(10):2324–31.

[68] Henry P, Thomas M, Clennell MB. Formation of natural gas hydrates in marine sediments: 2. Thermodynamic calculations of stability conditions in porous sediments. Journal of Geophysical Research: Solid Earth. 1999;104(B10):23005–22.

[69] Klauda JB, Sandler SI. Predictions of gas hydrate phase equilibria and amounts in natural sediment porous media. Marine and Petroleum Geology. 2003;20(5):459–70.

[70] Li S-L, Sun C-Y, Liu B, Feng X-J, Li F-G, Chen L-T, et al. Initial thickness measurements and insights into crystal growth of methane hydrate film. AIChE Journal. 2013;59(6):2145–54.

[71] Li S-L, Sun C-Y, Liu B, Li Z-Y, Chen G-J, Sum AK. New Observations and Insights into the Morphology and Growth Kinetics of Hydrate Films. Scientific Reports. 2014;4:4129.

[72] Peng BZ, Dandekar A, Sun CY, Luo H, Ma QL, Pang WX, et al. Hydrate Film Growth on the Surface of a Gas Bubble Suspended in Water. The Journal of Physical Chemistry B. 2007;111(43):12485–93.

[73] Vysniauskas A, Bishnoi PR. Kinetics of ethane hydrate formation. Chemical Engineering Science. 1985;40(2):299–303.

[74] Englezos P, Kalogerakis N, Dholabhai PD, Bishnoi PR. Kinetics of gas hydrate formation from mixtures of methane and ethane. Chemical Engineering Science. 1987;42(11):2659–66.

[75] Mochizuki T, Mori YH. Clathrate-hydrate film growth along water/hydrate-former phase boundaries—numerical heat-transfer study. Journal of Crystal Growth. 2006;290(2):642–52.

[76] De Graauw J, Rutten J. The Mechanism and Rate of Hydrate Formation. Conference The Mechanism and Rate of Hydrate Formation, vol. 1970. p. 103.

[77] Vysniauskas A, Bishnoi PR. A kinetic study of methane hydrate formation. Chemical Engineering Science. 1983;38(7):1061–72.

[78] Skovborg P, Rasmussen P. A mass transport limited model for the growth of methane and ethane gas hydrates. Chemical Engineering Science. 1994;49(8):1131–43.

[79] Yapa PD, Zheng L, Chen F. A Model for Deepwater Oil/Gas Blowouts. Marine Pollution Bulletin. 2001;43(7):234–41.

[80] Gong J, Shi B, Zhao J. Natural gas hydrate shell model in gas-slurry pipeline flow. Journal of Natural Gas Chemistry. 2010;19(3):261–6.

[81] Shi B-H, Gong J, Sun C-Y, Zhao J-K, Ding Y, Chen G-J. An inward and outward natural gas hydrates growth shell model considering intrinsic kinetics, mass and heat transfer. Chemical Engineering Journal. 2011;171(3):1308–16.

[82] Falenty A, Salamatin AN, Kuhs WF. Kinetics of CO_2-Hydrate Formation from Ice Powders: Data Summary and Modeling Extended to Low Temperatures. The Journal of Physical Chemistry C. 2013;117(16):8443–57.

[83] Shi B-H, Fan S-S, Lou X. Application of the shrinking-core model to the kinetics of repeated formation of methane hydrates in a system of mixed dry-water and porous hydrogel particulates. Chemical Engineering Science. 2014;109:315–25.

[84] Malegaonkar MB, Dholabhai PD, Bishnoi PR. Kinetics of carbon dioxide and methane hydrate formation. The Canadian Journal of Chemical Engineering. 1997;75(6):1090–9.

[85] Svandal A, Kvamme B, Grànàsy L, Pusztai T. The influence of diffusion on hydrate growth. Journal of Phase Equilibria and Diffusion. 2005;26(5):534–8.

[86] Buanes T, Kvamme B, Svandal A. Computer simulation of CO_2 hydrate growth. Journal of Crystal Growth. 2006;287(2):491–4.

[87] Uchida T, Ebinuma T, Kawabata Ji, Narita H. Microscopic observations of formation processes of clathrate-hydrate films at an interface between water and carbon dioxide. Journal of Crystal Growth. 1999;204(3):348–56.

[88] Mori YH. Estimating the thickness of hydrate films from their lateral growth rates: application of a simplified heat transfer model. Journal of Crystal Growth. 2001;223(1):206–12.

[89] Freer EM, Sami Selim M, Dendy Sloan E. Methane hydrate film growth kinetics. Fluid Phase Equilibria. 2001;185(1):65–75.

[90] Anwar MN, Fayyaz A, Sohail NF, Khokhar MF, Baqar M, Khan WD, et al. CO_2 capture and storage: A way forward for sustainable environment. Journal of Environmental Management. 2018;226:131–44.

[91] Haszeldine RS. Carbon Capture and Storage: How Green Can Black Be? Science. 2009;325(5948):1647–52.

[92] Mondal MK, Balsora HK, Varshney P. Progress and trends in CO_2 capture/separation technologies: A review. Energy. 2012;46(1):431–41.

[93] Chazallon B, Pirim C. Selectivity and CO_2 capture efficiency in CO_2–N_2 clathrate hydrates investigated by in-situ Raman spectroscopy. Chemical Engineering Journal. 2018;342:171–83.

[94] Davy H. The Bakerian lecture. On some of the combinations of oxymuriatic gas and oxygen, and on the chemical relations of these principles to inflammable bodies. Philos Trans R Soc London. 1811;101(PART I):1–35.

[95] Prah B, Yun R. CO_2 hydrate slurry transportation in carbon capture and storage. Applied Thermal Engineering. 2018;128:653–61.

[96] Ho MT, Allinson GW, Wiley DE. Reducing the Cost of CO_2 Capture from Flue Gases Using Pressure Swing Adsorption. Industrial & Engineering Chemistry Research. 2008;47(14):4883–90.

[97] Tam SS, Stanton ME, Ghose S, Deppe G, Spencer DF, Currier RP, et al. A high pressure carbon dioxide separation process for IGCC plants. Conference A high pressure carbon dioxide separation process for IGCC plants, Washington DC, USA. p. 14–7.

[98] Yang H, Fan S, Lang X, Wang Y, Nie J. Economic Comparison of Three Gas Separation Technologies for CO_2 Capture from Power Plant Flue Gas. Chinese Journal of Chemical Engineering. 2011;19(4):615–20.

[99] Babu P, Ong HWN, Linga P. A systematic kinetic study to evaluate the effect of tetrahydrofuran on the clathrate process for pre-combustion capture of carbon dioxide. Energy. 2016;94:431–42.

[100] Chen Z-Y, Chen C, Zhang Y, Xia Z-M, Yan K-F, Li X-S. Carbon dioxide and sulfur dioxide capture from flue gas by gas hydrate based process. Energy Procedia. 2017;142:3454–9.

[101] Kumar A, Sakpal T, Linga P, Kumar R. Influence of contact medium and surfactants on carbon dioxide clathrate hydrate kinetics. Fuel. 2013;105:664–71.

[102] Lee HJ, Lee JD, Linga P, Englezos P, Kim YS, Lee MS, et al. Gas hydrate formation process for pre-combustion capture of carbon dioxide. Energy. 2010;35(6):2729–33.

[103] Zheng J, Bhatnagar K, Khurana M, Zhang P, Zhang B-Y, Linga P. Semiclathrate based CO_2 capture from fuel gas mixture at ambient temperature: Effect of concentrations of tetra-n-butylammonium fluoride (TBAF) and kinetic additives. Applied Energy. 2018;217:377–89.

[104] Zheng J, Zhang P, Linga P. Semiclathrate hydrate process for pre-combustion capture of CO_2 at near ambient temperatures. Applied Energy. 2017;194:267–78.

[105] Li B, Xu T, Zhang G, Guo W, Liu H, Wang Q, et al. An experimental study on gas production from fracture-filled hydrate by CO_2 and CO_2/N_2 replacement. Energy Conversion and Management. 2018;165:738–47.

[106] He J, Liu Y, Ma Z, Deng S, Zhao R, Zhao L. A Literature Research on the Performance Evaluation of Hydrate-based CO_2 Capture and Separation Process. Energy Procedia. 2017;105:4090–7.

[107] Carter BO, Wang W, Adams DJ, Cooper AI. Gas Storage in “Dry Water” and “Dry Gel” Clathrates. Langmuir. 2010;26(5):3186–93.

[108] Hu G, Ye Y, Liu C, Meng Q, Zhang J, Diao S. Direct measurement of formation and dissociation rate and storage capacity of dry water methane hydrates. Fuel Processing Technology. 2011;92(8):1617–22.

[109] Lin W, Delahaye A, Fournaison L. Phase equilibrium and dissociation enthalpy for semi-clathrate hydrate of CO_2+TBAB. Fluid Phase Equilibria. 2008;264(1-2):220–7.

[110] Li S, Fan S, Wang J, Lang X, Wang Y. Semiclathrate Hydrate Phase Equilibria for CO_2 in the Presence of Tetra-n-butyl Ammonium Halide (Bromide, Chloride, or Fluoride). Journal of Chemical & Engineering Data. 2010;55(9):3212–5.

[111] Lin W, Dalmazzone D, Fürst W, Delahaye A, Fournaison L, Clain P. Thermodynamic properties of semiclathrate hydrates formed from the TBAB+TBPB water and CO_2+TBAB+TBPB+water systems. Fluid Phase Equilibria. 2014;372:63–8.

[112] Mohammadi AH, Eslamimanesh A, Belandria V, Richon D. Phase Equilibria of Semiclathrate Hydrates of CO_2, N_2, CH_4, or H_2 + Tetra-n-butylammonium Bromide Aqueous Solution. Journal of Chemical & Engineering Data. 2011;56(10):3855–65.

[113] Fukumoto A, Sales Silva LP, Paricaud P, Dalmazzone D, Fürst W. Modeling of the dissociation conditions of H_2+CO_2 semiclathrate hydrate formed with TBAB, TBAC, TBAF, TBPB, and $TBNO_3$ salts. Application to CO_2 capture from syngas. International Journal of Hydrogen Energy. 2015;40(30):9254–66.

[114] Linga P, Kumar R, Englezos P. The clathrate hydrate process for post and pre-combustion capture of carbon dioxide. Journal of Hazardous Materials. 2007;149(3):625–9.

[115] Ma ZW, Zhang P, Wang RZ, Furui S, Xi GN. Forced flow and convective melting heat transfer of clathrate hydrate slurry in tubes. International Journal of Heat and Mass Transfer. 2010;53(19):3745–57.

[116] Darbouret M, Cournil M, Herri J-M. Rheological study of TBAB hydrate slurries as secondary two-phase refrigerants. International Journal of Refrigeration. 2005;28(5):663–71.

[117] Oyama H, Shimada W, Ebinuma T, Kamata Y, Takeya S, Uchida T, et al. Phase diagram, latent heat, and specific heat of TBAB semiclathrate hydrate crystals. Fluid Phase Equilibria. 2005;234(1):131–5.

[118] Peng D-Y, Robinson DB. A New Two-Constant Equation of State. Industrial & Engineering Chemistry Fundamentals. 1976;15(1):59–64.

[119] Halder G. Introduction to chemical engineering thermodynamics: PHI Learning Pvt. Ltd., 2014.

[120] Haligva C, Linga P, Ripmeester JA, Englezos P. Recovery of Methane from a Variable-Volume Bed of Silica Sand/Hydrate by Depressurization. Energy & Fuels. 2010;24(5):2947–55.

[121] Babu P, Kumar R, Linga P. A New Porous Material to Enhance the Kinetics of Clathrate Process: Application to Precombustion Carbon Dioxide Capture. Environmental Science & Technology. 2013;47(22):13191–8.

[122] Kang SP, Lee H, Ryu BJ. Enthalpies of dissociation of clathrate hydrates of carbon dioxide, nitrogen, (carbon dioxide+ nitrogen), and (carbon dioxide + nitrogen+ tetrahydrofuran). The Journal of Chemical Thermodynamics. 2001;33(5):513–21.

[123] Zheng H, Huang Q, Wang W, Long Z, Kusalik PG. Induction Time of Hydrate Formation in Water-in-Oil Emulsions. Industrial & Engineering Chemistry Research. 2017;56(29):8330–9.

[124] Marcolongo JP, Mirenda M. Thermodynamics of Sodium Dodecyl Sulfate (SDS) Micellization: An Undergraduate Laboratory Experiment. Journal of Chemical Education. 2011;88(5):629–33.

[125] Koehler RD, Raghavan SR, Kaler EW. Microstructure and Dynamics of Wormlike Micellar Solutions Formed by Mixing Cationic and Anionic Surfactants. The Journal of Physical Chemistry B. 2000;104(47):11035–44.

[126] Kume G, Gallotti M, Nunes G. Review on Anionic/Cationic Surfactant Mixtures. Journal of Surfactants and Detergents. 2008;11(1):1–11.

[127] Zhang L, Kuang Y, Dai S, Wang J, Zhao J, Song Y. Kinetic enhancement of capturing and storing greenhouse gas and volatile organic compound: Micro-mechanism and micro-structure of hydrate growth. Chemical Engineering Journal. 2020;379:122357.

[128] Tang J, Zeng D, Wang C, Chen Y, He L, Cai N. Study on the influence of SDS and THF on hydrate-based gas separation performance. Chemical Engineering Research and Design. 2013;91(9):1777–82.

[129] Mehta SK, Bhasin KK, Chauhan R, Dham S. Effect of temperature on critical micelle concentration and thermodynamic behavior of dodecyldimethylethylammonium bromide and dodecyltrimethylammonium chloride in aqueous media. Colloids and Surfaces A: Physicochemical and Engineering Aspects. 2005;255(1):153–7.

[130] Xu C-G, Yu Y-S, Ding Y-L, Cai J, Li X-S. The effect of hydrate promoters on gas uptake. Physical Chemistry Chemical Physics. 2017;19(32):21769–76.

[131] Linga P, Daraboina N, Ripmeester JA, Englezos P. Enhanced rate of gas hydrate formation in a fixed bed column filled with sand compared to a stirred vessel. Chemical Engineering Science. 2012;68(1):617–23.

[132] Kumar A, Sakpal T, Linga P, Kumar R. Enhanced carbon dioxide hydrate formation kinetics in a fixed bed reactor filled with metallic packing. Chemical Engineering Science. 2015;122:78–85.

[133] Belandria V, Mohammadi AH, Eslamimanesh A, Richon D, Sánchez-Mora MF, Galicia-Luna LA. Phase equilibrium measurements for semi-clathrate hydrates of the (CO_2+N_2+tetra-n-butylammonium bromide) aqueous solution systems: Part 2. Fluid Phase Equilibria. 2012;322-323:105–12.

[134] Meysel P, Oellrich L, Raj Bishnoi P, Clarke MA. Experimental investigation of incipient equilibrium conditions for the formation of semi-clathrate hydrates from quaternary mixtures of (CO_2+N_2+TBAB+H_2O). The Journal of Chemical Thermodynamics. 2011;43(10):1475–9.

[135] Cuevas A, Febrero M, Fraiman R. An anova test for functional data. Computational Statistics & Data Analysis. 2004;47(1):111–22.

[136] Mahmood ME, Al-Koofee DA. Effect of temperature changes on critical micelle concentration for tween series surfactant. Global Journal of Science Frontier Research Chemistry. 2013;13(4):1–7.

[137] Chou DK, Krishnamurthy R, Randolph TW, Carpenter JF, Manning MC. Effects of Tween 20® and Tween 80® on the Stability of Albutropin During Agitation. Journal of Pharmaceutical Sciences. 2005;94(6):1368–81.

[138] Zhong Y, Rogers RE. Surfactant effects on gas hydrate formation. Chemical Engineering Science. 2000;55(19):4175–87.

[139] Daniel-David D, Guerton F, Dicharry C, Torré J-P, Broseta D. Hydrate growth at the interface between water and pure or mixed CO_2/CH_4 gases: Influence of pressure, temperature, gas composition and water-soluble surfactants. Chemical Engineering Science. 2015;132:118–27.

[140] Shi M, Lang X, Wang Y, von Solms N, Fan S. Investigation of the Growth Kinetics of Tetra-n-butylammonium Bromide Hydrate Formation in Small Spaces. Energy & Fuels. 2019;33(4):3473–82.

[141] Wilson P, Haymet A. Hydrate formation and re-formation in nucleating THF/water mixtures show no evidence to support a “memory” effect. Chemical engineering journal. 2010;161(1–2):146–50.

[142] Park J, Shin K, Kim J, Lee H, Seo Y, Maeda N, et al. Effect of Hydrate Shell Formation on the Stability of Dry Water. The Journal of Physical Chemistry C. 2015;119(4):1690–9.

[143] Rasoolzadeh A, Javanmardi J, Eslamimanesh A, Mohammadi AH. Experimental study and modeling of methane hydrate formation induction time in the presence of ionic liquids. Journal of Molecular Liquids. 2016;221:149–55.

[144] Poling BE, Prausnitz JM, O'connell JP. The properties of gases and liquids. 5th ed: Mcgraw-hill New York, 2001.

[145] Mori YH, Mochizuki T. Mass transport across clathrate hydrate films — a capillary permeation model. Chemical Engineering Science. 1997;52(20):3613–6.

[146] Uchida T. Physical property measurements on CO_2 clathrate hydrates. Review of crystallography, hydration number, and mechanical properties. Waste Management. 1998;17(5):343–52.

[147] Sun Q, Kang YT. Review on CO_2 hydrate formation/dissociation and its cold energy application. Renewable and Sustainable Energy Reviews. 2016;62:478–94.

[148] Karpiński PH. Crystallization as a mass transfer phenomenon. Chemical Engineering Science. 1980;35(11):2321–4.

[149] Wang J, Zhang L, Ge K, Dong H. Capillary pressure in the anisotropy of sediments with hydrate formation. Fuel. 2021;289:119938.

[150] Babu P, Yee D, Linga P, Palmer A, Khoo BC, Tan TS, et al. Morphology of Methane Hydrate Formation in Porous Media. Energy & Fuels. 2013;27(6):3364–72.

[151] Wang X, Dennis M. Phase Equilibrium and Formation Behavior of the CO_2–TBPB Semiclathrate Hydrate for Cold Storage Applications. Journal of Chemical & Engineering Data. 2017;62(3):1083–93.

[152] Hirata A, Mori YH. How liquids wet clathrate hydrates: some macroscopic observations. Chemical Engineering Science. 1998;53(14):2641–3.

[153] Liang H, Guan D, Shi K, Yang L, Zhang L, Zhao J, et al. Characterizing Mass-Transfer mechanism during gas hydrate formation from water droplets. Chemical Engineering Journal. 2022;428:132626.

[154] Chun M-K, Lee H. Kinetics of formation of carbon dioxide clathrate hydrates. Korean Journal of Chemical Engineering. 1996;13(6):620–6.

[155] Ownby DW, Prapaitrakul W, King AD. The solubility of carbon dioxide and nitrous oxide in aqueous solutions of cetyltrimethylammonium bromide, sodium dodecyl sulfate, sodium 1-heptanesulfonate, and sodium perfluorooctanoate. Journal of Colloid and Interface Science. 1988;125(2):526–33.

[156] Caskey JA, Barlage WB. A study of the effects of soluble surfactants on gas absorption using liquid laminar jets. Journal of Colloid and Interface Science. 1972;41(1):52–62.

[157] Liu W, Li Y, Zhang L, Shen S, Yang M, Zhao J, et al. Modeling Gas Hydrate Formation from Ice Powders Based on Diffusion Theory. Theoretical Foundations of Chemical Engineering. 2019;53(2):305–17.

[158] Carroll J. Natural gas hydrates: a guide for engineers: Gulf Professional Publishing, 2020.

[159] Liang S, Liang D, Wu N, Yi L, Hu G. Molecular Mechanisms of Gas Diffusion in CO_2 Hydrates. The Journal of Physical Chemistry C. 2016;120(30):16298–304.

[160] Zhang Y, Li X-S, Chen Z-Y, Xia Z-M, Wang Y, Li G. Experimental and modeling study on controlling factor of methane hydrate formation in silica gels. Applied Energy. 2018;225:827–34.

[161] Dashti H, Thomas D, Amiri A. Modeling of hydrate-based CO_2 capture with nucleation stage and induction time prediction capability. Journal of Cleaner Production. 2019;231:805–16.

[162] Jakobsen HA. Chemical Reactor Modeling: Multiphase Reactive Flows: Springer Berlin Heidelberg, 2008.

[163] Huang D, Fan S. Thermal Conductivity of Methane Hydrate Formed from Sodium Dodecyl Sulfate Solution. Journal of Chemical & Engineering Data. 2004;49(5):1479–82.

[164] Balasuwatthi P, Dechabumphen N, Saiwan C, Scamehorn JF. Contact angle of surfactant solutions on precipitated surfactant surfaces. II. Effects of surfactant structure, presence of a subsaturated surfactant, pH, and counterion/surfactant ratio. Journal of Surfactants and Detergents. 2004;7(1):31–40.

[165] Riazi MR. A new method for experimental measurement of diffusion coefficients in reservoir fluids. Journal of Petroleum Science and Engineering. 1996;14(3):235–50.

[166] Zhang F, Wang X, Wang B, Lou X, Lipiński W. The Effect of Silica Gel Nanopores and Surfactants on CO_2 Hydrate Formation Kinetics: An Experimental and Modeling Study Based on Shrinking Core Model. SSRN Electronic Journal. 2022.

[167] Penman HL. Gas and vapour movements in the soil: I. The diffusion of vapours through porous solids. The Journal of Agricultural Science. 1940;30(3):437–62.

[168] Bhatia SK. Directional autocorrelation and the diffusional tortuosity of capillary porous media. Journal of Catalysis. 1985;93(1):192–6.

[169] Froment GF, Bischoff KB, De Wilde J. Chemical reactor analysis and design: Wiley New York, 1990.

[170] Fateen S-EK, Khalil MM, Elnabawy AO. Semi-empirical correlation for binary interaction parameters of the Peng–Robinson equation of state with the van der Waals mixing rules for the prediction of high-pressure vapor–liquid equilibrium. Journal of Advanced Research. 2013;4(2):137–45.

[171] Søreide I, Whitson CH. Peng-Robinson predictions for hydrocarbons, CO_2, N_2, and H_2S with pure water and NaCI brine. Fluid Phase Equilibria. 1992;77:217–40.